Ph.D. Dissertation

Synoptic–dynamic characteristics of summertime heavy rainfall events in the Republic of Korea

한국 여름철 집중호우의 종관 및 역학적 특징

February 2023

School of Earth and Environmental Sciences

Seoul National University

Atmospheric Science Major

Chanil Park

Synoptic–dynamic characteristics of summertime heavy rainfall events in the Republic of Korea

한국 여름철 집중호우의 종관 및 역학적 특징

Submitting a Ph.D. Dissertation
October 2022

School of Earth and Environmental Sciences
Seoul National University
Atmospheric Science Major

Chanil Park

Confirming the Ph.D. Dissertation
written by Chanil Park
January 2023

Chair	Chang-Hoi Ho (Seal)
Vice Chair	Seok-Woo Son (Seal)
Examiner	Yukari Takayabu (Seal)
Examiner	Sang-Hun Park (Seal)
Examiner	Dong-Hyun Cha (Seal)

ABSTRACT

Heavy rainfall events (HREs) are the most frequent natural disaster from which people in South Korea recurrently suffer every summer. However, our understanding of their mechanisms has been still limited because many previous studies were confined to case studies or qualitative analyses. In this dissertation, the synoptic–dynamic characteristics of HREs in the summer monsoon period in South Korea are elaborated both quantitatively and qualitatively based on all historical events that occurred in the recent four decades. First, by separately considering the HREs resulting from tropical cyclones (TCs; 18.9%) and those not directly related to TCs (81.1%), their climatological features are drawn through composite and statistical analyses. This result is then extended to their further synoptic–dynamic details as below.

By numerically solving the quasigeostrophic omega equation, it is found that the vertical motion of non-TC-induced HREs (hereafter, simply HREs) is initially driven dynamically, but diabatic uplift becomes dominant in the mature stage of HREs. This implies the importance of dynamic processes in triggering HREs and nonlinear dynamic–diabatic feedback in the subsequent growth of HREs. By decomposing Q vectors into shearwise and transverse components to delineate the dynamical processes, it is further revealed that the dynamic omega is closely associated with a baroclinically-deepening trough in the upper troposphere. The role of thermally-direct secondary circulation on the entrance region of the upper-level jet, which has been emphasized in the literature as a key driver of HREs, turns out to be relatively minor.

The quasigeostrophic diagnosis of vertical motion of HREs can be robustly applied to most summertime HREs, but the clustering analysis shows that HREs could occur under various surface weather patterns depending on the strengths and/or locations of surface synoptic-scale cyclones and the North Pacific high. Each cluster exhibits a distinct temporal evolution of surface weather patterns with different favorable seasons and regions. This result provides important forecasting factors to be differently considered depending on the synoptic categorization of HREs.

While most previous studies on TC rainfall in South Korea have focused on the characteristics of TC itself and local factors (e.g., topography), it is found that TC-induced HREs (hereafter, TC-HREs) are also largely sensitive to midlatitude condition. The TC-HREs under strongly baroclinic condition are characterized by amplifying tropopause circulation (by negative potential vorticity advection by TC-induced divergent outflow) and structural changes of TC (reminiscent of extratropical transition). The synergistic TC–midlatitude flow interaction allows for widely enhanced quasigeostrophic forcing for ascent, causing heavy rainfall even before TC gets close to South Korea. The TC-HREs under weakly baroclinic condition, in contrast, do not accompany the meandering tropopause flow. In the absence of strong interaction with midlatitude flow, TC rapidly dissipates after entering midlatitude, and the upward motion is confined to the inherent diabatic TC convection. As a result, heavy rainfall occurs only when TC locates in the right vicinity of the country.

Lastly, the record-breaking monsoon rainfall in the summer of 2020 is investigated. The abrupt change of HRE nature in late July is particularly of interest. While the HREs from 29 June to 27 July (P1) were determined by the passage of extratropical cyclones, those from 28 July to 15 August (P2) mainly occurred by the quasi-stationary monsoon rainband and mesoscale instability thereon. This sudden synoptic transition is explained by atmospheric teleconnections. During P1, the subtropical high anomalously extended westward but its northward expansion was hindered by the suppressed convection over the South China Sea. In contrast, the enhanced South China Sea convection in P2 prompted an abrupt northward jump of the subtropical high. The resulting monsoon circulations established favorable environments for extratropical cyclones and monsoon rainband, respectively, in the two subperiods. The atmosphere–ocean coupled mode over the Indo-western Pacific was particularly related to the suppressed convection over the South China Sea in P1. The summer North Atlantic oscillation also secondarily contributed to the anomalous monsoon flows in P1 and P2 with opposite phases, although the reasons for its synchronized phase transition with the South China Sea convection is still

unclear. The summer of 2020 implies that multiscale analyses would be beneficial in future work for a better understanding of HREs.

Keywords: Heavy rainfall events, Synoptic–dynamic meteorology, East Asian summer monsoon (Changma), Quasigeostrophic diagnosis, South Korea

Student Number: 2017-20561

LIST OF TABLES

LIST OF FIGURES

Figure 2.7. The left panels are the number of **a** HREs and **b** TC-HREs in 10-day bins in JJAS (colored bars) overlaid with rainfall climatology (mm day^{-1}, black line). The right panels are spatial distributions of the probability of occurrence of **c** HREs and **d** TC-HREs (%, colored square) overlaid with terrain (m, shading). The probability of occurrence means the conditional probability that a given ASOS station records an HRE (or TC-HRE) when the event occurs in South Korea.

Figure 3.1. Composites of the 250-hPa GPH (gpm, black contours), 500-hPa ω (blue contours with a 0.04-Pa s^{-1} interval), 250-hPa horizontal wind speed (shading) and **IVT** anomaly (kg m^{-1} s^{-1}, vectors) for the 318 HREs in their mature stage. The **IVT** anomaly is shown only for the statistically significant values at the 95% confidence level, based on a two-tailed Student's *t* test.

Figure 3.2. Schematic illustration of the typical QG vertical motion by **a** the transverse Q vector and **b** shearwise Q vector around the jet streak, and **c** by the shearwise Q vector around the trough in the Northern Hemisphere. Gray dotted lines denote the isentropes with warm air to the south, and black and purple arrows indicate the geostrophic streamlines and Q vectors, respectively. The shaded regions in pink and apricot, respectively, denote the QG descent and ascent. The **n** and **s** indicate the cross-isentropic and along-isentropic unit vectors, respectively. Diagrams of **a** and **b** are partly taken from Martin (2014).

Figure 3.3. Lagged composites of **a** 250-hPa GPH (gpm, contours) and its anomalies (gpm, shading), and **b** 850-hPa GPH (gpm, contours), its anomalies (gpm, shading) and **IVT** anomaly (kg m^{-1} s^{-1}, vectors) at –36, –18 and 0 h. The GPH anomalies are stippled when statistically significant at the 95% confidence level. The **IVT** anomaly in **b** is shown only when statistically significant at the 95% confidence level. A two-tailed Student's *t* test is used.

Figure 3.4. a Lagged composites of ω (contours with a 0.04-Pa s^{-1} interval), dynamic forcing (10^{-18} m kg^{-1} s^{-1}, shading) and Q vector (10^{-12} m^2 kg^{-1} s^{-1}, vectors) at 500 hPa at –36, –18 and 0 h. **b** As in **a** but for diabatic forcing at 500 hPa and **IVT** anomaly (kg m^{-1} s^{-1}, vectors). The **IVT** anomaly in **b** is shown only when statistically significant at the 95% confidence level, based on a two-tailed Student's *t* test. Note that the color bar range in **b** is ten times larger than that in **a**. The boxed regions denote the centers of upward motion at 500 hPa except for –36 h when the upward motion is less organized. The boxed region at 0 h is identical to that in Fig. 2.3b.

Figure 3.5. a Lagged composites (–36, –18 and 0 h) of the latitude-pressure cross section of ω_{Dyn} (blue contours with a 0.02-Pa s^{-1} interval), horizontal wind speed (>12 m s^{-1}, black contours with a 4-m s^{-1} interval) and dynamic forcing (10^{-18} m kg^{-1} s^{-1}, shading) averaged over the longitudinal band indicated at the bottom right corner of each panel. The longitudinal ranges chosen here are identical to the boxed regions in Fig. 3.4. **b** As in **a**, but for ω_{Dia} and diabatic forcing. The approximate location of South Korea is denoted with three horizontal black lines. Note that the color bar range in **b** is three times larger than that in **a**.

Figure 3.6. Vertical profiles of ω (black solid), ω_{QG} (black dashed), ω_{Dyn} (blue dashed), ω_{Beta} (green dashed) and ω_{Dia} (red dashed) averaged over the boxed regions in Fig. 3.4 in **a** the developing stage (–18 h) and **b** the mature stage (0 h) of HREs. For ω_{QG}, ω_{Dyn} and ω_{Dia}, the 95% confidence interval is shaded based on a bootstrap test with 10,000 times resampling.

Figure 4.9. As in Fig. 2.4a, but for the six HRE clusters: 850-hPa θ_e (K, shading) and the Petterssen frontogenesis function applied to the 850-hPa θ_e [blue contours for positive values with a 1-K (100 km day)$^{-1}$ interval]. The order of panels follows that of descriptions in the main text.

Figure 4.10. As in Fig. 2.4c, but for the six HRE clusters: longitude-pressure cross section of GPH anomalies (gpm, shading) and vertical velocity (contours with a 0.04 Pa s^{-1} interval). The order of panels follows that of descriptions in the main text.

Figure 4.11. a ω (solid line), ω_{QG} (dashed line), ω_{Dyn} (blue bars) and ω_{Dia} (red bars) at 500 hPa in the mature stage (0 h) of the six HRE clusters estimated over the boxed region in the right panel of Fig. 2.3b. The ω_{Beta} is not shown as it is negligibly small. The ratio of ω_{Dyn} to ω_{Dia} is annotated on the top of the bars. **b** As in **a**, but for ω_{Dyn} (blue line), ω_n (green bars) and ω_s (sky-blue). The order of bars follows that of descriptions in the main text.

Figure 5.1. Infrared imagery of transitioning typhoons Ginger at **a** 0332 UTC 28, **b** 0032 UTC 29, and **c** 1232 UTC 29 September 1997, and Stella at **d** 0032 UTC 15, **e** 1232 UTC 15, and **f** 1232 UTC 16 September 1998. The figure is taken from Klein et al. (2000).

Figure 5.2. Overview of modification of upper-level midlatitude flow by transitioning TCs. The dark red line denotes the meandering tropopause waveguide separating stratospheric high PV air (dark gray) and tropospheric low PV air (light gray). The ellipse shaded by orange denotes the jet streak. The purple semitransparent area indicates the area of increased forecast uncertainty. The figure is taken from Keller et al. (2019).

Figure 5.3. Schematic representation of midlatitude flow amplification by the divergent outflow of a TC. The black contours, shadings and vectors denote the PV, horizontal wind speed and divergent wind, respectively, near the tropopause level. The figure is taken from Archambault et al. (2013).

Figure 5.4. Tracks of TCs involved in TC-HREs in South Korea in JJAS 1979–2020 with different colors depending on the status (e.g., TD: orange, TC: purple, ETC: blue). The locations of TCs at 0 h (mature stage of TC-HREs) are marked by green dots. The tropical cyclogenesis is denoted by purple dots. A thick black line and the circles thereon indicate the mean track and daily TC locations from -8 day to +3 day (open circle denotes the mean TC location at 0 h), respectively. The area enclosed by the black dotted line is the domain for determining TC-HREs.

Figure 5.5. a,**b** The 1×2 SOM clustering results. The plotted variable is the composited 2-PVU surface height (km) at 0 h for C1 and C2, respectively, over the clustering domain (30°–53°N and 105°–145°E). The mean location of TCs is indicated by TC symbol. **c**,**d** The number of TC-HREs in 10-day bins in JJAS for C1 and C2, respectively.

Figure 5.6. a,**b** As in Fig. 5.4, but for C1 and C2, respectively, in a narrower domain.

Figure 5.7. a,**b** Time series of 12-h accumulated rainfall amount at the station where the maximum 12-h accumulated rainfall is recorded at 0 h for C1 and C2, respectively. **c**,**d** Composites of the maximum 12-h accumulated rainfall amount (mm) during TC-HREs across 57 stations for C1 and C2, respectively. The terrain height (m) is shaded in brown.

Figure 5.8. Lagged composites (–48, –24, 0 and +24 h) of 2-PVU surface height (km, black contours) and its anomaly (km, shading), and horizontal wind speed at 2-PVU surface (green contours with a 3-m s^{-1} interval from 27 m s^{-1}) for **a**–**d** C1 TC-HREs and **e**–**h** C2 TC-HREs. The statistically significant anomalies at the 95% confidence level based on a two-tailed Student's *t* test are stippled. The mean location of TCs is indicated by the TC symbol.

Figure 5.9. Lagged composites (–48, –24, 0 and +24 h) of GPH (gpm, contours) and its anomaly (gpm, shading) at 700 hPa, and **IVT** (>300 kg m^{-1} s^{-1}, vectors) for **a**–**d** C1 TC-HREs and **e**–**h** C2 TC-HREs. The statistically significant anomalies at the 95% confidence level based on a two-tailed Student's *t* test are stippled. The terrain higher than 3,000 m is masked by gray.

Figure 5.10. Lagged composites (–48, –24, 0 and +24 h) of 700-hPa GPH (gpm, contours) and its anomaly (gpm, shading) in the TC-relative frame for **a**–**d** C1 TC-HREs and **e**–**h** C2 TC-HREs.

Figure 5.11. Lagged composites (–48, –24, 0 and +24 h) of longitude–pressure cross section of GPH anomaly (gpm, shading) and PV anomaly (contours with a 0.1-PVU interval) latitudinally averaged over the boxed region in Fig. 2.5b (33°–39°N) for **a**–**d** C1 TC-HREs and **e**–**h** C2 TC-HREs. The dynamic tropopause (2 PVU) is marked by a thick contour. Only the PV anomalies statistically significant at the 95% confidence level based on a two-tailed Student's *t* are shown. The statistically significant GPH anomaly is stippled. The longitudinal center of South Korea is marked by a purple triangle.

Figure 5.12. Lagged composites (–48, –24, 0 and +24 h) of latitude–pressure cross section of PV (PVU, shading), ω (contours with a 0.04-Pa s^{-1} interval), horizontal wind speed (green contours with a 3-m s^{-1} interval from 27 m s^{-1}), and meridional-vertical wind (>5 m s^{-1}, vectors; ω is multiplied by an aspect ratio of -45.29) longitudinally averaged over the boxed region in Fig. 2.5b (124°–131°E) for **a**–**d** C1 TC-HERs and **e**–**h** C2 TC-HREs. The dynamic tropopause (2 PVU) is highlighted by a thick contour. The mean latitudinal position of TCs is indicated by the TC symbol. The latitudinal center of South Korea is marked by a purple triangle.

Figure 5.13. Composites of PV tendency budget for C1 TC-HREs at 0 h: **a** rate of local PV change ($\frac{\partial P}{\partial t}$; shading), **b** rotational wind (m s^{-1}, vectors) and its resulting PV advection ($-\mathbf{V}_\psi \cdot \nabla P$; shading), and **c** divergent wind (m s^{-1}, vectors) and its resulting PV advection ($-\mathbf{V}_\chi \cdot \nabla P$; shading) averaged for the layer of 250–150 hPa. Unit is PVU day^{-1}. The 250–150-hPa layer-mean PV is also contoured (unit: PVU). The mean location of TCs is indicated by the TC symbol. **d**–**f** As in **a**–**c** but for C2 TC-HREs at 0 h.

Figure 5.14. Time series of the 250–150-hPa layer-averaged PV advections by rotational ($-\mathbf{V}_\psi \cdot \nabla P$; dotted lines) and divergent winds ($-\mathbf{V}_\chi \cdot \nabla P$; solid lines), and rate of local PV change ($\frac{\partial P}{\partial t}$; bars) averaged over the boxed regions "A" (colored in orange) and "B" (colored in navy) in Figs. 5.13a,d for **a** C1 TC-HREs and **b** C2 TC-HREs. Unit is PVU day^{-1}.

Figure 5.15. Vertical profiles of ω from ERA5, and ω_{QG}, ω_{Dyn}, ω_{Beta}, ω_{Dia} and ω_{bf} obtained from omega equation inversion, which are averaged around South Korea (33°–39°N and 124°–131°E; boxed region in Fig. 2.5b) for **a** C1 TC-HREs and **b** C2 TC-HREs at 0 h. The 95% confidence interval is shaded based on the 10,000 times of bootstrap resampling. Unit is Pa s^{-1}.

Figure 5.16. Composites of **a** ω_s (Pa s^{-1}, shading), $Q_s\mathbf{s}$ (10^{-12} m^2 kg s^{-1}, vectors) and GPH (gpm, contours), and **b** ω_n (Pa s^{-1}, shading), $Q_n\mathbf{n}$ (10^{-12} m^2 kg s^{-1}, vectors) and horizontal wind speed (m s^{-1}, contours) at 250 hPa for C1 TC-HREs at 0 h. **c**,**d** As in **a**,**b** but for 700 hPa. Only the horizontal wind speed greater than 27 m s^{-1} and 12 m s^{-1} are contoured in **b** and **d**, respectively. The best track-based mean TC center is indicated by the TC symbol.

Figure 5.17. As in Fig. 5.16, but for C2 TC-HREs.

Figure 5.18. Time series of **a** ω, ω_{QG}, ω_{Dyn}, and ω_{Dia}, and **b** ω_{Dyn} by the upper (400–100 hPa; subscript *u*) and lower layers (1000–400 hPa; subscript *l*), and their transverse and shearwise components averaged around South Korea (33°–39°N and 124°–131°E; boxed region in Fig. 2.5b) for C1 TC-HREs from –48 h to +24 h. **c**,**d** As in **a**,**b**, but for C2 TC-HREs.

Figure 5.19. The box-whisker plots of lifetime minimum center pressure **a** for all TCs in C1 and C2, and **b** for the resampled TCs in C1 and C2. The TCs are resampled by constraining their lifetime minimum center pressure to range from 925 hPa to 975 hPa. As a result, 30 and 14 TCs are retained in C1 and C2, respectively, in the resampled sample. The orange line and green triangle denote the median and mean, respectively.

Figure 6.1. a Yearly time series of JJAS accumulated rainfall (black line) and its anomaly (colored bars) for the period of 1971–2020. Here, the anomaly is defined as a deviation from the 50-year (1971–2020) climatology, and its ± 1.0 standard deviation is marked by dotted lines. **b** Daily time series of daily accumulated rainfall amount in the summer of 2020 (gray bars) and the 50-year climatology (black line). A 9-day moving average is applied. The first and second rainy periods in 2020 are denoted by apricot shadings. In **a** and **b**, the accumulated rainfall amounts are averaged over 45 stations with continuous observations from 1971 to 2020. **c** Hourly time series of the 12-hour accumulated rainfall amounts in JJAS 2020. Rainfall amounts greater than 110 mm $(12\ h)^{-1}$ are highlighted in four different colors depending on their associated synoptic systems, i.e., MRB (red), ETC (blue), ETC after ET (purple) and TC (green). In **c**, the maximum rainfall amounts among 91 stations operated in 2020 are shown. The areas shaded in sky-blue and pink denote P1 (29 June–27 July) and P2 (28 July–15 August), respectively.

Figure 6.2. The 850-hPa GPH (contours, gpm) and relative vorticity (shading, CVU) truncated at T42 spatial resolution for all HREs (including TC-HREs) listed in Table 6.1. A snapshot at the reference time of each HRE (adjusted to the nearest 6-hourly mark) is shown. The title of each panel is colored in accordance with the associated synoptic systems (red, blue, purple, and green for MRB, ETC, ET, and TC, respectively).

Figure 6.3. As in Fig. 6.2, but for satellite images (10.5-mm infrared channel).

Figure 6.4. Tracks of TCs mentioned in Table 6.1. The stages of TD or ETC are indicated by dashed lines.

Figure 6.5. Composited synoptic structures of the four HREs in P1 (HREs 2–5 in Table 6.1). **a** GPH (gpm, contours) at 850 hPa, IVT anomaly (kg m^{-1} s^{-1}, shading) and **IVT** anomaly (>100 kg m^{-1} s^{-1}, vectors). **b** Vertical motion at 500 hPa (blue contours with a 0.2-Pa s^{-1} interval), 1.5- and 3-PVU at the 350-K isentropic surface (black contours), and horizontal wind speed at 250 hPa (m s^{-1}, shading). **c** GPH at 500 hPa (gpm, contours) and θ_e at 850 hPa (K, shading). The 5,840- and 5,880-gpm contours are highlighted with thick lines. **d** Latitude-pressure cross section of θ_e (K, shading) averaged over 123°–133°E. The 336-K θ_e is

highlighted with a dashed line. The approximate meridional location of South Korea is denoted with three horizontal black lines.

Figure 6.6. As in Fig. 6.5 but for the six HREs in P2 (HREs 6–8 and HREs 10–12 in Table 6.1).

Figure 6.7. Hovmöller diagram (time-latitude) of IVT anomaly (kg m^{-1} s^{-1}, shading), 5,840- and 5,880-gpm GPHs at 500 hPa (thick black line), and their climatologies (thick green line) averaged over 123°–133°E during the period of 29 June–15 August 2020 (P1+P2). A 9-day moving average is applied. The approximate meridional location of South Korea is indicated by two thin black lines.

Figure 6.8. a,**c** The GPH at 500 hPa (gpm, black contours), θ_e anomaly at 850 hPa (K, shading) and **IVT** anomaly (>100 kg m^{-1} s^{-1}, vectors) in **a** P1 and **c** P2. The 5,840 and 5,880 gpm, and their climatologies are denoted by thick black and green lines, respectively. The terrain higher than 1500 m is masked by gray shading. **b**,**d** The GPH (gpm, black contours) and horizontal wind speed anomaly (m s^{-1}, shading) at 250 hPa in **b** P1 and **d** P2. The 11010 gpm and its climatology are denoted by thick black and green lines, respectively.

Figure 6.9. Hovmöller diagram (longitude-time) of the T42-filtered relative vorticity at 850 hPa (shading, CVU) averaged over **a** 30°–40°N and **b** 42°–52°N during the period of 29 June–15 August 2020 (P1+P2). The approximate zonal location of South Korea is indicated by two thin black lines. In **a**, the ETCs that triggered the HREs are marked by yellow triangles.

Figure 6.10. ψ anomaly at 500 hPa (contours with a 0.1×10^{-7} m^2 s^{-1}), horizontal wind anomaly at 500 hPa (>3 m s^{-1}, vectors) and OLR anomaly (W m^{-2}, shading) in **a** P1 and **b** P2.

Figure 6.11. The 500-hPa ψ anomaly (10^{-7} m^2 s^{-1}, contours and shading) and **IVT** anomaly (kg m^{-1} s^{-1}, vectors) when the SCS OLR index is **a** above +1.0σ and **b** below –1.0σ for the period of 29 June–15 August from 1979 to 2019. **c**,**d** As in **a**,**b** but for **c** the SCS OLR index >+1.0σ and the SNAO index <–1.0σ and **d** the SCS OLR index <–1.0σ and the SNAO index >+1.0σ. The statistically significant ψ anomalies at the 90% confidence level based on Student's t test are stippled. Only the statistically significant **IVT** anomalies at the same confidence level are shown. Two boxed regions denote the SCS (100°–130°E, 10°–22.5°N) and eastern North Atlantic (10°W–25°E, 52°–72°N). The number of days considered is indicated in the upper-right corner of each plot. The number of degrees of freedom, by considering consecutive days as one event, is given in parenthesis.

Figure 6.12. Daily time series of the SCS OLR index and SNAO index normalized by their one standard deviation during the period of 29 June–15 August 2020 (P1+P2). A 9-day running average is applied.

Figure 6.13. a Monthly time series of SST anomaly (K) over the Niño 3.4 region (5°S–5°N, 190°–240°E) from January 2018 to October 2020. **b** Daily time series of SST anomaly (K) over the tropical Indian Ocean (40°–100°E, 15°S–15°N; green) and SCS (100°–130°E, 10°–22.5°N; red) during the period of 29 June–15 August 2020 (P1+P2). A 9-day moving average is applied. **c** As in Fig. 6.10 but for GPH at 500 hPa (gpm, black contours), OLR anomaly (W m^{-2}, shading) and 10-m horizontal wind anomaly (>1 m s^{-1}, vectors) in P1. The 5,880 gpm and its climatology are also plotted by thick black and green lines, respectively.

Figure 6.14. Phase diagram of BSISO mode 1 during the period of 29 June–15 August 2020 (P1+P2). See Lee et al. (2013) for details of the BSISO index.

Contents

Chapter 1. Introduction

1.1. Background

1.1.1. Precipitation climatology in South Korea

One of the most important meteorological factors that characterize the summer climate of South Korea is a large amount of precipitation. Approximately 66% of annual precipitation is concentrated from June to September (JJAS), a summer monsoon period of the country (see a line in Fig. 1.1). However, this is not simply explained by the continuous rainfall with moderate intensity. Instead, this warm-season peak of precipitation amount is closely related to heavy rainfall events (HREs) of which 90% occur in JJAS (see colored bars in Fig. 1.1). In recent decades, there were several catastrophic HREs in the country. In August 1998, for example, the 18-day lasting HRE occurred, causing nationwide flash floods (Choi et al. 2008; Lee et al. 2008a). At the end of August 2002, a daily rainfall in excess of 870 mm was observed on the east coast during the passage of typhoon Rusa (Park and Lee 2007). More recently, South Korea experienced record-breaking monsoon rainfall in the summer of 2020 due to the consecutive HREs (see chapter 6 for details of this extraordinary summer).

During the last three decades (1973–2005), annual precipitation in South Korea has increased due to the increase in both frequency and intensity of warm-season HREs (Jung et al. 2011). The regional climate model simulations suggest that Further increases in HRE frequency and intensity are expected under climate change scenarios (Cha et al. 2016; Kim et al. 2018). Therefore, an improved understanding of the dynamic and thermodynamic characteristics of HREs is an essential and still ongoing task to produce reliable predictions of HREs and thereby mitigate their socioeconomic impacts.

1.1.2. East Asian summer monsoon (EASM)

The summertime HREs in South Korea are significantly influenced by the EASM. In general, the EASM becomes pronounced as the North Pacific high (NPH; also known as the western North Pacific subtropical high), expands toward the east coast of the Asian continent, which allows southwesterly monsoon flow along its northern boundary. The early part of the EASM is often characterized by thousands-kilometer-long monsoon rainband (MRB) developing along the quasi-stationary monsoon front (Ninomiya 1984; Kodama 1992; Wang and LinHo 2002; Chen et al. 2004). Late in the EASM, the EASM rainfall becomes dominated by tropical cyclones (TCs) and midlatitude frontal activities, as the western ridge of the NPH shifts eastward due to the developing monsoon trough in the subtropical western North Pacific (Chen et al. 2004; Guo et al. 2017). These two distinct phases of the EASM produce a well-known bimodal rainfall distribution over East Asia (Wang and LinHo 2002; Chen et al. 2004; Lee et al. 2017), which is also evident in South Korea (Fig. 1.1).

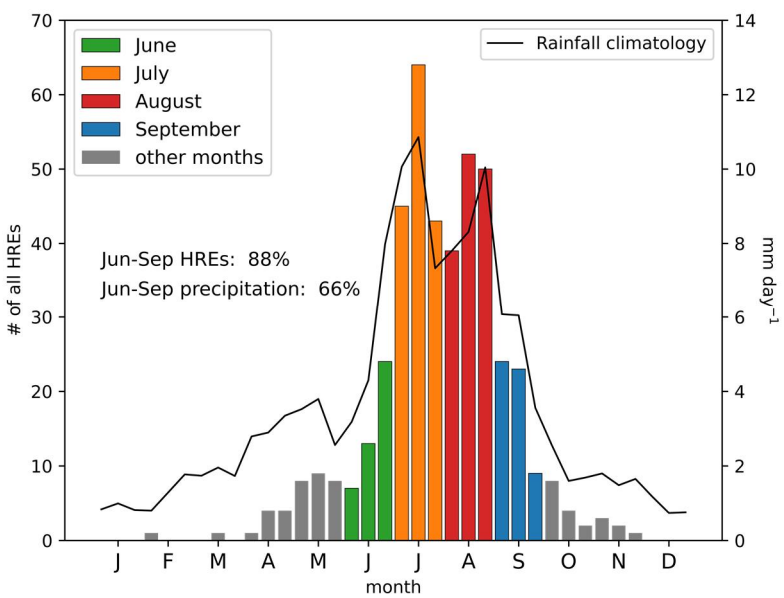

Figure 1.1. The number of all HREs in 10-day bins over the period of 1979–2018 (colored bars) overlaid with rainfall climatology (black line, mm day^{-1}). The HREs are defined as 12-h accumulated rainfall greater than 110 mm in any single weather station in South Korea.

1.1.3. Large-scale modulation of EASM

The EASM can be remotely influenced by atmospheric teleconnections. For example, the enhanced convection over the warm tropical Indian Ocean in the post–El Niño summer often leads to the increased monsoon southwesterly toward East Asia by organizing an anomalous anticyclone over the subtropical western North Pacific, which is the so-called Indo–western Pacific Ocean capacitor (IPOC; Xie et al. 2009, 2016). A meridional propagation of the Rossby wave excited by convection over the South China Sea (SCS), known as the Pacific–Japan (PJ) pattern (Nitta 1987; Kosaka and Nakamura 2006), can also drive abnormal behaviors of the NPH on intraseasonal to interannual time scales (Kosaka et al. 2011; Kubota et al. 2016; Noh et al. 2021).

The extratropical zonal wave trains also exert impacts on the East Asian summer climate. In boreal summer, two latitudinally well-separated waveguides are observed over the Eurasian continent (Chowdary et al. 2019). One is the waveguide for the circumglobal teleconnection pattern and the Silk Road along the subtropical jet at ~40°N (Ding and Wang 2005; Hong and Lu 2016). The other is along the large meridional gradient of static stability in northern Eurasia (Iwao and Takahashi 2008; Xu et al. 2019). The Rossby wave excited by the summer North Atlantic Oscillation (SNAO; Folland et al. 2009; Osborne et al. 2020) tends to propagate along this high-latitude waveguide (Wu et al. 2009; Seo et al. 2012; Yamaura and Tomita 2011; Li and Ruan 2018). The zonal wave trains along these two waveguides not only modulate large-scale components of the EASM (e.g., NPH and Okhotsk high) but also organize a quasi-stationary trough or ridge in the upper troposphere, bringing anomalous weather in East Asia (Nakamura and Fukamachi 2004; Kosaka et al. 2011; Orsolini et al. 2015; Liu et al. 2019). In chapter 6, it is found that the large-scale modulation of EASM by atmospheric teleconnection played a role in the record-breaking rainfall in the summer of 2020 in South Korea.

1.1.4. Changma

In a more regional sense, the Korean summer monsoon—a subsystem of the EASM known as "Changma"—is considered to be determined by five air masses with differing thermodynamic characteristics: 1) the maritime tropical air mass centered over the subtropical western North Pacific; 2) the monsoon tropical air mass related to the intertropical convergence zone; 3) the continental tropical air mass over central China, 4) the continental polar air mass from Siberia, and 5) the maritime polar air mass from the Okhotsk Sea (Fig. 1.2; Lee et al. 2017). For example, the large-scale MRB along the quasi-stationary monsoon front is typically considered to be the result of a clash between these air masses (Matsumoto et al. 1971; Tomita et al. 2011; Seo et al. 2011, 2015). The climatological background of Changma is more complicated because both the temperature and moisture contrasts are pronounced across the monsoon frontal zone (Seo et al. 2011; Lee et al. 2017). This contrasts with the Chinese (Meiyu) and Japanese summer monsoons (Baiu) which are characterized solely by the moisture and temperature gradients, respectively, due to the geographical location of the five air masses (Matsumoto et al. 1971; Tomita et al. 2011). It is suggested that the air mass perspective provides a useful framework to understand the summer monsoon rainfall and its variability in East Asia (e.g., Tomita et al. 2011; Seo et al. 2015; Kawasaki et al. 2021).

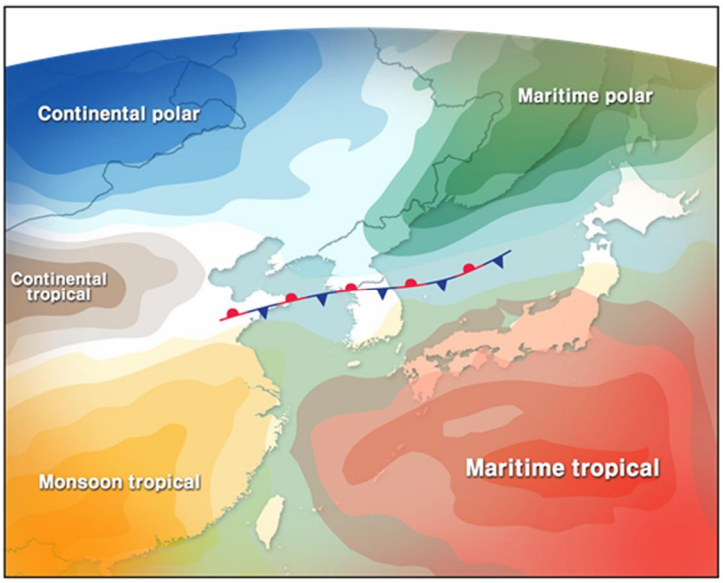

Figure 1.2. Schematic representation of the five warm-season air masses around the Korean Peninsula and quasi-stationary monsoon front.

1.1.5. Synoptic features of HREs

Although EASM (and Changma) provide a favorable environment for summer monsoon rainfall, HREs in South Korea have finer synoptic-scale (several hundred to a few thousand kilometers) structures that cannot be purely explained by monsoon circulation or air mass variability. In the case of South Korea, the reported synoptic conditions of the HREs in the literature can be summarized as follows (Lee et al. 1998; Shin and Lee 2005; Lee et al. 2008a,b; Hong and Lee 2009; Jeong et al. 2016; Kang et al. 2021):

I. A northward expansion of the NPH, a well-defined quasi-stationary monsoon front, and a strong southwesterly low-level jet (LLJ) supplying a tremendous amount of water vapor from the subtropics

II. An enhanced local baroclinicity and the associated upper-level jet (ULJ) responsible for vertical motion to the south of its entrance region via a thermally direct secondary circulation (Sawyer 1956; Eliassen 1962)

It has been found that the HREs preferably occur to the north of the LLJ nose and the south of the ULJ entrance (Lee et al. 1998; Lee et al. 2008a,b). In particular, the ULJ–LLJ coupling via secondary circulation (Fig. 1.3) has long been understood as a key driver of the vertical motion during HREs (the vertical motion mechanisms are revisited in chapter 3). The LLJ-induced moisture transport is often driven into a plume of tropospheric water vapor flux, known as an atmospheric river (Park et al. 2021a; Kwon et al. 2022). Based on the upper-tropospheric potential vorticity (PV) map, Horinouchi (2014) and Horinouchi and Hayashi (2017) demonstrated that the monsoon rainfall and moisture transport can be transiently modulated by baroclinic Rossby wave activities in the upper troposphere.

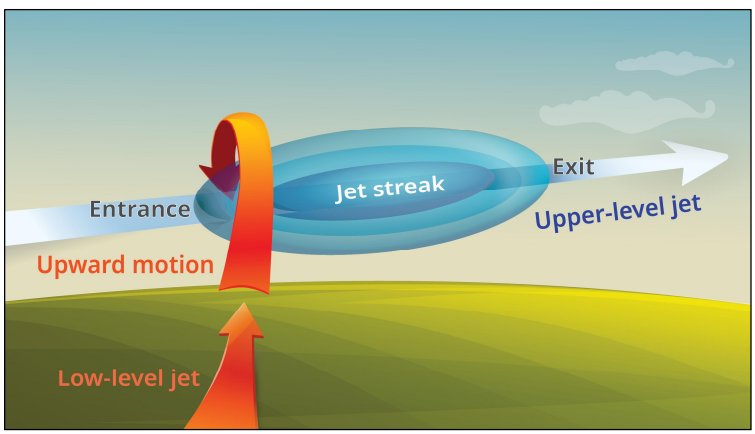

Figure 1.3 Schematic illustration of vertical coupling of ULJ and LLJ via a thermally-direct secondary circulation at the entrance region of the ULJ streak.

1.1.6. Mesoscale features of HREs

On a further finer scale, HREs in South Korea often accompany the mesoscale organized features which are responsible for the highly localized and spatially complicated nature of HREs (Jo et al. 2020). For example, the mesoscale convective systems (MCSs) whose horizontal scale ranges from a few to several hundred kilometers are often embedded in the synoptic background during the HREs (Sun and Lee 2002; Lee and Kim 2007; Shin et al. 2015, 2019; Jeong et al. 2016; Kang et al. 2021). By considering the morphological characteristics of MCSs

involved in HREs, Lee and Kim (2007) manually categorized MCSs therein into four types: 1) isolated thunderstorms, 2) convection bands, 3) squall lines, and 4) cloud clusters. The MCSs occasionally affect the same region for several hours through the regeneration of new convection cells, known as back-building behavior (Jeong et al. 2016; Kang et al. 2021). By conducting the cloud-resolving model simulations, Kang et al. (2021) emphasized the role of the high sea surface temperature (SST) of the Yellow Sea in the back-building development of the convection band-type MCSs.

1.1.7. Thermodynamic characteristics of HREs

Other important characteristics of HREs in South Korea involve their thermodynamic properties. Hong (2004) asserted that the HREs tend to occur under the moist adiabatic near-neutral condition with only a low-to-moderate amount of convective available potential energy (CAPE), which is generally smaller than that of the deep convective thunderstorms over the U.S. Great Plains, although similarly low-CAPE flooding events have been also reported in the central U.S. (e.g., Schumacher and Johnson 2008). Instead, they emphasized the role of a strong baroclinic environment around the Korean Peninsula, which facilitates the synoptic-scale forcing for HREs. In a similar vein, Sohn et al. (2013) reported that HREs generally occur through the warm-cloud processes with ample moisture fed by the organized synoptic-scale circulation (e.g., atmospheric rivers). According to Sogn and Sohn (2015), such warm-type HREs are more responsible for flood events over the Korean peninsula than those by deep convective clouds due to their longer duration and wider rainfall area (Doswell et al. 1996). Similar thermodynamic characteristics have been also reported for the Japanese HREs (Yokoyama et al. 2017; Hamada and Takayabu 2018).

1.1.8. Tropical cyclones (TCs)

The HREs in South Korea are also caused by TCs generated over the western North Pacific basin (i.e., Typhoon). According to the Korea Meteorological Administration (KMA), about three TCs make landfall in the country in a year

(KMA 2011). Park and Lee (2007) and Lee and Choi (2010) reported that an HRE by typhoon Rusa (2002) was reinforced by the juxtaposition of orographic lifting and the upper-level divergence on the equatorward side of the ULJ entrance. The super typhoons Maemi (2003) and Ewiniar (2006) hit South Korea with severe flooding events across the country although they exhibited distinct tracks (Choi et al. 2013). More recently, typhoon Chaba (2016) caused a record-breaking local rainfall [319 mm $(3\ h)^{-1}$] in the southeastern part of South Korea. The numerical experiments demonstrated that this HRE was reinforced by the warm SST anomaly in the East China Sea and the local topography in the HRE region (Cho et al. 2022).

Beyond case studies, some studies conducted statistical analyses of TC rainfall in South Korea. Nam et al. (2018) reported that only a small deviation of TC track in the west-east direction can lead to a largely different distribution of weather impacts in South Korea. Kim et al. (2019) found that the rainfall areas of TCs approaching the Korean Peninsula significantly increase with environmental vertical wind shear. Byun and Lee (2012) and Baek et al. (2015) analyzed HREs occurring in advance of TC arrival (i.e., predecessor rainfall events; Galarneau et al. 2010; Moore et al. 2013). They indicated that the proper midlatitude conditions (e.g., upstream trough and entrance region of ULJ) facilitate the warm and moist air remotely supplied by TCs to be lifted, leading to heavy rainfall in South Korea.

1.2. Aims of dissertation

As discussed in section 1.1, the summertime HREs in South Korea are characterized by multiscale atmospheric circulations with distinct thermodynamic characteristics. The HREs can be also determined by TCs. Such inherently complex nature of warm-season HREs in South Korea makes their comprehensive understanding and successful forecasting across time scale quite challenging.

As a step toward a better grasp of HREs in summer monsoon, this dissertation addresses their synoptic-scale characteristics that should be indispensably well understood for their successful daily forecasting. To draw robust and climatologically meaningful conclusions, the historical HREs in the past four decades are considered while the HREs in the summer of 2020 are also addressed separately as a case study. The HREs resulting from TCs (TC-HREs) and those not directly related to TCs (simply, HREs) are separately considered. This dissertation aims to provide a refined explanation for the synoptic–dynamic details of HREs and TC-HREs, of which some are reconfirmed or revisited, or even newly reported.

The rest of this dissertation is organized as follows. In chapter 2, the climatological characteristics of HREs and TC-HREs are explored through composite analyses. Chapter 3 quantitatively assesses the vertical motion mechanisms of HREs using the quasigeostrophic (QG) framework. In chapter 4, diverse surface weather patterns of HREs are identified through clustering analysis. Chapter 5 investigates the role of midlatitude baroclinic condition in TC-HREs. Chapter 6 conducts the case study of record-breaking monsoon rainfall in the summer of 2020. Each chapter is summarized in chapter 7 with further discussion on the directions for future study.

Chapter 2. Climatological features of HREs and TC-HREs

Note: The contents of this chapter are taken from Park et al. (2021b) titled "Diverse synoptic weather patterns of warm-season heavy rainfall events in South Korea" published in *Monthly Weather Review.* (Vol. **149**, 3875–3893, https://doi.org/10.1175/MWR-D-20-0388.1). Some modifications have been made from the original article for the organization of the dissertation.

2.1. Motivation

Climatologically, 90% of annual HREs are concentrated in JJAS in South Korea (Fig. 1.1). Due to their substantial socio-economic impacts, their meteorological characteristics have been continuously explored (see references in section 1.1), but most studies focused on a single or a few cases. Although the case study is beneficial to report peculiar meteorological aspects of a specific event, addressing many cases is also very important to extract their climatological information. Lee et al. (1998) and Shin et al. (2015) considered more than 60 HREs to understand to better understand their characteristics. However, their analysis period does not exceed 10 years, which is still insufficient to draw general conclusions. The lack of the study considering many cases is also true for TC-HREs.

By using the 40-year-long (1979–2018) record of precipitation data from the evenly-distributed weather stations in South Korea, it is found that a total of 392 HREs (including TC-HREs) occurred in JJAS over the past 40 years. In this chapter, the climatological features of HREs and TC-HREs are first documented. This chapter will also serve as the foundation for the detailed synoptic–dynamic analyses of HREs and TC-HREs in the later chapters.

2.2. Data and methods

2.2.1. Data

Hourly precipitation data recorded at the Automated Synoptic Observing System (ASOS) of the KMA are used to identify HREs. Excluding stations on Jeju Island due to the different regional climate from mainland Korea, a total of 57 ASOS stations with continuous observations from 1979 to 2018 are considered. The TC best track data offered by the Regional Specialized Meteorological Center (RSMC)-Tokyo Typhoon Center are also used to determine TC-HREs. Meteorological variables from the six-hourly European Centre for Medium-Range Weather Forecasts (ECMWF) interim reanalysis (ERA-Interim; Dee et al. 2011) with 1.5°×1.5° horizontal grid spacing and 37 pressure levels are used to analyze the synoptic features of HREs and TC-HREs in the summer monsoon season (JJAS). Anomaly fields are calculated by subtracting the 40-year 6-h climatology.

2.2.2. Definition of HRE and TC-HRE

The HREs are identified with the KMA criteria. Specifically, a rainfall event with 12-h accumulated rainfall greater than 110 mm at any single ASOS station is defined as an HRE. If the HREs are observed several times at multiple stations within 12 h, only the HRE with the largest amount of 12-h accumulated rainfall is chosen. This effectively removes the redundant HREs sharing the same synoptic environment. As a result, a total of 392 events are identified for 1979–2018, accounting for 88% of all-season HREs (Fig. 1.1). The reference time of each HRE (0 h) is defined as the center of the 12-h window for the maximum 12-h accumulated rainfall (e.g., 0600 UTC for the maximum 12-h accumulated rainfall during 0000–1200 UTC). In other words, the reference time denotes the mature stage of HREs.

The HREs concurrent with TCs near the Korean Peninsula (i.e., TC-HREs) are separately considered. These events are determined by analyzing TC best tracks provided by the RSMC–Tokyo Typhoon Center. Following the KMA criteria (KMA 2011), the HRE is considered to be a direct result of the TC if a TC is located within the domain of 32°–40°N and 120°–138°E without completing the extratropical

transition (ET) to an extratropical cyclone (ETC) or weakening to a tropical depression (TD). The tracks of TCs involved in TC-HREs are shown in Fig. 2.1.

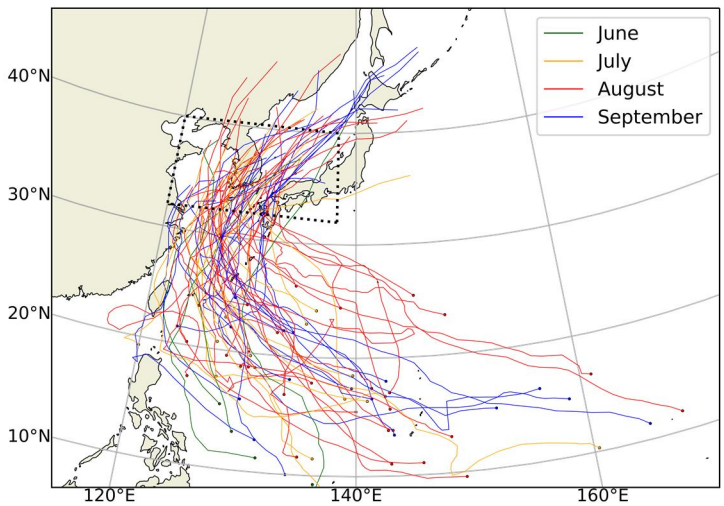

Figure 2.1. Tracks of TCs involved in TC-HREs for 1979–2018 with different colors depending on months. For clarity, the tracks for the grades of TD and ETC are not expressed. The dots denote the genesis location of TCs. The closed area by a dotted line denotes the KMA area for TC monitoring (32°–40°N, 120°–138°E).

The remaining HREs are considered non-TC HREs (i.e., HREs). The HREs and TC-HREs account for 81.1% (318 events) and 18.9% (74 events) of total HREs. Figure 2.2 shows hourly time series of 12-h accumulated rainfall at the station of the maximum 12-h accumulated rainfall for HREs and TC-HREs. On average, the accumulated rainfall is greater in TC-HREs than in HREs (cf. bold lines) although the individual events exhibit substantial event-to-event spread (thin lines; 30 mm greater at 0 h). The duration is also about 3 h longer in TC-HREs (Table 2.1). However, those differences fall within their respective ± 1 standard deviation, suggestive of substantial event-by-event spreads.

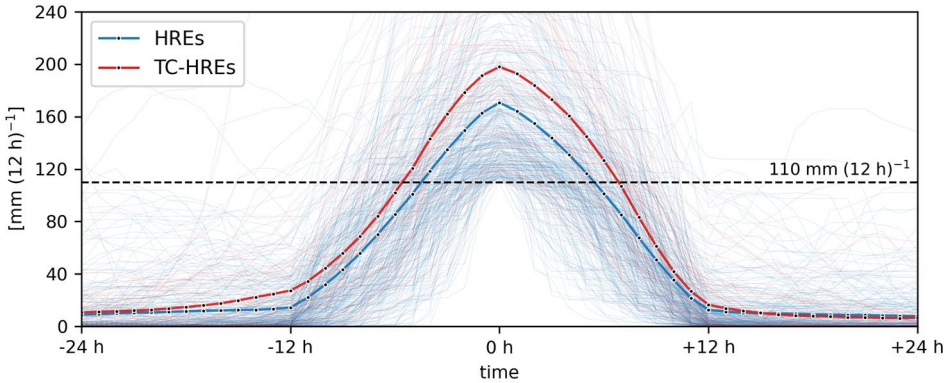

Figure 2.2. Hourly time series of 12-h accumulated rainfall for individual HREs and TC-HREs (thin lines) at the station of maximum accumulated 12-h rainfall, and their means (bold lines). The 0 h denotes the reference time. The dashed black horizontal line indicates 110 mm (12 h)$^{-1}$.

Table 2.1. Summary of the HREs and TC-HREs. The first three rows are synoptic description, and preferred occurrence period and region. The fourth and fifth rows are averages of the maximum 12-h accumulated rainfall amount (mm) and duration (h) with their ±1.0 standard deviation. The sixth through eighth rows represent the magnitude, and zonal and meridional components of **IVT** (kg m^{-1} s^{-1}) with their ±1.0 standard deviation, which are estimated at 0 h over the boxed region in the right panel of Fig. 2.3b for HREs and Fig. 2.5b for TC-HREs.

	HREs (81.1%)	TC-HREs (18.9%)
Synoptic description	*Migrating cyclone with northwestward expansion of the NPH*	*Synergetic interaction between TC and midlatitude flow*
Preferred period	First and second rainy periods	Second rainy period
Preferred region	South coast and west of mountainous region	South and east coasts
Max.12-h acc. rainfall	170.7 ± 60.9	198.0 ± 82.0
HRE duration	15.3 ± 10.4	18.2 ± 12.5
|IVT|	449.8 ± 181.2	706.2 ± 304.2
Zonal **IVT**	292.0 ± 194.6	-101.2 ± 277.9
Meridional **IVT**	240.6 ± 166.0	378.5 ± 357.0

2.3. Composited synoptic conditions

2.3.1. HREs

Figure 2.3a shows the temporal evolution of the mean sea-level pressure (SLP), its anomaly, relative vorticity at 850 hPa and **IVT** (see appendix A1) for HREs at 36, 18 and 0 h before the reference time (hereafter, –36, –18, and 0 h). Here, the relative vorticity is smoothed at a T42 resolution to focus on the synoptic-scale disturbances. At –36 h, the NPH expands northwestward, and a negative SLP anomaly appears over eastern China. Although the negative SLP anomaly is not well organized at –36 h, it rapidly intensifies within a day as traveling northeastward. Note that at 0 h, it develops into a well-defined surface cyclone with an intensity of ~2 cyclonic vorticity units (CVU; 1 CVU$\equiv 10^{-5}$ s^{-1}) and locates over the Yellow Sea, enhancing the southwesterly **IVT** between the cyclone and the NPH.

Figure 2.3b shows the temporal evolution of the 250-hPa geopotential height (GPH) and horizontal wind speed, as well as the 500-hPa vertical motion. In the upper troposphere, the meandering baroclinic wave is evident. Note that the upper-level trough–ridge couplet develops from the west with an accelerating ULJ in between. The upper-level trough is located immediately west of the surface cyclone, suggestive of its baroclinic development. At 0 h, South Korea is positioned on the east of the trough and the equatorward side of the jet entrance, a favorable condition for the dynamically-forced upward motion (see blue contours). The vertical motion mechanisms of HREs will be quantitatively assessed in chapter 4.

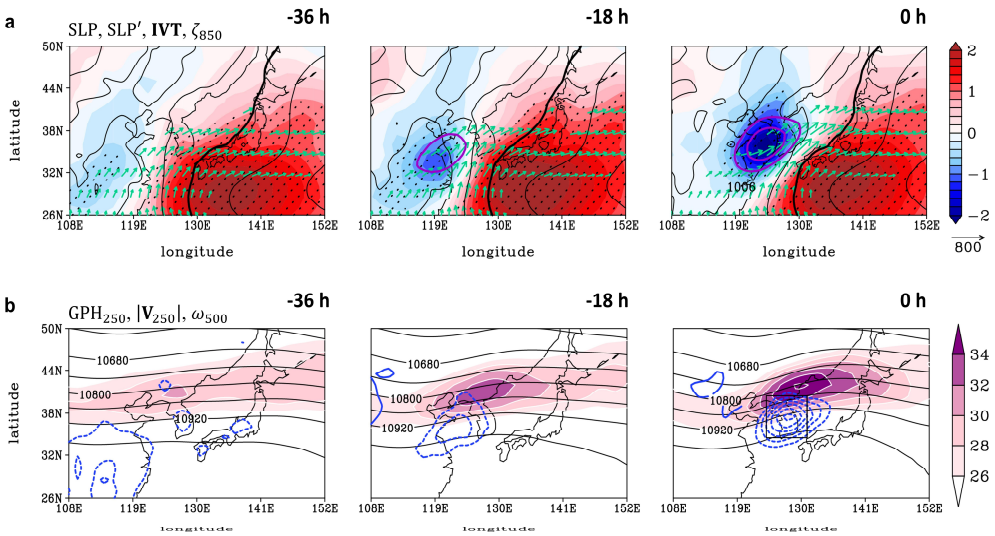

Figure 2.3. Time evolution (–36 h, –18 h and 0 h) of synoptic circulation patterns of HREs: **a** SLP (hPa, black contours), SLP anomalies (hPa, shading), **IVT** (>300 kg m^{-1} s^{-1}, vectors) and the 850-hPa relative vorticity truncated to a T42 resolution (purple contours with a 1-CVU interval starting from 1 CVU), and **b** GPH (gpm, black contours) and horizontal wind speed (m s^{-1}, shading) at 250 hPa, and vertical velocity at 500 hPa (Pa s^{-1}, blue contours with a 0.04 Pa s^{-1} interval). In **a**, the 1010-hPa contour is highlighted in bold. The SLP anomalies are stippled when statistically significant at the 95% confidence level based on a two-tailed Student's *t* test. In **b**, the boxed region in the rightmost panel denotes the core of the 500-hPa ascent (34.5°–40.5°N, 124°–131°E).

Figure 2.4 provides further synoptic details of the mature HREs. At 850 hPa, a horizontal gradient of equivalent potential temperature (θ_e) is pronounced around the Korean Peninsula (Fig. 2.4a). This θ_e gradient appears to be established partly by the advection of warm moist air through the southwesterly **IVT** (see Fig. 2.3a). Pettersson's frontogenesis function (see appendix A2) clearly shows that the frontogenesis occurs along the large θ_e gradient (blue contours). In the vertical, θ_e exhibits a moist-adiabatically unstable condition in the boundary layer, especially to the south (Fig. 2.4b). The free troposphere, however, shows a near-neutral or only weakly unstable condition. This condition may be favorable for convective instability in the near-surface level and further self-maintenance of the convection in the free troposphere, which can significantly amplify HREs. The specific humidity over South Korea is higher than over the subtropics in nearly the entire troposphere (blue contours), which facilitates the successive diabatic enhancement of the HREs. This free-tropospheric high specific humidity has been also reported for the Japanese HREs (Yokoyama et al. 2017; Hamada and Takayabu 2018).

The GPH anomalies exhibit a westward-tilted (i.e., baroclinic) vertical structure with dual minima in the upper and lower troposphere (Fig. 2.4c). A rising motion is evident between the negative and positive GPH anomalies, which is a typical feature of a developing baroclinic system in midlatitudes. On the equatorward side of the ULJ core, horizontal wind divergence collocates with the near-surface convergence beneath (Fig. 2.4d), facilitating the thermally direct secondary circulation (Lee et al. 2008b) and its further contribution to the low-level frontogenesis through a semigeostrophic feedback (Yuan et al. 2020).

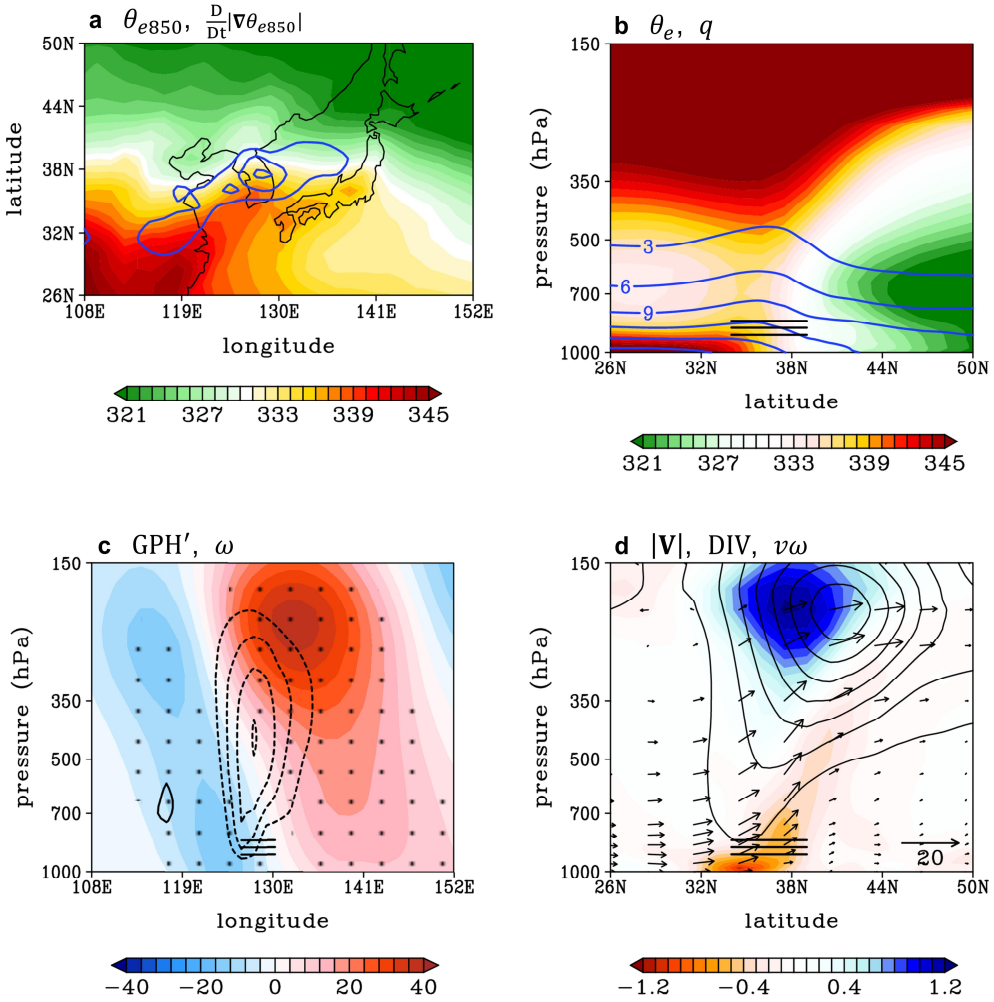

Figure 2.4. Thermodynamic and dynamic structures of the mature HREs (0 h): **a** 850-hPa θ_e (K, shading) and the Petterssen frontogenesis function applied to the 850-hPa θ_e [blue contours for positive values with a 1-K (100 km day)$^{-1}$ interval], **b** latitude-pressure cross section of θ_e (K, shading) and specific humidity (g kg^{-1}, contours), **c** longitude-pressure cross section of GPH anomalies (gpm, shading) and vertical velocity (contours with a 0.04 Pa s^{-1} interval), and **d** latitude-pressure cross section of horizontal wind speed (>12 m s^{-1}, contours with a 4 m s^{-1} interval), horizontal mass divergence (10^{-5} s^{-1}, shading), and meridional-vertical wind (m s^{-1}, vectors; vertical velocity is multiplied by an aspect ratio of –32.72). In **b**–**d**, the plotted variables are longitudinally or latitudinally averaged over the boxed region in the rightmost panel of Fig. 2.3b. The three horizontal lines in **b**–**d** indicate the approximate location of South Korea. In **c**, the GPH anomalies are stippled when statistically significant at the 95% confidence level based on a two-tailed Student's *t* test.

2.3.2. TC-HREs

Figure 2.5 shows the synoptic evolution of TC-HREs. The TC is generally located over the East China Sea at –36 h and moves poleward along the western boundary of the NPH in time (Fig. 2.5a; see also Fig. 2.1). In the mature stage (0 h), the TC is positioned immediately southwest of the Korean Peninsula. At this time, the cyclonic vorticity of the TC reaches ~6 CVU—three times larger than the cyclone in the HREs (cf. Figs. 2.3a and 2.5a). Along the right side of the TC, a large amount of moisture is transported toward Korea as manifested by south-southeasterly **IVT**.

In the upper troposphere, a trough–ridge couplet is found in midlatitudes (Fig. 2.5b). On the top of the ridge, the ULJ develops, placing its entrance region to the north of the Korean Peninsula. Although the ULJ accelerates in time, the trough–ridge couplet stays in place with no eastward propagation. This synoptic configuration induces a well-organized region of ascent over South Korea at –36 and –18 h, which is well separated from the direct impact of the TC (i.e., eyewall convection; see blue contours). Given the abundant moisture remotely fed by the TC, this midlatitude ascent may cause predecessor rainfall events before the TC arrives (e.g., Byun and Lee 2012; Baek et al. 2015). In the mature stage (0 h), the TC convection merges with the midlatitude ascent, generating a more rigorous uplift over South Korea. The amplification of the upper-level flow from –36 to 0 h is likely supported by a diabatic outflow of TC (Archambault et al. 2013; Grams and Archambault 2016). Accordingly, TC-HREs could be explained by the result of synergetic interaction between TCs and nearby midlatitude baroclinic waves. This is indeed a typical feature of the transitioning TCs in baroclinic zones (Evans et al. 2017; Keller et al. 2019). The role of midlatitude baroclinic condition in TC-HREs will be more detailed in chapter 5.

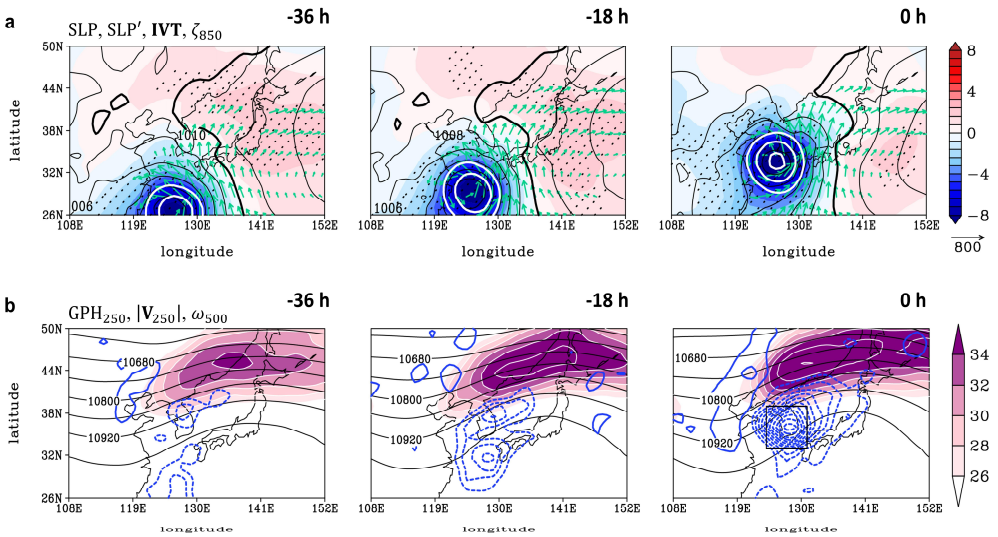

Figure 2.5. As in Fig. 2.3, but for TC-HREs. In **a**, the 850-hPa T42 relative vorticity is contoured in white with a two times larger interval than in Fig. 2.3a (2-CVU interval). The shading range in **a** is four times larger than that in Fig. 2.3a. The boxed region in the rightmost panel denotes the core of the 500-hPa ascent (33°–39°N, 124°–131°E).

Further dynamic and thermodynamic details of the mature TC-HREs are shown in Fig. 2.6. At 850 hPa, a tongue of the high θ_e stretching from south to north is observed (Fig. 2.6a) due to the southerly dominant **IVT** (see also Fig. 2.5a). Along the northern side of the high θ_e tongue, strong frontogenesis occurs, particularly over the Korean Peninsula (blue contours). As in HREs, the vertical structure of θ_e shows convectively unstable condition in the boundary layer and near-neutral condition in the free troposphere (Fig. 2.6b), but θ_e is overall larger than that in HREs (cf. Figs. 2.4b and 2.6b). As in HREs, the GPH anomalies exhibit a westward tilted vertical structure (Fig. 2.6c), representing the transitioning TC. However, the negative GPH anomalies in the lower troposphere are stronger than those in the upper troposphere, which manifests a still warm-core nature of the TC. On the equatorward side of the ULJ core, upper-level divergence and lower-level convergence are well collocated with stronger magnitudes than those in HREs (cf. Figs. 2.4d and 2.6d). In particular, the strong poleward cross-jet flow is evident in the upper troposphere, which is consistent with the fact that the diabatic outflow of the transitioning TC significantly contributes to the downstream flow amplification (Archambault et al. 2015; Grams and Archambault 2016).

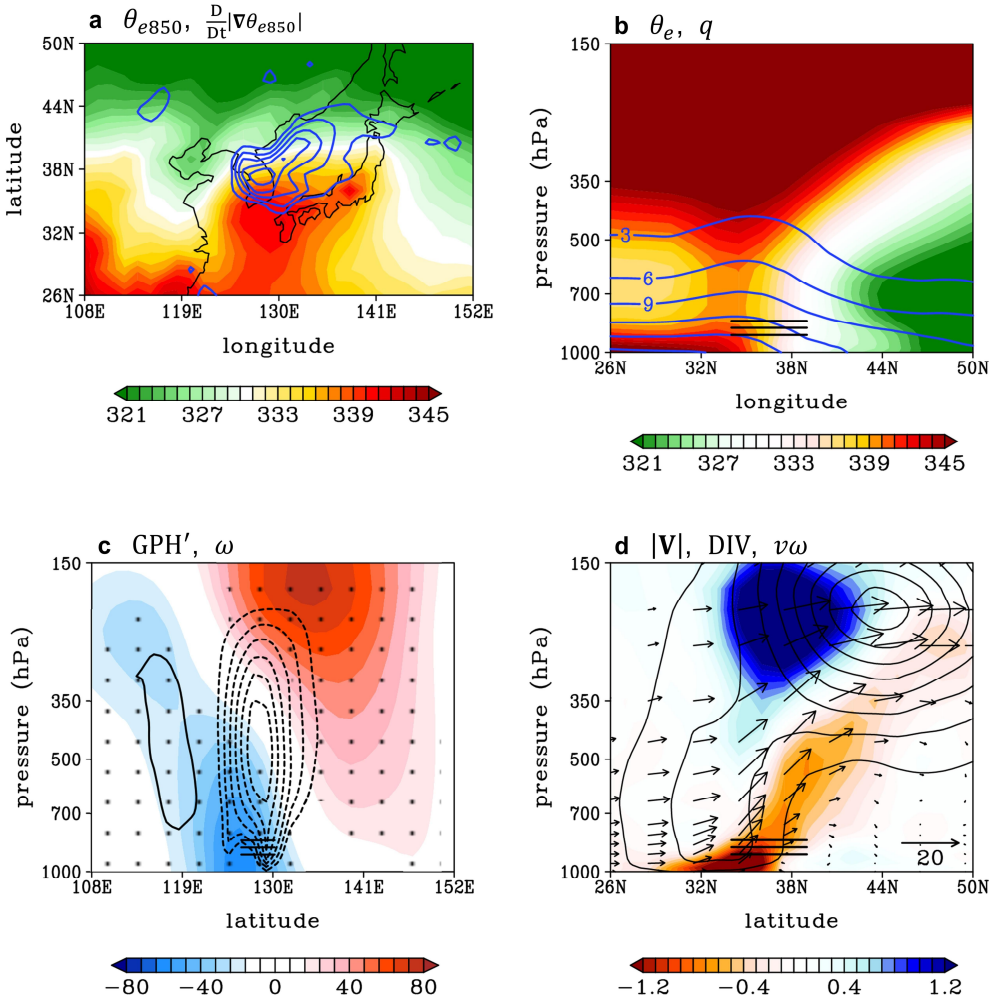

Figure 2.6. As in Fig. 2.4, but for TC-HREs. Note that the shading range in **c** is two times larger than that in Fig. 2.4c.

2.4. Spatiotemporal occurrence distributions

The HREs and TC-HREs are also clearly differentiated by their spatiotemporal occurrence distributions. Figures 2.7a,b show their temporal occurrence distributions in 10-day bins. The HREs have two frequency peaks, which is consistent with the climatological first (late June–July) and second rainy periods (mid-August–mid-September; Fig. 2.7a). In contrast, TC-HREs are more frequent in the second rainy period (Fig. 2.7b). This is consistent with the fact that the western North Pacific TC activity is more pronounced in late summer than early summer (Chen et al. 2004; Guo et al. 2017).

Figures 2.7c,d present the spatial occurrence distributions of HREs and TC-HREs across the 57 ASOS stations. Both HREs and TC-HREs are frequently observed along the south coast. However, they show sharp differences related to the north–south-oriented mountains. While HREs preferentially occur in the western side of the mountainous areas, TC-HREs are largely confined to the east coast. This difference can be explained by the different directions of moisture transport between HREs versus TC-HREs. As summarized in Table 2.1, HREs are often accompanied by the southwesterly **IVT** impinging on the western slope of the mountains (see also Fig. 2.3a). In contrast, the south-southeasterly **IVT** in TC-HREs is favorable for moisture convergence and orographic lifting the on the eastern edge of the mountains (see also Fig. 2.5a).

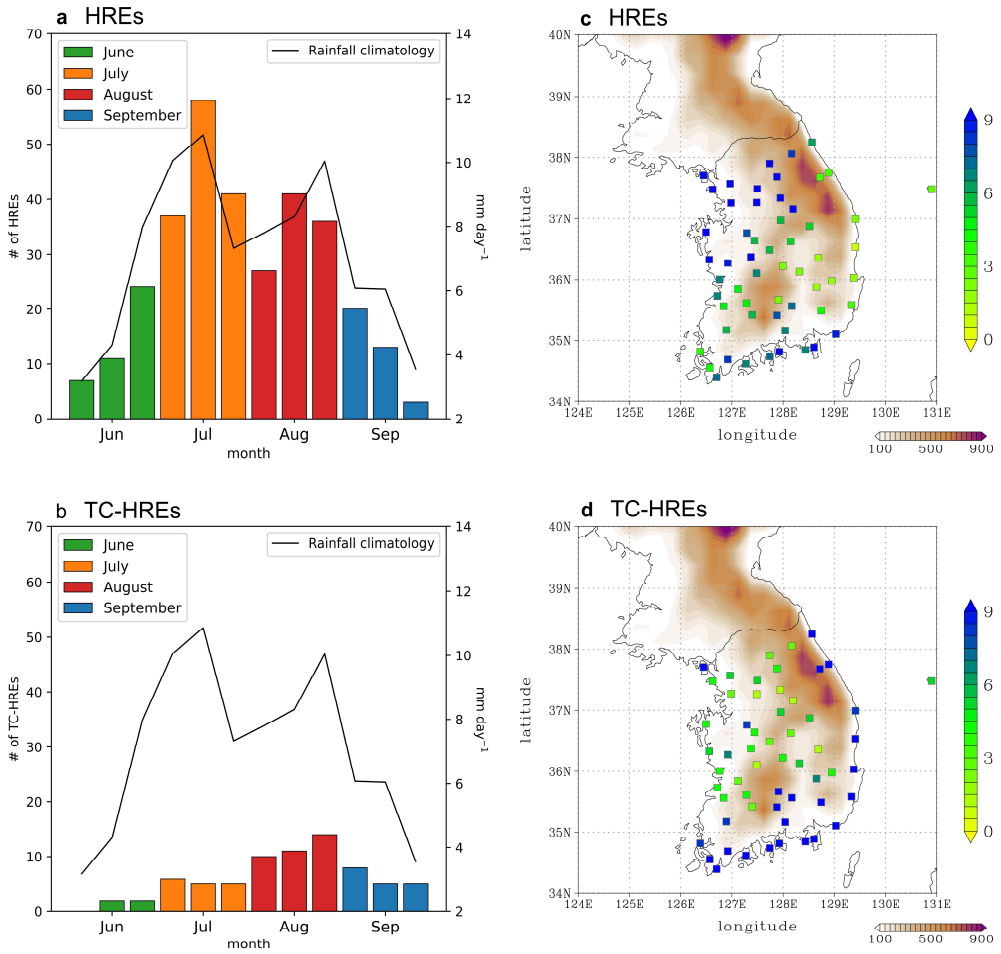

Figure 2.7. The left panels are the number of **a** HREs and **b** TC-HREs in 10-day bins in JJAS (colored bars) overlaid with rainfall climatology (mm day^{-1}, black line). The right panels are spatial distributions of the probability of occurrence of **c** HREs and **d** TC-HREs (%, colored square) overlaid with terrain (m, shading). The probability of occurrence means the conditional probability that a given ASOS station records an HRE (or TC-HRE) when the event occurs in South Korea.

Chapter 3. Quasi-geostrophic diagnosis of HREs

Note: The contents of this chapter are taken from Park et al. (2021c) titled "Role of baroclinic trough in triggering vertical motion during summertime heavy rainfall events in Korea" published in *Journal of the Atmospheric Sciences*. (Vol. **78**, 1687–1702, https://doi.org/10.1175/JAS-D-20-0216.1). Some modifications have been made from the original article for the organization of the dissertation.

3.1. Motivation

As stated in section 1.1.5, HREs preferably occur to the north of the LLJ nose and the south of the ULJ entrance (Lee et al. 1998; Lee et al. 2008a,b). In particular, the vertical coupling of ULJ and LLJ through thermally-direct secondary circulation (Fig. 1.3) has been considered as a key driver of the vertical motion during HREs. However, previous studies have been mostly based on case studies or qualitative analyses. Although a strong upward motion is indeed observed at the south of the ULJ entrance in the composite of 318 HREs for 1979–2018 (Fig. 3.1), it is not conclusive yet whether the vertical motion is mostly explained by the ULJ-driven secondary circulation.

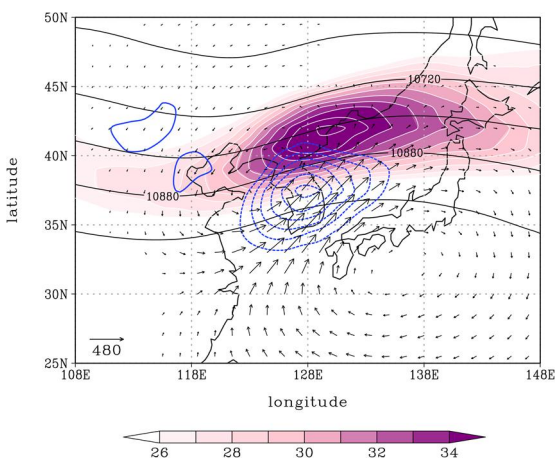

Figure 3.1. Composites of the 250-hPa GPH (gpm, black contours), 500-hPa ω (blue contours with a 0.04-Pa s^{-1} interval), 250-hPa horizontal wind speed (shading) and **IVT** anomaly (kg m^{-1} s^{-1}, vectors) for the 318 HREs in their mature stage. The **IVT** anomaly is shown only for the statistically significant values at the 95% confidence level, based on a two-tailed Student's *t* test.

In QG omega equation, the synoptic-scale vertical motion is often diagnosed by computing Q-vector convergence (Hoskins et al. 1978; Hoskins and Pedder 1980; Holton 2004). The Q vector can be further decomposed into the transverse (cross-isentropic) and shearwise (along-isentropic) components (Keyser et al. 1988, 1992; Bluestein 1993). Their roles in QG vertical motion are schematized in Fig. 3.2. The transverse Q vector at the entrance of the jet streak is related to geostrophic frontogenesis and points to the warm air (Fig. 3.2a). It induces the ascent at the south and the descent at the north of the jet entrance. The opposite is true at the jet exit. In contrast, the shearwise Q vector is related to the rotation of the isentropes by the geostrophic flow. At the north of the jet streak, an eastward shearwise Q-vector is typically generated, inducing a decent-ascent couplet (Fig. 3.2b). Collectively, the dynamic uplift at the south of the jet entrance, noted by "A" in Fig. 3.2b, results from both the transverse and shearwise Q vectors.

The configuration shown in the top half of Figs. 3.2a,b can be also applied to the trough without a jet streak (Fig. 3.2c). Although not highlighted in previous studies, a well-defined upper-level trough is frequently observed during the HREs (see black contours in Fig. 3.1). This implies that the shearwise Q-vector forcing to the east of the trough, noted by "B" in Fig. 3.2c, can play a crucial role in setting the HREs.

The vertical motion during the HREs could be driven not only by dry dynamics but also by diabatic forcing, as they occur in the moisture-rich environment (Sohn et al. 2013; Song and Sohn 2015; Horinouchi and Hayashi 2017; see also vectors in Fig. 3.1). In fact, the diabatic forcing is not independent of dynamic forcing. They strongly interact through nonlinear dynamic-diabatic feedback (Fink et al. 2012; Nie and Sobel 2016).

Figures 3.1 and 3.2 implies that the vertical motion of HREs is not explained simply by secondary circulation at the ULJ entrance. In this chapter, the dynamic and diabatic contributions to the vertical motion of the HREs are quantified in the QG framework. For a better grasp of the dynamic processes, the Q vector is decomposed into the transverse and shearwise components.

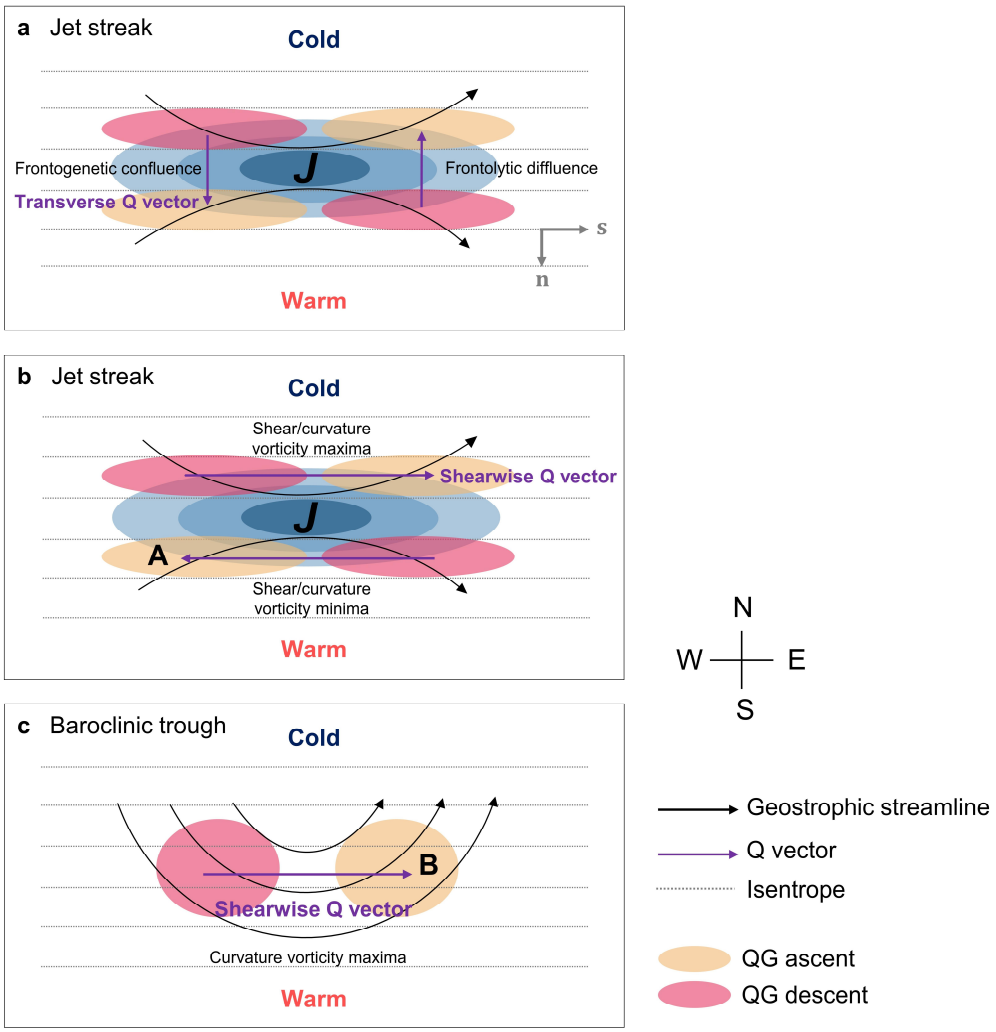

Figure 3.2. Schematic illustration of the typical QG vertical motion by **a** the transverse Q vector and **b** shearwise Q vector around the jet streak, and **c** by the shearwise Q vector around the trough in the Northern Hemisphere. Gray dotted lines denote the isentropes with warm air to the south, and black and purple arrows indicate the geostrophic streamlines and Q vectors, respectively. The shaded regions in pink and apricot, respectively, denote the QG descent and ascent. The **n** and **s** indicate the cross-isentropic and along-isentropic unit vectors, respectively. Diagrams of **a** and **b** are partly taken from Martin (2014).

3.2. Data and methods

3.2.1. Dataset

The dataset used here is identical to that in chapter 2. The 318 HREs in JJAS during 1979–2018 and the 6-hourly ERA-Interim reanalysis data with 1.5°×1.5° horizontal grid spacing and 37 pressure levels are also used. Anomaly fields are calculated by subtracting the 40-year 6-h climatology.

In this chapter, a diabatic temperature tendency ($\dot{T}_{Dia}$) predicted by the ECMWF model is further retrieved to quantify the diabatic contribution to the vertical motion in the QG omega equation. In ERA-Interim data, $\dot{T}_{Dia}$ is offered as forecast fields at 0000–0600 UTC, 0000–1200 UTC, 1200–1800 UTC and 1200–2400 UTC but adjusted to the 6-h interval to keep the consistency with other variables. For example, $\dot{T}_{Dia}$ at 0600 UTC is determined as $\frac{\dot{T}_{Dia}\ [0000\text{–}1200\ \mathrm{UTC}]\times 12\ \mathrm{h} - \dot{T}_{Dia}[0000\text{–}0600\ \mathrm{UTC}]\times 6\ \mathrm{h}}{6\ \mathrm{h}}$.

3.2.2. QG diagnosis of vertical motion

The nature of vertical motion is examined in the QG framework (Hoskins et al. 1978; Hoskins and Pedder 1980; Holton 2004). In the Q-vector-form QG omega equation (see appendix B1), there are three QG forcing terms: Q-vector convergence, i.e., $-2\boldsymbol{\nabla}\cdot\mathbf{Q}$, planetary vorticity advection by thermal wind, i.e., $f_0\beta_0\frac{\partial v_g}{\partial p}$ and Laplacian of diabatic heating (mostly from latent heating), i.e., $-\frac{\kappa}{p}\nabla^2 J$. Hereafter, they are referred to as dynamic, beta and diabatic forcings, and their resulting vertical motions are denoted by ω_{Dyn}, ω_{Beta} and ω_{Dia}, respectively. Each omega component is obtained by numerically solving the equation with each QG forcing one by one. The vertical motion by all QG forcings are referred to as ω_{QG} ($\omega_{QG} = \omega_{Dyn} + \omega_{Beta} + \omega_{Dia}$). The Dirichlet boundary condition ($\omega = 0$) is applied to the lateral and vertical boundaries. The numerical details of the QG omega equation inversion is provided in appendix B2.

3.2.3. Transverse and shearwise components of Q vector

By considering the orientation of Q vector with respect to the isentropes, the Q vector can be further decomposed into the transverse ($Q_n\mathbf{n}$) and shearwise ($Q_s\mathbf{s}$) components in a natural coordinate (Keyser 1988, 1992; Bluestein 1993). Their resulting vertical motions are referred to as ω_n and ω_s ($\omega_{Dyn} = \omega_n + \omega_s$). By definition, they are the Lagrangian measures for the magnitude and direction changes of the potential temperature gradient, respectively, following the geostrophic wind. The $Q_n\mathbf{n}$, which is parallel to the potential temperature gradient, is generated when the geostrophic wind is confluent (or diffluent) toward the potential temperature gradient (Fig. 3.2a). As such, $Q_n\mathbf{n}$ pointing to warm air is indicative of geostrophic frontogenesis. In contrast, $Q_s\mathbf{s}$, which is perpendicular to the potential temperature gradient, is generated when geostrophic wind rotates the isentropes (Figs. 3.2b,c). The $Q_s\mathbf{s}$ with warm air to the right is indicative of the cyclonic rotation of the isentropes.

It is notable that Q_n corresponds to the half of dry dynamic forcing in the Sawyer–Eliassen equation. Meanwhile, $-2\boldsymbol{\nabla}\cdot Q_s\mathbf{s}$ is well approximated by the geostrophic relative vorticity advection by the thermal wind that was originally discussed in Sutcliffe (1947) as a key factor for the development and propagation of midlatitude cyclones. This indicates that transverse Q vector is closely related to the transverse (i.e., cross-frontal) secondary circulation whereas shearwise Q vector is closely associated with baroclinic waves in midlatitudes. For more mathematical and physical details of the two Q vector components, see appendix B3.

3.3. QG forcing: Dynamic versus diabatic forcings

In this subsection, the contributions of dynamic and diabatic forcings to vertical motion are quantitatively examined. Figure 3.3 shows the upper- and lower-tropospheric evolutions of HREs, which are already investigated in section 2.3.1. In the upper troposphere, a negative–positive couplet of GPH anomaly appears on the far west of the Korean Peninsula at –36 h (Fig. 3.3a). This perturbation travels eastward in time and grows into a well-defined trough and ridge at 0 h. In the lower troposphere, a synoptic-scale cyclone develops right downstream of the upper-level trough with an enhanced moisture supply via the southwesterly LLJ on its leading edge (Fig. 3.3b). As discussed in section 2.3.1, Fig. 3.3 indicates that HREs are primarily caused by the vertically well-defined baroclinic system. More importantly, this may suggest that the vertical motion triggering HREs cannot be simply explained by the thermally direct secondary circulation at the entrance region of the ULJ.

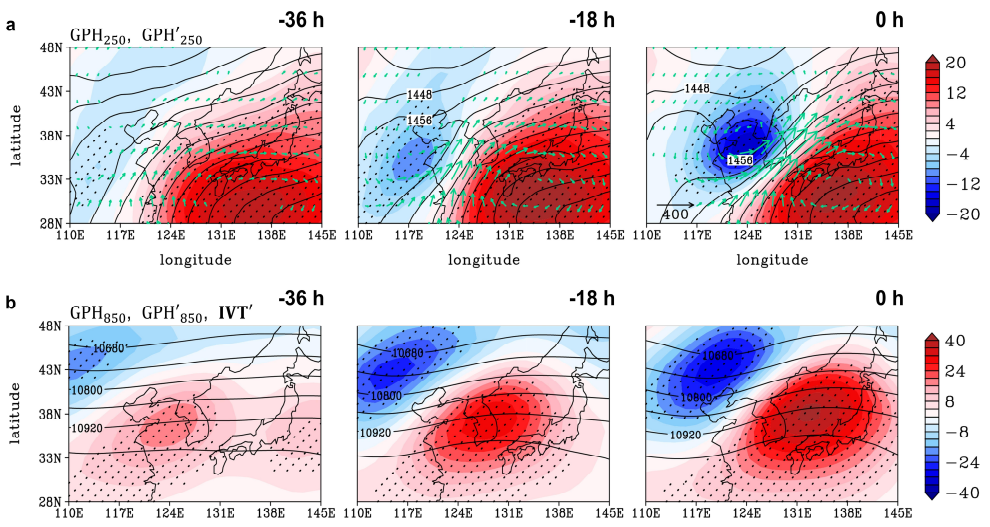

Figure 3.3. Lagged composites of **a** 250-hPa GPH (gpm, contours) and its anomalies (gpm, shading), and **b** 850-hPa GPH (gpm, contours), its anomalies (gpm, shading) and **IVT** anomaly (kg m^{-1} s^{-1}, vectors) at –36, –18 and 0 h. The GPH anomalies are stippled when statistically significant at the 95% confidence level. The **IVT** anomaly in **b** is shown only when statistically significant at the 95% confidence level. A two-tailed Student's *t* test is used.

Figure 3.4a presents the spatial distribution of ω, Q vector, and its convergence at 500 hPa. An initial vertical motion over eastern China at –36 h is associated with dynamic forcing (shading). As the baroclinic wave develops and propagates eastward (see Fig. 3.3), the intensity of dynamic forcing increases. At –18 and 0 h, the spatial extent and the center of dynamic forcing match well with those of upward motion. It is noticeable from Fig. 3.4a that Q-vector convergence over the HRE region accompanies Q-vector divergence on its northwest. This dipolar pattern of the dynamic forcing is suggestive of the significant contribution of shearwise Q-vector forcing (see Fig. 3.2c). Although not shown, this structure also appears at 250 hPa but slightly shifts northwestward due to the vertically tilted nature of the baroclinic wave (Yin and Battisti 2004). More details of the dynamic forcing are further discussed in the next section.

Figure 3.4b illustrates the spatial distribution of diabatic forcing and **IVT** anomaly. While the diabatic forcing is nearly absent at –36 h, it significantly strengthens within a day and becomes much stronger than the dynamic forcing at 0 h (cf. the rightmost panels in Figs. 3.4a,b where shading interval is different by an order of magnitude). Compared to dynamic forcing, diabatic forcing is more localized over the Korean Peninsula in the mature stage (0 h). This is anticipated because most of the diabatic forcing must be due to the latent heat release during HREs (note that **IVT** anomaly is well collocated with the diabatic forcing). Although not shown, beta forcing is negligibly small.

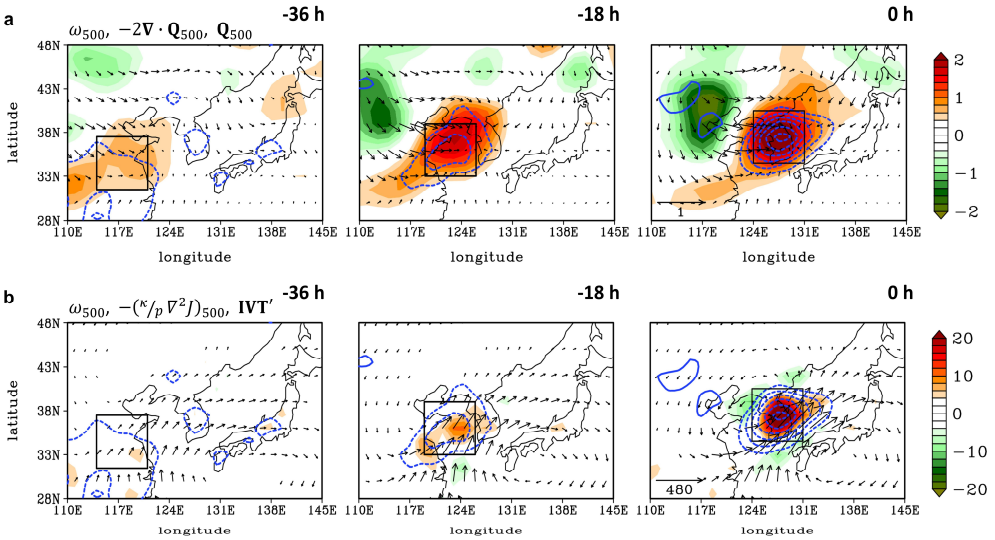

Figure 3.4. a Lagged composites of ω (contours with a 0.04-Pa s^{-1} interval), dynamic forcing (10^{-18} m kg^{-1} s^{-1}, shading) and Q vector (10^{-12} m^2 kg^{-1} s^{-1}, vectors) at 500 hPa at –36, –18 and 0 h. **b** As in **a** but for diabatic forcing at 500 hPa and **IVT** anomaly (kg m^{-1} s^{-1}, vectors). The **IVT** anomaly in **b** is shown only when statistically significant at the 95% confidence level, based on a two-tailed Student's *t* test. Note that the color bar range in **b** is ten times larger than that in **a**. The boxed regions denote the centers of upward motion at 500 hPa except for –36 h when the upward motion is less organized. The boxed region at 0 h is identical to that in Fig. 2.3b.

Figure 3.5 shows the latitude–pressure cross section of the dynamic and diabatic forcings and the resulting vertical motions (i.e., ω_{Dyn} and ω_{Dia}). Although the ULJ becomes coupled with LLJ in time, the dynamic forcing is maximized at the ULJ core, not on its southern flank (Fig. 3.5a), which contrasts with the conceptual model in Figs. 3.2a,b. This suggests that the secondary circulation at the ULJ entrance, which has been highlighted in the literature, is not likely a dominant mechanism of dynamic uplift of the HREs. As the dynamic forcing is enhanced and extended downward with a poleward tilt, the slantwise dynamic uplift also strengthens downward with its maximum in the upper to middle troposphere.

At –36 h, diabatic forcing is nearly absent, and the associated uplift is spatially limited in comparison to dynamic uplift (Fig. 3.5b). This indicates that the

upper-level dynamic forcing triggers the diabatic forcing. However, the diabatic uplift rapidly increases and becomes much stronger than dynamic uplift at 0 h. Unlike the dynamic forcing, the diabatic forcing is upright with its maximum in the midtroposphere. As a result, the diabatic uplift is upright and maximized in the middle to lower troposphere.

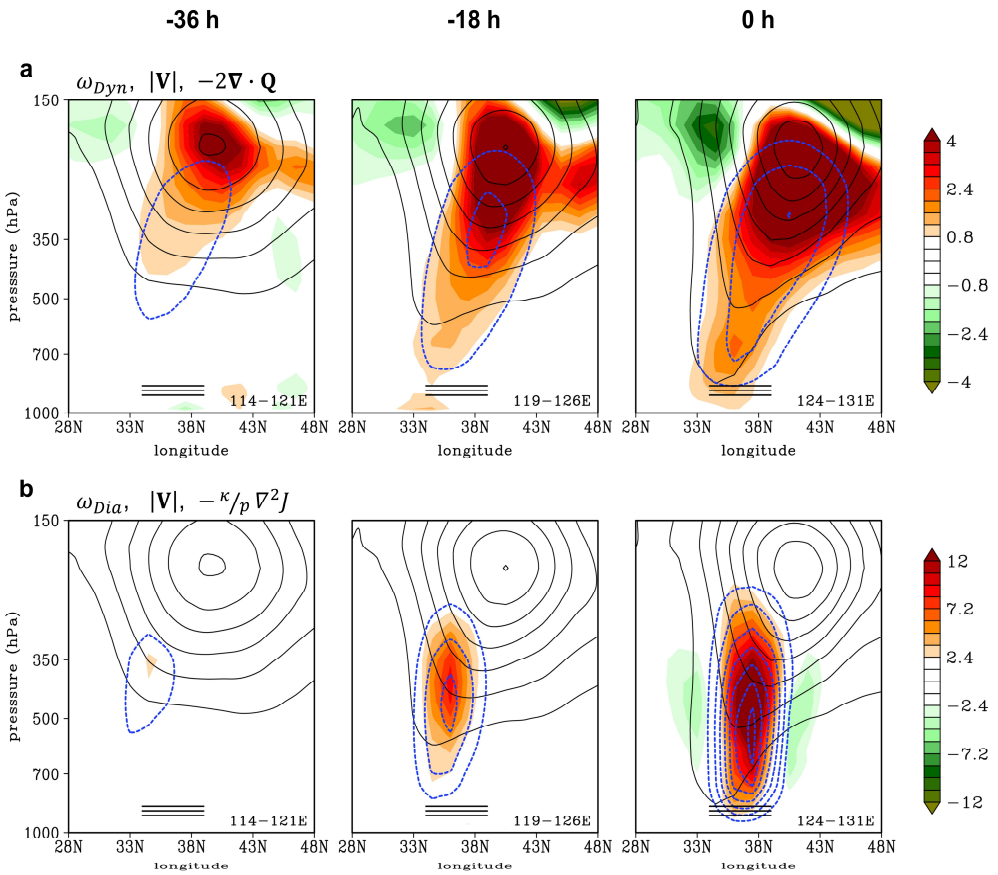

Figure 3.5. a Lagged composites (–36, –18 and 0 h) of the latitude-pressure cross section of ω_{Dyn} (blue contours with a 0.02-Pa s^{-1} interval), horizontal wind speed (>12 m s^{-1}, black contours with a 4-m s^{-1} interval) and dynamic forcing (10^{-18} m kg^{-1} s^{-1}, shading) averaged over the longitudinal band indicated at the bottom right corner of each panel. The longitudinal ranges chosen here are identical to the boxed regions in Fig. 3.4. **b** As in **a**, but for ω_{Dia} and diabatic forcing. The approximate location of South Korea is denoted with three horizontal black lines. Note that the color bar range in **b** is three times larger than that in **a**.

Figure 3.6 presents the relative importance of dynamic, beta and diabatic forcings in QG vertical motion. The numerically-solved QG omega (ω_{QG}) successfully reproduces the ERA-Interim vertical motion (ω), although its magnitude is slightly underestimated in the upper troposphere and overestimated in the lower troposphere. The location of the maximum magnitude is also slightly different between ω_{QG} and ω. This may be partly caused by the boundary conditions that force ω_{QG} to be zero, the invalidity of the QG approximation near the surface, and the uncertainty of convective parameterization in the forecast model.

The ω_{QG} is well explained by dynamic and diabatic forcings with a negligible beta effect. It is of note that their relative importance changes sharply from –18 to 0 h. The ω_{Dyn} and ω_{Dia} are nearly comparable at –18 h, but ω_{Dia} surpasses ω_{Dyn} at 0 h, becoming about 1.7 times stronger at 500 hPa. This result indicates that although the dynamic uplift precedes the initial stage of HREs (see also Fig. 3.4), the diabatic uplift becomes dominant in the mature stage of the HREs. If the boxed region over which the inversed omega is averaged is narrowed, ω_{Dia} becomes more dominant. This sensitivity is anticipated because the diabatic forcing is localized in the HRE region as seen in Fig. 3.4b.

It is also important to note that ω_{Dyn} has a maximum magnitude at ~350 hPa whereas ω_{Dia} exhibits a maximum magnitude at ~500 hPa. This structural difference, i.e., top-heavy ω_{Dyn} versus bottom-heavy ω_{Dia}, is consistent with Fig. 3.5. The bottom-heavy ω_{Dia} is also consistent with the fact that the warm-season HREs in South Korea generally occur through the warm-cloud processes (Sohn et al. 2013). Here, it should be stated that ω_{Dyn} and ω_{Dia} are not independent but must strongly interact with each other. Although not quantified, their nonlinear interaction may strengthen the low-level cyclone and thus moisture transport, maintaining or even strengthening ω_{Dia}.

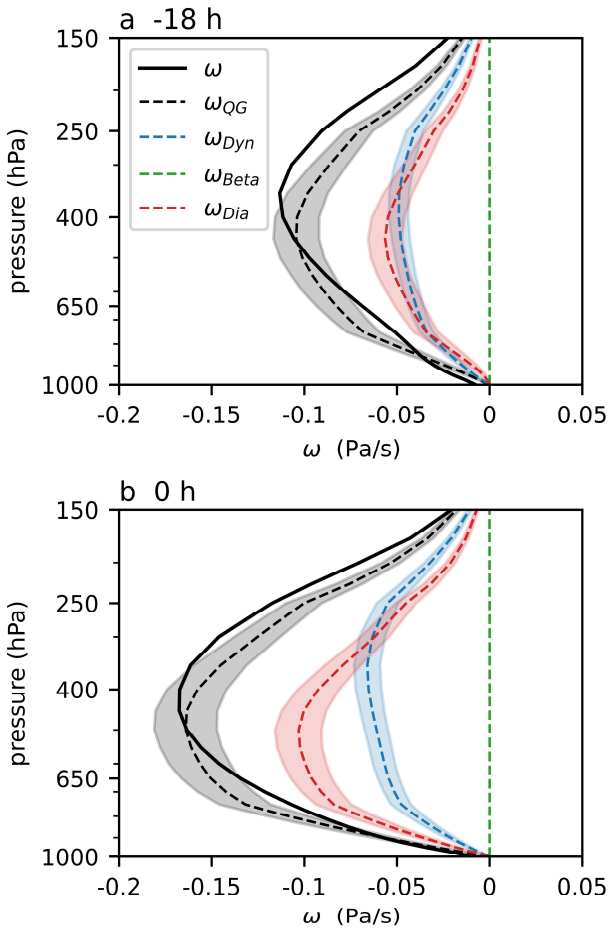

Figure 3.6. Vertical profiles of ω (black solid), ω_{QG} (black dashed), ω_{Dyn} (blue dashed), ω_{Beta} (green dashed) and ω_{Dia} (red dashed) averaged over the boxed regions in Fig. 3.4 in **a** the developing stage (–18 h) and **b** the mature stage (0 h) of HREs. For ω_{QG}, ω_{Dyn} and ω_{Dia}, the 95% confidence interval is shaded based on a bootstrap test with 10,000 times resampling.

3.4. QG dynamic forcing: Transverse versus shearwise Q-vector forcings

The previous subsection shows that the diabatic omega dominates the upward motion in the mature stage of HREs. However, it does not simply mean that HREs are self-generated or self-maintaining. Considering that the latent heat release is passive in nature, the dynamically-forced uplift should be given so as to stimulate and further sustain the condensational heating (note in Fig. 3.5 that the diabatic omega at –36 h is spatially limited compared to the dynamic omega). In this regard, the nature of dynamic forcing needs to be further disentangled for a better understanding of HREs.

Motivated by the dipolar Q-vector forcing shown in Fig. 3.4a, the dynamic forcing is decomposed into the transverse ($Q_n\mathbf{n}$) and shearwise components ($Q_s\mathbf{s}$). Figure 3.7 shows the transverse and shearwise Q vectors, and their forcings at 500 hPa at 0 h. Both the transverse and shearwise Q-vector convergences have their maximum over the Korean Peninsula, but the latter is much stronger than the former. This indicates that the shearwise Q-vector forcing is more important than the transverse Q-vector forcing for dynamic uplift.

The shearwise Q vector converges east of the trough (Fig. 3.7b), consistent with the idealized model shown in Fig. 3.2c. However, the transverse Q-vector forcing in Fig. 3.7a differs from the idealized model shown in Fig. 3.2a. The $Q_n\mathbf{n}$ crosses the jet entrance, but only on the poleward side of the jet. This results in a $Q_n\mathbf{n}$ convergence right over the jet streak, not at the south of the entrance region. This poleward-confined $Q_n\mathbf{n}$ is likely caused by a weak temperature gradient at the south of the jet streak (see thickness lines in Fig. 3.9). This is also consistent with the presence of geostrophic warm advection along the jet axis, which shifts the thermally direct secondary circulation within the jet entrance region to promote ascent beneath the jet streak, not its equatorward side (Martin 2014).

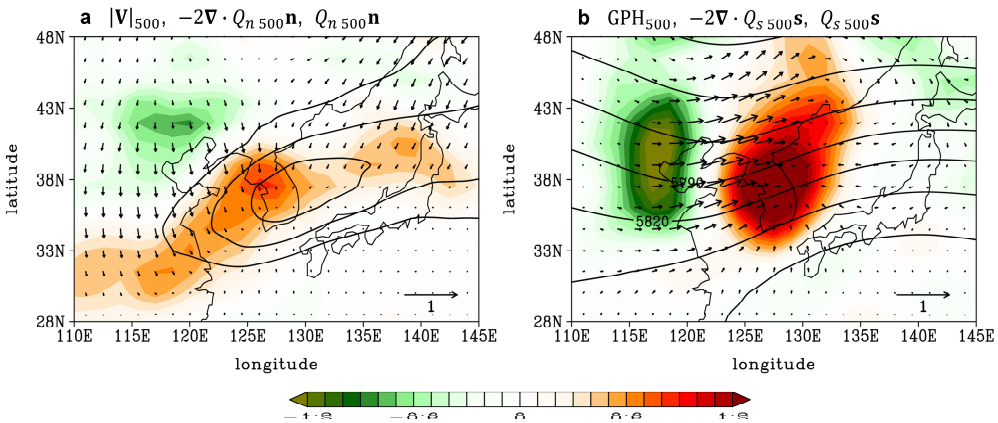

Figure 3.7. Composites of **a** horizontal wind speed (>12 m s^{-1}, contours with a 2-m s^{-1} interval), $Q_n\mathbf{n}$ forcing (10^{-18} m kg^{-1} s^{-1}, shading) and $Q_n\mathbf{n}$ (10^{-12} m^2 kg^{-1} s^{-1}, vectors), and **b** GPH (gpm, contours), $Q_s\mathbf{s}$ forcing (10^{-18} m kg^{-1} s^{-1}, shading) and $Q_s\mathbf{s}$ (10^{-12} m^2 kg^{-1} s^{-1}, vectors) at 500 hPa at 0 h.

Figure 3.8 displays the spatial pattern of 500-hPa ω_n and ω_s at 0 h. Although both of them show the maximum uplift over the Korean Peninsula, ω_n is elongated in the southwest-northeast direction with a positive value to the northwest and a negative value to the southeast (Fig. 3.8a). In contrast, ω_s exhibits a positive-negative dipolar pattern in the zonal direction (Fig. 3.8b). This is consistent with Keyser et al. (1988, 1992) who indicated that the latter develops into a cellular pattern on the scale of the baroclinic disturbance, while the former is organized into a banded structure on the scale of the embedded frontal zone. For both ω_n and ω_s, the ascent is greater in magnitude than the descent.

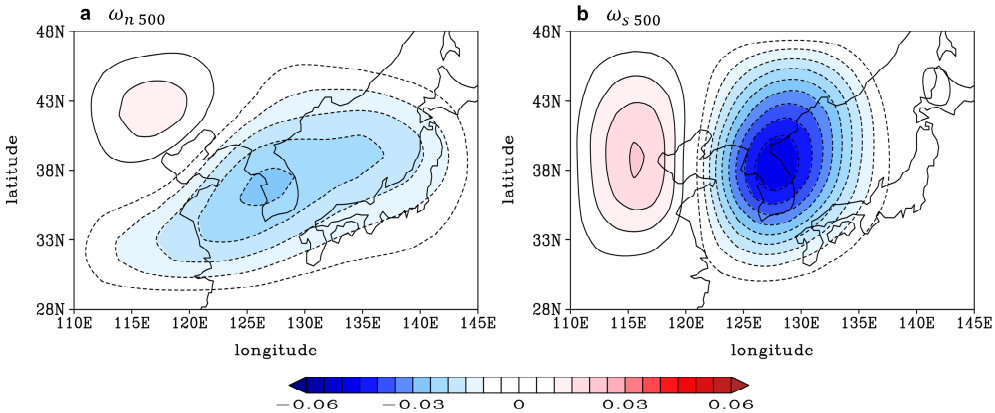

Figure 3.8. Composites of **a** ω_n and **b** ω_s at 500 hPa at 0 h. Unit is Pa s^{-1}.

As shown in Figs. 3.2b,c, the shearwise Q-vector forcing can be associated with both the confluent flow at the jet entrance and baroclinic trough. However, a pair of divergence and convergence around the trough (Fig. 3.7b), and the resulting dipolar vertical motion (Fig. 3.8b) indicate that the deepened baroclinic trough is a primary source of the shearwise Q-vector forcing. To understand the related processes, the 500-hPa geostrophic shear vorticity and geostrophic curvature vorticity (see appendix A3) are computed in Fig. 3.9. While the positive and negative shear vorticities are distributed at the poleward and equatorward sides of the jet (Fig. 3.9a), the curvature vorticities are organized in the zonal direction in a close relationship with a trough and ridge (Fig. 3.9b). As stated in section 3.2.3, the shearwise Q-vector forcing is generally well approximated to the geostrophic vorticity advection by thermal wind (see also appendix B2), and this is also true for the present cases (figure not shown). While the thickness lines are nearly normal to the shear vorticity gradient (Fig. 3.9a), they have a relatively smaller angle with the curvature vorticity gradient (Fig. 3.9b). Accordingly, it can be concluded that most of the geostrophic vorticity advection by thermal wind is due to the curvature vorticity by the trough rather than the shear vorticity by the jet streak (note that thermal wind is parallel to thickness lines with warm air to the right in the Northern

Hemisphere). Similar patterns also appear at 250 hPa although the patterns slightly shift northwestward (figure not shown). This result confirms that the dynamic uplift of HREs is mostly generated by the baroclinically-deepening trough.

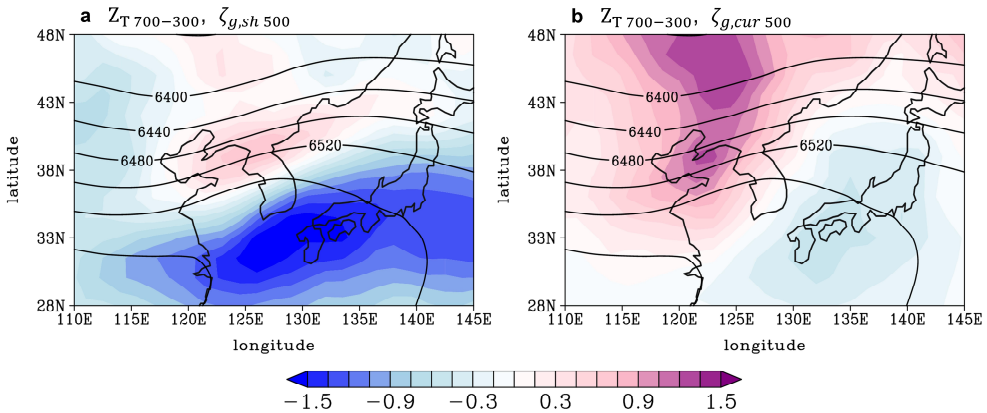

Figure 3.9. Composites of **a** thickness between 700 hPa and 300 hPa (gpm, contours), and geostrophic shear vorticity (CVU, shading) at 500 hPa at 0 h. **b** As in **a**, but for geostrophic curvature vorticity.

Figure 3.10 illustrates the vertical structure of the transverse and shearwise Q-vector forcings and the resulting vertical motions (i.e., ω_n and ω_s). The sum of these two components corresponds to Fig. 3.5a. Throughout the troposphere, Q-vector convergence is largely due to the shearwise component (Fig. 3.10b) rather than the transverse component (Fig. 3.10a) in the mature stage of HREs. Although ω_n is only slightly greater than ω_s at –36 h, the intensity of the shearwise Q-vector forcing and the resulting uplift (i.e., ω_s) increase much faster in time than the transverse counterparts. This is especially true in the middle to lower troposphere, because the shearwise Q-vector forcing, which is initially confined around the ULJ core, significantly extends downward in time. This emphasizes again that the dynamic uplift is closely related to a baroclinically organized trough.

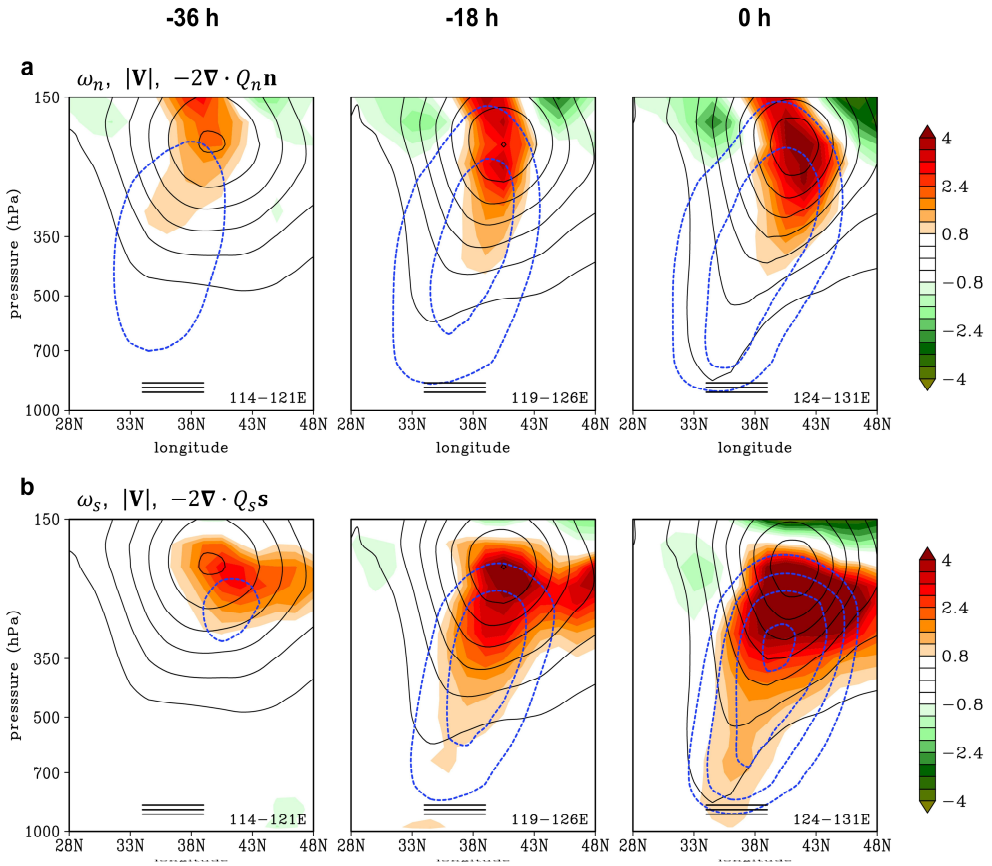

Figure 3.10. As in Fig. 3.5a, but the blue contours and shading are replaced by **a** ω_n (0.01-Pa s^{-1} interval) and $Q_n\mathbf{n}$ forcing (10^{-18} m kg^{-1} s^{-1}), and **b** ω_s (0.01-Pa s^{-1} interval) and $Q_s\mathbf{s}$ forcing (10^{-18} m kg^{-1} s^{-1}).

Figures 3.11a,b compare the vertical profiles of the transverse omega and shearwise omega at –18 and 0 h. Although ω_s is only slightly stronger than ω_n at –18 h (Fig. 3.11a), the former becomes much stronger than the latter at 0 h, becoming about 1.8 times stronger at 500 hPa (Fig. 3.11b). More importantly, ω_n does not change much from –18 to 0 h whereas ω_s increases considerably, which is consistent with the transient growth of the shearwise Q-vector forcing in Fig. 3.10b.

Here, it should be stated that the magnitude of forcing at a certain level cannot be directly translated to the intensity of vertical motion at that level because of the elliptic nature of the QG omega equation. To determine the most important layer inducing dynamic uplift and compare the vertical organization of the transverse versus shearwise Q-vector forcings, the QG omega equation is repeatedly solved by considering the upper- (400–100 hPa), mid- (650–400 hPa), and lower-layer (1000–650 hPa) forcings separately (Figs. 3.11c,d). Not surprisingly, each partitioned forcing is most influential in proximity to its respective layer. As such, the maximum ω_n and ω_s in the midtroposphere are mainly driven by the upper- and mid-layer processes, but the lower-layer processes are negligible. In all layers, a significant increase in ω_s is observed, while ω_n is nearly unchanged. Again, this highlights that the vertically organized baroclinic wave and its undulation play a crucial role in organizing the dynamic uplift in HREs.

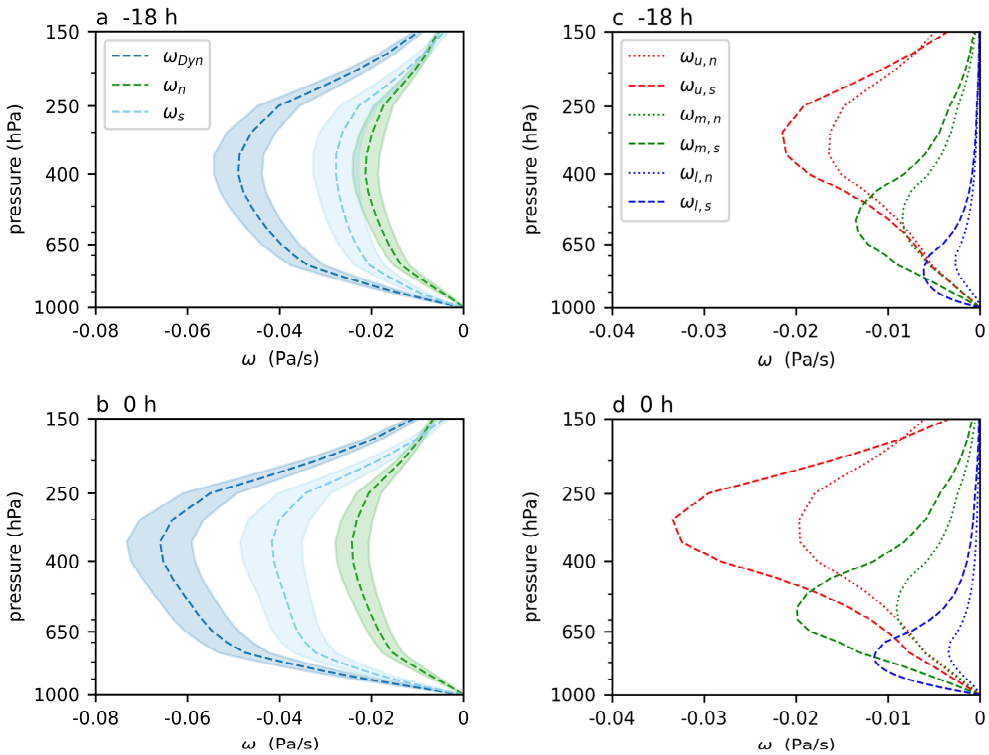

Figure 3.11. Vertical profiles of vertical motion (Pa s^{-1}) averaged over the boxed regions in Fig. 3.4. The left panels show ω_{Dyn} (blue dashed), ω_n (green dashed) and ω_s (sky-blue dashed) in **a** the developing stage (–18 h) and **b** the mature stage (0 h) of HREs. The 95% confidence interval is shaded based on a bootstrap test with 10,000 times resampling. The right panels show ω_n (dotted) and ω_s (dashed) induced by the upper (400–100 hPa; red), middle (650–400 hPa; green) and lower (1000–650 hPa; blue) layers, which are denoted by the subscripts u, m and l, respectively, in **c** the developing stage (–18 h) and **d** the mature stage (0 h) of HREs.

Table 3.1 summarizes the fractional contributions of vertical motion by diabatic, transverse Q-vector, and shearwise Q-vector forcings in the upper, middle, and lower layers at 0 h. The contributions of diabatic and dynamic forcings are ~63% and ~37%, respectively, at 500 and 850 hPa, while those are transitioned to ~45% and ~55%, respectively, at 250 hPa. Among the dynamic contribution, the shearwise component is about 1.8 times larger than the transverse component at 250 and 500 hPa, and 2.4 times larger at 850 hPa.

Table 3.1. Fractional contributions (%) of vertical motion by diabatic, transverse Q-vector and shearwise Q-vector forcings to ω_{QG} at 250 hPa, 500 hPa and 850 hPa averaged over the boxed region in Fig. 3.4 in the mature stage of HREs (0 h). Forcings in the upper (*u*; 400–100 hPa), middle (*m*; 650–400 hPa) and lower (*l*; 1000–650 hPa) layers are separately considered.

	Diabatic forcing				Transverse Q-vector forcing				Shearwise Q-vector forcing			
	u	*m*	*l*	Total	*u*	*m*	*l*	Total	*u*	*m*	*l*	Total
ω_{QG250}	30.9	13.1	1.1	45.1	17.9	2.4	0.3	20.6	29.5	4.3	0.5	34.3
ω_{QG500}	15.7	43.2	4.0	62.9	7.4	5.3	0.6	13.3	10.6	11.5	1.7	23.8
ω_{QG850}	6.5	25.8	31.2	63.5	4.1	3.9	2.8	10.8	5.2	8.4	12.2	25.8

3.5. Discussion

The result indicates that HREs are triggered *primarily* by baroclinically deepening disturbances and *secondarily* by thermally direct secondary circulation on the jet entrance region with a further self-sustaining process by diabatic forcing. Here, a new conceptual model of HREs is suggested (Fig. 3. 12). This conceptual model contrasts with the previous one which emphasized the ageostrophic secondary circulation as a key driver of HRes (see section 1.1.5).

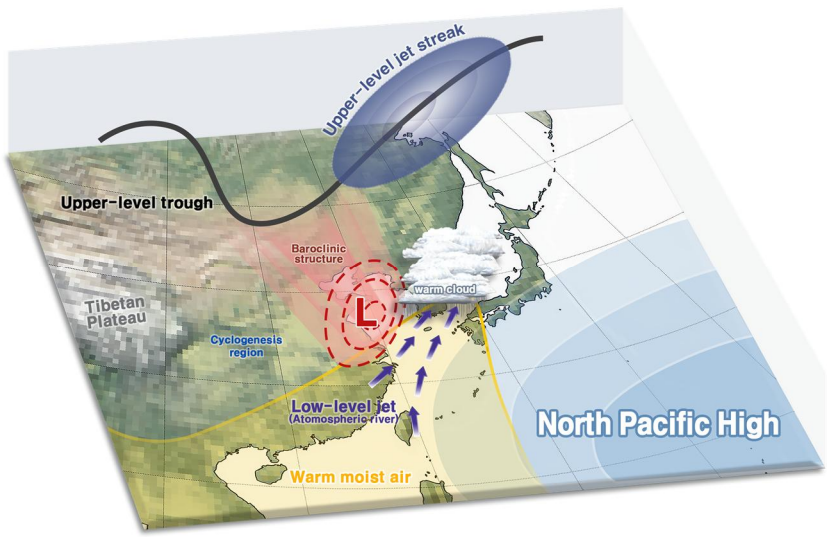

Figure 3.12. An updated conceptual model of HREs, which describes the typical 3D structure of warm-season HREs in South Korea.

The sensitivity of QG diagnosis to different reanalysis data is tested by repeating the analyses with the fifth-generation atmospheric reanalysis from the ECMWF (ERA5; Hersbach et al. 2020). It is found that ω_{QG} from the ERA5 data still well produces the reanalyzed omega (figure not shown). However, ω_{QG} from the ERA5 data is slightly larger than that obtained from the ERA-Interim data. This difference mostly comes from the greater ω_{Dia} in the ERA5 than that in the ERA-Interim data, whereas ω_{Dyn} does not differ between the two reanalyses. It is likely because the ERA5 data, which are produced by a higher-resolution model than the

ERA-Interim data, is more favorable for the convective updraft and its resulting latent heat impact on the grid-scale vertical motion. Nevertheless, the key conclusion of this study remains unchanged.

The result of this chapter is somewhat different from previous studies. After Uccellini and Johnson (1979), many studies on the summertime HREs in South Kore have related the vertical motion of the HREs to the thermally direct secondary circulation at the ULJ entrance. However, this chapter demonstrates that HREs are organized by baroclinic perturbation coupled with moist processes. Although the ULJ and LLJ collocate in the mature stage of the HREs, they are not quasi-stationary but connected by the transient baroclinic waves. Accordingly, to better understand and predict the HREs, the developing baroclinic disturbances need to be considered even in the summer monsoon period when the baroclinicity is generally weak.

Although not in South Korea, Yokoyama et al. (2020) also emphasized the role of an upper-level trough in the HRE in Japan in July 2018. This similar result suggests that the dominance of the shearwise Q-vector forcing may be common in East Asian HREs. This idea is supported by a few studies that have highlighted the importance of upper-level disturbances in transiently enhancing moisture transport and monsoon rainfall in East Asia summer (Horinouchi 2014; Park et al. 2015; Horinouchi and Hayashi 2017). In this regard, this study could be extended to Meiyu and Baiu HREs. However, it is of note that the recent study by Zhao et al. (2023) showed that the long-traveling HREs along the Yangtze River basin are dominated by diabatic heating.

Chapter 4. Diverse synoptic weather patterns of HREs

Note: The contents of this chapter are taken from Park et al. (2021b) titled "Diverse synoptic weather patterns of warm-season heavy rainfall events in South Korea" published in *Monthly Weather Review.* (Vol. **149**, 3875–3893, https://doi.org/10.1175/MWR-D-20-0388.1). Some modifications have been made from the original article for the organization of the dissertation.

4.1. Motivation

The climatological and quantitative dynamical analyses in chapters 2 and 3, improved our understanding of the general synoptic–dynamic characteristics of HREs. However, it would be further beneficial to investigate the potential diversity of HREs in terms of their synoptic weather patterns. The composite of 318 HREs exhibits the statistically significant surface cyclone and the anomalous NPH in the lower troposphere (see Figs. 2.3 and 3.3). Given the substantial subseasonal variation and low-frequency variability of Changma, however, there might be considerable event-to-event differences in the surface circulation patterns of HREs which should be obscured in the composites. In China and Japan, the typical synoptic weather patterns related to HREs have been objectively classified (e.g., Ohba et al. 2015; Nguyen-Le et al. 2017; Zhao et al. 2019), but such analysis is still lacking for the South Korean HREs.

This chapter provides a comprehensive but still compact synoptic view of HREs. By applying the self-organizing map (SOM) to SLP fields around the Korean Peninsula, the historical HREs are classified into six clusters, and their synoptic details are compared. The result also provides useful guidance for HRE prediction by depicting important factors to be differently considered depending on their synoptic categorization.

4.2. Data and methods

4.2.1. Dataset

The dataset used here is identical to that in chapter 2. The 318 HREs in JJAS during 1979–2018 and the 6-hourly ERA-Interim reanalysis data with 1.5°×1.5° horizontal grid spacing and 37 pressure levels are also used. Anomaly fields are calculated by subtracting the 40-year 6-h climatology. Anomaly fields are calculated by subtracting the long-term (40 years) 6-h climatology.

To compare the vertical motion mechanisms between the clusters, the components of QG omega, which are obtained by inverting the QG omega equation in chapter 3, are utilized. The vertical motion by beta forcing (ω_{Beta}) is not present in this chapter as it is negligible (see Fig. 3.6).

4.2.2. Classification of HREs

By utilizing the SOM algorithm, the 318 HREs are objectively classified based on their surface weather patterns (see appendix C1 for the details of SOM). As the clustering property, SLP fields 6 h before the reference time of HREs (i.e., at –6 h) are used because the SLP effectively summarizes surface weather conditions on a synoptic weather chart. The considered domain is 27°–47°N and 112°–136°E. For the node array, a 1×6 array is selected based on the following rationale: the one-dimensional array can result in more clearly distinguished clusters due to the self-organizing nature of the SOM that locates similar clusters adjacently. More importantly, a one-dimensional array is desirable as it forces the nodes to be arranged in a sequence that can be reflective of the subseasonal variation in the background SLP fields (i.e., from early to late summer), allowing a more physically interpretable result. After multiple sensitivity tests with different node sizes systematically varying in only one dimension ($1 \times n$), six nodes are found to be ideal for summarizing the surface weather patterns of HREs. Other SOM parameters follow the suggestions of Liu et al. (2006) and are summarized in Table 4.1.

Table 4.1. SOM parameters specified in this chapter.

SOM Parameters	Selected option
Input data	ERA-Interim SLP fields at –6 h over 27–47°N & 112–136°E
Array of nodes	1×6
Topology of node	Rectangular
Shape of map	Sheet
Initialization method	Linear initialization
Training method	Batch training
Neighborhood function	Epanechnikov function
Neighborhood radius	6 (initial), 1 (final)
Number of iterations	3,000 (rough training), 6,000 (fine tuning)

4.3. Overview of the SOM clustering results

Figure 4.1 presents the SOM result—SLP composites at –6 h over the clustering domain for the six clusters (C1–C6). Due to the self-organizing nature of the SOM, the result shows continuous SLP patterns with adjacent clusters. Note that closer to C1, a more pronounced low SLP appears, but approaching C6, a high SLP becomes dominant.

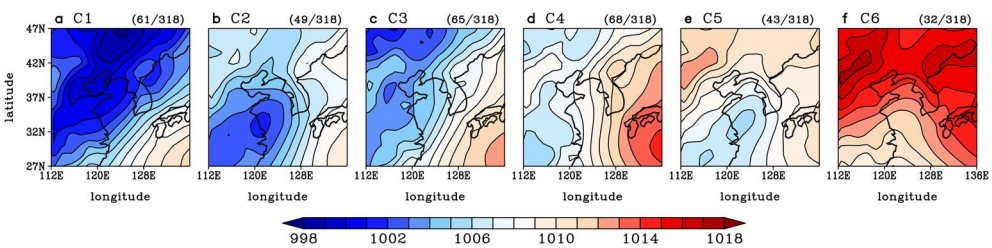

Figure 4.1. The results of the 1×6 SOM clustering applied to HREs. The plotted variable is the composited –6-h SLP fields for the six clusters (C1–C6) over the clustering domain (27°–47°N and 112°–136°E).

Table 2.1 summarizes the six clusters of HREs. Although slight differences are found in HRE intensity and duration between the six clusters, those differences fall within their respective ± 1 standard deviation (Table 4.2). This implies that event-to-event spreads are larger than cluster-to-cluster differences in HRE intensity and duration.

Table 4.2. Summary of the six HRE clusters. The first nine rows are in compliance with those in Table 2.1.

	C1 (19.2%)	C3 (20.4%)	C2 (15.4%)	C5 (13.5%)	C4 (21.4%)	C6 (10.0%)
Synoptic description	*Quasi-stationary frontal boundary between low and high*		*Extratropical cyclone from eastern China*		*Local disturbance at the edge of the NPH*	*Moisture pathway between continental and oceanic highs*
Preferred period	First rainy period		First and second rainy periods	Second rainy period	First and second rainy periods	Second rainy period
Preferred region	West of mountainous region		Indistinct preferred region		West of mountainous region	Southwest coast
Max.12-h acc. rainfall	186.8 ± 89.8	170.6 ± 52.7	163.1 ± 41.5	163.9 ± 53.6	172.8 ± 56.1	161.4 ± 45.6
HRE duration	16.7 ± 11.0	14.0 ± 9.0	15.8 ± 10.5	16.0 ± 14.1	15.5 ± 8.8	13.1 ± 8.3
|IVT|	571.0 ± 197.7	502.2 ± 173.4	436.4 ± 170.3	359.0 ± 134.1	415.1 ± 140.2	328.0 ± 148.3
Zonal **IVT**	455.9 ± 172.6	358.2 ± 156.5	198.7 ± 195.2	178.8 ± 172.1	275.1 ± 141.1	176.2 ± 169.5
Meridional **IVT**	254.4 ± 176.3	269.2 ± 177.5	255.0 ± 184.4	196.7 ± 156.3	243.1 ± 142.5	187.7 ± 137.3

However, those clusters are well differentiated by their spatiotemporal occurrence distributions (Fig. 4.2). Moving from left to right across the clusters, the preferred occurrence period tends to shift from the early to late summer (Fig. 4.2a). For instance, C1 and C3 peak in July while C5 and C6 favor August and September, respectively. In contrast, C2 and C4 exhibit bimodal frequency peaks with a tail to the left. This gradual transition in the temporal distribution from C1 to C6 can be anticipated from the use of the one-dimensional node array due to the self-organizing nature of the SOM.

Differences are also found in their spatial distributions (Fig. 4.2b). While The C1 HREs predominantly occur in the west of the elevated terrain, C6 is largely confined to the southwest coast. The C3 and C4 are also frequent in the western half of the country, but the extent is less distinct than C1. The C2 and C5 are relatively spread across the country.

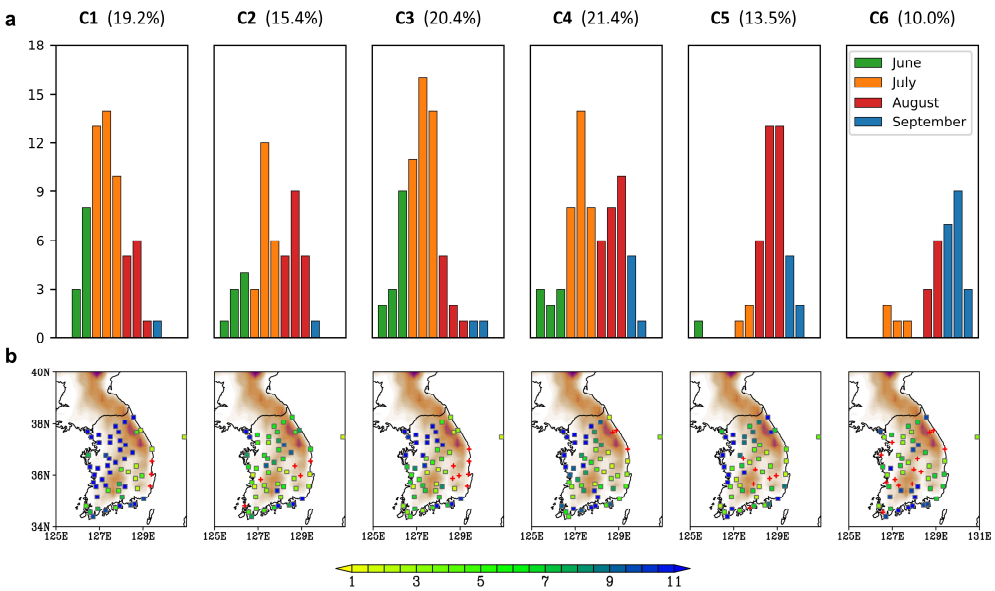

Figure 4.2. As in Fig. 2.7, but for the six HRE clusters: **a** the number of HREs in 10-day bins in JJAS (colored bars), and **b** the spatial distributions of the probability of occurrence (%, colored square) for each cluster. In **b**, the ASOS stations where no HRE was observed are marked by red crosses.

In section 4.4, the synoptic characteristics of the six HRE clusters are further detailed. Figures 4.3–4.8 shows the time evolutions of surface and upper-tropospheric circulation as done for the total HREs in Fig. 2.3. To facilitate discussion, the clusters that share common surface weather patterns are grouped. For example, the synoptic background of C1 and C3 can be explained as a quasi-stationary frontal boundary between low and high SLPs. In contrast, C2 and C5 feature a direct influence from an ETC. The C4 and C6 are not grouped with any other since they exhibit unique surface patterns.

The dynamic/thermodynamic details are also compared between the six clusters, as done for the total HREs in Fig. 2.4. In all clusters, the vertical structure of θ_e features a favorable condition for convective instability, and the upper-level divergence and low-level convergence are well collocated to each other as in the total HREs (figure not shown). However, the horizontal distribution of 850-hPa θ_e and the vertical structure of GPH anomaly differ between clusters in association with their distinct surface weather patterns. They are given in Figs. 4.9 and 4.10, respectively.

The vertical motion mechanisms, which are explored for the total HREs in chapter 3, are also diagnosed for the six HRE clusters individually. In all clusters, ω_{QG} reasonably well reproduces the reanalyzed vertical motion. Besides, diabatic uplift (i.e., ω_{Dia}) is robustly greater than dynamic uplift (ω_{Dyn}) in the mature stage of HREs (Fig. 4.11a). The ω_{Dyn} is also more associated with the shearwise vertical motion (ω_s) than the transverse counterpart (ω_n) in all clusters (Fig. 4.11b). This implies that the key conclusion of chapter 3 can be applied to individual HRE clusters. Nevertheless, the relative importance of each omega component is slightly different between the clusters, and this is briefly mentioned wherever necessary.

4.4. Synoptic patterns of the six HRE clusters

4.4.1. Quasi-stationary frontal boundary between low and high (C1 and C3)

The C1 and C3 account for 39.6% of non-TC HREs. They are characterized by a region of low SLP over northeastern China (north of the Korean Peninsula) and high SLP over the northwestern Pacific, forming a quasi-stationary frontal zone and large-scale southwesterly **IVT** in between (Figs. 4.3a and 4.4a). The high θ_e stretching from southwest to northeast and frontogenetic activity along its large gradient are evident (Figs. 4.9a,b). However, C1 and C3 are differentiated by the relative strengths of the lows and highs. While C1 is characterized by a stronger low with a relatively weak high (Fig. 4.3a), C3 features somewhat comparable strengths of low and high (Fig. 4.4a). This background difference is likely associated with the differing seasonal march of the NPH, as manifested by the 1010-hPa isobar (cf. thick black lines in Figs. 4.3a and 4.4a).

In both clusters, a strong southwesterly **IVT** already develops along the frontal boundary at –36 h. This moisture transport further intensifies in time, significantly affecting the western side of the Korean Peninsula (Fig. 4.2b). The **IVT** magnitude in this HRE group is largest compared to other clusters (Table 4.2). The transient increase in **IVT** can be explained by a transient cyclone developing between the low and high. At –36 h, a cyclonic vorticity core appears over eastern China (see white and purple contours in Figs. 4.3a and 4.4a, respectively). This early disturbance (~1 CVU) travels along the frontal boundary with continuous intensification to ~2–3 CVU at 0 h with a weak baroclinic vertical structure with a statistically significant negative GPH anomaly centered in the lower troposphere (Figs. 4.10a,b). Note that this cyclone is well separated from the quasi-stationary cyclonic core over northeastern China. This feature reflects the importance of multiscale interactions between the quasi-stationary pressure systems and the transient cyclones in setting HREs.

Figures 4.3b and 4.4b illustrate the upper-level circulation of C1 and C3, respectively. In both clusters, the upper-level trough develops and propagates

eastward in time, phasing with the surface frontal cyclone. On the eastern side of the trough, the midlevel ascent is well organized. However, C1 and C3 are somewhat different in the location of the upper-level trough and ULJ streak. The trough in C1 comes from the northwest of the Korean Peninsula, and the jet streak develops along the base of the trough (Fig. 4.3b). In contrast, the trough in C3 comes from the west of the Korean Peninsula, and the relatively weaker jet streak organizes on the east of the trough axis (Fig. 4.4b). In both clusters, ω_s is greater than ω_n (Fig. 4.11b), implying an important role of the isentropes rotation by the trough in dynamically forced uplift (ω_{Dyn}).

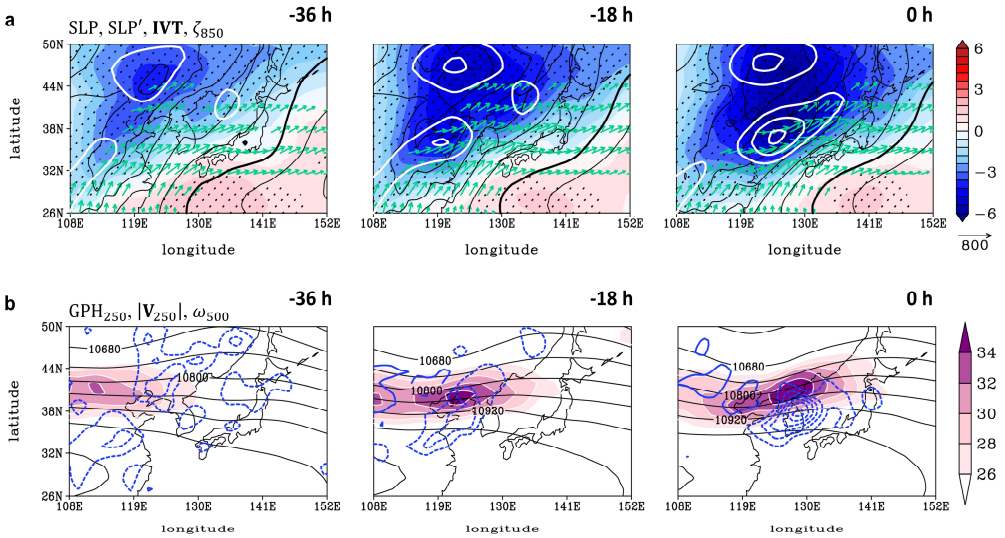

Figure 4.3. As in Fig. 2.3, but for C1 HREs. The 850-hPa T42 relative vorticity in **a** is contoured in white. Note that the shading range in **a** is 3 times larger than that in Fig. 2.3a.

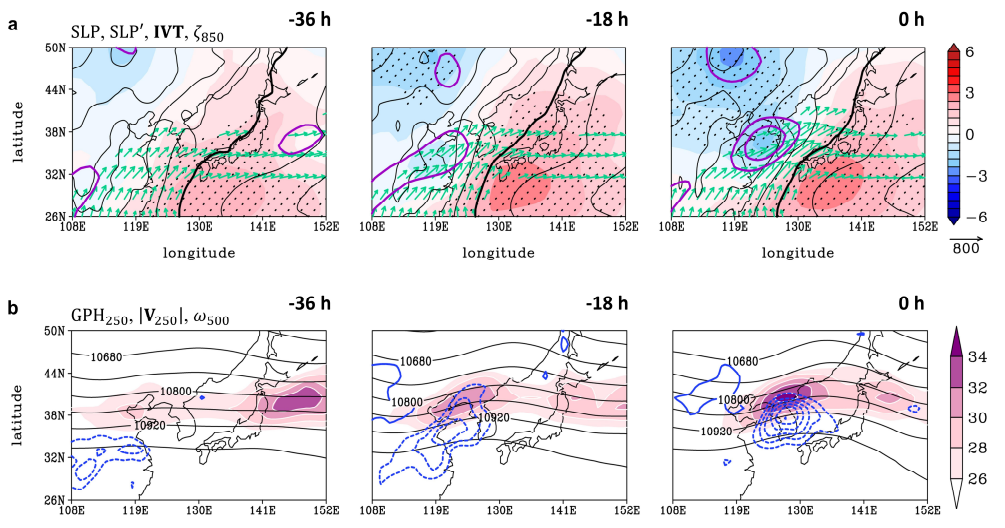

Figure 4.4. As in Fig. 2.3, but for C3 HREs. Note that the shading range in **a** is 3 times larger than that in Fig. 2.3a.

4.4.2. ETC from eastern China (C2 and C5)

The C2 and C5 account for 28.9% of non-TC HREs and represent the direct impact of an ETC. At –36 h, a weak cyclone with an intensity of ~1 CVU appears over eastern China (Figs. 4.5a and 4.6a). This early-stage disturbance continues to intensify as it propagates northeastward, especially when encountering the Yellow Sea at –18 h. In the mature stage (0 h), the cyclone is located immediately west of the Korean Peninsula with an intensity of ~3 CVU. The cyclone has a westward tilted structure in the vertical with a minimum GPH anomaly in the upper troposphere (Figs. 4.10c,d), which is a typical feature of baroclinic instability. Unlike C1 and C3 in which the large-scale pressure systems pre-induce southwesterly **IVT**, the cyclones in C2 and C5 by themselves produce substantial **IVT**. The **IVT** exhibits stronger southerly components than westerly components, which likely results in less skewed HRE occurrences toward the western side of the country compared to C1 and C3 (Fig. 4.2b).

Despite the similar extent of intensification (~3 CVU at 0 h), the cyclone in C2 tends to deepen more than the one in C5 (cf. blue shadings in Figs. 4.5a and 4.6a). This indicates that not only the mass fields (e.g., SLP) but also the kinematic fields (e.g., vorticity) need to be carefully monitored in forecasting the ETC-induced HREs in South Korea. Another noticeable difference is the background SLP. While C2 is dominated solely by the well-deepened ETC (Fig. 4.5a), C5 is also characterized by the background high SLP (and its positive anomalies) over the Asian continent and the northwestern Pacific Ocean (Fig. 4.6a). This likely explains why the cyclone in C5 has comparable cyclonic vorticity to that in C2 despite the weaker negative SLP anomaly. The high SLP surrounding the cyclone can contribute to the increased pressure gradient around the cyclone and thereby to the sufficiently strong vorticity.

Figures 4.5b and 4.6b depict similar upper-level flows to each other. The upper-level trough deepens and propagates eastward from the west, which is consistent with the developing surface cyclone. The ULJ streak also develops on the east of the trough with its entrance region to the north of South Korea at 0 h. The strong 500-hPa upward motion is evident in the east of the trough and the

equatorward side of the jet entrance. Comparison of ω_n and ω_s reveals that the rotating effect by the trough is more important than geostrophic frontogenesis around the jet entrance in generating ω_{Dyn} for both clusters (Fig. 4.11b). However, the relative contribution of ω_n is greater in C5 possibly due to the stronger ULJ (cf. shadings in Figs. 4.5b and 4.6b), which may force stronger frontogenetic confluence on the entrance region, and also possibly due to the relatively weaker baroclinic organization (cf. Figs. 4.10c,d), which may induce weaker isentropes rotation throughout the troposphere.

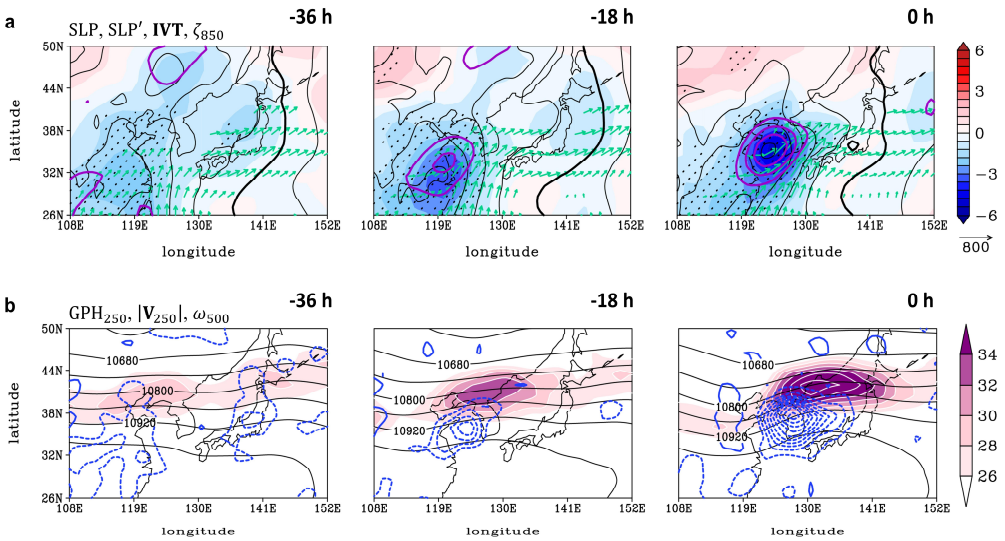

Figure 4.5. As in Fig. 2.3, but for C2 HREs. Note that the shading range in **a** is 3 times larger than that in Fig. 2.3a.

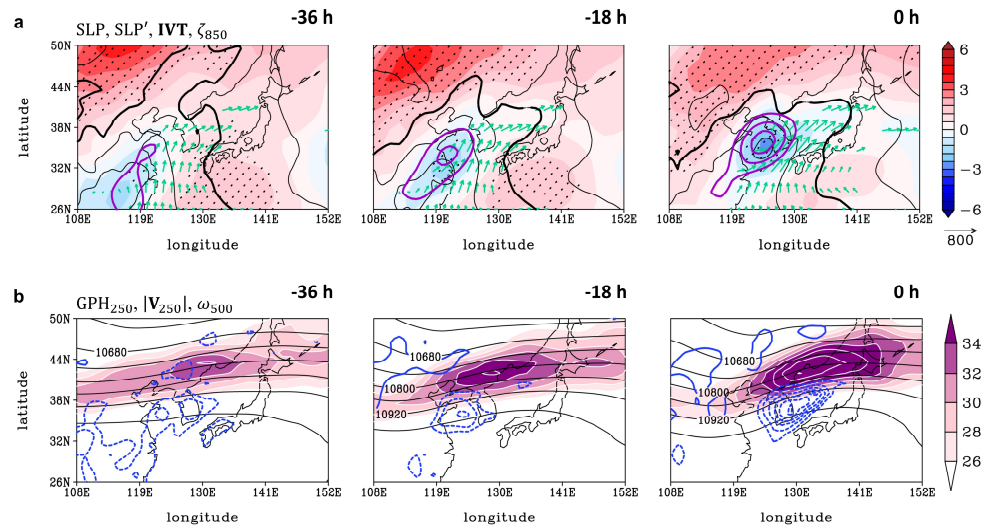

Figure 4.6. As in Fig. 2.3, but for C5 HREs. Note that the shading range in **a** is 3 times larger than that in Fig. 2.3a.

4.4.3. Local disturbance at the edge of the NPH (C4)

The C4 composes 21.4% of non-TC HREs. This HRE type is dominated by a positive SLP anomaly centered southeast of Korea (Fig. 4.7a). This anomalous high is interpreted as the expanded NPH toward the Korean Peninsula (see the 1010-hPa isobar). In stark contrast to the previous clusters, the SLP and its anomaly patterns are nearly invariant with no statistically significant synoptic-scale perturbation. Instead, the expanded NPH induces strong southwesterly **IVT** along its northwestern boundary, affecting the western part of South Korea (Fig. 4.2b). At 0 h, a region of weak transient cyclonic vorticity (~1 CVU) is observed over the Yellow Sea. The absence of negative SLP anomalies and the sudden appearance of relatively weak cyclonic vorticity imply that C4 HREs are triggered by a local disturbance along the boundary of the NPH. Perhaps, C4 HREs are not likely well forecasted based on the traditional synoptic analysis, and higher-resolution analyses would be required.

In the upper troposphere, the weak upper-level trough and ULJ streak are found, but they are nearly stationary without propagation or strengthening in time (Fig. 4.7b). This is consistent with the nearly invariant SLP pattern in Fig. 4.7a. The C4 HREs exhibit a nearly barotropic vertical structure (Fig. 4.10e), implying no interaction between the upper and lower troposphere. Nevertheless, the QG omega equation inversion reveals that ω_{Dyn} plays a nonnegligible role in the upward motion over South Korea (Fig. 4.11a), with a larger contribution of ω_s than ω_n (Fig. 4.11b).

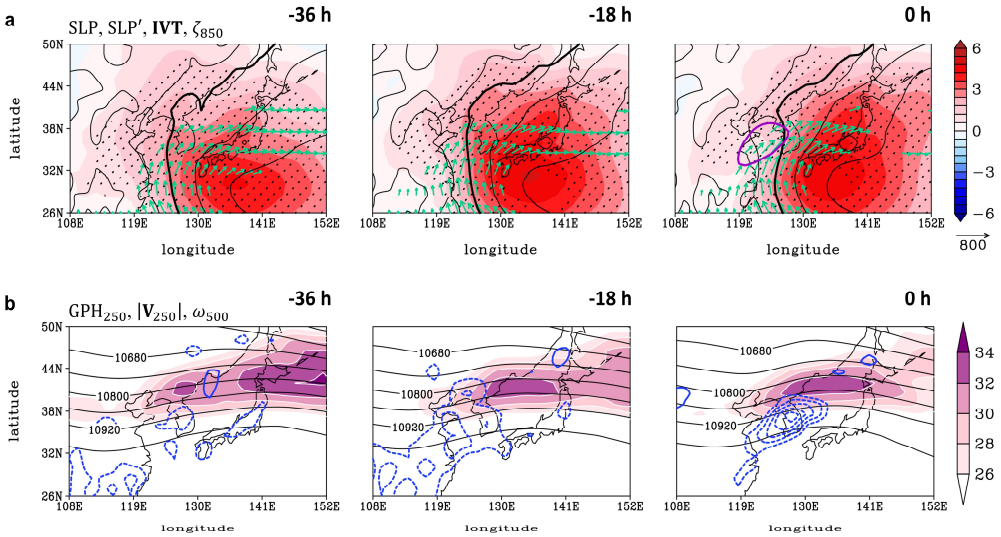

Figure 4.7. As in Fig. 2.3, but for C4 HREs. Note that the shading range in **a** is 3 times larger than that in Fig. 2.3a.

4.4.4. Moisture pathway between continental and oceanic highs (C6)

The C6 HREs mostly occur in late August and September (Fig. 4.2a). They are characterized by overwhelmingly high SLP (and its positive anomalies) over the Asian continent and the northwestern Pacific (Fig. 4.8a). Although C6 has the smallest fraction of non-TC HREs (only 10.0%), this pattern consistently appears in a series of SOM sensitivity tests, implying that C6 is neither a statistical artifact nor a random collection of events. From –36 to –18 h, moisture transport occurs between the continental and oceanic highs but mostly over the East China Sea. At 0 h, however, the southwesterly **IVT** reaches Korea with a sudden development of the surface trough between the two large-scale surface highs. The cyclonic vorticity over the surface trough is quite strong (~2 CVU), building the moisture pathway toward Korea from the East China Sea. It is found that various weather systems are randomly involved (e.g., remote effect of TCs, meso-α- to synoptic-scale cyclone, local instability, etc.), implying a necessity of further case-by-case investigation beyond this background-based classification.

In the upper troposphere, a weak upper-level trough is observed far upstream at –36 h (Fig. 4.2b). The trough continuously deepens while propagating eastward. At 0 h, the trough is located immediately west of South Korea with the downstream ULJ whose entrance region is positioned to the north of South Korea. Note that the ULJ in C6 is strongest compared to other clusters, possibly due to the increased surface baroclinicity in late summer (Fig. 4.9f). In the east of the upper-level trough and south of the ULJ entrance, the strong ascent is organized, implying a contribution from the dynamically forced ascent (i.e., ω_{Dyn}) to the development of the surface trough and HREs (see Fig. 4.11a). As in other clusters, ω_s is greater than ω_n (Fig. 4.11b), but the relative contribution of ω_n to ω_{Dyn} is largest in C6. This is possibly due to the strongest ULJ which may allow the strongest frontogenetic confluence on its entrance region.

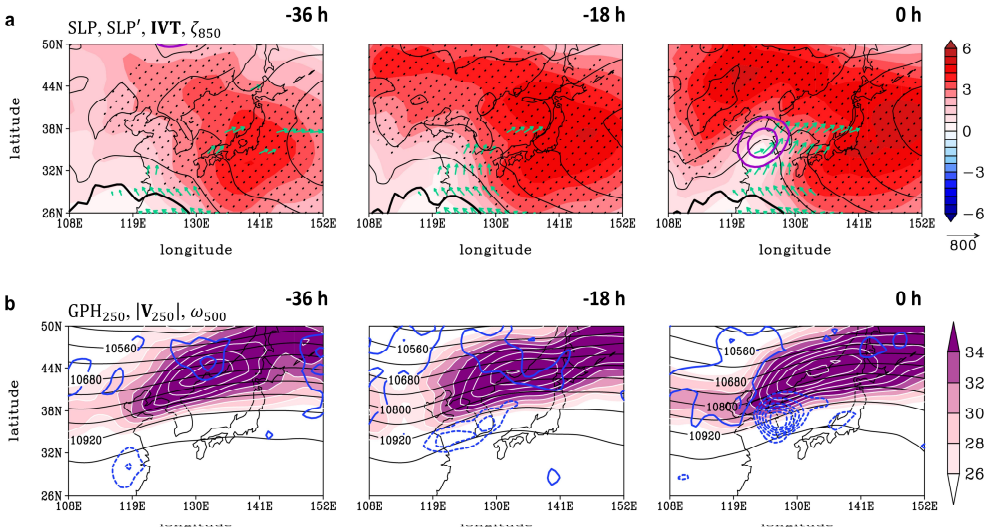

Figure 4.8. As in Fig. 2.3, but for C6 HREs. Note that the shading range in **a** is 3 times larger than that in Fig. 2.3a.

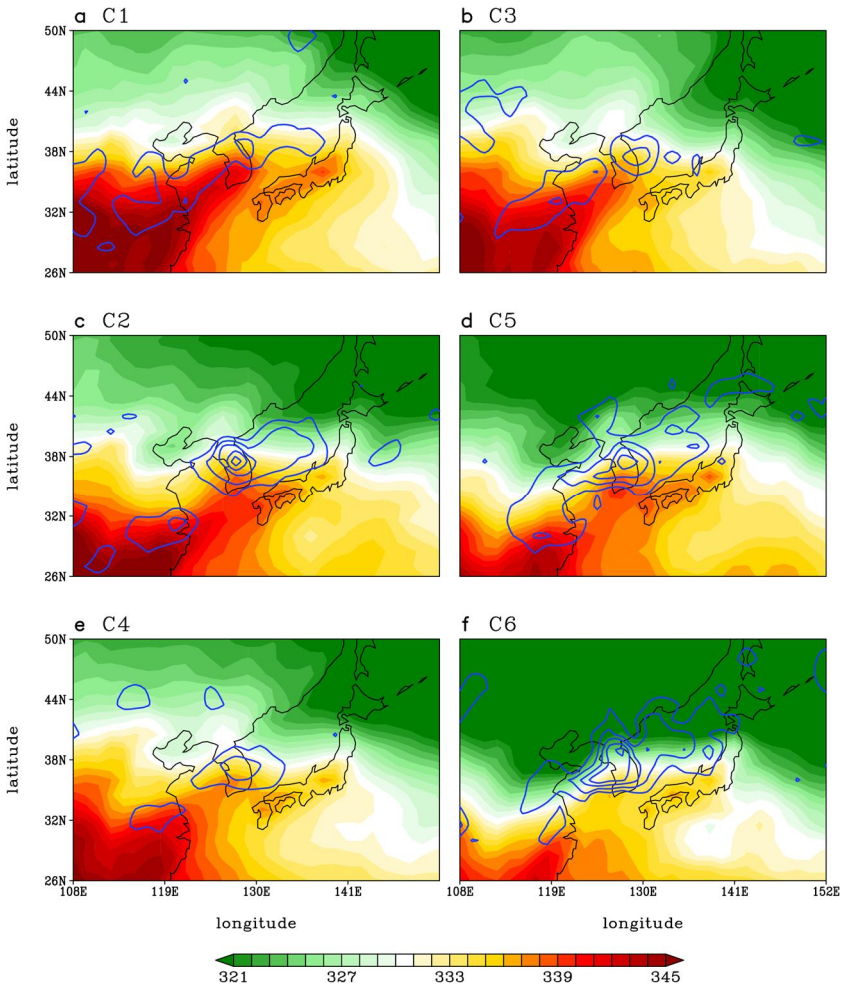

Figure 4.9. As in Fig. 2.4a, but for the six HRE clusters: 850-hPa θ_e (K, shading) and the Petterssen frontogenesis function applied to the 850-hPa θ_e [blue contours for positive values with a 1-K (100 km day)$^{-1}$ interval]. The order of panels follows that of descriptions in the main text.

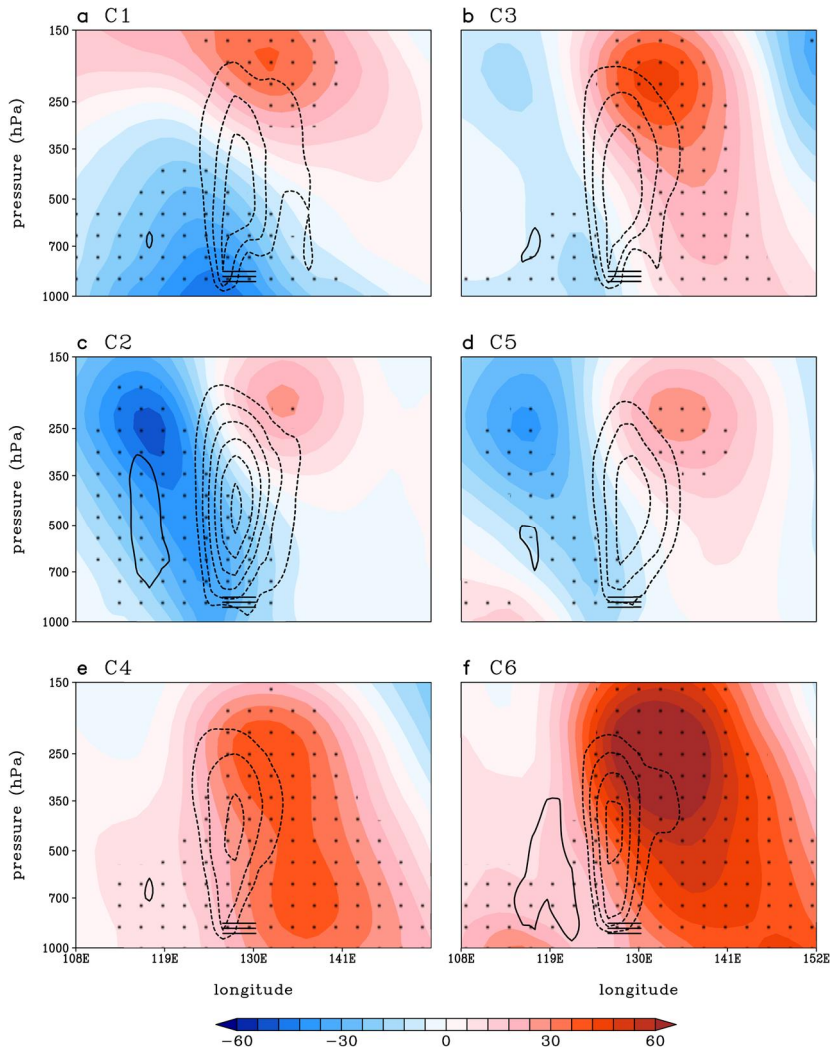

Figure 4.10. As in Fig. 2.4c, but for the six HRE clusters: longitude-pressure cross section of GPH anomalies (gpm, shading) and vertical velocity (contours with a 0.04 Pa s^{-1} interval). The order of panels follows that of descriptions in the main text.

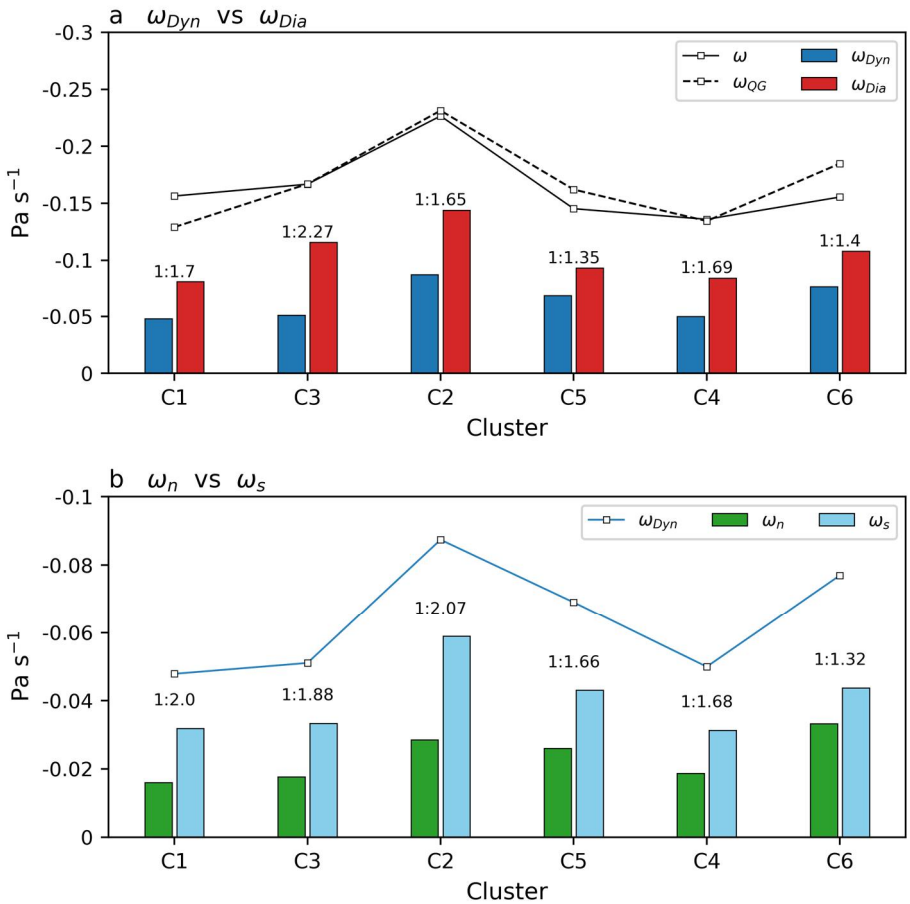

Figure 4.11. a ω (solid line), ω_{QG} (dashed line), ω_{Dyn} (blue bars) and ω_{Dia} (red bars) at 500 hPa in the mature stage (0 h) of the six HRE clusters estimated over the boxed region in the right panel of Fig. 2.3b. The ω_{Beta} is not shown as it is negligibly small. The ratio of ω_{Dyn} to ω_{Dia} is annotated on the top of the bars. **b** As in **a**, but for ω_{Dyn} (blue line), ω_n (green bars) and ω_s (sky-blue). The order of bars follows that of descriptions in the main text.

4.5. Discussion

This study suggests different forecasting factors depending on the HRE types. For C1 HREs and C3 HREs, a transient cyclone between the quasi-stationary low and high should be carefully monitored, because it has a substantial local cyclonic vorticity although the cyclone is not clearly distinguished in mass fields (e.g., SLP). For C2 HREs and C5 HREs, both the SLP and low-level relative vorticity need to be considered because the ETC can strongly intensify (i.e., large cyclonic vorticity) despite only weakly deepened SLP (e.g., C5). To better predict C4 HREs, the traditional synoptic analysis may be insufficient because there is no spatially organized disturbance. Instead, a higher-resolution model with well-tuned physical parameterizations is likely necessary. The C6 HREs accompany a strong upper-level trough and jet, and thus it should be noted that various rainfall systems can develop in the given synoptic background.

Beyond the SLP fields, other properties are also available in SOM clustering to examine different aspects of HREs. For example, dynamic tropopause could be an option if the upper-level modulation of the HREs is of interest (e.g., Agel et al. 2019). The upper-tropospheric disturbance often transiently modulates the East Asian summer rainfall (Horinouchi 2014; Horinouchi and Hayashi 2017) as we have seen for the summertime HREs in South Korea in chapter 3. Extracting diverse upper-tropospheric patterns of HREs and examining their differing dynamical impacts on surface weather conditions will shed additional light on HRE dynamics.

Chapter 5. Role of midlatitude condition in TC-HREs

Note: This chapter will be submitted to journal as a stand-alone paper titled "Role of midlatitude baroclinic condition in heavy rainfall events induced by tropical cyclones in South Korea".

5.1. Motivation

The climatological analyses in chapter 2 have found that about 18.9% of HREs in the summer monsoon season are directly caused by TCs. Such TC-HREs are often accompanied by a meandering and amplifying upper-level flow and a jet streak, implying a synergistic interaction between TCs and midlatitude flow. Although there have been numerous studies on the meteorological factors associated with TC rainfall in South Korea, including local topography (Park and Lee 2007; Lee and Choi 2010; Cho et al. 2022), regional sea surface temperature (Cho et al. 2022), track of TCs (Nam et al. 2018) and environmental vertical wind shear (Kim et al. 2019), how the midlatitude conditions affect HREs when TCs make landfall has received relatively less attention.

The recurving TCs in the western North Pacific strongly interact with midlatitude flow (Klein et al. 2000; Kitabatake 2011). The structural changes of TCs and midlatitude flow during ET have been extensively studied (see section 5.2), but it is still questionable how TC–midlatitude flow interaction alters the characteristics of TC-HREs, especially in East Asia. Only a few studies have been conducted on the landfalling hurricanes in eastern North America (Atallah and Bosart 2003; Atallah et al. 2007; Milrad et al. 2009). Such analyses are, however, still lacking in East Asia. A few studies have addressed midlatitude conditioning (Byun and Lee 2012; Baek et al. 2015), but their analyses were confined to the indirect impacts of TCs (i.e., predecessor rainfall events).

Beyond the qualitative description of TC-HREs in chapter 2, this chapter elucidates their synoptic–dynamic details in the context of TC–midlatitude flow interaction. It is worth mentioning that although the analyses are heavily based on the literature on ET, all HREs are examined regardless of whether TCs

undergo/complete ET or not (e.g., Atallah et al. 2007; Milrad et al. 2009). This approach allows a flexible but still physically meaningful explanation for TC-HREs in terms of TC–midlatitude flow interaction.

5.2. Literature review of ET

It may be beneficial to briefly summarize the previous studies on ET, which will be basic prior knowledge for later analyses. Overall, there are two scientific branches of ET; one is about TC itself, and the other is about the midlatitude response to transitioning TCs.

5.2.1. Structure changes of TC

In baroclinic zones, transitioning TCs lose their tropical features and become extratropical. In the early stage of ET, a warm frontal region and an extensive cirrus cloud begin to develop to the north-northeast of TCs (Fig. 5.1; Harr and Elsberry 2000; Klein et al. 2000). Over time, the upright TC convection is replaced by the slantwise ascent along the moist isentropes poleward deviated from the TC center (Grams et al. 2013a). Such structural changes are manifested as the erosion of TC's warm core and the increase in thermal asymmetry in the cyclone phase space Hart (2003). As ET proceeds, the wind and precipitation fields also become different from those when TCs are purely tropical entities (Powell 1982; Atallah et al. 2007; Evans and Hart 2008; Milrad et al. 2009). The proper phasing with an upstream trough catalyzes ET and post-ET intensification of TCs by prompting the Petterssen–Smebye Type-B cyclogenesis (Petterssen and Smebye 1971; Harr and Elsberry 2000; Hart et al. 2006; Ritchie and Elsberry 2003, 2007). For a more comprehensive review of TC evolution in baroclinic zones, see Evans et al. (2017).

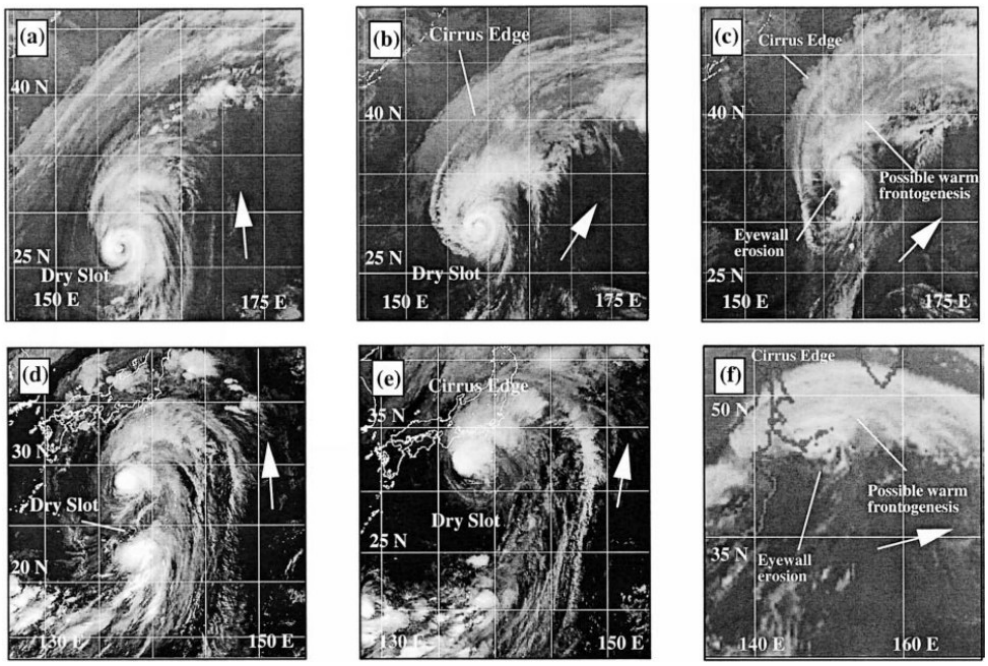

Figure 5.1. Infrared imagery of transitioning typhoons Ginger at **a** 0332 UTC 28, **b** 0032 UTC 29, and **c** 1232 UTC 29 September 1997, and Stella at **d** 0032 UTC 15, **e** 1232 UTC 15, and **f** 1232 UTC 16 September 1998. The figure is taken from Klein et al. (2000).

5.2.2. Impacts on midlatitude flow

The midlatitude flow also dramatically changes through interaction with TC. The extratropical response to transitioning TC is characterized by an amplification of a trough–ridge couplet and jet stream in the vicinity of TCs, and the subsequent Rossby wave dispersion which is a source of downstream forecast uncertainty (Fig. 5.2). The related underlying dynamics have been diagnosed in the literature by borrowing the budget equations of PV (e.g., Archambault et al. 2013, 2015; Grams and Archambault 2016; Riboldi et al. 2019) and local eddy kinetic energy (e.g., Harr and Dea 2009; Quinting and Jones 2016; Keller 2017) which both well explains the amplification and dispersion of Rossby waves in midlatitudes (Wirth et al. 2018).

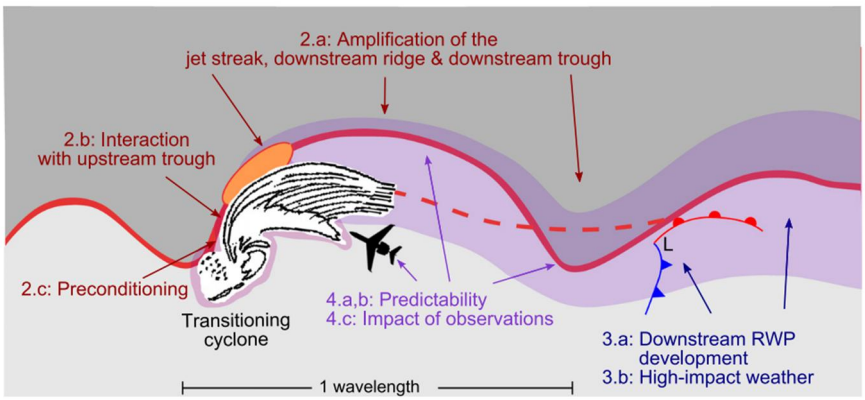

Figure 5.2. Overview of modification of upper-level midlatitude flow by transitioning TCs. The dark red line denotes the meandering tropopause waveguide separating stratospheric high PV air (dark gray) and tropospheric low PV air (light gray). The ellipse shaded by orange denotes the jet streak. The purple semitransparent area indicates the area of increased forecast uncertainty. The figure is taken from Keller et al. (2019).

In the PV argument, a key process responsible for the TC–midlatitude flow interaction is the upper-level divergent outflow of TCs. The TC divergent outflow is primarily sourced from diabatic heating although it is also partly influenced by dry dynamic forcing (Grams and Archambault 2016; Quinting and Jones 2016). It transports relatively low-PV air from low latitudes toward the steeply-sloped tropopause in midlatitudes, resulting in a northward deflection of the midlatitude waveguide and an amplified upper-level ridge (Fig. 5.3; Archambault et al. 2013, Grams et al. 2013a). If there is a trough upstream, its eastward progression is often decelerated by TC divergent outflow, prompting the juxtaposition of the trough and TCs when they arrive in baroclinic zones (Grams et al. 2013a; Riboldi et al. 2019). Such phase-locked structure strongly supports the downstream development from the initially perturbed midlatitude by transitioning TCs (Grams et al. 2013b; Archambault et al. 2015; Grams and Archambault 2016; Quinting and Jones 2016; Riboldi et al. 2019). The downstream TC impact is also verified in numerical models with idealized setups (Riemer et al. 2008; Riemer and Jones 2010, 2014). For a more comprehensive review, see Keller et al. (2019).

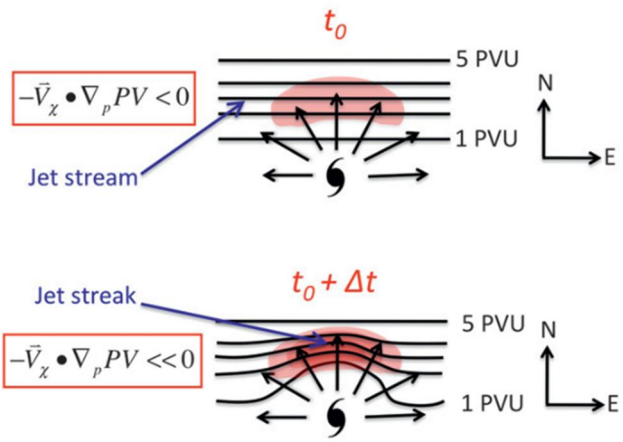

Figure 5.3. Schematic representation of midlatitude flow amplification by the divergent outflow of a TC. The black contours, shadings and vectors denote the PV, horizontal wind speed and divergent wind, respectively, near the tropopause level. The figure is taken from Archambault et al. (2013).

5.3. Data and methods

5.3.1. Data

Hourly precipitation data recorded at the ASOS of the KMA and the TC best track data of the RSMC-Tokyo Typhoon Center are used to identify the TC-HREs. As in previous chapters, stations on Jeju Island are not considered. As in the previous chapters, only the summer monsoon period (JJAS) is considered but for the slightly extended period 1979–2020.

The atmospheric fields are taken from the ERA5 with a 1.5°×1.5° horizontal resolution and 37 pressure levels at 6-h time intervals. The variables on the 2-potential vorticity units (PVU; 1 PVU≡10-6 K kg-1 m2 s-1) surface with the same resolution are also retrieved. To remove small-scale features, the 2-PVU level variables are truncated to a T42 resolution (~750-km resolution at 38°N). Anomaly is defined as deviation from the 6-h climatology. Unlike in chapter 3 in which the diabatic temperature tendency ($\dot{T}_{Dia}$) is directly retrieved from the ECMWF model,

$\dot{T}_{Dia}$ is indirectly estimated as the residual of the thermodynamic equation $\dot{T}_{Dia} = \frac{\partial T}{\partial t} + \mathbf{V} \cdot \boldsymbol{\nabla} T - \omega \frac{p}{R_d} \sigma$ where $\sigma = -d\ln\theta / \rho dp$ is the static stability parameter.

5.3.2. Definition of TC-HREs

The TC-HREs are identified in a similar manner to chapter 2. Following the KMA criteria, events with 12-h accumulated rainfall of 110 mm or more at any single station are first searched. The events are considered to be independent if they are separated for at least 12 h. The HREs are considered to be directly induced by TCs when a TC is located within the domain of 32°–35° and 120°–135°E at least once during HREs. If an identical TC causes multiple TC-HREs, only the event with the TC nearest to the Korean Peninsula is selected. This allows a total of 68 TC-driven HREs in South Korea[1].

As in previous chapters, the reference time (0 h) is defined as the center of the 12-h window of the maximum 12-h accumulated rainfall. Note that the reference time denotes the mature stage of TC-HREs and is not related to the commencement of ET (e.g., Hart 2003; Torn and Hakim 2015) nor the time of maximum TC–midlatitude flow interaction (e.g., Archambault et al. 2013, 2015; Riboldi et al. 2019).

Figure 5.4 shows the tracks of 68 TCs causing TC-HREs in South Korea. Although the location of tropical cyclogenesis is substantially scattered over the subtropical western North Pacific (purple dots), the tracks themselves are well clustered. The mean track shows that TCs are located to the east of Taiwan in the western North Pacific at –48 h and recurve over the East China Sea at –24 h (black solid line). At 0 h, TCs are on average located right southwest of the Korean Peninsula (white circle; 126.52°E and 33.41°N). About 81% of TCs complete ET

[1]The TC-HREs in this chapter are slightly fewer than those in chapter 2 despite a 2-year-longer analysis period. This is because the narrower domain is used for determining TC-HREs, and the repeating events by an identical TC are excluded. This allows clearer composites and more accurate quantification of their dynamics at the minor expense of sample size.

after landfall in South Korea and continue to propagate northeastward as extratropical cyclones.

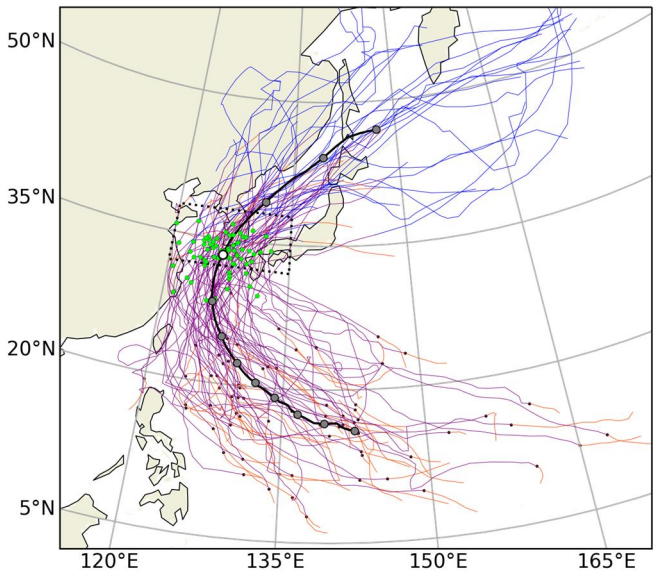

Figure 5.4. Tracks of TCs involved in TC-HREs in South Korea in JJAS 1979–2020 with different colors depending on the status (e.g., TD: orange, TC: purple, ETC: blue). The locations of TCs at 0 h (mature stage of TC-HREs) are marked by green dots. The tropical cyclogenesis is denoted by purple dots. A thick black line and the circles thereon indicate the mean track and daily TC locations from -8 day to +3 day (open circle denotes the mean TC location at 0 h), respectively. The area enclosed by the black dotted line is the domain for determining TC-HREs.

5.3.3. Classification of TC-HREs

The TC-HREs are objectively classified by utilizing a SOM algorithm (Appendix C). As a clustering property, the dynamic tropopause (2-PVU surface height) at 0 h over 30°–53°N and 105°–145°E is considered. The extent of TC–midlatitude flow interaction is known to be largely sensitive to midlatitude upper-level conditions (Archambault et al. 2015; Quinting and Jones 2016; Riboldi et al. 2019). As an indicator of a waveguide for synoptic disturbances (Martius et al. 2010; Bowley et al. 2019), the dynamic tropopause well captures not only the Rossby wave

undulation but also the jet strength (deduced from its horizontal gradient) at the tropopause level, which represent the baroclinic environment.

We adopt 1×2 node array in SOM analysis to keep the comparison as simple as possible. Although more nodes are available, two nodes are found to be sufficient to summarize the tropopause patterns during TC-HREs. The clustering with more nodes results in the separation of the well-defined clusters into different clusters, leading to a loss of generality (figure not shown). Other parameters in SOM algorithm follow the suggestions of Liu et al. (2006) and are summarized in Table 5.1. The TCs in clusters 1 and 2 (referred to as C1 and C2) are listed in Table 5.2.

Table 5.1. SOM parameters specified in this chapter.

SOM Parameters	Selected option
Input data	ERA5 2-PVU-surface height fields at 0 h over 30°–53°N & 105°–145°E
Array of nodes	1×2
Topology of node	Rectangular
Shape of map	Sheet
Initialization method	Linear initialization
Training method	Batch training
Neighborhood function	Epanechnikov function
Neighborhood radius	2 (initial), 1 (final)
Number of iterations	1,000 (rough training), 2,000 (fine tuning)

Table 5.2. List of TC-HREs in C1 and C2. The reference time is in UTC.

Cluster 1 (58.8%)			Cluster 2 (41.2%)		
Num	Reference time	TC name (ID)	Num	Reference time	TC name (ID)
1	1979.08.17.00	Irving (7910)	1	1979.08.24.17	Judy (7911)
2	1980.09.10.18	Orchid (8013)	2	1981.07.31.17	Ogden (8110)
3	1984.08.20.21	Holly (8410)	3	1981.09.02.09	Agnes (8118)
4	1985.08.13.20	Lee (8509)	4	1982.08.13.16	Cecil (8211)
5	1985.08.31.08	Odessa (8512)	5	1982.08.27.04	Ellis (8213)
6	1986.06.24.10	Nancy (8605)	6	1985.08.10.08	Kit (8508)
7	1986.08.27.20	Vera (8613)	7	1990.07.11.07	Robyn (9007)
8	1987.07.15.11	Thelma (8705)	8	1991.08.23.02	Gladys (9112)
9	1987.08.30.17	Dinah (8712)	9	1994.08.01.07	Brendan (9411)
10	1989.07.28.13	Judy (8911)	10	1994.08.10.01	Doug (9413)
11	1990.09.01.00	Abe (9015)	11	1995.07.23.10	Faye (9503)
12	1991.09.27.02	Mireille (9119)	12	1999.07.26.23	Neil (9905)
13	1992.08.18.19	Kent (9211)	13	2002.07.05.10	Rammasun (0205)
14	1992.09.24.02	Ted (9219)	14	2002.08.31.09	Rusa (0215)
15	1993.08.10.00	Robyn (9307)	15	2006.07.10.00	Ewiniar (0603)
16	1995.08.24.23	Janis (9507)	16	2006.08.19.10	Wukong (0610)
17	1999.08.02.08	Olga (9907)	17	2010.08.10.21	Dianmu (1004)
18	1999.09.19.15	Ann (9917)	18	2010.09.06.16	Malou (1009)
19	1999.09.23.19	Bart (9918)	19	2011.08.07.13	Muifa (1109)
20	2000.07.10.09	Kai-Tak (0004)	20	2012.07.18.18	Khanun (1207)
21	2000.09.15.11	Saomai (0014)	21	2014.08.02.07	Nakri (1412)
22	2003.06.19.00	Soudelor (0306)	22	2014.09.23.17	Fung-Wong (1416)
23	2003.09.12.14	Maemi (0314)	23	2015.07.12.03	Chan-Hom (1509)
24	2004.06.20.12	Dianmu (0406)	24	2017.07.03.19	Nanmadol (1703)
25	2004.07.04.05	Mindulle (0407)	25	2018.07.03.07	Prapiroon (1807)
26	2004.08.18.02	Megi (0415)	26	2019.07.19.21	Danas (1905)
27	2004.09.06.22	Songda (0418)	27	2019.08.11.14	Lekima (1909)
28	2005.09.06.05	Nabi (0514)	28	2020.08.05.00	Hagupit (2004)
29	2007.09.16.05	Nari (0711)			
30	2010.09.01.14	Kompasu (1007)			
31	2011.06.25.21	Meari (1105)			
32	2012.08.27.17	Bolaven (1215)			
33	2012.08.30.01	Tembin (1214)			
34	2012.09.16.22	Sanba (1216)			
35	2015.08.24.22	Goni (1515)			
36	2018.08.23.01	Soulic (1819)			
37	2019.08.15.04	Krosa (1910)			
38	2019.09.22.05	Tapah (1917)			
39	2020.09.02.16	Maysak (2009)			
40	2020.09.06.22	Haishen (2010)			

5.3.4. PV tendency equation

The temporal evolution of the tropopause pattern is analyzed by computing the PV tendency budget on the isobaric surface (appendix D). The PV tendency, $\frac{\partial P}{\partial t}$, is contributed by the horizontal PV advection ($-\mathbf{V}\cdot\boldsymbol{\nabla}P$), the vertical PV advection, ($-\omega\frac{\partial P}{\partial p}$), and the diabatic PV generation ($-g\left[(\zeta+f)\frac{\partial\dot{\theta}_{Dia}}{\partial p}+\frac{\partial\dot{\theta}_{Dia}}{\partial y}\frac{\partial u}{\partial p}-\frac{\partial\dot{\theta}_{Dia}}{\partial x}\frac{\partial v}{\partial p}\right]$). The horizontal advection can be further decomposed into that by rotational ($\mathbf{V}_\psi$) and divergent winds ($\mathbf{V}_\chi$) using the Helmholtz decomposition theorem:

$$-\mathbf{V}\cdot\boldsymbol{\nabla}P=-\mathbf{V}_\psi\cdot\boldsymbol{\nabla}P-\mathbf{V}_\chi\cdot\boldsymbol{\nabla}P$$

During ET, the upper-level $\mathbf{V}_\psi$ can be associated with midlatitude baroclinic waves, cyclonic PV tower of TC, and anomalous anticyclone by TC outflow (Riemer and Jones 2010; Quinting and Jones 2016). In contrast, $\mathbf{V}_\chi$ can be sourced from TC inner-core convection and slantwise ascent along the baroclinic zone with different relative importance depending on the stages of ET (Grams et al. 2013a; Grams and Archambault 2016). However, we do not further decompose $\mathbf{V}_\psi$ and $\mathbf{V}_\chi$ into those by specific processes as the current partitioning is sufficient to assess the TC–midlatitude flow interaction at the tropopause level.

5.3.5. QG omega equation

The vertical motion mechanisms are quantitatively assessed by numerically solving the Q-vector-form QG omega equation (appendix B). To detail the dynamical processes responsible for vertical motion during TC-HREs, Q vectors are decomposed into transverse ($Q_n\mathbf{n}$) and shearwise components ($Q_s\mathbf{s}$) as done for non-TC HREs in chapter 3. Unlike chapter 3, however, the omega at the bottom boundary (1,000 hPa) has non-zero values possibly because of the higher-resolution topography in the model of ERA5 than that of ERA-Interim. To consider the bottom boundary effect on the numerically obtained omega fields, the QG omega equation is additionally solved without any forcing but with the reanalyzed omega at the lower boundary. The resulting vertical motion (ω_{bf}) is linearly combined with other omega

components to construct the QG vertical motion ($\omega_{QG} = \omega_{Dyn} + \omega_{Beta} + \omega_{Dia} + \omega_{bf}$). This is the typical procedure to obtain the general solution of the nonhomogeneous-form linear differential equation.

5.4. Overview of the SOM clustering results

Given the fact that TC–midlatitude flow interaction is sensitive to the midlatitude condition, TC-HREs are grouped into those under strong baroclinic condition (C1) and those under weak baroclinic condition (C2) by applying SOM analysis to the 2-PVU surface height field at 0 h. Figure 5.5 displays the dynamic tropopause height (i.e., 2-PVU surface height) patterns of the two clusters. The C1 account for 58.8% of TC-HREs (40 events). It is characterized by a well-defined trough-ridge couplet in midlatitudes (Fig. 5.5a). The remaining 41.2% (28 events) belong to C2 which features a weak undulation of tropopause height (Fig. 5.5b). The horizontal gradient of tropopause height is also much smaller in C2 than in C1, implying a weaker jet stream (i.e., weak baroclinicity) during C2 TC-HREs.

The C1 and C2 TC-HREs have different occurrence seasons. While the former frequently occur in late summer to early fall (Fig. 5.5c) when local baroclinicity is strong, the latter are common in mid-summer when local baroclinicity is rather weak (Fig. 5.5d). This reflects the subseasonal variation of local baroclinicity in East Asia associated with the phases of the EASM.

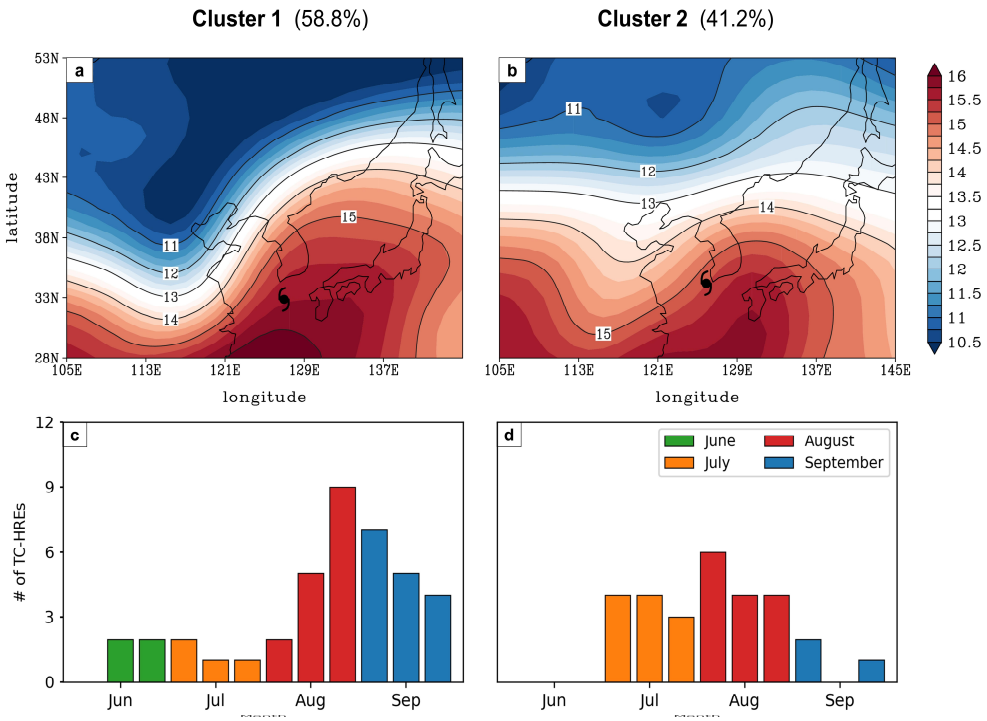

Figure 5.5. a,**b** The 1×2 SOM clustering results. The plotted variable is the composited 2-PVU surface height (km) at 0 h for C1 and C2, respectively, over the clustering domain (30°–53°N and 105°–145°E). The mean location of TCs is indicated by TC symbol. **c**,**d** The number of TC-HREs in 10-day bins in JJAS for C1 and C2, respectively.

The difference between the two clusters is also found in TC tracks (Fig. 5.6). The C2 TCs tend to recurve later but more sharply than C1 TCs. More importantly, while C2 TCs are located in the right vicinity of the Korean Peninsula at 0 h (on average, 126.96°E and 32.86°N; Fig. 5.6b), C1 TCs are located farther south with only a few landfalling TCs (on average, 125.89°E and 34.20°N; Fig. 5.6a). The mean distance between TC and the station of maximum 12-h accumulated rainfall is 417 km in C1 but 307 km in C2. This indicates that TC-HREs under the strongly baroclinic condition can be more remotely influenced by TCs and reach the mature stage even before TCs get close to the heavy rainfall region. After TC-HREs, C1 TCs leave South Korea more rapidly than C2 TCs (cf. daily TC locations on the mean tracks).

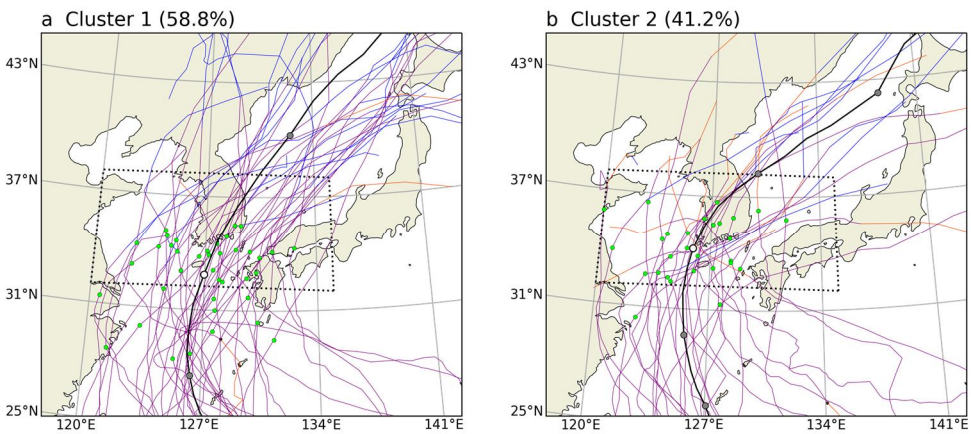

Figure 5.6. a,**b** As in Fig. 5.4, but for C1 and C2, respectively, in a narrower domain.

Figures 5.7a,b shows the time series of 12-h accumulated rainfall of C1 and C2 TC-HREs at the station where the maximum 12-h accumulated rainfall is recorded. Locally, the HRE criterion is maintained for ~13 h which is shorter than the TC-HRE duration over South Korea (~19 h). However, no significant difference is found in local rainfall intensity between the two clusters. Although the accumulated rainfall amount of C2 TC-HREs exhibits a larger event-to-event variability than C1 TC-HREs (thin lines), the event-averaged rainfall exhibits a quantitatively similar amount and temporal evolution (thick lines).

Instead, the spatial distribution shows a subtle difference between the two clusters (Figs. 5.7c,d). While the southern and eastern coasts of the Korean Peninsula are most vulnerable to TC rainfall regardless of clusters, more accumulated rainfall is observed inland in C1, particularly in the west of the mountains. This implies that C1 TCs have a wider rainfall area with a higher risk of nationwide impact.

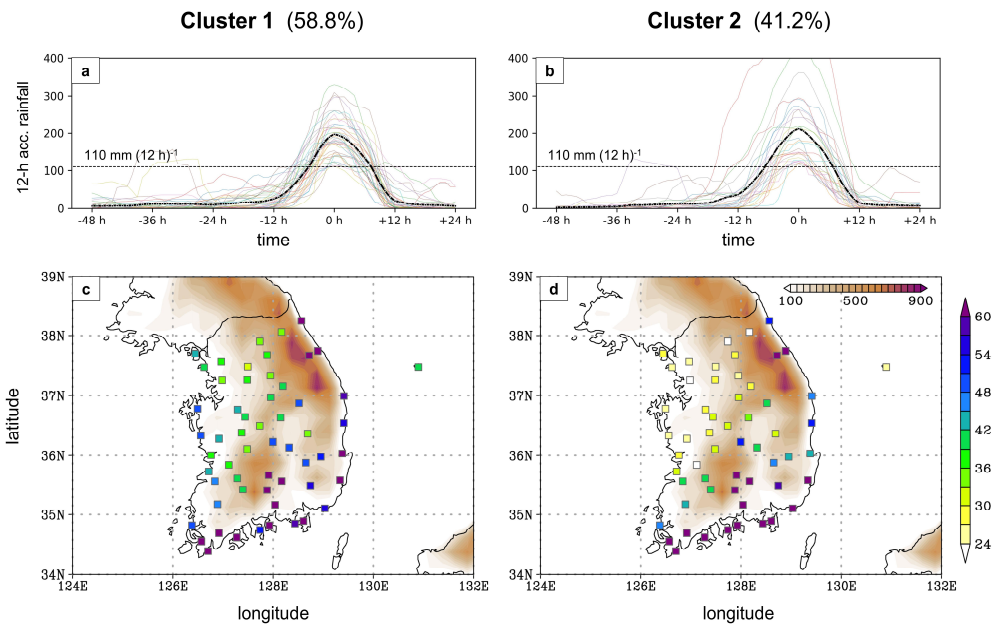

Figure 5.7. a,b Time series of 12-h accumulated rainfall amount at the station where the maximum 12-h accumulated rainfall is recorded at 0 h for C1 and C2, respectively. **c,d** Composites of the maximum 12-h accumulated rainfall amount (mm) during TC-HREs across 57 stations for C1 and C2, respectively. The terrain height (m) is shaded in brown.

5.5. Synoptic evolutions under different tropopause patterns

What determines the different TC locations at 0 h and the spatial distribution of accumulated rainfall amount between the two clusters? Those differences can be explained by TC–midlatitude flow interaction. When their interactions are strong, the associated QG ascent to the north of TC can enhance precipitation over a broad area even before the arrival of TCs. Such synoptic features, different between the two clusters, are analyzed in this subsection.

5.5.1. Upper- and low-level evolutions

Figure 5.8 compares the temporal evolution of tropopause-level circulation between C1 and C2. In C1 TC-HREs, negative and positive tropopause height anomalies appear across the Korean Peninsula at –48 h (Fig. 5.8a). These tropopause anomalies develop into a well-defined trough-ridge couplet in time (Figs. 5.8b,c). This upper-level configuration is favorable for synoptic-scale ascent and baroclinic growth of surface weather systems. In particular, the trough is negatively tilted, which typically prompts ET and post-ET intensification of TCs (Hart et al. 2006). The ridge building is particularly distinct, even stronger than the trough deepening. This sharpens the horizontal gradient of tropopause height with a well-defined entrance region of a westerly jet to the north of South Korea. If the thermally-direct secondary circulation is organized at the entrance region of the jet, this may enhance the vertical motion over the rainfall region.

It is noticeable from Figs. 5.8a–d, that the trough–ridge couplet is nearly stationary while TCs approach the rainfall region. This upper-level anchoring is distinguished from the non-TC-related HREs during which the baroclinic trough is highly transient (chapter 3). Following the northeastward translation of TCs at +24 h, the ridge expands northward (Fig. 5.8d). The upstream trough also slightly extends eastward, implying the termination of upper-level anchoring after TCs are fully embedded in midlatitude westerly.

The wave undulation does not take place in C2 TC-HREs (Figs. 5.8e–h). As TCs approach the rainfall region, positive tropopause height anomaly becomes

pronounced. However, the tropopause pattern does not change much in time. Although a trough-like signal appears upstream at –24 h and 0 h, its deepening is not evident as manifested by the absence of a negative tropopause height anomaly (Figs. 5.8f,g). Moreover, the trough is positively tilted, which generally precludes the ET and post-ET intensification of TCs (Hart et al. 2006). The ridge building is observed to the northeast of TCs, but it is also much weaker than that in C1. The ULJ is also still weaker than that in C1.

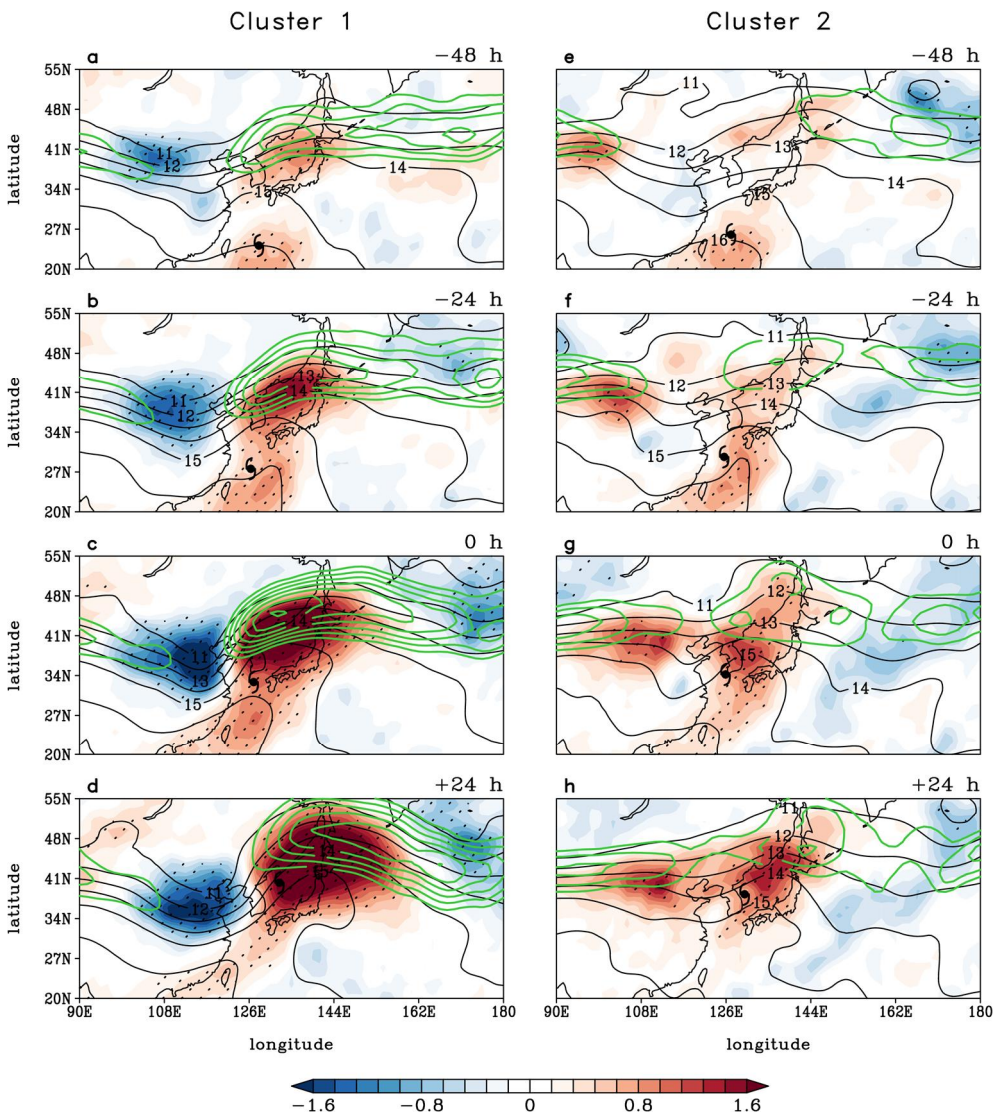

Figure 5.8. Lagged composites (–48, –24, 0 and +24 h) of 2-PVU surface height (km, black contours) and its anomaly (km, shading), and horizontal wind speed at 2-PVU surface (green contours with a 3-m s^{-1} interval from 27 m s^{-1}) for **a**–**d** C1 TC-HREs and **e**–**h** C2 TC-HREs. The statistically significant anomalies at the 95% confidence level based on a two-tailed Student's *t* test are stippled. The mean location of TCs is indicated by the TC symbol.

The different temporal evolution between the two clusters is also evident in the lower troposphere (Fig. 5.9). At –48 h, TCs of the two clusters have comparable intensity (cf. Figs. 5.9a,e). Over time, the 700-hPa cyclonic anomaly of GPH, related to TCs, continuously grows even though TCs move poleward away from the subtropical warm sea surface (Figs. 5.9a–c). Although weakened, the cyclonic anomaly still has an organized structure when it is embedded in midlatitude westerly at +24 h (Fig. 5.9d). This cyclonic anomaly is likely fostered by the upper-level forcing through their baroclinic development. The anticyclonic and cyclonic anomalies to the east also grow in time, which is likely the barotropic response to the downstream development in the tropopause level.

In contrast, C2 TCs exhibit rapid dissipation during their progression, especially from –24 h to +24 h (Figs. 5.9e–h). More importantly, they are still isolated from midlatitude flow at 0 h (Fig. 5.9g). This indicates that C2 TC-HREs occur when TCs are still in the tropical-dominant stage (more details will be addressed later).

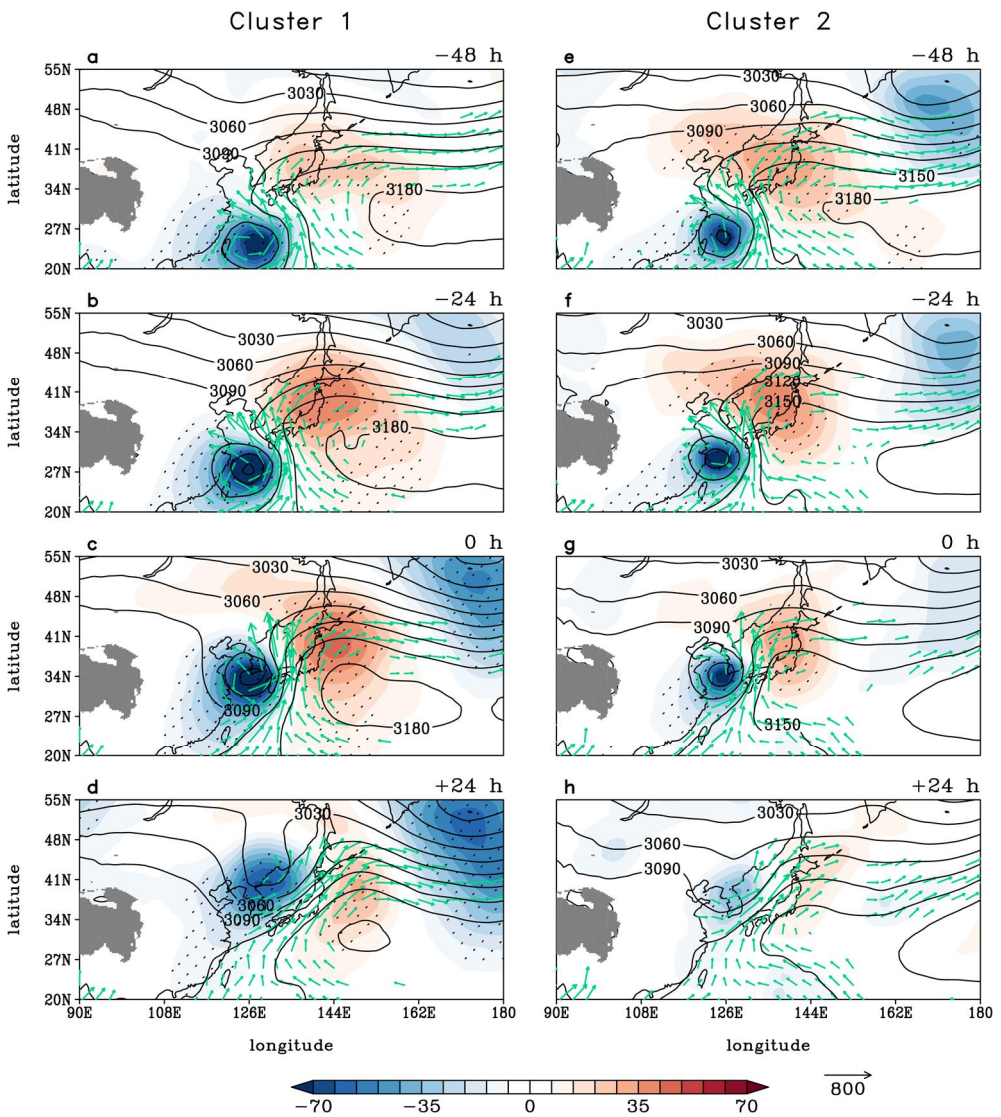

Figure 5.9. Lagged composites (–48, –24, 0 and +24 h) of GPH (gpm, contours) and its anomaly (gpm, shading) at 700 hPa, and **IVT** (>300 kg m^{-1} s^{-1}, vectors) for **a**–**d** C1 TC-HREs and **e**–**h** C2 TC-HREs. The statistically significant anomalies at the 95% confidence level based on a two-tailed Student's *t* test are stippled. The terrain higher than 3,000 m is masked by gray.

Here, it should be stated that the different evolution of TCs between C1 and C2 is not an artifact of composite analysis in which TC locations differ by events. The TC-centered composite clarifies that while C1 TCs maintain their intensity with slight size expansion (Figs. 5.10a–d), C2 TCs diminish from –24 h to +24 h (Figs. 5.10e–h). This is consistent with the above findings (Fig. 5.9). It is also worth to indicate the size expansion of C1 TCs is consistent with asymmetric radial expansion of the wind field observed during ET (Evans and Hart 2008). In fact, according to best track data, most C1 TCs (92.5%) continue their lifecycle as extratropical cyclones whereas only 64.3% of C2 TCs complete ET during or after TC-HREs.

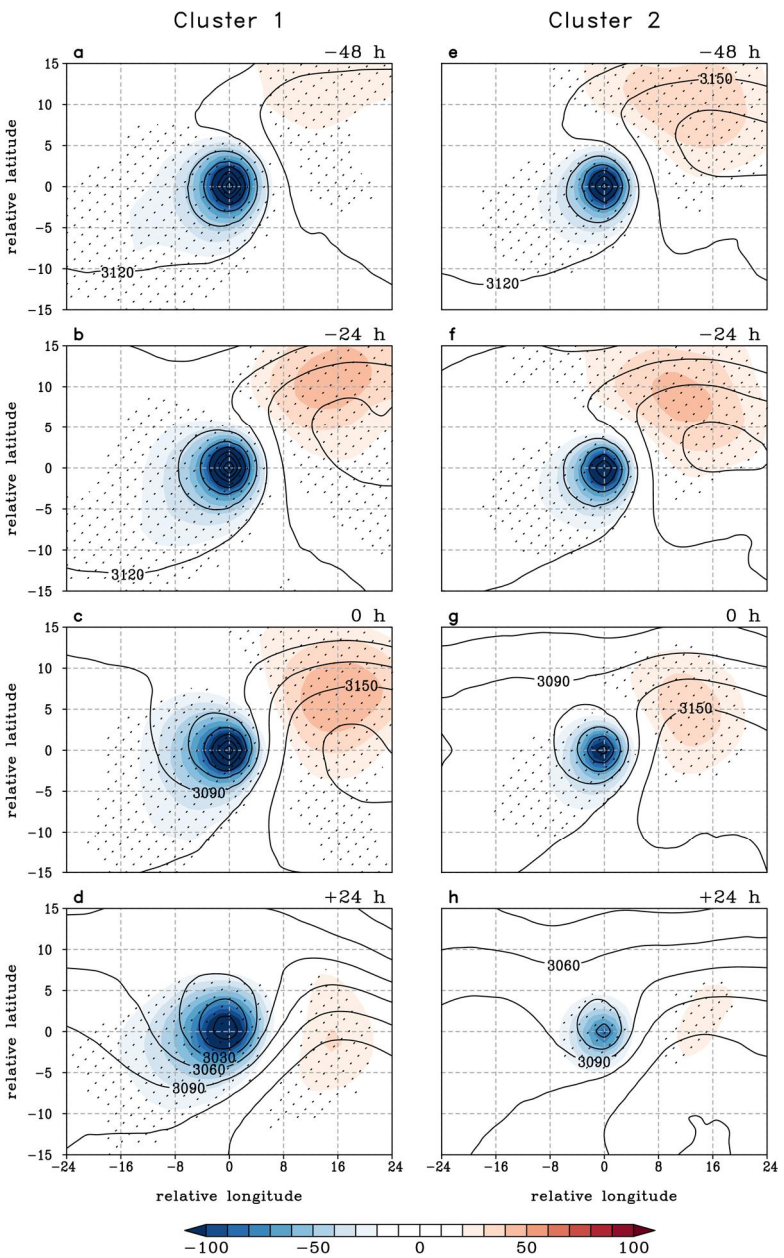

Figure 5.10. Lagged composites (–48, –24, 0 and +24 h) of 700-hPa GPH (gpm, contours) and its anomaly (gpm, shading) in the TC-relative frame for **a**–**d** C1 TC-HREs and **e**–**h** C2 TC-HREs.

5.5.2. Vertical cross sections

The temporal evolution of synoptic circulation is further compared with the vertical cross sections. Figures 5.11a–d represent GPH and PV anomalies in the longitude-pressure plane at 33°–39°N for C1. The upper-level trough and ridge already appear at –48 h (Fig. 5.11a). Until 0 h, the trough and ridge amplify in time (see also strengthening PV anomalies), to a greater extent for the ridge (Figs. 5.11b,c). More importantly, the upper-level trough stays in place until the arrival of TCs. It is finally phase-locked with TCs at 0 h, showing a well-defined baroclinic structure (Fig. 5.11c). This structure is maintained for the next 24 h, while the trough slightly extends eastward due to the northeastward deviation of TCs from South Korea (Fig. 5.11d).

The C2 TCs are not supported by the upper-level flow (Figs. 5.11e–h). At –48 h, an equivalent-barotropic positive GPH anomaly appears to the east of South Korea (Fig. 5.11e). As TCs approach, positive GPH anomaly becomes widely pronounced in the upper troposphere to the west and over the rainfall region (Figs. 5.11f,g). As a result, TCs are still confined below 400 hPa with no interaction with an upstream trough at 0 h (Fig. 5.11g). The positive PV anomaly emerges right over the rainfall region, but this likely represents cyclonic PV tower of TCs and diabatic response to heavy rainfall.

The above results indicate that while C1 TCs begin to extract energy from the baroclinically unstable midlatitude background, C2 TCs remain as warm-core systems with no or very weak support from the midlatitude flow. This is consistent with the different evolution of low-level circulation anomalies in Figs. 5.9 and 5.10.

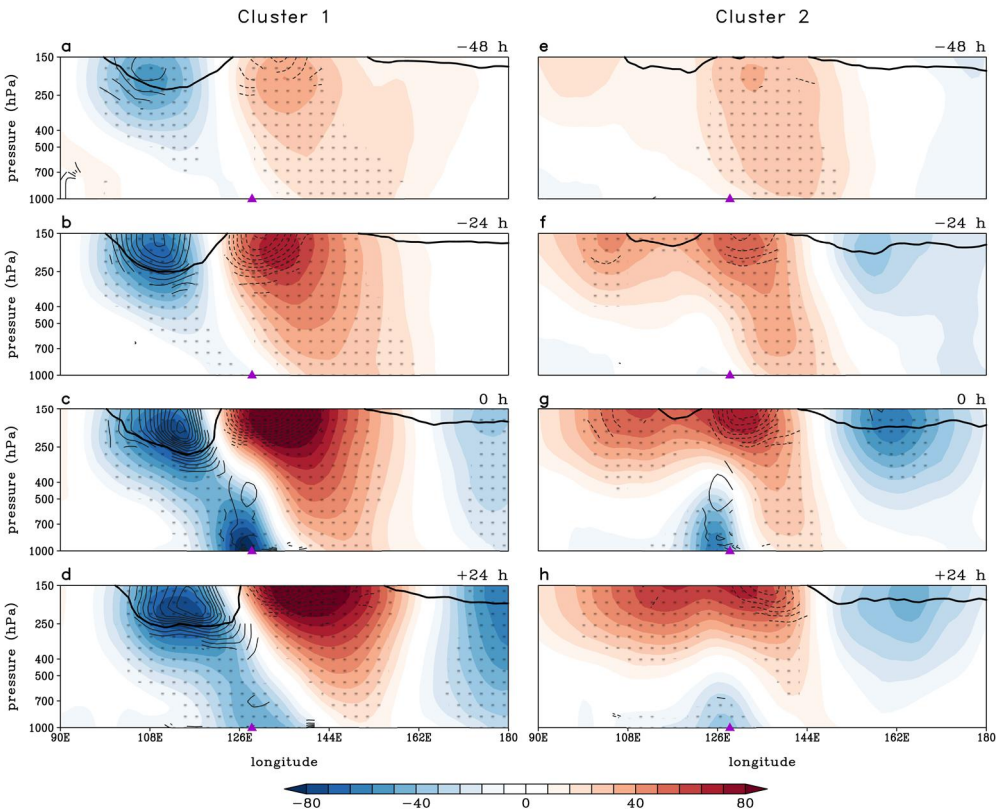

Figure 5.11. Lagged composites (–48, –24, 0 and +24 h) of longitude–pressure cross section of GPH anomaly (gpm, shading) and PV anomaly (contours with a 0.1-PVU interval) latitudinally averaged over the boxed region in Fig. 2.5b (33°–39°N) for **a**–**d** C1 TC-HREs and **e**–**h** C2 TC-HREs. The dynamic tropopause (2 PVU) is marked by a thick contour. Only the PV anomalies statistically significant at the 95% confidence level based on a two-tailed Student's *t* are shown. The statistically significant GPH anomaly is stippled. The longitudinal center of South Korea is marked by a purple triangle.

Figure 5.12 shows the temporal evolution of the latitude-pressure cross section at 124–131°E. In C1 TC-HREs, two ascending cores are found at –48 h, i.e., the upright TC convection in the subtropics and the relatively weak slantwise ascent on the south of the ULJ (Fig. 5.12a). They are still discernible at –24 h (Fig. 5.12b) but subsequently merged at 0 h, producing vigorous convection over South Korea (Fig. 5.12c). It is important from Fig. 5.12c to note that strong vertical motion, responsible for heavy rainfall, is largely slantwise and centered on the north of TCs.

This is indicative of the collapse of TC eyewall convection and the development of a warm conveyor belt, which are often observed during ET (Grams et al. 2013a; Grams and Archambault 2016). In the upper troposphere, the poleward outflow impinges on the steeply-sloped tropopause (thick black line), injecting the low-PV air and thereby lifting the tropopause height from –48 h to 0 h. As TCs leave South Korea at +24 h, strong convection is no longer present (Fig. 5.12d). The tropopause also restores its height possibly because the upstream trough restarts its eastward propagation.

A strong poleward outflow in the upper troposphere in C1 could be explained not only by strong upward motion but also by small inertial stability to the north of TCs. Inertial stability, which is defined as $I^2 = (f + 2v_t/r)(f + \zeta)$ in a cylindrical coordinate system where v_t and r are the tangential wind (positive for counterclockwise) and the radial distance from the TC center, measures the resistance to radial motion. The ULJ to the north of TCs and deepened trough to the west of TCs locally reduce v_t, ζ, and thereby I^2, allowing an enhanced poleward outflow in the upper troposphere (Komaromi and Doyle 2018; Finocchio and Doyle 2019).

In C2 TC-HREs, only TC convection is observed at –48 h without a preconditioning midlatitude ascent (Fig. 5.12e). The vertical motion is still upright with its center in the right vicinity of TCs at –24 h (Fig. 5.12f). Although it becomes slightly tilted poleward at 0 h, it is mostly upright in contrast to the vertical motion in C1 TC-HREs (cf. Figs. 5.12c,g). The upper-level poleward outflow is also weak, explaining the indistinct tropopause evolution (see next section for details). This result again demonstrates that TCs and midlatitude flows do not experience a significant structural change during C2 TC-HREs.

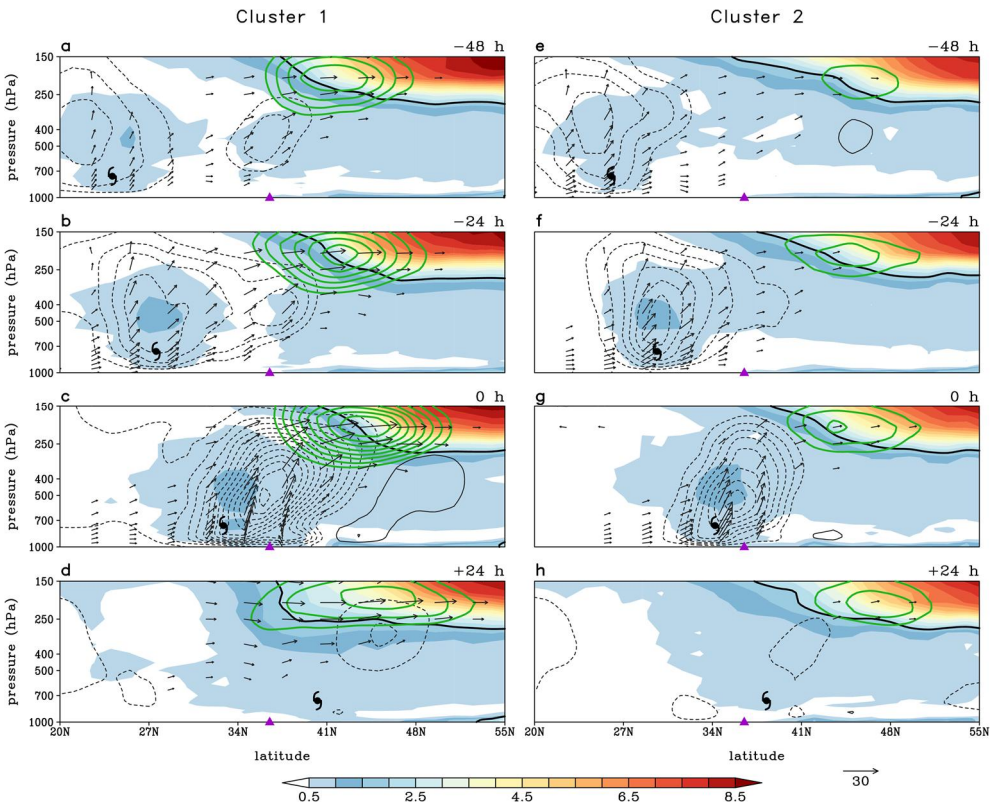

Figure 5.12. Lagged composites (–48, –24, 0 and +24 h) of latitude–pressure cross section of PV (PVU, shading), ω (contours with a 0.04-Pa s^{-1} interval), horizontal wind speed (green contours with a 3-m s^{-1} interval from 27 m s^{-1}), and meridional-vertical wind (>5 m s^{-1}, vectors; ω is multiplied by an aspect ratio of -45.29) longitudinally averaged over the boxed region in Fig. 2.5b (124°–131°E) for **a**–**d** C1 TC-HERs and **e**–**h** C2 TC-HREs. The dynamic tropopause (2 PVU) is highlighted by a thick contour. The mean latitudinal position of TCs is indicated by the TC symbol. The latitudinal center of South Korea is marked by a purple triangle.

5.6. Quantitative assessments

5.6.1. TC influence on the tropopause circulation

The evolutions of lower and upper-level circulations are not independent of each other as hinted from C1 TC-HREs. Beyond the qualitative description, the synoptic evolution of the tropopause height pattern is further analyzed by computing the PV tendency equation (Eq. D1.1). To consider the subseasonal and latitudinal variations of tropopause where TC–midlatitude flow interaction is strongest, the PV tendency budget is vertically averaged over the layer of 250–150 hPa (e.g., Archambault et al. 2013, 2015). The sum of all PV budget terms well reproduces the observed tendency for both C1 and C2 (figure not shown). Below, only the horizontal advection terms (i.e., $-\mathbf{V}_{\psi} \cdot \boldsymbol{\nabla} P$ and $-\mathbf{V}_{\chi} \cdot \boldsymbol{\nabla} P$) are shown as the vertical advection, $-\omega \frac{\partial P}{\partial p}$, and diabatic production, $-g\left[(\zeta + f)\frac{\partial \dot{\theta}_{Dia}}{\partial p} + \frac{\partial \dot{\theta}_{Dia}}{\partial y}\frac{\partial u}{\partial p} - \frac{\partial \dot{\theta}_{Dia}}{\partial x}\frac{\partial v}{\partial p}\right]$, are found to be negligible (figure not shown).

Figure 5.13a presents the upper-level PV tendency at 0 h for C1 TC-HREs. A positive tendency to the east of the trough and a negative tendency along the ridge are evident. The latter is much stronger than the former, explaining the rapid ridge building described earlier. This PV tendency pattern prompts the cyclonic wrap-up of the upstream trough and the amplification of trough-ridge couplet without eastward propagation (e.g., Riemer and Jones 2014; Quinting and Jones 2016).

This PV tendency is however the combined result of the rotational advection and divergent advections. The rotational wind, which is undulating but not perfectly parallel to iso-PV lines, produces a pair of weak negative and strong positive PV advections in the western and eastern flanks of the trough, respectively (Fig. 5.13b). However, the positive advection is largely counteracted by the negative PV advection by divergent wind (Fig. 5.13c). The negative PV advection by divergent flow occurs over a broader area and is also responsible for the pronounced negative PV tendency along the ridge (cf. Figs. 5.13a,c). This indicates that both the upper-level wave amplification and the anchoring of the upstream trough are the result of synergistic TC–midlatitude flow interaction at the tropopause level.

The PV tendency in C2 TC-HREs is almost negligible (Fig. 5.13d) because both the rotational and divergent PV advections are unstructured (Figs. 5.13e,f). A weak advection by rotational wind is explained by the weak undulation of iso-PV lines (i.e., small zonal PV gradient) and the weak magnitude of rotational wind, which all indicate the suppressed baroclinicity. A weak advection by divergent wind is also attributed to the small meridional PV gradient and the weak divergent outflow, with the latter being again associated with weak upward motion and large inertial stability to the north of TCs (cf. Figs. 5.12c,g) as mentioned earlier.

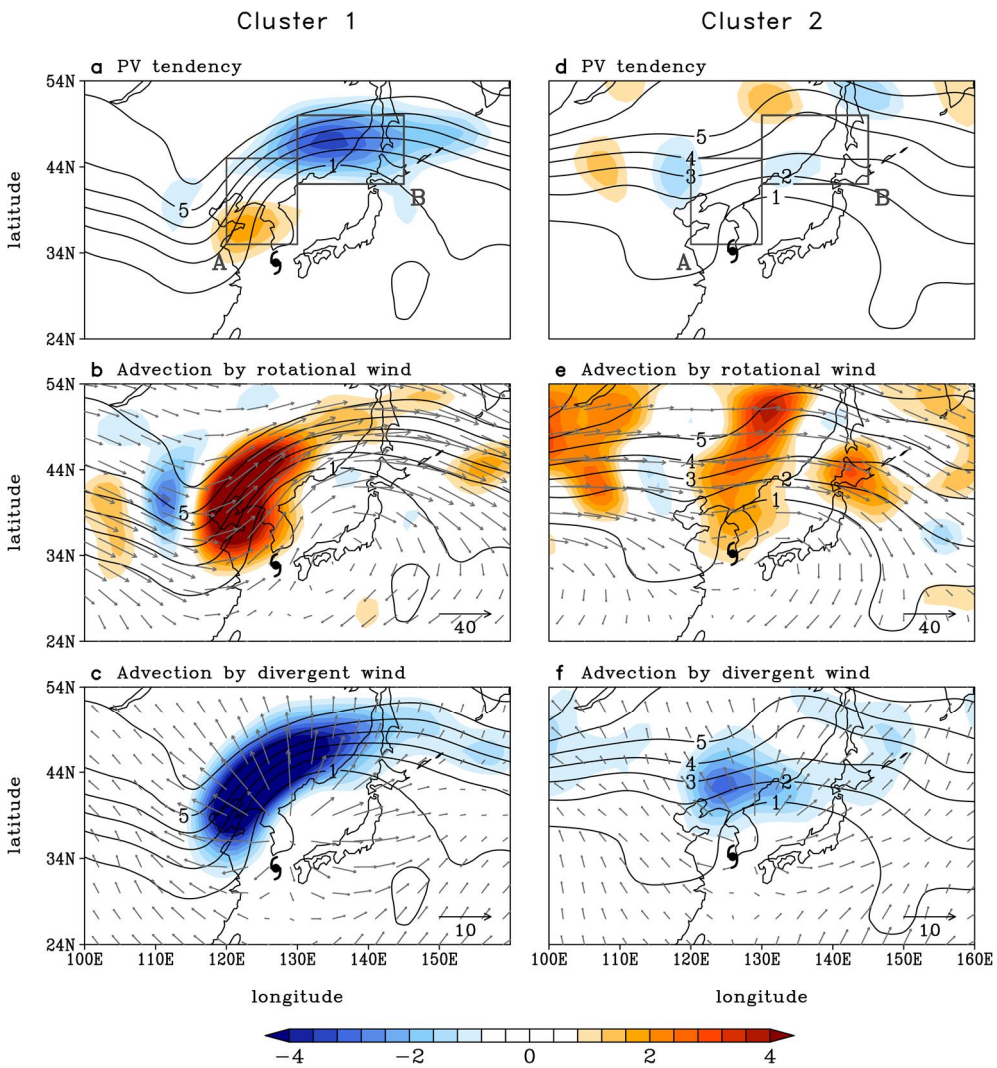

Figure 5.13. Composites of PV tendency budget for C1 TC-HREs at 0 h: **a** rate of local PV change ($\frac{\partial P}{\partial t}$; shading), **b** rotational wind (m s^{-1}, vectors) and its resulting PV advection ($-\mathbf{V}_{\psi} \cdot \nabla P$; shading), and **c** divergent wind (m s^{-1}, vectors) and its resulting PV advection ($-\mathbf{V}_{\chi} \cdot \nabla P$; shading) averaged for the layer of 250–150 hPa. Unit is PVU day^{-1}. The 250–150-hPa layer-mean PV is also contoured (unit: PVU). The mean location of TCs is indicated by the TC symbol. **d**–**f** As in **a**–**c** but for C2 TC-HREs at 0 h.

Figure 5.14a displays the time evolutions of the total PV tendency, rotational PV advection, and divergent PV advection averaged over the eastern flank of the upper-level trough and around the ridge during C1 TC-HREs (denoted by "A" and "B", respectively, in Fig. 5.13a). In "A", the positive PV advection by rotational wind (orange dashed line) is largely counteracted by the negative PV advection by divergent wind (orange solid line) from –48 h to –6 h. The latter is slightly stronger than the formal. The resulting negative PV tendency (orange bar) continuously hinders the eastward progression of the trough. At 0 h, the PV tendency switches its sign from negative to positive, due to a rapid increase in rotational PV advection. This indicates that the trough begins to move eastward as TCs recurve and subsequently become fully embedded in midlatitude westerly.

In "B", the negative PV tendency gets stronger in time until 0 h (navy bar), because of the divergent PV advection (navy solid line). This is consistent with the downstream ridge building mentioned earlier. The net PV tendency weakens afterward and changes its sign at +18 h as the rotational PV advection sharply increases (navy dashed line). This is again indicative of the eastward progression of the upstream trough after vertical coupling with TCs.

During C2 TC-HREs, PV tendencies over "A" and "B" do not change much for the analysis period (Fig. 5.14b). This is due to weak and time-invariant rotational and divergence PV advections, which largely cancel with each other (see colored lines). This implies that TC–midlatitude flow interaction is continuously feeble in the tropopause level both before and after the arrival of TCs.

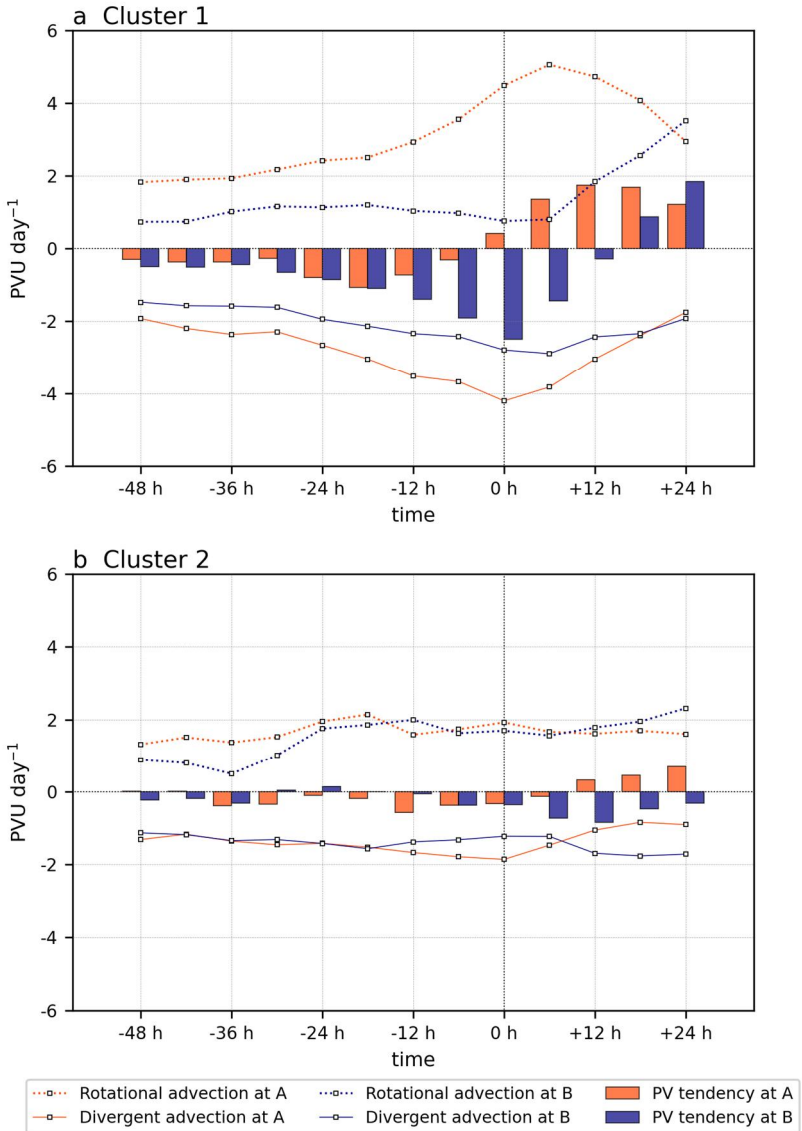

Figure 5.14. Time series of the 250–150-hPa layer-averaged PV advections by rotational ($-\mathbf{V}_\psi \cdot \nabla P$; dotted lines) and divergent winds ($-\mathbf{V}_\chi \cdot \nabla P$; solid lines), and rate of local PV change ($\frac{\partial P}{\partial t}$; bars) averaged over the boxed regions "A" (colored in orange) and "B" (colored in navy) in Figs. 5.13a,d for **a** C1 TC-HREs and **b** C2 TC-HREs. Unit is PVU day^{-1}.

5.6.2. QG diagnosis of vertical motion

The nature of vertical motion is also analyzed by inverting the QG omega equation. Figure 5.15 shows the vertical profile of omega averaged over 33°–39°N and 124°–131°E in the mature stage of C1 and C2 TC-HREs. Overall, ω_{QG} reasonably well reproduces the reanalyzed omega ω for both clusters (cf. black dashed versus solid lines). The ω_{QG} in the free atmosphere is mostly explained by the diabatic vertical motion (ω_{Dia}) and dynamic vertical motion (ω_{Dyn}). The boundary effect (ω_{bf}) is confined within the boundary layer, while the beta effect is negligible. It is important to note that the vertical motion of C1 TC-HREs is stronger than that of C2 TC-HREs although local rainfall intensity is comparable (cf. Figs. 5.7a,b). This may imply that the latter cannot be fully explained by QG dynamics. The errors of ω_{QG} are indeed larger in C2 than in C1 (cf. Figs. 5.15a,b).

Focusing on QG processes, both ω_{Dia} and ω_{Dyn} are stronger throughout the troposphere during C1 TC-HREs, compared to C2 TC-HREs. This is particularly evident in ω_{Dyn}. At 500 hPa, ω_{Dyn} in C1 is 3.5 times stronger than that in C2, whereas ω_{Dia} is only 1.4 times stronger. This shows the importance of dynamic ascent in determining C1 TC-HREs rather than C2 TC-HREs. Besides, ω_{Dyn} exhibits a structural difference. While ω_{Dyn} in C1 is top-heavy with a maximum magnitude at ~400 hPa, that in C2 is almost flat with a maximum magnitude at ~700 hPa (cf. blue lines in Figs. 5.15a,b). This indicates that only C1 TC-HREs are strongly influenced by the dynamical processes in the upper troposphere.

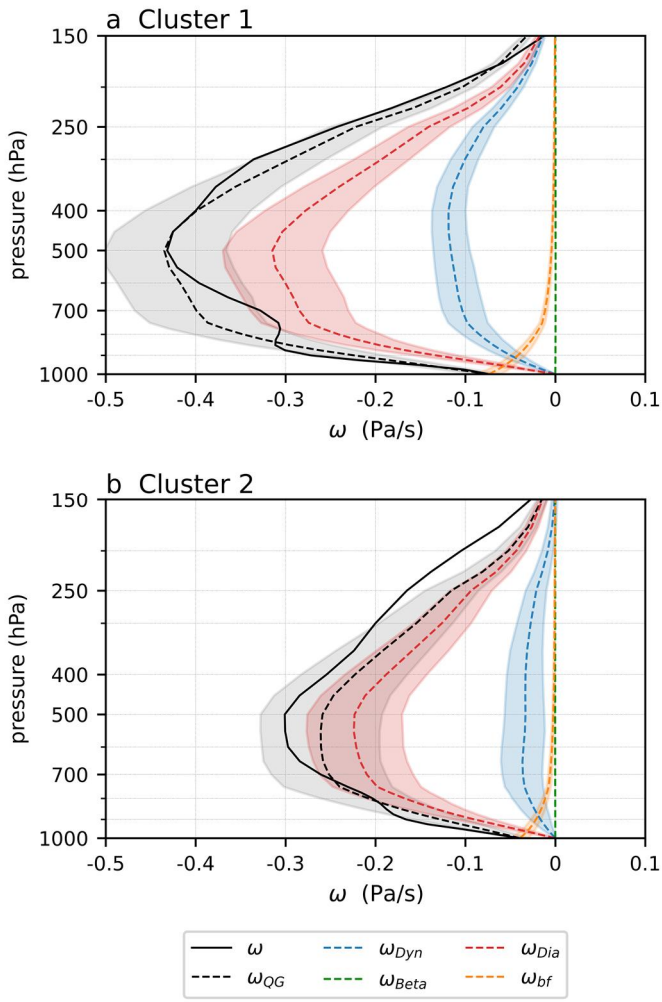

Figure 5.15. Vertical profiles of ω from ERA5, and ω_{QG}, ω_{Dyn}, ω_{Beta}, ω_{Dia} and ω_{bf} obtained from omega equation inversion, which are averaged around South Korea (33°–39°N and 124°–131°E; boxed region in Fig. 2.5b) for **a** C1 TC-HREs and **b** C2 TC-HREs at 0 h. The 95% confidence interval is shaded based on the 10,000 times of bootstrap resampling. Unit is Pa s^{-1}.

To scrutinize the nature of dynamic ascent, ω_{Dyn} is decomposed into the transverse (ω_n) and shearwise components (ω_s) in Figs. 5.16 and 5.17. The ω_s and ω_n are separately shown at 250 hPa and 700 hPa at 0 h. During C1 TC-HREs, the upper-level undulating flow induces the northeastward shearwise Q vectors from the upstream trough and the southwestward shearwise Q vectors from the downstream ridge (Fig. 5.16a). Their convergence generates negative ω_s (ascending). The cross-jet transverse Q vectors are equatorward at the jet entrance region, suggestive of geostrophic frontogenesis and thermally-direct secondary circulation (Fig. 5.16b). Their convergence on the south of the jet entrance generates negative ω_n over the wide area encompassing the Korean Peninsula. This ω_n combined with ω_s explains the top-heavy ω_{Dyn} in Fig. 5.15a.

In the lower troposphere, C1 TCs embedded in the baroclinic zone drive strong northeastward shearwise Q vectors (Fig. 5.16c), implying the cyclonic rotation of the isentropes. The resulting vertical motion consists of the azimuthal wavenumber-1 pattern of the ascent over South Korea and the descent behind the TCs. To the north and northeast of TCs, equatorward transverse Q vectors develop (Fig. 5.16d). This can be explained by the impingement of southerly wind along the eastern flank of TCs on the baroclinic zone and the resulting warm frontogenesis which is often observed to the north-northeast of transitioning TCs (Klein et al. 2000; Harr and Elsberry 2000).

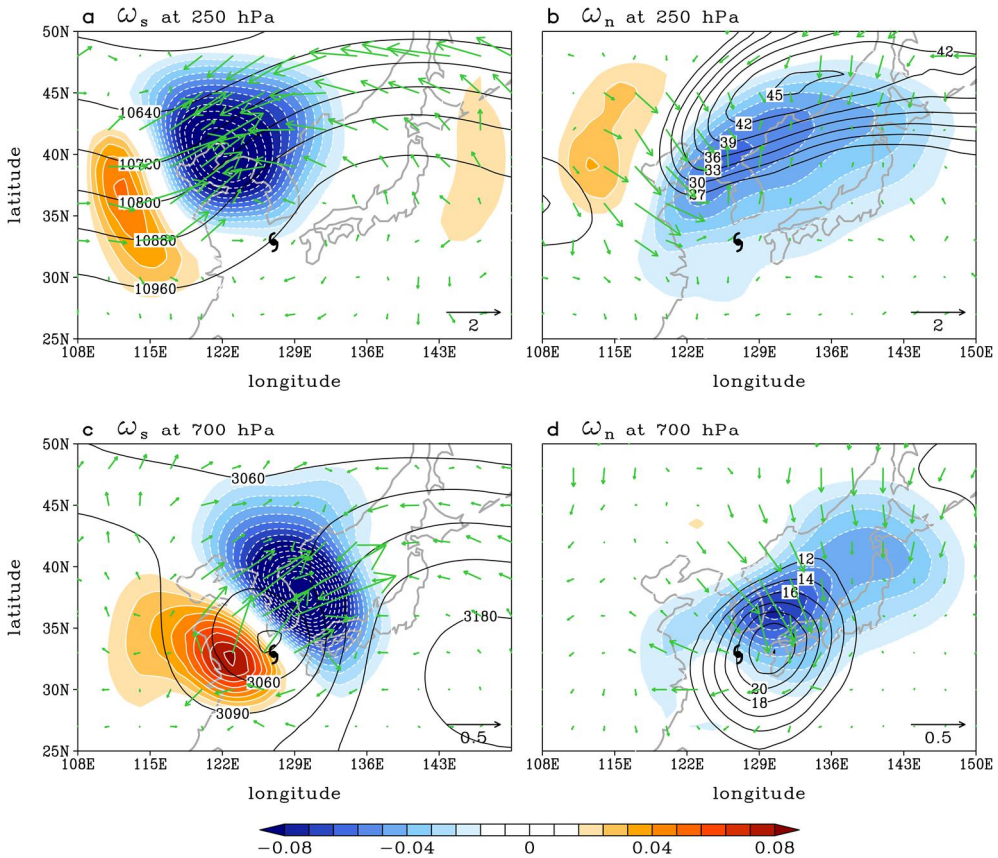

Figure 5.16. Composites of **a** ω_s (Pa s^{-1}, shading), Q_s**s** (10^{-12} m^2 kg s^{-1}, vectors) and GPH (gpm, contours), and **b** ω_n (Pa s^{-1}, shading), Q_n**n** (10^{-12} m^2 kg s^{-1}, vectors) and horizontal wind speed (m s^{-1}, contours) at 250 hPa for C1 TC-HREs at 0 h. **c**,**d** As in **a**,**b** but for 700 hPa. Only the horizontal wind speed greater than 27 m s^{-1} and 12 m s^{-1} are contoured in **b** and **d**, respectively. The best track-based mean TC center is indicated by the TC symbol.

The organized vertical motion does not appear during C2 TC-HREs. As anticipated from Fig. 5.15b, the dynamic ascent is faint in both the upper and lower troposphere (Fig. 5.17). This is again explained by weak flow in the upper troposphere (Figs. 5.17a,b) and relatively weak TC-induced circulation in the lower troposphere (Figs. 5.17c,d). The latter is partly due to the weaker TCs compared to those in C2. However, when TC-HREs are subsampled so that TCs therein have comparable intensity, similar results are still found (not shown). The small magnitude of the horizontal potential temperature gradient, which can be deduced based on thermal wind relation, could also contribute to weak Q vector components [see Eqs. (B3.4c,d) in appendix B3 for the kinematic expression of shearwise and transverse Q vectors].

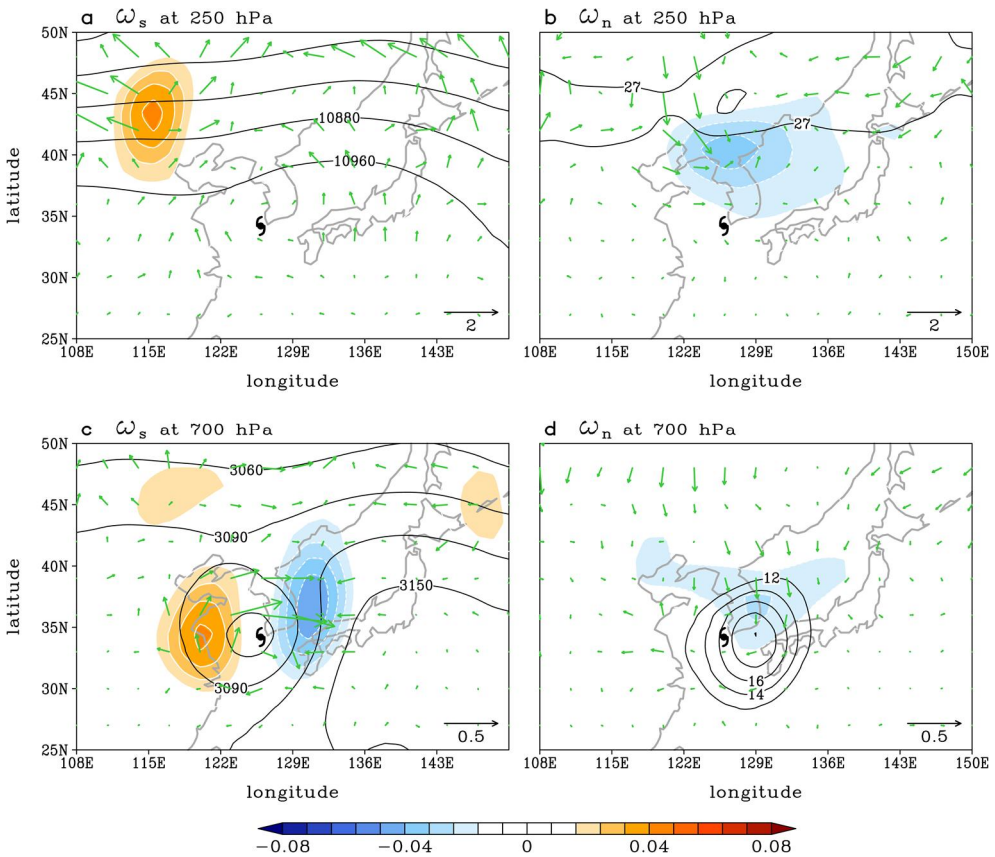

Figure 5.17. As in Fig. 5.16, but for C2 TC-HREs.

Figures 5.18a,c display the temporal evolution of each omega component evaluated at 500 hPa, the level of the strongest vertical motion (Fig. 5.15). Again, the vertical motion is reasonably well reproduced by ω_{QG}. In C1, ω_{Dyn} is non-negligible even at –48 h (Fig. 5.18a). It gradually strengthens from –24 h and reaches the maximum intensity at –6 h and 0 h. The ω_{Dia} is initially weaker than ω_{Dyn} but rapidly increases from –24 h when rainfall starts to increase (Fig. 5.7a). In the mature stage of TC-HREs, ω_{Dyn} and ω_{Dia} explain 26.7% and 72.4% of ω_{QG}, respectively. This contrasts to ω_{Dyn} in C2 which remains weak until 0 h (Fig. 5.18c). The ω_{QG} is instead dominated by ω_{Dia} which rapidly intensifies from –24 h. In the mature stage of C2 TC-HREs, ω_{Dia} accounts for 86.2% of ω_{QG}. In both clusters, ω_{QG} sharply weakens after 0 h.

The evolution of ω_{Dyn} is detailed by dividing it into ω_n and ω_s (Figs. 5.18b,d). To further compare the relative contributions of upper-level midlatitude flow and low-level TC circulation, QG omega equation is also solved by separately considering the forcings in the upper (1000–400 hPa) and lower layers (400–100 hPa). The result demonstrates that the ω_n in C1, which is driven by both the upper and lower layers, moderately changes in time (dark blue and orange bars in Fig. 5.18b). A rapid increase in dynamic ascent from –24 h to 0 h is mostly attributed to ω_s from both upper and lower layers (light blue and yellow bars). This highlights the important role of the amplifying upper-level trough-ridge couplet and the approach of TCs in organizing C1 TC-HREs. At +6 h, the lower-layer-driven ω_s suddenly changes its sign due to the descending motion behind TCs (see Fig. 5.16c), contributing to the rapid weakening of the ascent after the passage of TCs. Not surprisingly, ω_n and ω_s do not change much in C2 (Fig. 5.18d). Only a slight increase is observed for the lower-layer-driven ω_s from –18 h to 0 h.

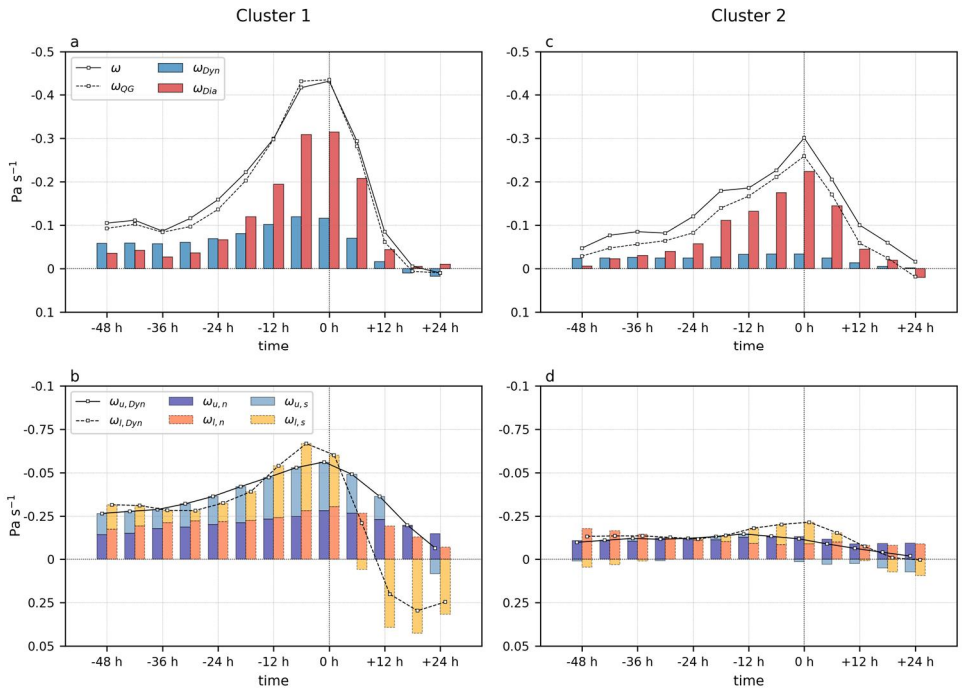

Figure 5.18. Time series of **a** ω, ω_{QG}, ω_{Dyn}, and ω_{Dia}, and **b** ω_{Dyn} by the upper (400–100 hPa; subscript u) and lower layers (1000–400 hPa; subscript l), and their transverse and shearwise components averaged around South Korea (33°–39°N and 124°–131°E; boxed region in Fig. 2.5b) for C1 TC-HREs from –48 h to +24 h. **c**,**d** As in **a**,**b**, but for C2 TC-HREs.

Taken together, while the upward motion during C1 TC-HREs is the result of the joint influence of midlatitude upper-level flow and low-level TC circulation through their synergistic interaction, the upward motion during C2 TC-HREs is more dominated by inherent diabatic TC convection. The widely-enhanced QG dynamic ascent in C1 explains why C1 TC-HREs can occur even before the arrival of TCs, whereas C2 TC-HREs occur only when TCs are located in the right vicinity of the rainfall region (cf. Figs. 5.6a,b). It also explains more inland rainfall in C1 than that in C2 (cf. Figs. 5.7c,d). This also supports the statistical result of Kim et al. (2019) that TCs under strong background vertical wind shear (i.e., enhanced local baroclinicity) accompany a broad rainfall area, especially in the TC-track direction.

5.7. Discussion

It should be stated that TCs in C1 and C2 are not identical. The lifetime minimum central pressure of C1 is on average lower than that of C2 by 14 hPa (Fig. 5.19a). This indicates that C1 TCs more strongly develop before encountering baroclinic zones. The sensitivity of the results to TC intensity is briefly tested by resampling TC-HREs so that TCs in the two clusters have a similar distribution of lifetime minimum central pressure (Fig. 5.19b). We find the essentially same results are obtained with resampled events (figures not shown). This is consistent with Archambault et al. (2013) who reported that the initial TC state is secondary to the extent of TC–midlatitude flow interaction.

It is also worth mentioning that the similar synoptic features of C1 and C2 TC-HREs have been also reported for the landfalling hurricanes in eastern North America (Atallah et al. 2007; Milrad et al. 2009). It implies that the characteristics of TC–midlatitude flow interaction and its influences on TC-HREs may share similarities regardless of heavy rainfall region and TC origin. Therefore, this study can be extended to TC-HREs in neighboring countries (e.g., eastern China and Japan) given the prevalent baroclinic Rossby waves in East Asia summer (Horinouchi and Hayashi 2017). A direct comparison between different regions would be helpful to generalize the present study. To increase the sample size, high-resolution climate models could be utilized. Recent studies have shown that high-resolution global climate models can reliably simulate TC tracks (e.g., Li et al. 2021). Using such models, the possible changes of C1 and C2 in a warming climate could be also explored.

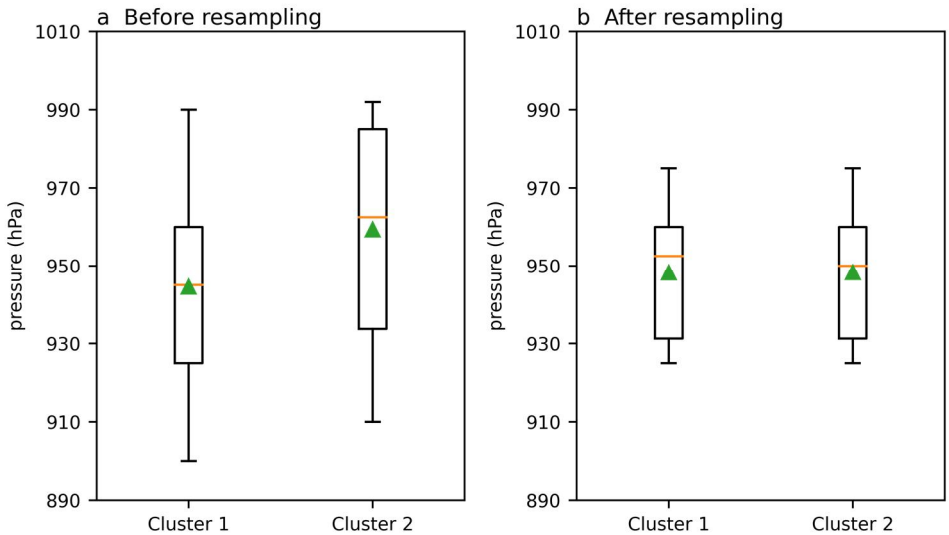

Figure 5.19. The box-whisker plots of lifetime minimum center pressure **a** for all TCs in C1 and C2, and **b** for the resampled TCs in C1 and C2. The TCs are resampled by constraining their lifetime minimum center pressure to range from 925 hPa to 975 hPa. As a result, 30 and 14 TCs are retained in C1 and C2, respectively, in the resampled sample. The orange line and green triangle denote the median and mean, respectively.

Chapter 6. Record-breaking rainfall in the summer of 2020

Note: The contents of this chapter are taken from Park et al. (2021d) titled "Record-breaking summer rainfall in South Korea in 2020: Synoptic characteristics and the role of large-scale circulations" published in *Monthly Weather Review.* (Vol. **149**, 3085–3100, https://doi.org/10.1175/MWR-D-21-0051.1). Some modifications have been made from the original article for the organization of the dissertation.

6.1. Motivation

In the summer of 2020, destructive floods consecutively occurred across South Korea, causing 46 fatalities and billion-dollar economic losses (KMA 2021). The accumulated rainfall during JJAS was approximately 53% larger than climatology, breaking the record since 1971. This extreme summer rainfall was closely associated with consecutive HREs. In the meanwhile, a large number of flash floods were also reported in China in June–July and Japan in early July (Liu et al. 2020; Takaya et al. 2020; Araki et al. 2021; Horinouchi et al. 2021; Zhang et al. 2021; Zhou et al. 2021). This indicates that the HREs in South Korea were not local phenomena but a regional manifestation of an abnormal East Asian summer monsoon (EASM) in 2020. However, no study has reported South Korean HREs that were not necessarily driven by the same mechanisms as the Chinese and Japanese HREs, requiring separate analyses.

The present chapter investigates the record-breaking summer rainfall in 2020 in South Korea. The peculiar feature of the 2020 summer is the dramatic change in the synoptic natures of HREs in late July. While the HREs from late June to late July were triggered by ETCs, the subsequent HREs were mainly caused by MRB from late July to mid-August. This HRE transition was quite sudden and not reported in Meiyu and Baiu regions. By analyzing large-scale circulation over the Nothern Hemisphere, it is suggested that the atmospheric teleconnections induced by the SCS convection and summer North Atlantic oscillation (SNAO) played a critical role in their rapid transition.

6.2. Data and methods

The hourly precipitation data recorded at weather stations of the KMA (i.e., ASOS) are used to analyze both the 2020 summer rainfall (91 stations) and the climatology for the period of 1971–2020 (45 stations). The weather stations on Jeju Island are excluded because of different synoptic variability from those in the Korean Peninsula. To investigate atmospheric circulations, the six-hourly Japanese 55-year Reanalysis (JRA-55; Kobayashi et al. 2015) interpolated onto a 1.25°×1.25° spatial resolution is used. Convective activity in the tropical ocean is quantified by using the daily interpolated outgoing longwave radiation (OLR) at a 2.5°×2.5°spatial resolution from the National Oceanic and Atmospheric Administration (NOAA; Liebmann and Smith 1996) for the same analysis period. The anomaly is defined as a deviation from the long-term (1979–2020) climatology.

For the period of 2018–2020, the daily SST anomaly from the NOAA Optimum Interpolation SST V2 High Resolution Dataset is also used. For 2020, the daily index of boreal summer intraseasonal oscillation (BSISO; Lee et al. 2013) provided by the Asia Pacific Economic Cooperation (APEC) Climate Center (APCC) and the best track data offered by the RSMC-Tokyo Typhoon Center are also utilized.

The HREs occurred in JJAS 2020 are identified similarly to the previous chapters. By analyzing the hourly precipitation data recorded at 91 weather stations, an event with 12-h accumulated rainfall greater than 110 mm at any single station is defined as an HRE. Individual HREs are considered to be independent if they are separated for at least 12 h. This allows a total of 15 HREs including 3 TC-HREs. Unlike in chapters 2 and 5, TC-HREs are determined by manually analyzing the status and location of TCs instead of applying the fixed criteria. The HREs (including TC-HREs) and their information are summarized in Table 6.1.

Table 6.1. List of the HREs (including TC-HREs) in JJAS 2020. HRE ID (third column) follows the temporal order of occurrence. The TC name is indicated in the rightmost column. See Fig. 6.4 for the track of each TC.

Period	HRE	ID	Date	Maximum 12-h rainfall	Maximum 1-h rainfall	Synoptic system	Remark
First rainy period (from early June to mid-August)		1	12 UTC 12–20 UTC 12 Jun	134.3 mm (19 UTC 12 Jun)	50.1 mm (15 UTC 12 Jun)	MRB	
	P1	2	11 UTC 29–07 UTC 30 Jun	187.0 mm (00 UTC 30 Jun)	56.3 mm (23 UTC 29 Jun)	ETC	
		3	15 UTC 9–06 UTC 10 Jul	207.9 mm (00 UTC 10 Jul)	54.8 mm (03 UTC 10 Jul)	ETC	
		4	13 UTC 12–02 UTC 13 Jul	151.1 mm (19 UTC 12 Jul)	31.8 mm (22 UTC 12 Jul)	ETC	Additional contribution of MRB
		5	06 UTC 23–00 UTC 24 Jul	210.7 mm (15 UTC 23 Jul)	70.4 mm (13 UTC 23 Jul)	ETC	
	P2	6	18 UTC 28–04 UTC 30 Jul	191.4 mm (22 UTC 28 Jul)	55.5 mm (00 UTC 29 Jul)	MRB	
		7	13 UTC 1–10 UTC 3 Aug	254.8 mm (21 UTC 1 Aug)	69.8 mm (14 UTC 2 Aug)	MRB	
		8	23 UTC 4–02 UTC 5 Aug	115.9 (00 UTC 5 Aug)	26.8 mm (23 UTC 4 Aug)	MRB	Indirect contribution of Hagupit
		9	16 UTC 5–00 UTC 6 Aug	134.0 mm (20 UTC 5 Aug)	42.6 mm (21 UTC 5 Aug)	ET	Hagupit
		10	22 UTC 6–07 UTC 8 Aug	344.4 mm (23 UTC 7 Aug)	81.5 mm (22 UTC 7 Aug)	MRB	
		11	20 UTC 8–07 UTC 9 Aug	132.5 mm (23 UTC 8 Aug)	38.0 mm (23 UTC 8 Aug)	MRB	
		12	08 UTC 10–20 UTC 10 Aug	118.2 mm (18 UTC 10 Aug)	38.5 mm (14 UTC 10 Aug)	MRB	Indirect contribution of Jangmi
Second rainy period (from late August to mid-September)		13	04 UTC 26–14 UTC 26 Aug	139.9 mm (09 UTC 26 Aug)	48.2 mm (12 UTC 26 Aug)	TC	TC-HRE (Bavi)
		14	03 UTC 2–22 UTC 2 Sep	234.0 mm (13 UTC 2 Sep)	57.4 mm (09 UTC 2 Sep)	TC	TC-HRE (Maysak)
		15	15 UTC 6–06 UTC 7 Sep	224.0 mm (22 UTC 6 Sep)	55.9 mm (22 UTC 6 Sep)	TC	TC-HRE (Haishen)

6.3. Overview of the 2020 summer rainfall

6.3.1. Record-breaking rainfall amount

Figure 6.1a shows the yearly variation of the JJAS accumulated rainfall in South Korea. The summer rainfall exhibits substantial interannual variability with more frequent wet summers in the last two decades (see sky-blue bars). In 2020, the summer rainfall amount was 1250 mm, 53% greater than climatology, breaking the record in the past 50 years. This unprecedented rainy summer emerged after 7-year-long dry summers (see orange bars).

Figure 6.1b presents the subseasonal variation of the daily rainfall in 2020 (bar) and its long-term climatology (line). Climatologically, there are two rainfall peaks, i.e., one in mid-July and the other in late August. They are well divided by a relatively dry spell in between (Lee et al. 2017). In 2020, however, the first rainfall peak appeared in early August, about 25 days later than the climatological first peak. The withdrawal of the first rainy period was also delayed by about 15 days compared to the climatological withdrawal in late July. In mid-August, the rainfall amount sharply decreased. It was then followed by the second rainy period from late August to mid-September.

Figure 6.1c shows the hourly time series of the maximum 12-h accumulated rainfall amount across 91 weather stations operated in 2020. There were 15 HREs in JJAS with 11 non-TC HREs in 29 June–15 August with distinct synoptic features between the two subperiods: 29 June–27 July (P1; sky-blue shading) and 28 July–15 August (P2; pink shading). Later, three TC-HREs occurred in the second rainy period.

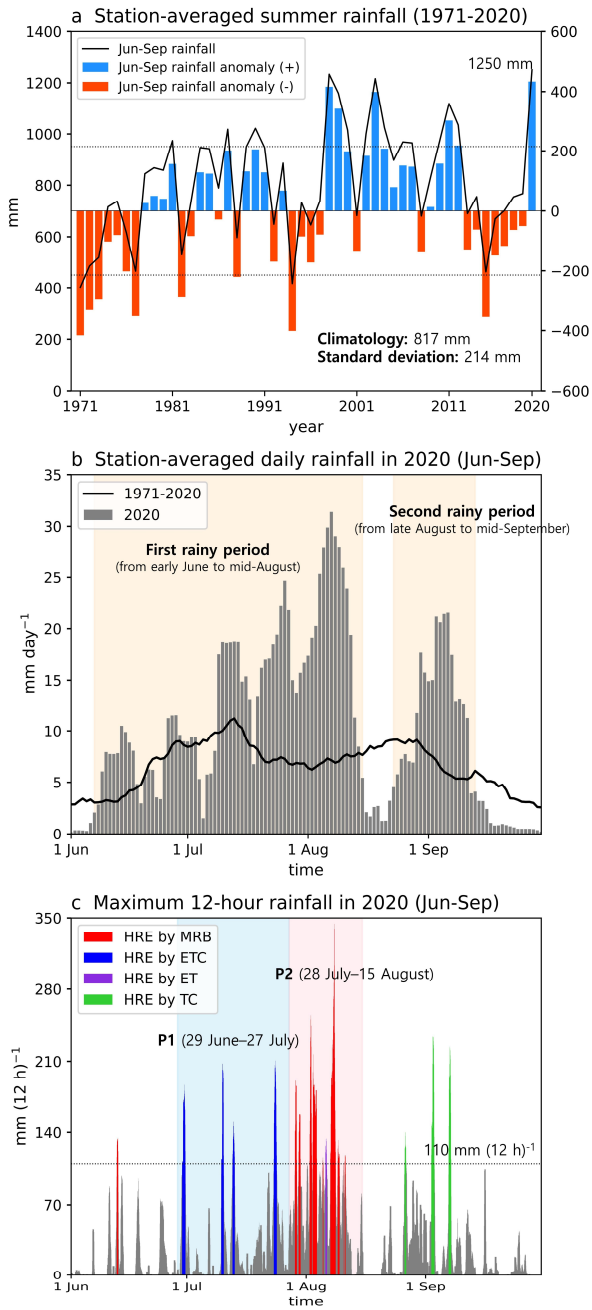

Figure 6.1. a Yearly time series of JJAS accumulated rainfall (black line) and its anomaly (colored bars) for the period of 1971–2020. Here, the anomaly is defined as a deviation from the 50-year (1971–2020) climatology, and its ±1.0 standard deviation is marked by dotted lines. **b** Daily time series of daily accumulated rainfall amount in the summer of 2020 (gray bars) and the 50-year climatology (black line). A 9-day moving average is applied. The first and second rainy periods in 2020 are denoted by apricot shadings. In **a** and **b**, the accumulated rainfall amounts are averaged over 45 stations with continuous observations from 1971 to

2020. **c** Hourly time series of the 12-hour accumulated rainfall amounts in JJAS 2020. Rainfall amounts greater than 110 mm $(12\ h)^{-1}$ are highlighted in four different colors depending on their associated synoptic systems, i.e., MRB (red), ETC (blue), ETC after ET (purple) and TC (green). In **c**, the maximum rainfall amounts among 91 stations operated in 2020 are shown. The areas shaded in sky-blue and pink denote P1 (29 June–27 July) and P2 (28 July–15 August), respectively.

6.3.2. Weather patterns of the HREs

The weather patterns of all HREs are briefly reviewed in this section. Figure 6.2 presents the GPH and relative vorticity at 850 hPa for individual HREs in their mature stage. The relative vorticity is smoothed to a T42 spatial resolution to distinguish synoptic-scale disturbances from mesoscale perturbations. The infrared satellite images are also shown in Fig. 6.3.

Based on synoptic weather systems involved in HREs, 15 HREs in 2020 summer can be classified into four categories: 1) MRB, 2) ETC, 3) ETC after ET, and 4) TC. While the HRE 1 developed along the early MRB (Figs. 6.2a and 6.3a), the subsequent HREs 2–5 in P1 were triggered by the ETCs (Figs. 6.2b–e). The cold or occluded front was well defined in Figs. 6.3b–e as a key feature of the ETC. Although the HREs 2 and 3 accompanied the zonally organized MRB, the MRB was located in the south of the Korean Peninsula (Figs. 6.3b,c). During the HRE 4, the MRB reached the southern tip of the Korean Peninsula (Fig. 6.3d), implying its additional or indirect contribution to the HRE.

The HREs 6–12 in P2, however, show no sign of ETCs. They mostly developed along the MRB over the Korean Peninsula (Figs. 6.2f–l and 6.3f–l), except for the HRE 9 which was driven by the ET of TC Hagupit (Figs. 6.2i and 6.3i). The HREs 8 and 12 were also indirectly influenced by TCs Hagupit and Jangmi, which were located over eastern China and the northeast of the Korean Peninsula, respectively (Figs. 6.2h,l and 6.3h,l). In the case of HREs 6–8 and 10–12, cyclonic circulation appeared in the north of the Korean Peninsula (Figs. 6.2f–h, j–l), implying their partial contribution to the formation of the MRB over the Korean Peninsula by forming the confrontation with the NPH to the south.

The last three HREs (HREs 13–15) directly resulted from TCs Babi, Maysak, and Haishen, which approached the southwest, south, and southeast of the Korean Peninsula, respectively (Figs. 6.2m–o and 6.3m–o; see also Fig. 6.4 for the tracks of TCs involved in these TC-HREs).

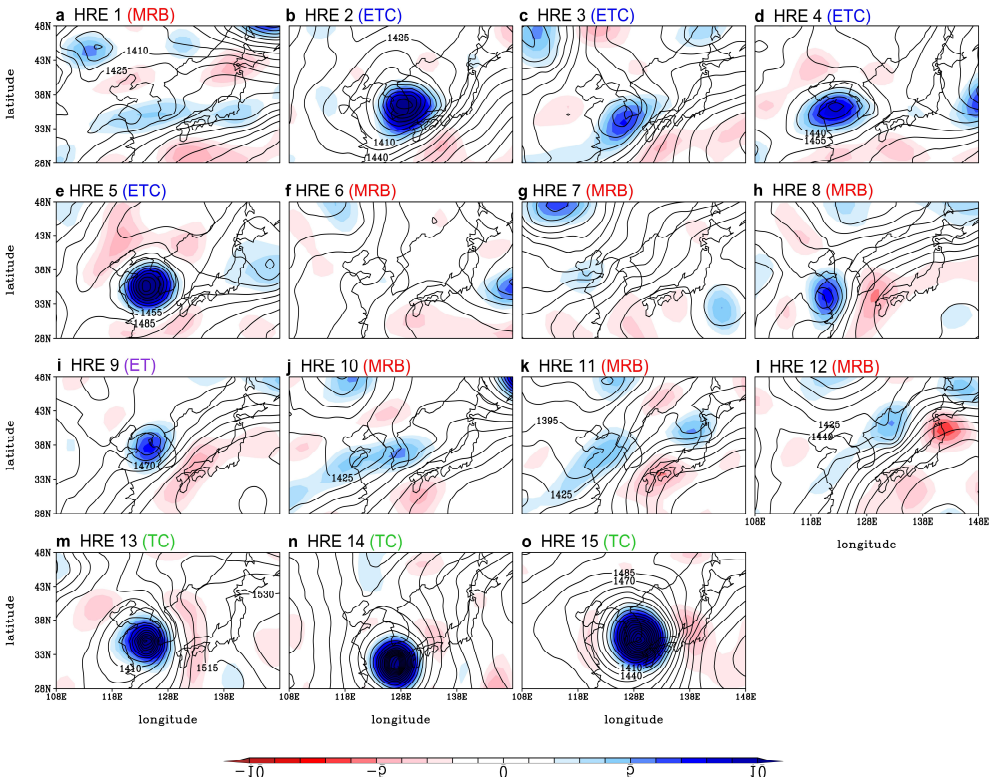

Figure 6.2. The 850-hPa GPH (contours, gpm) and relative vorticity (shading, CVU) truncated at T42 spatial resolution for all HREs (including TC-HREs) listed in Table 6.1. A snapshot at the reference time of each HRE (adjusted to the nearest 6-hourly mark) is shown. The title of each panel is colored in accordance with the associated synoptic systems (red, blue, purple, and green for MRB, ETC, ET, and TC, respectively).

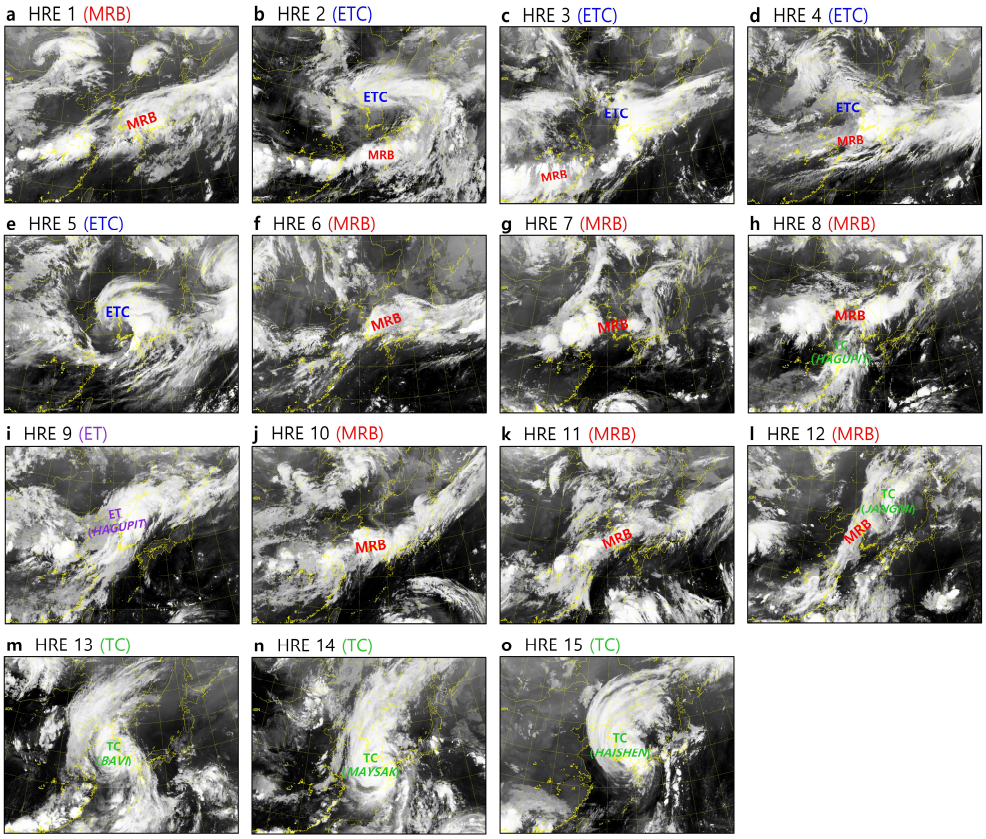

Figure 6.3. As in Fig. 6.2, but for satellite images (10.5-mm infrared channel).

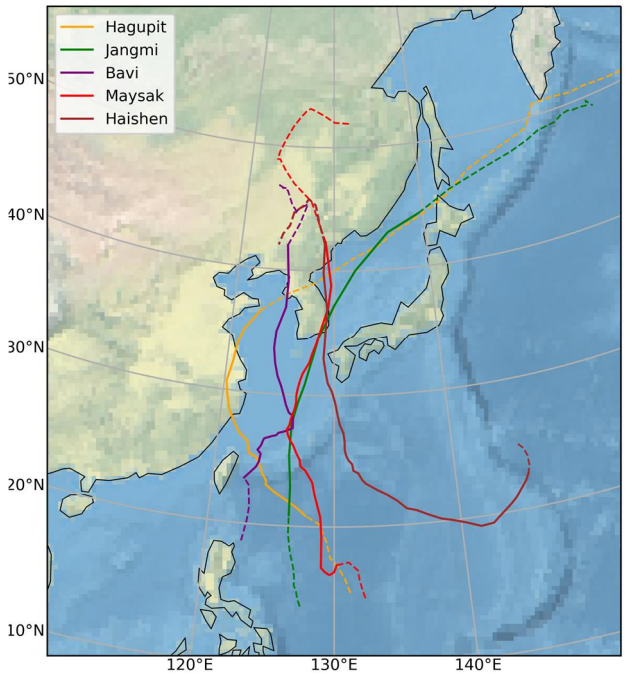

Figure 6.4. Tracks of TCs mentioned in Table 6.1. The stages of TD or ETC are indicated by dashed lines.

Table 6.1 summarizes the nature of each HRE. It is evident that the HRE type abruptly changed from ETC to MRB in late July and then to TC in late August (see also Fig. 6.1c). Although the TCs and their contribution to the late-monsoon rainfall in East Asia are reasonably well documented (e.g., Chen et al. 2004; Guo et al. 2017; see also Figs. 2.7a,b), the rapid transition from ETC-related HREs to MRB-related HREs is not well documented. Such a transition is rare, and not observed in China and Japan in the summer of 2020. In this regard, this study mainly addresses the HREs in P1 and P2, and their abrupt transition. Note in Fig. 6.1c that the HREs in P1 occurred intermittently, whereas those in P2 occurred somewhat persistently. This temporal difference is closely related to the HRE-type difference (i.e., ETC versus MRB).

6.4. Subseasonal variation of HREs and background flow

6.4.1. Synoptic characteristics of HREs in P1 and P2

The composite map shows that the synoptic pattern of HREs in P1 is characterized by an ETC in the southwest of the Korean Peninsula (Fig. 6.5a). This cyclone accompanies a large amount of moisture transport on its southeastern flank (see vectors). This weather pattern resembles C2 and C5 of non-TC HREs in chapter 4 (i.e., ETC from eastern China). In Fig. 6.5c, the warm sector of the ETC is manifested by high 850-hPa θ_e. Likewise, low θ_e appears on the rear side of the ETC where dry air intrudes (Browning 1990). Such moisture distributions are also evident in the satellite images (see Figs. 6.3b–e).

Figure 6.5b shows the meandering upper-level PV, suggestive of the baroclinic nature of the ETC. A strong upward motion at 500 hPa is located on the east of the upper-level PV intrusion (black contours) and south of the ULJ entrance (shading), which is the favorable region for a dynamically-forced uplift. When the ETC develops, the NPH whose boundary is often identified by the 5,840- and 5,880-gpm lines at 500 hPa is positioned south of Japan (see thick contours in Fig. 6.5c). Figure 6.5d shows that a large meridional gradient of θ_e is evident across the Korean Peninsula with a poleward tilt, implying a strong baroclinicity over the country. However, its vertical gradient is rather small. This indicates that the HREs in P1 occurred under moist-adiabatically near-neutral or only weakly unstable condition.

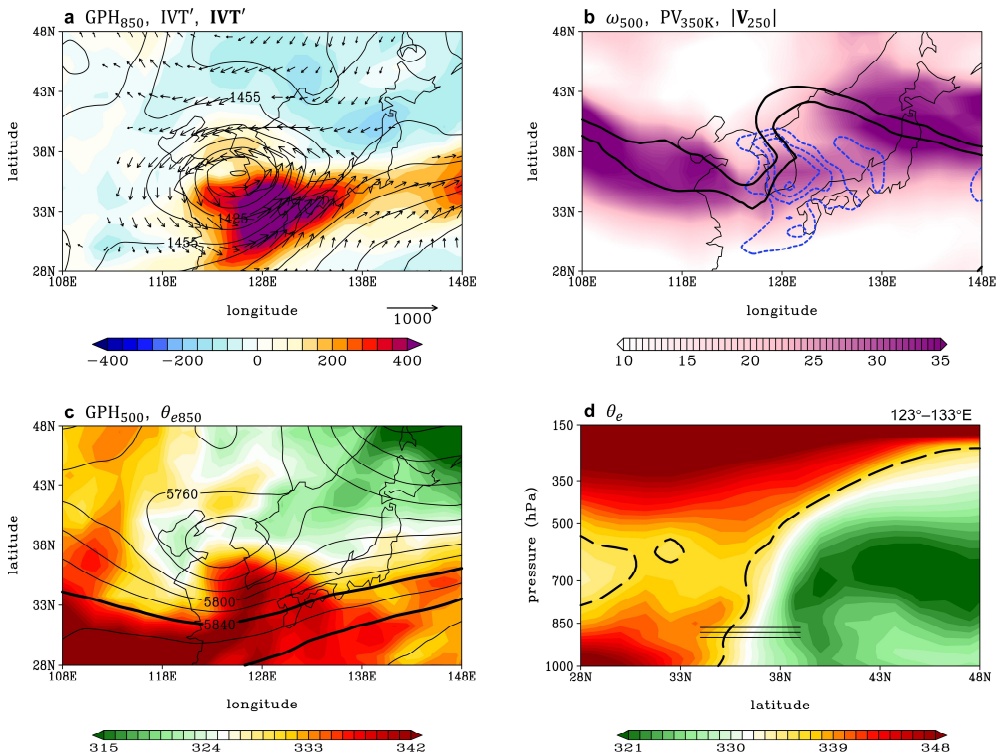

Figure 6.5. Composited synoptic structures of the four HREs in P1 (HREs 2–5 in Table 6.1). **a** GPH (gpm, contours) at 850 hPa, IVT anomaly (kg m^{-1} s^{-1}, shading) and **IVT** anomaly (>100 kg m^{-1} s^{-1}, vectors). **b** Vertical motion at 500 hPa (blue contours with a 0.2-Pa s^{-1} interval), 1.5- and 3-PVU at the 350-K isentropic surface (black contours), and horizontal wind speed at 250 hPa (m s^{-1}, shading). **c** GPH at 500 hPa (gpm, contours) and θ_e at 850 hPa (K, shading). The 5,840- and 5,880-gpm contours are highlighted with thick lines. **d** Latitude-pressure cross section of θ_e (K, shading) averaged over 123°–133°E. The 336-K θ_e is highlighted with a dashed line. The approximate meridional location of South Korea is denoted with three horizontal black lines.

In P2, the HREs show different dynamic and thermodynamic features from those in P1. Here, the HRE 9 is excluded because it was driven by a transitioned TC, unlike the other HREs in P2. Around the Korean Peninsula, no synoptic-scale disturbance appears (Fig. 6.6a). Instead, a large amount of moisture is transported toward the Korean Peninsula along the NPH boundary. This is a typical circulation pattern favorable for the enhanced MRB (Ninomiya and Shibagaki 2007). The continental low, which is observed in northeastern China (see 1,425-gpm contour), likely in part contributes to the formation of a confluent zone over the Korean Peninsula by blocking the northward expansion of the NPH. This circulation pattern is similar to C1 and C3 of non-TC HREs in chapter 4 (i.e., quasi-stationary frontal boundary between low and high).

Figure 6.6b shows that the ULJ (shading) and high PV (black contours) are positioned more northward but less undulating than those in P1. The midlevel upward motion (blue contours) is somewhat elongated to the south of the upper-level high PV. This result is consistent with Horinouchi (2014) and Horinouchi and Hayashi (2017), who asserted that given the southwesterly low-level moisture transport, the precipitation band can be enhanced on the southern side of the upper-level high PV although it is only weakly undulating. The upward motion in P2 is notably weaker than that in P1 despite similar or stronger rainfall intensity (see Fig. 6.1c).

The weak synoptic forcings (e.g., absence of ETC, zonally elongated upper-level PV and weak grid-scale vertical motion) imply that the HREs in P2 mainly resulted from local instability within the MRB. The moist-adiabatically unstable condition, as inferred from $\partial\theta_e/\partial z < 0$ in the lower troposphere (Fig. 6.6d), supports this conjecture. The 5,840- and 5,880-gpm lines of the 500-hPa GPH are located directly over the Korean Peninsula (Fig. 6.6c), where a strong positive IVT anomaly is observed (see Fig. 6.6a).

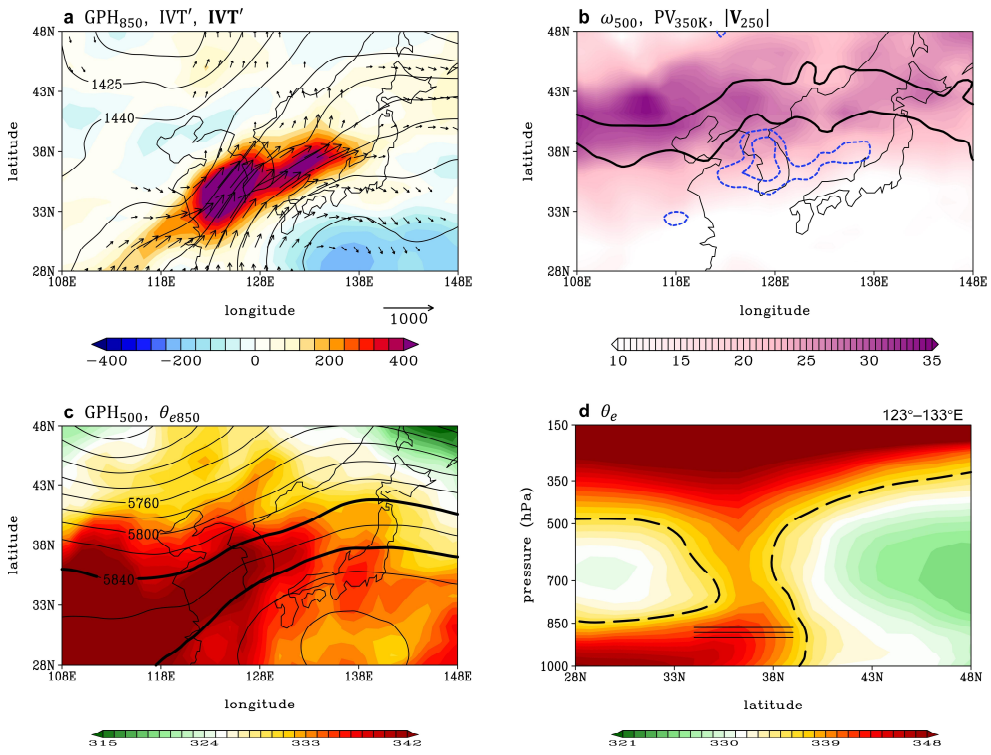

Figure 6.6. As in Fig. 6.5 but for the six HREs in P2 (HREs 6–8 and HREs 10–12 in Table 6.1).

6.4.2. Background monsoon flows in P1 and P2

Consistent with HRE changes, EASM circulation abruptly changed from P1 to P2. Figure 6.7 presents the time-latitude evolution of IVT anomaly and latitudinal position of the NPH boundary averaged over 123°–133°E. To smooth out the short-term fluctuation, a 9-day moving average is applied. In P1, the 5,840-gpm line was located south of its climatological position (cf. thick black and green lines). As a result, the monsoonal IVT anomalously intensified at approximately 30°N but weakened in the north, including South Korea. Note that the positive IVT anomaly over South Korea in Fig. 6.5a is a result of transient moisture supply by the ETC, not by the quasi-stationary monsoon flow along the NPH boundary. In late July, however, the 5,840-gpm line abruptly shifted northward. The 5,880-gpm line, whose climatology is not identified anymore, also shifted northward, forming an enhanced pressure gradient along the NPH boundary. This allowed anomalously intensified IVT over the latitude of South Korea throughout P2.

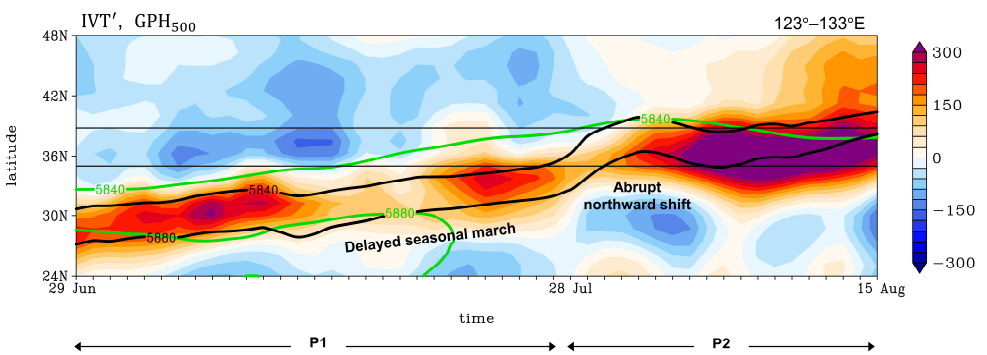

Figure 6.7. Hovmöller diagram (time-latitude) of IVT anomaly (kg m^{-1} s^{-1}, shading), 5,840- and 5,880-gpm GPHs at 500 hPa (thick black line), and their climatologies (thick green line) averaged over 123°–133°E during the period of 29 June–15 August 2020 (P1+P2). A 9-day moving average is applied. The approximate meridional location of South Korea is indicated by two thin black lines.

To more thoroughly compare the background flows between P1 and P2, the mid- and upper-level circulation patterns are examined in Fig. 6.8 over a broader domain. In P1, the NPH largely extends westward (Fig. 6.8a), as indicated by the 5,880-gpm line of the 500-hPa GPH, whose westernmost tip is positioned approximately 15° west of its climatology (cf. thick black and green lines). However, in the north, quasi-stationary ridge and trough are anchored over northeastern China and South Korea, respectively. This persistent trough over South Korea likely blocked the northward march of the NPH (cf. 5,840-gpm GPH and its climatology between 115° and 135°E), resulting in the southwesterly **IVT** anomaly and positive 850-hPa θ_e anomaly from southeastern China to western Japan. Over South Korea, in contrast, the northeasterly **IVT** anomaly and negative 850-hPa θ_e anomaly are evident.

The upper-tropospheric circulation in P1 is characterized by a large South Asian high (Fig. 6.8b). Compared to the climatology, the South Asian high extends well eastward to the south of the Korean Peninsula (cf. thick green and black lines). This is consistent with Ren et al. (2015), who found that the westward extension of the NPH could be concurrent with the eastward extension of the South Asian high. Along the northern rim of the South Asian high, the ULJ is strengthened (shading).

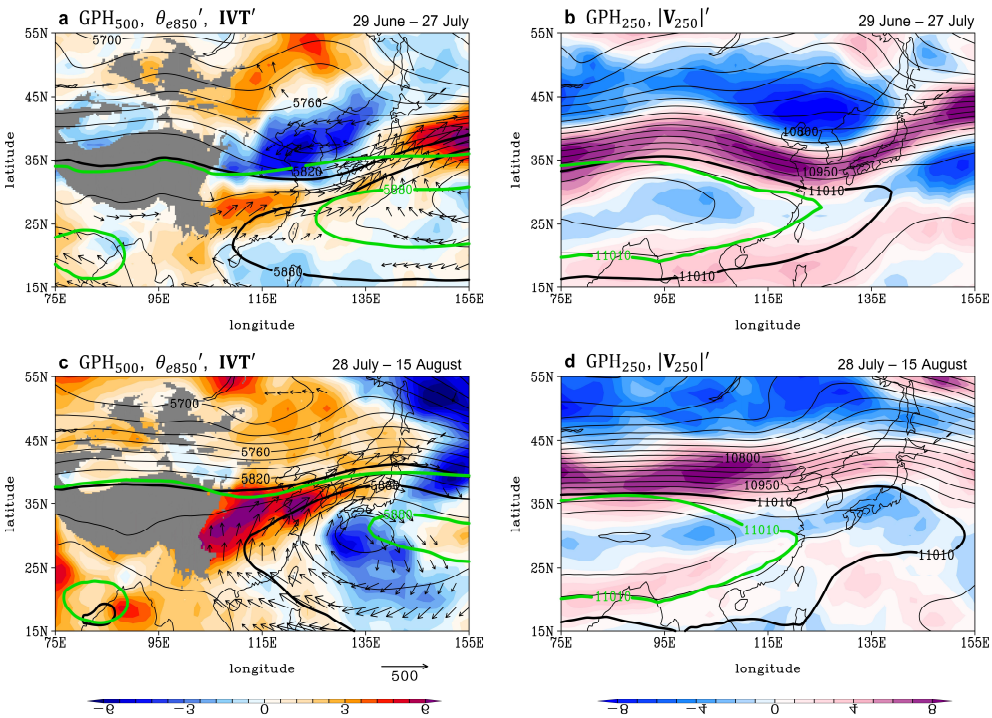

Figure 6.8. a,**c** The GPH at 500 hPa (gpm, black contours), θ_e anomaly at 850 hPa (K, shading) and **IVT** anomaly (>100 kg m^{-1} s^{-1}, vectors) in **a** P1 and **c** P2. The 5,840 and 5,880 gpm, and their climatologies are denoted by thick black and green lines, respectively. The terrain higher than 1500 m is masked by gray shading. **b**,**d** The GPH (gpm, black contours) and horizontal wind speed anomaly (m s^{-1}, shading) at 250 hPa in **b** P1 and **d** P2. The 11010 gpm and its climatology are denoted by thick black and green lines, respectively.

The monsoon circulation depicted in Figs. 6.8a,b is favorable for the MRB to develop from southeastern China to western Japan but not over the Korean Peninsula. Instead, South Korea was frequently affected by ETCs in P1 (Fig. 6.9a). By analyzing daily weather maps, it turns out that these ETCs were originated from southeastern China, a famous cyclogenesis region (Lee et al. 2020; Kang et al. 2020). Kang et al. (2020) explained that the intensification of these ETCs is strongly tied to diabatic processes. Anomalously warm and humid conditions in southeastern China, manifested by a positive 850-hPa θ_e anomaly in Fig. 6.8a, can support the genesis and early development of the ETC in the region (Cho et al. 2018). The intensified ULJ on the northern flank of the South Asian high (Fig. 6.8b) can help to steer the ETC toward South Korea. The quasi-stationary trough over South Korea (Figs.

6.8a,b) may further contribute to the deepening of ETC when it arrives. This can explain why four HREs occurred in P1, although the MRB deviated southward from the Korean Peninsula.

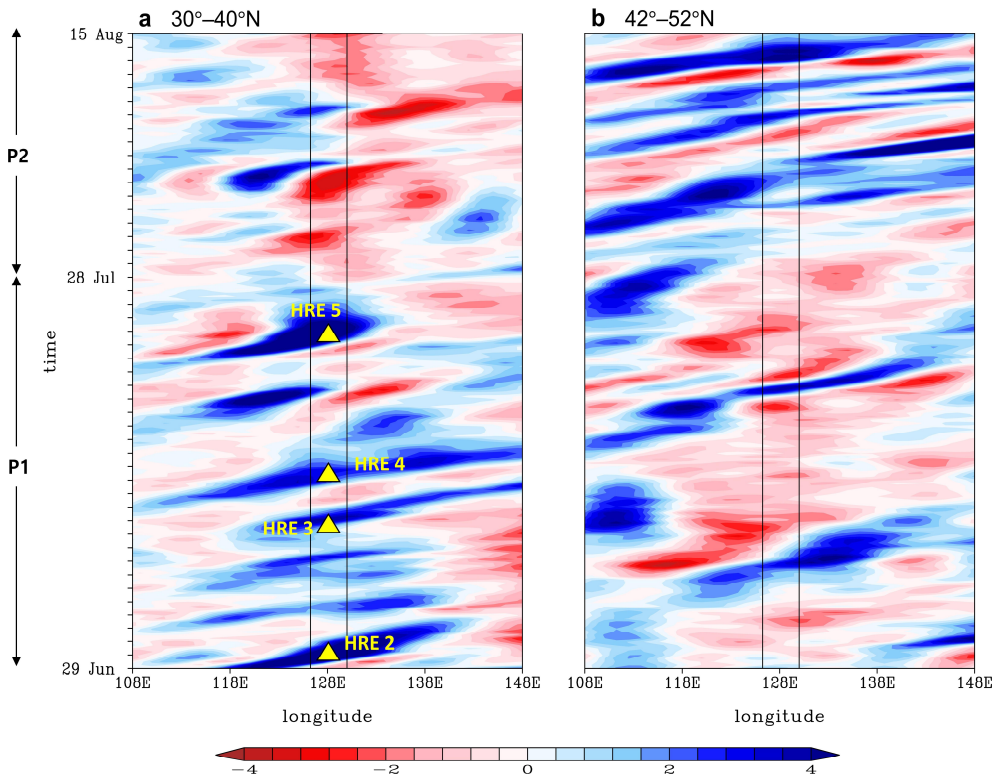

Figure 6.9. Hovmöller diagram (longitude-time) of the T42-filtered relative vorticity at 850 hPa (shading, CVU) averaged over **a** 30°–40°N and **b** 42°–52°N during the period of 29 June–15 August 2020 (P1+P2). The approximate zonal location of South Korea is indicated by two thin black lines. In **a**, the ETCs that triggered the HREs are marked by yellow triangles.

The monsoon circulation in P2 is very different from that in P1. The most important feature is the northward expansion of the NPH (Fig. 6.8c), which is also evident in Fig. 6.7. As the quasi-stationary trough, which is observed over South Korea in P1, disappears in P2, the 5,840- and 5,880-gpm lines jump northward. Although this can be partly due to the seasonal march of EASM, the abrupt expansion of the NPH is well distinguished from its climatological evolution. Note that the 5,880-gpm line, whose climatology is confined to the southeast of Japan, locates immediately south of the 5,840-gpm line (see also Fig. 6.7). This means the pressure gradient is largely enhanced along the northern boundary of the NPH, creating the strong southwesterly **IVT** anomaly toward Korea. Consistently, the positive 850-hPa θ_e anomaly is widely distributed from the leeward side of the Tibetan Plateau to the Korean Peninsula. This strong quasi-stationary moisture transport along the NPH boundary likely allowed MRB to develop over the Korean Peninsula.

In the upper troposphere, the South Asian high extended eastward (Fig. 6.8d). Consistent with the northward expansion of the NPH, the eastern ridge of the South Asian high also shifted northward (see thick black line). The ULJ is also intensified in the north of South Korea, which provides a favorable condition for the precipitation band over the Korean Peninsula. As the overall monsoon system moved northward, the ETC tracks also jumped to higher latitudes, no longer passing over South Korea (Fig. 6.9b).

6.5. Possible mechanisms of the monsoon circulation change

The monsoon circulation during P1 is exceptional in that the NPH anomalously extended westward, but its northward march was delayed. However, the NPH suddenly expanded northward in late July, transporting a large amount of moisture toward the Korean Peninsula during P2. This section suggests the possible mechanisms for this abrupt change in monsoon circulation, which is responsible for the distinct synoptic features of the HREs between P1 and P2.

6.5.1. Meridional wave train by the SCS convection

Figures 6.10a,b present the 500-hPa streamfunction (ψ), OLR and 500-hPa wind anomalies averaged over P1 and P2, respectively. In P1, positive OLR anomaly (i.e., suppressed convection) and positive ψ anomaly appear over the SCS (Fig. 6.10a). These suppressed convection and anticyclonic circulation anomalies, which are consistent with the westward extension of the NPH (see Fig. 6.8a), can act as a source of stationary Rossby wave. The resulting wave train forms tripole ψ anomalies in the meridional direction, i.e., anticyclonic anomaly over the SCS, cyclonic anomaly over the Korean Peninsula and anticyclonic anomaly over northeastern China. This is reminiscent of the PJ pattern (Nitta 1987; Kosaka and Nakamura 2006), although the wave train pattern is slightly different from a canonical PJ pattern (see section 6.5.3 for details). The associated wave activity flux defined by Takaya and Nakamura (2001) is dominant in the lower troposphere (see appendix A4), which is a typical feature of the PJ pattern (Kosaka and Nakamura 2006).

It is important to note that the cyclonic lobe of the wave train is consistent with the quasi-stationary trough over South Korea seen in Fig. 6.8a. This implies that the delayed northward march of the NPH in P1 likely resulted from the PJ-like pattern forced by the suppressed SCS convection. The anticyclonic lobe over northeastern China is also consistent with the quasi-stationary ridge in Fig. 6.8a. The prolonged MRB to the south of the Korean Peninsula is manifested by a negative OLR anomaly from southeastern China to western Japan. To the east of Japan, an

anticyclonic anomaly is also observed, which is likely a wave response to the enhanced convection along the prolonged MRB.

In P2, the OLR anomaly over the SCS switches its sign to negative (enhanced convection; Fig. 6.10b). This leads to the disappearance of the anticyclonic ψ anomaly over the SCS. The anticyclonic anomaly instead becomes dominant in the north, with a center at the right south of western Japan. This anticyclonic anomaly is consistent with the northward expansion of the NPH and the enhanced pressure gradient along its northern boundary seen in Fig. 6.8c. The line-shaped negative OLR anomaly on the northern rim of the anticyclonic anomaly manifests the enhanced MRB over the Korean Peninsula. The anticyclonic ψ anomaly over northeastern China, which is maintained in P1, also changes to a cyclonic ψ anomaly. Although further analyses are required, the disappearance of the anticyclonic anomaly over the SCS and the subsequent northward expansion of the NPH are likely circulation response to the enhanced SCS convection. In section 6.5.3, the role of the SCS convection in the EASM circulation anomaly is further evaluated by conducting long-term data analysis.

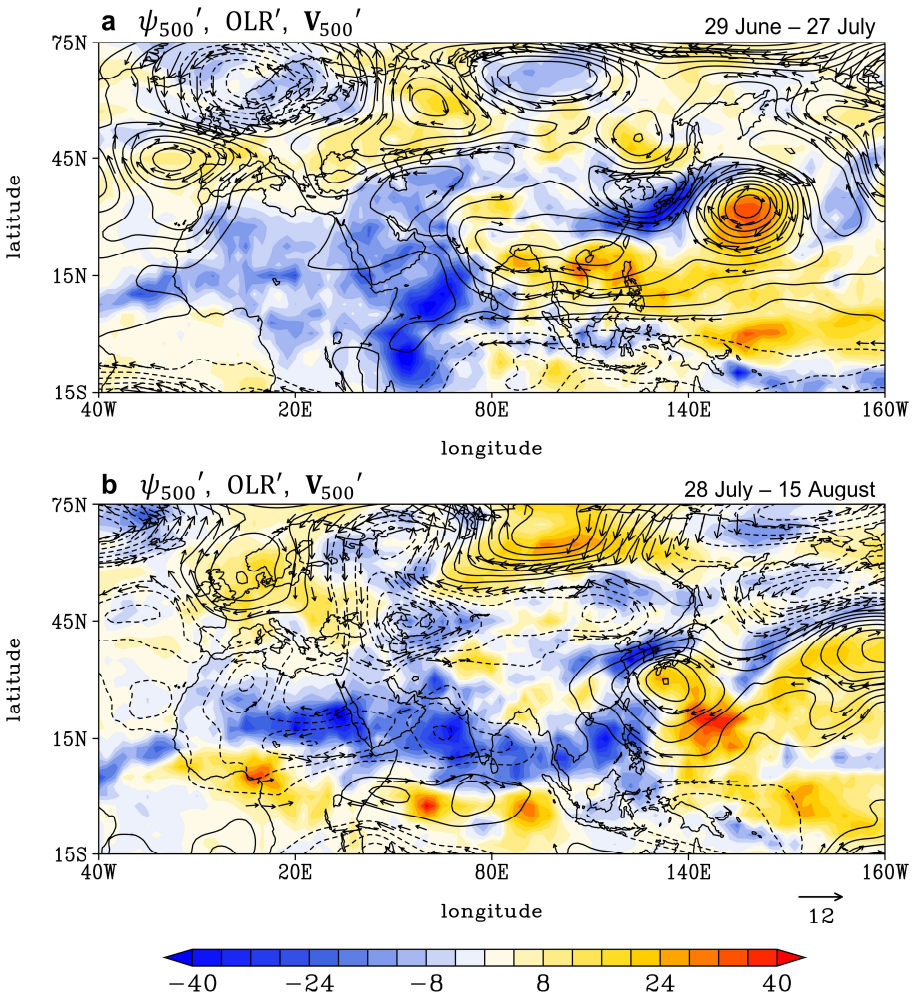

Figure 6.10. ψ anomaly at 500 hPa (contours with a 0.1×10^{-7} m^2 s^{-1}), horizontal wind anomaly at 500 hPa (>3 m s^{-1}, vectors) and OLR anomaly (W m^{-2}, shading) in **a** P1 and **b** P2.

6.5.2. Zonal wave train by the SNAO

Figure 6.10 also shows a zonal wave train in high latitudes. In P1, for instance, a wave train starting from the cyclonic anomaly over the eastern North Atlantic develops downstream (Fig. 6.10a). The wave train pattern consists of an anticyclonic lobe over the Ural Mountains, a cyclonic lobe over central Siberia, and an anticyclonic lobe over northeastern China. This pattern, which has an equivalent barotropic structure with a stronger wave activity flux in the upper troposphere (see appendix A4), resembles the typical teleconnection pattern over northern Eurasia in the boreal summer (Iwao and Takahashi 2008; Xu et al. 2019). The circulation anomaly over the North Atlantic, which is similar to the negative phase of the SNAO, suggests that the SNAO-related divergent flow might be a source of the high-latitude wave train (Wu et al. 2009; Li and Ruan 2018).

In P2, the ψ anomaly over the eastern North Atlantic changes its sign to positive (Fig. 6.10b), exhibiting a positive SNAO. Note that the northern Eurasian wave pattern also shows an opposite phase to that in P1. This implies that the abrupt change in monsoon circulation from P1 to P2 was also likely influenced by the SNAO-induced zonal wave train. Recently, Liu et al. (2020) proposed the subseasonal phase transition of the SNAO as a key regulator of extreme rainfall around the Yangtze River in the early summer of 2020. They suggested that a positive SNAO on 11–25 June and a negative SNAO on 30 June–13 July led to the different synoptic characteristics of quasi-stationary monsoon front between the two periods. However, their analysis cannot be directly applied to the present study because of different analysis periods. The possible role of the SNAO in the East Asian circulation anomalies in P1 and P2 is further explored in the next subsection.

6.5.3. Combined effect of the SCS convection and SNAO

To evaluate the general role of the SCS convection and SNAO on EASM circulation, composite maps are constructed for the days when SCS OLR anomaly is well defined or when both SCS OLR and SNAO anomalies are at work for the period of 29 June–15 August from 1979 to 2019 (Fig. 6.11). Note that the year 2020 is excluded. Here, the SCS convection is indexed as the area-mean OLR anomaly over the SCS (10°–22.5°N, 100°–130°E). In a similar way, the SNAO index is defined as the area-mean 500-hPa GPH anomaly over the eastern North Atlantic (52°–72°N, 10°W–25°E). Only the days when each index is greater than ± 1.0 standard deviation (σ) in magnitude are selected to increase the signal-to-noise ratio. The statistically significant values at the 90% confidence level are determined based on the Student's *t* test. When counting the number of degrees of freedom, continuous days with no break are considered as a single event.

The composite 500-hPa ψ anomaly for the SCS OLR index above 1.0σ (i.e., enhanced SCS convection) exhibits a canonical PJ pattern (Fig. 6.11a). An opposite phase of the PJ pattern is also obtained for the SCS OLR index below -1.0σ (i.e., suppressed SCS convection; Fig. 6.11b). These wave patterns along the east coast of the Eurasian continent are somewhat different from those in the summer of 2020. For the suppressed SCS convection, the cyclonic lobe centered to the east of the Korean Peninsula is excessively extended in a northwestward-southeastward direction (Fig. 6.11a), while the lobe in P1 is more localized over the Korean Peninsula (Fig. 6.10a). The anticyclonic ψ anomaly over northeastern China, which is evident in P1, also does not appear in Fig. 6.11a. Similarly, the anticyclonic lobe for the enhanced SCS convection is excessively extended in a northwestward-southeastward direction (Fig. 6.11b). It contrasts with the case in P2, which is characterized by the northern boundary of the anticyclonic anomaly right over the Korean Peninsula (Fig. 6.10b). These results indicate that the SCS convection alone may not fully explain the anomalous background flow and its abrupt change from P1 to P2.

When both the SCS convection and SNAO are considered, the East Asian circulation anomalies more resemble those in the summer of 2020. With the SCS OLR index above 1.0σ and the SNAO index below –1.0σ (Fig. 6.11c), tripole ψ anomalies are organized over the SCS, east of the Korean Peninsula and northeastern China. Although the cyclonic lobe is slightly shifted eastward compared to that in P1, it is well sandwiched between the two anticyclonic lobes in the north and south as in P1 (Fig. 6.10a). An anticyclonic anomaly to the east of Japan is also better captured.

The composited ψ anomalies for the SCS OLR index below –1.0σ and the SNAO index above 1.0σ also depict a qualitatively more similar pattern to the case of P2 (Fig. 6.11d). Compared to Fig. 6.11b, the spatial extent of the anticyclonic lobe is noticeably reduced due to the cyclonic ψ anomaly in the north. The horizontal gradient of the anticyclonic ψ anomaly is also stronger over the Korean Peninsula. This allows a stronger southwesterly **IVT** anomaly toward the Korean Peninsula (cf. vectors in Figs. 6.11b,d), providing a favorable condition for MRB development. However, the cyclonic anomaly over the SCS in Fig. 6.11d does not match with no anomaly in Fig. 6.10b, suggesting additional factors in setting low-latitude circulation in P2. Although not shown, the overall result is not sensitive to the presence versus absence of the summertime El Niño–Southern Oscillation signal.

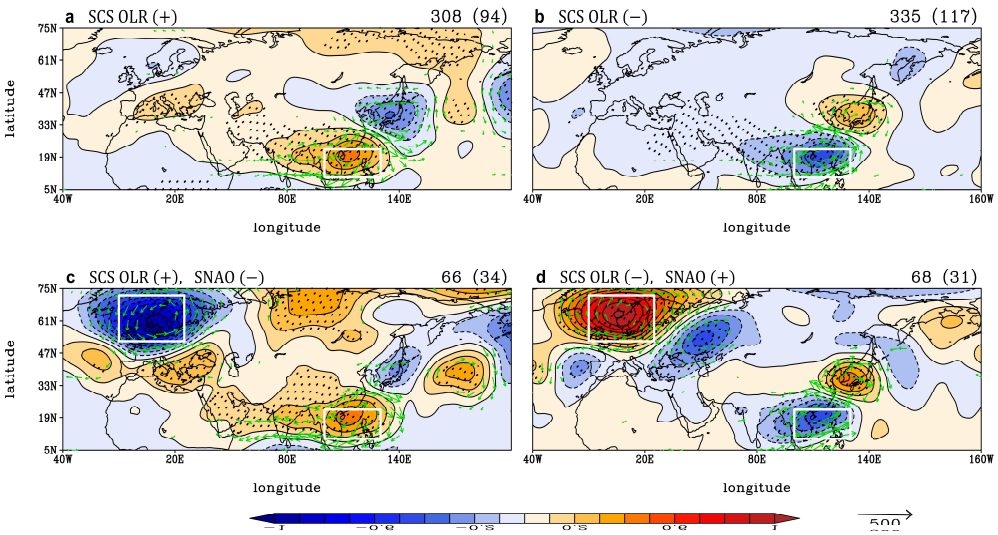

Figure 6.11. The 500-hPa ψ anomaly (10^{-7} m^2 s^{-1}, contours and shading) and **IVT** anomaly (kg m^{-1} s^{-1}, vectors) when the SCS OLR index is **a** above +1.0σ and **b** below –1.0σ for the period of 29 June–15 August from 1979 to 2019. **c**,**d** As in **a**,**b** but for **c** the SCS OLR index >+1.0σ and the SNAO index <–1.0σ and **d** the SCS OLR index <–1.0σ and the SNAO index >+1.0σ. The statistically significant ψ anomalies at the 90% confidence level based on a Student's *t* test are stippled. Only the statistically significant **IVT** anomalies at the same confidence level are shown. Two boxed regions denote the SCS (100°–130°E, 10°–22.5°N) and eastern North Atlantic (10°W–25°E, 52°–72°N). The number of days considered is indicated in the upper-right corner of each plot. The number of degrees of freedom, by considering consecutive days as one event, is given in parenthesis.

The above results suggest that the anomalous monsoon circulation around the Korean Peninsula and its sharp change from P1 to P2 are likely explained by the combined effects of the SCS convection and SNAO. Figure 6.12 indeed shows that both the SCS OLR and SNAO indices simultaneously changed their signs at the end of July, although the reason for their synchronization remains unclear. The previous study by Seo et al. (2012), who attributed the extraordinary behavior of the NPH in July 2011 to the joint effect of the SCS convection and SNAO, further strengthens our argument. Perhaps, numerical model simulations imposed by diabatic or divergent forcings would be helpful to confirm this observation-based argument.

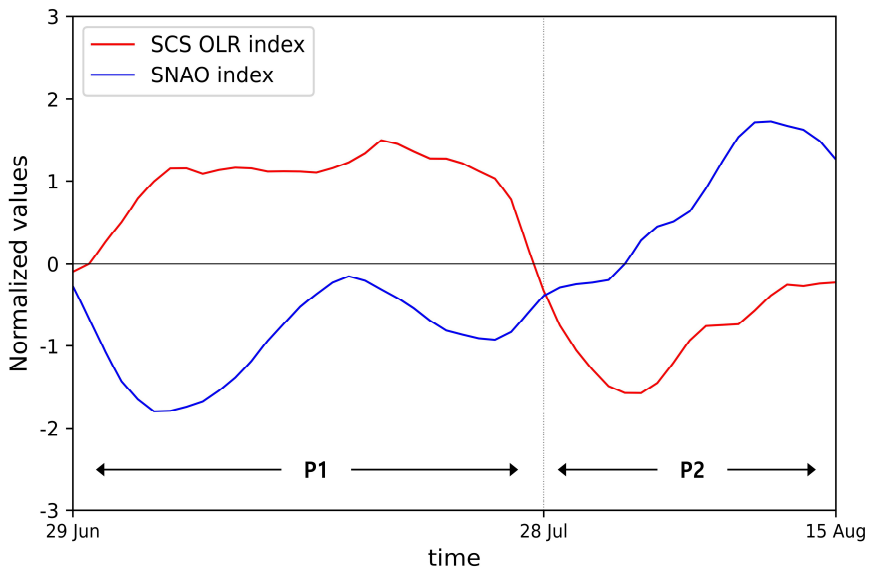

Figure 6.12. Daily time series of the SCS OLR index and SNAO index normalized by their one standard deviation during the period of 29 June–15 August 2020 (P1+P2). A 9-day running average is applied.

6.6. Discussion

6.6.1. IPOC effect

The westward extension of the NPH and the suppressed convection over the SCS in P1 (see Fig. 6.10a) are likely the response to a large-scale atmosphere–ocean coupled mode. More specifically, it is speculated that the IPOC effect (Xie et al. 2009, 2016), which is briefly mentioned in section 1.1.3, has likely played a role. The IPOC effect is briefly summarized as follows. The wintertime El Niño typically decays in the following spring (Tziperman et al. 1998). However, the associated tropical Indian Ocean warming, which is dictated by ocean dynamics and local air–sea interactions (Xie et al. 2002; Du et al. 2009), often persists until early summer, resulting in enhanced convection over the tropical Indian Ocean. This enhanced convection drives eastward-propagating baroclinic Kelvin waves into the equatorial western Pacific as a Gill-type response (Gill 1980). In the lower troposphere, the Kelvin wave–induced Ekman divergence over the subtropical western North Pacific can enhance the anticyclonic circulation.

A similar condition is evident in P1. The 2019/20 wintertime El Niño rapidly decayed in the spring of 2020 (Fig. 6.13a), but the associated SST anomaly of the tropical Indian Ocean remained positive in P1 (Fig. 6.13b). Figure 6.13c clearly shows the enhanced convection over the tropical Indian Ocean (blue shading) and the divergent near-surface northeasterly anomaly from the SCS to the Bay of Bengal (vectors). This greatly resembles the typical IPOC mode (see Fig. 15 in Xie et al. 2016). Note that the near-surface divergent flow matches well with the westward extension of the NPH in P1.

Meanwhile, Takaya et al. (2020) and Zhou et al. (2021) indicated that the preceding winter El Niño was not sufficiently strong to allow the IPOC mode. According to their analyses, the tropical Indian Ocean warming in the early summer of 2020 was likely caused not only by the preceding El Niño but also by the super Indian Ocean dipole in August–October 2019. Zhang et al. (2021) further indicated that the exceptionally persistent Madden–Julian oscillation also contributed to the enhanced convection over the Indian Ocean.

The IPOC-driven westward enhancement of the NPH was also observed in June, prior to the PJ-like pattern in P1 (figure not shown). This implies that the suppressed SCS convection in P1, which acts as a source of the PJ-like pattern, likely resulted from the westward extension of the NPH forced by the IPOC effect. This IPOC–PJ relationship was previously proposed by Xie et al. (2009, 2016) and further supported by a significant correlation between the PJ pattern and the preceding winter El Niño (Kosaka et al. 2011; Kubota et al. 2016). Kim and Kug (2021) indeed verified the delayed PJ response to the warm tropical Indian Ocean. They showed that the warm tropical Indian Ocean often induces an anticyclonic anomaly over the subtropical western North Pacific via equatorial Kelvin wave propagation, and the delayed PJ response brings a cold temperature anomaly to the Korea–Japan region.

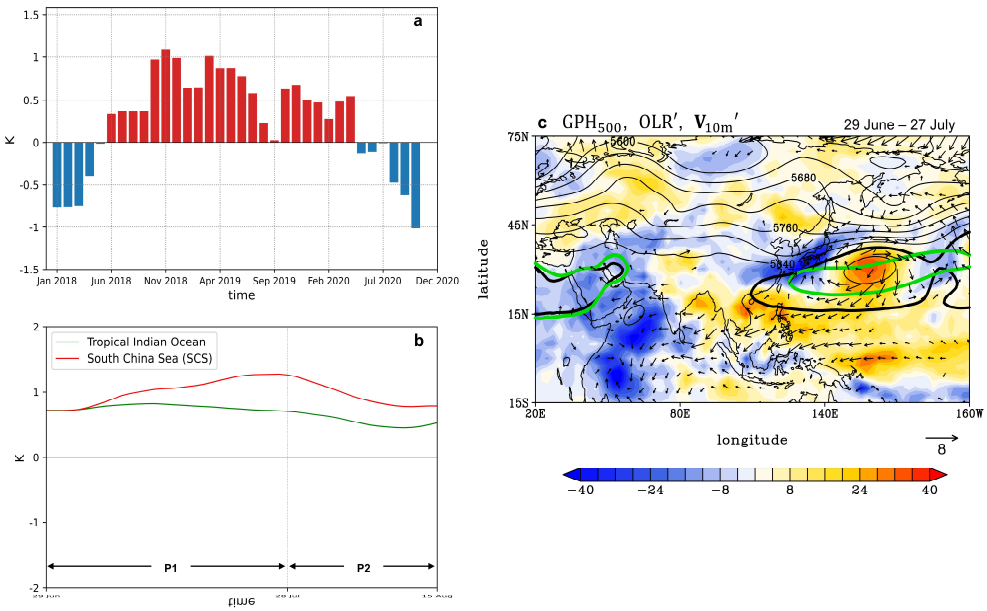

Figure 6.13. a Monthly time series of SST anomaly (K) over the Niño 3.4 region (5°S–5°N, 190°–240°E) from January 2018 to October 2020. **b** Daily time series of SST anomaly (K) over the tropical Indian Ocean (40°–100°E, 15°S–15°N; green) and SCS (100°–130°E, 10°–22.5°N; red) during the period of 29 June–15 August 2020 (P1+P2). A 9-day moving average is applied. **c** As in Fig. 6.10 but for GPH at 500 hPa (gpm, black contours), OLR anomaly (W m^{-2}, shading) and 10-m horizontal wind anomaly (>1 m s^{-1}, vectors) in P1. The 5,880 gpm and its climatology are also plotted by thick black and green lines, respectively.

6.6.2. BSISO

It is unclear why the OLR anomaly over the SCS sharply changed its sign in late July. Since the SST anomaly over the SCS did not change much from P1 to P2 (Fig. 6.13b), this transition is likely explained by the atmospheric internal variability such as BSISO. The BSISO phase indeed abruptly changed from P1 to P2 (Fig. 6.14). While the BSISO was mostly in phase 2 during P1, that during P2 was predominantly in phase 5. Their transition was quite sudden with only a few days of no active BSISO in between. Note that the OLR anomalies over the Indo–western Pacific Ocean in P1 and P2 greatly resemble the typical OLR patterns of BSISO phases 2 and 5, respectively (see Fig. 9 in Lee et al. 2013).

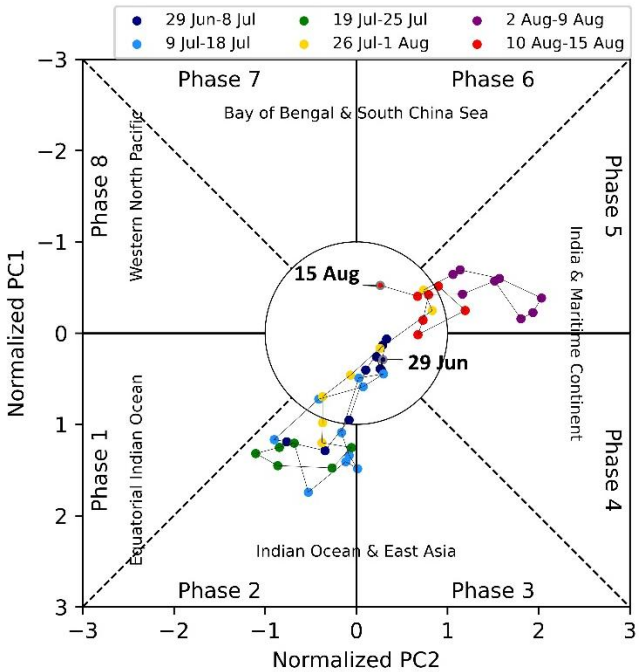

Figure 6.14. Phase diagram of BSISO mode 1 during the period of 29 June–15 August 2020 (P1+P2). See Lee et al. (2013) for details of the BSISO index.

6.6.3. Other possible factors

There might be other factors that affected the record-breaking summer rainfall in South Korea. For example, the westward extension of the NPH in P1 may be influenced by the nonlinear interactions between El Niño–Southern Oscillation and the annual cycle of background flow, so-called the combination mode (Stuecker et al. 2013, 2015). According to Stuecker et al. (2015), the combination mode can lead to anomalous anticyclonic circulation over the Northwest Pacific when the La Niña phase grows in the boreal summer, as in June–July 2020 (Fig. 6.13a). This may have constructively worked together with the IPOC effect to enhance the NPH in P1.

The upper-level GPH at ~35°–40°N in P1(Fig. 6.8b) is reminiscent of the Silk Road pattern (Hong and Lu 2016), which was pointed out by Horinouchi et al. (2021) as a cause of the prolonged heavy rainfall in western Japan in early July 2020. In 2020 summer, the Arctic experienced the amplified warming and the SST in the Northern Hemisphere was anomalously warm almost everywhere except for the equatorial eastern Pacific due to the developing La Niña (figure not shown). Their possible impacts on the record-breaking rainfall also deserve attention.

It is notable that the wet summers in Korea have become more frequent in the last two decades compared to the 1970s and 1980s (see blue bars in Fig. 6.1a). This long-term change may result from the monsoon circulation change in response to anthropogenic warming. By examining regional climate model simulations, Kim et al. (2018) asserted that the intensity and frequency of the Korean HREs will continue to increase in the future. Although the role of anthropogenic warming on the regional HRE is beyond the scope of this study, such analysis (e.g., Imada et al. 2020) would be valuable for better understanding the record-breaking rainfall in summer of 2020.

Chapter 7. Conclusions and final remarks

7.1. Overall

The extreme summertime precipitation in South Korea is affected by various atmospheric circulations on a wide range of scales with distinct dynamic and thermodynamic characteristics (see chapter 1). Among others, this dissertation attempts to comprehensively analyze the synoptic-scale processes of HREs. Following the KMA criteria, an HRE is defined as a rainfall event with more than 110 mm (12 h)$^{-1}$ at any single weather station. The HREs directly induced by TCs (i.e., TC-HREs) are separately considered. By analyzing all historical HREs and TC-HREs over the past four decades, this study produces climatologically reliable results with statistical significance. Not only qualitative and statistical investigations (e.g., composites and clustering analyses) but also quantitative dynamical assessments (e.g., budget analyses) are conducted to elaborate on the synoptic–dynamic details of HREs and TC-HREs. As a case study, the record-breaking rainfall in the summer of 2020 is also analyzed to document the peculiar features of HREs during this abnormally wet summer. The overall structure of this dissertation can be schematized as shown in Fig. 7.1. In the following subsection, the key results of each chapter are summarized.

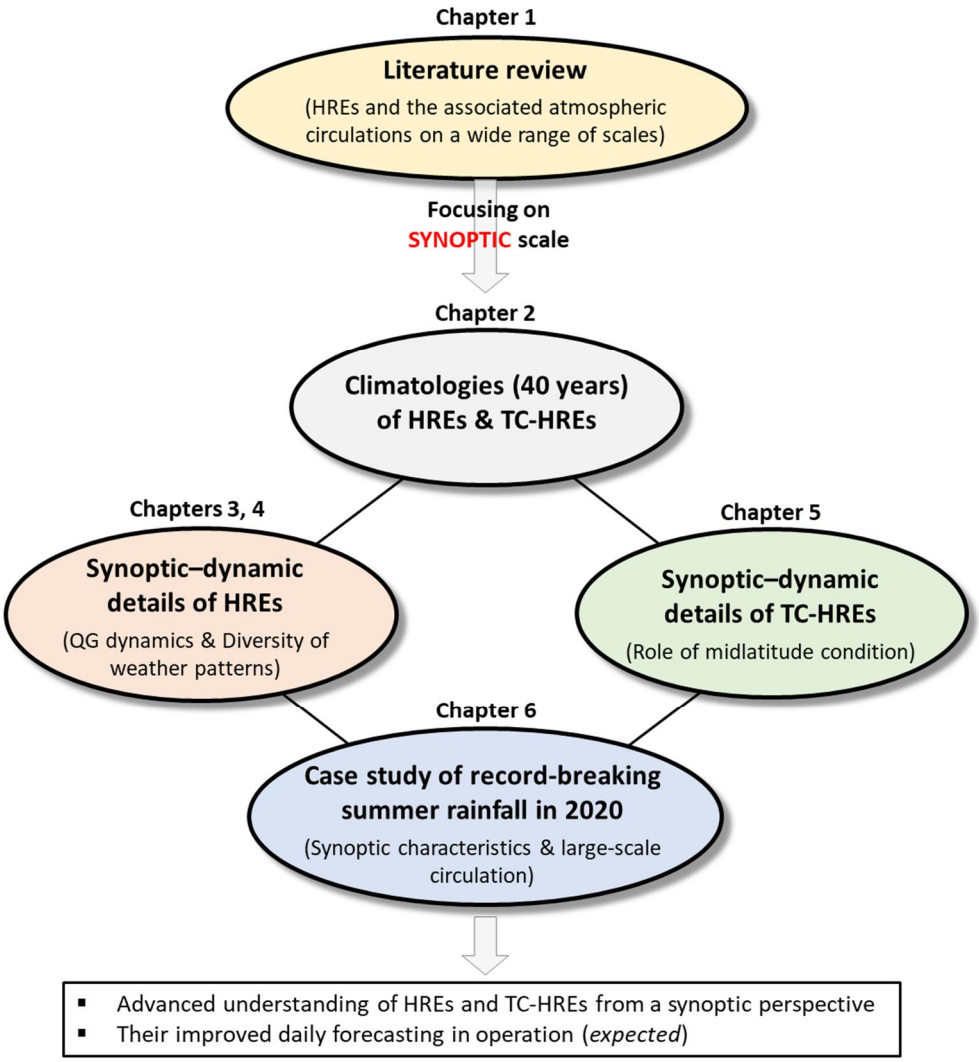

Figure 7.1. Structure of this dissertation.

7.2. Summary of dissertation

7.2.1. Chapter 2 “Climatological features of HREs and TC-HREs”

The climatologies of the 392 HREs occurred in South Korea in JJAS 197–2018 are examined. By considering HREs and TC-HREs separately, they are summarized as follows (see also Table 2.1):

I. *HREs (81.1%)*: A migrating surface cyclone from eastern China and a northwestward expansion of the NPH induce strong southwesterly moisture transport toward the Korean Peninsula. In the upper troposphere, a trough and jet streak develop in the west and north of South Korea, providing a favorable condition for the dynamically-forced uplift. The atmosphere is moist-adiabatically unstable in the boundary layer but near-neutral in the free troposphere. The HREs have two frequency peaks in the first and second rainy periods and favor the south coast and west of the north–south-oriented mountains.

II. *TC-HREs (18.9%)*: The TC-HREs are characterized not only by poleward-moving TC but also by its phasing with midlatitude baroclinic flow, implying their synergetic interaction. An upward motion often develops over South Korea even before the TC arrives because of already well-defined upper-level trough and jet, suggestive of the possibility of predecessor rainfall events. In the mature stage, the TC is located immediately southwest of the Korean Peninsula with tremendous south-southeasterly moisture transport and highly amplified upper-level flow. The TC-HREs favor the second rainy period along the south and east coasts.

7.2.2. Chapter 3 "Quasi-geostrophic diagnosis of HREs"

The mechanisms of the vertical motion responsible for HREs are quantitatively examined in QG framework. By solving the QG omega equation, it is found that the initial vertical motion is triggered by dynamic forcing from the upper troposphere, which is consistent with the significant upper-level disturbances prior to HREs. In the developing stage of HREs, the dynamic omega (ω_{Dyn}) is comparable to the diabatic omega (ω_{Dia}), but ω_{Dia} becomes dominant over ω_{Dyn} in the mature stage of HREs as the latent heat release rapidly increases. The ω_{Dyn} and ω_{Dia} are maximized in the upper and middle troposphere, respectively.

The nature of dynamic uplift is further detailed by decomposing the Q vectors into the transverse and shearwise components. It turns out that the shearwise omega (ω_s), rapidly increases and becomes much stronger than the transverse omega (ω_n) in the mature stage of the HREs. Investigation of the geostrophic vorticity by shear and curvature reveals that the shearwise Q-vector forcing is mostly due to the well-defined trough. This confirms that the dynamic forcing during HREs is mostly driven by a baroclinically deepening trough, which contrasts with previous studies that have emphasized the role of a thermally-direct secondary circulation at the entrance region of ULJ. Based on this result, a new conceptual model describing the three-dimensional synoptic structure of HREs is suggested (Fig. 3.12).

7.2.3. Chapter 4 "Diverse synoptic weather patterns of HREs"

By applying a SOM algorithm to SLP fields of HREs, their six dominant surface weather patterns are identified. Their synoptic characteristics are compared in detail through composite analyses. By grouping clusters that share common surface weather patterns, four categories of HREs are finally drawn and summarized as follows (see also Table 4.2):

I. *Quasi-stationary frontal boundary between low and high (C1 and C3; 39.6%)*: This HRE group is characterized by a continental low over northeastern China and an oceanic high corresponding to the NPH, resulting in a quasi-stationary

frontal boundary in between. Strong southwesterly moisture transport and a frontal cyclone develop between two large-scale pressure systems. The low SLP anomaly is more pronounced than the high SLP anomaly in C1, whereas their strengths are nearly comparable in C3.

II. *ETC from eastern China (C2 and C5; 28.9%)*: This HRE group features an ETC originating from eastern China, which develops via baroclinic instability. The cyclone produces strong moisture transport along its leading edge with a stronger southerly component. Although similar in cyclonic vorticity, the cyclone in C2 deepens more than that in C5. While C2 is characterized solely by the well-deepened cyclone, C5 is described also by the surrounding high SLP.

III. *Local disturbance at the edge of the NPH (C4; 21.4%)*: This HRE type is dominated by the expanded NPH, which induces strong southwesterly moisture transport along its boundary. In the absence of an organized synoptic-scale disturbance, the HREs are likely triggered by a local disturbance on the NPH boundary. Compared to other clusters, the daily synoptic weather map is nearly invariant in time.

IV. *Moisture pathway between continental and oceanic highs (C6; 10.0%)*: The background weather pattern is characterized by high SLPs over the Asian continent and the northwestern Pacific. In between, a surface pressure trough develops, building a moisture transport pathway from the East China Sea toward Korea. With a well-defined upper-level trough and jet streak, various rainfall systems can be involved.

In all clusters, the upper-level trough and jet streak are present, although their strength and/or location slightly differ. The QG omega equation inversion reveals that in all clusters ω_{Dia} is greater than ω_{Dyn} with ω_s dominating over ω_n, although their relative contributions vary across the clusters. While C1 and C3 favor the first rainy period, C5 and C6 prefer the second rainy period. The C2 and C4 frequently occur both in the first and second rainy periods. Spatially, C1, C3, and

C4 mainly occur in the western half of the elevated terrain, while C6 is biased in the southwest coast of the country. The C2 and C5 exhibit no distinct occurrence region compared to other clusters.

7.2.4. Chapter 5 "Role of midlatitude condition in TC-HREs"

How the TC-HREs are modulated by midlatitude baroclinic condition is analyzed. This is achieved by classifying TC-HREs into two clusters by applying SOM analysis to dynamic tropopause (2 PVU) height fields. The two clusters, characterized by strongly (C1) versus weakly (C2) baroclinic conditions, are then compared through composite and dynamic budget analyses. Their synoptic–dynamic details can be summarized as follows.

I. *TC-HREs under strongly baroclinic condition (C1; 58.8%)*: These TC-HREs are most popular in late summer and develop through the synergistic interactions between TCs and midlatitude flow. On the tropopause, the trough-ridge couplet and jet streak are well defined and amplify as TCs approach. The upstream trough is anchored by the divergent outflow of TCs, prompting a phase locking with TCs when they arrive. The TCs undergo significant structural changes (e.g., size expansion, westward tilt and slantwise ascent) reminiscent of ET. Both the upper-level meandering flow and low-level TC circulation drive QG dynamic uplift which further supports diabatic uplift.

II. *TC-HREs under weakly baroclinic condition (C2; 41.2%)*: These TC-HREs are commonly found in mid-summer. The midlatitude preconditioning is characterized by a non-organized upper-level pattern. In the absence of TC–midlatitude flow interaction, the upper-level flow does not change much. The TCs also rapidly dissipate during and after HREs while retaining their tropical features (e.g., warm core and upright TC convection). The QG dynamic uplift is weak and spatially limited. Instead, the vertical motion is more dominated by the inherent diabatic TC convection.

The contrasting midlatitude conditions lead to different weather impacts between the two clusters. The mature C1 TC-HREs are observed even before TCs get sufficiently close to South Korea. In contrast, C2 TC-HREs are in the mature stage only when TCs are located in the right vicinity of the country. Moreover, C1 causes more inland rainfall while rainfall impact by C2 is confined to the south and east coasts of the Korean Peninsula. This is in line with the widely-enhanced QG dynamic uplift in C1.

7.2.5. Chapter 6 “Record-breaking rainfall in the summer of 2020”

In the summer of 2020, record-breaking monsoon rainfall occurred in South Korea, causing destructive floods across the country. This hydrological extreme was closely associated with 15 consecutive HREs. These HREs show three distinct synoptic features. All HREs from 29 June to 27 July (P1) were intermittently produced by developing ETCs, whereas those from 28 July to 15 August (P2) persistently occurred along the MRB. After a short dry spell, three TC-HREs occurred again in late summer. The transition from P1 to P2 was quite sudden, which was not observed for Chinese and Japanese HREs in June–July 2020.

In P1, the NPH anomalously extended westward via the IPOC effect. However, its northward expansion was delayed due to a quasi-stationary trough anchored over South Korea. Under this condition, the MRB was maintained to the south of the Korean Peninsula. Instead, the ETCs initiated over southeastern China frequently traveled across the Korean Peninsula, resulting in four HREs. In P2, the NPH rapidly expanded northward, and the pressure gradient along its northern boundary was considerably enhanced compared to its climatological state. This allowed strong southwesterly moisture transport toward the Korean Peninsula, forming the MRB over the region. Local convective instability along the MRB triggered six HREs.

The abrupt change of background monsoon flow in late July was remotely forced by atmospheric teleconnections. In P1, the SCS convection was anomalously

suppressed, resulting in a PJ-like pattern. The associated quasi-stationary trough over South Korea hindered the NPH from progressing northward. However, the SCS convection became strong in late July. The circulation response to the enhanced convection resulted in an abrupt northward expansion of the NPH in P2. On top of the meridional wave train, the SNAO-induced zonal wave train was also organized in northern Eurasia with opposite phases between P1 (negative SNAO) and P2 (positive SNAO). Although the reason for this synchronized phase changes of SCS convection and SNAO is unclear, the long-term data analysis suggests that when the SNAO is accompanied, the SCS convection-induced meridional wave train pattern more successfully mimics the East Asian circulation anomalies in both P1 and P2.

This result demonstrates that the summertime HREs can change their characteristics on subseasonal time scale by remote forcings from both tropics and extratropics. Therefore, not only the local processes (i.e., synoptic conditions) but also the remote processes (i.e., teleconnections) need to be taken into account for improved understanding and prediction of HREs.

7.3. Future directions

This dissertation comprehensively explores the synoptic–dynamic characteristics of HREs and TC-HREs. The results can be directly used to assist the skillful prediction of HREs and TC-HREs on daily time scale. However, further studies from other perspectives are still necessary given that extreme rainfall in the summer monsoon period in South Korea is influenced by atmospheric circulations on a wide range of scales (see chapter 1). A good example is the record-breaking summer rainfall in 2020 (chapter 6). In 2020 summer, the synoptic conditions of HREs were modulated by atmospheric teleconnections. It would be beneficial to investigate more comprehensively how large-scale atmospheric variabilities could modulate individual HRE-producing weather systems in EASM. Such analyses will allow us to bridge climate science and synoptic meteorology, thereby contributing to the successful medium-range forecasting of summertime extreme rainfall.

Although not seriously addressed in this dissertation, the mesoscale dynamics also need to be well understood. It is well known that the movement and spatiotemporal scale of mesoscale flows (e.g., MCSs, convective updrafts) considerably determine the local rainfall intensity and its duration (Doswell et al. 1996). In South Korea, HREs have a highly localized nature, which is spatially much smaller than their synoptic-scale setup (Jo et al. 2020). Such finer feature is likely associated with mesoscale perturbations with various morphologies superimposed on the synoptic-scale flow (see section 1.1.6). The large event-to-event variability of duration and rainfall amount of HREs and TC-HREs (Table 2.1) suggests that future works need to consider not only synoptic-scale but also mesoscale details by combining high-resolution observations and numerical model experiments. Such multiscale analyses encompassing synoptic and mesoscale dynamics would be particularly important in the future climate because summertime precipitation in South Korea is projected to be more affected by local convective activity under global warming (Cha et al. 2016; Kim et al. 2018; Lee et al. 2022).

Appendix A

A1. Integrated water vapor transport

The tropospheric moisture transport is evaluated using a flux-form vertically integrated water vapor transport:

$$\mathbf{IVT} = -\frac{1}{g}\int_{1000\ \mathrm{hPa}}^{300\ \mathrm{hPa}} q(u\mathbf{i} + v\mathbf{j})dp, \qquad \text{(A1.1)}$$

where g is the gravitational acceleration; u and v are the zonal and meridional winds, respectively; q is the specific humidity; p is the atmospheric pressure; **i** and **j** are the unit vectors in the zonal and meridional directions, respectively. Its scalar magnitude (i.e., $|\mathbf{IVT}|$) is referred to as IVT. Note that anomalies of **IVT** and IVT are not identical to each other.

A2. 2D frontogenesis

The low-level frontogenesis is evaluated using the two-dimensional Petterssen's kinematic frontogenesis function (Petterssen 1936; Keyser et al. 1988) applied to θ_e:

$$F_n = \frac{\mathrm{D}}{\mathrm{Dt}}|\nabla\theta_e| = -\frac{1}{2}|\nabla\theta_e|(D - E\cos 2\beta), \qquad \text{(A2.1)}$$

where $\frac{\mathrm{D}}{\mathrm{Dt}} = \frac{\partial}{\partial t} + u\frac{\partial}{\partial x} + v\frac{\partial}{\partial y}$; $\nabla = \frac{\partial}{\partial x}\mathbf{i} + \frac{\partial}{\partial y}\mathbf{j}$; $D = \frac{\partial u}{\partial x} + \frac{\partial v}{\partial y}$ is the horizontal mass divergence; $E = \left({E_{st}}^2 + {E_{sh}}^2\right)^{1/2}$ is the magnitude of total deformation, where $E_{st} = \frac{\partial u}{\partial x} - \frac{\partial v}{\partial y}$ and $E_{sh} = \frac{\partial v}{\partial x} + \frac{\partial u}{\partial y}$ are the stretching and shearing deformations, respectively. The angle $\beta = \delta - \alpha$ is defined as the difference between the angle of local orientation of the axis of dilatation, i.e., $\delta = \frac{1}{2}\arctan(E_{sh}/E_{st})$, and that of the isentrope, i.e., $\alpha = \arctan\left(-\frac{\partial\theta_e}{\partial x}/\frac{\partial\theta_e}{\partial y}\right)$.

A3. Curvature and shear components of geostrophic relative vorticity

The geostrophic shear vorticity ($\zeta_{g,sh}$) and curvature vorticity ($\zeta_{g,cur}$) are computed as (Bell and Keyser 1993)

$$\zeta_{g,sh} = \frac{1}{|\mathbf{V_g}|^2}\left[u_g v_g\left(\frac{\partial u_g}{\partial x} - \frac{\partial v_g}{\partial y}\right) + {v_g}^2\frac{\partial v_g}{\partial x} - {u_g}^2\frac{\partial u_g}{\partial y}\right], \tag{A3.1a}$$

$$\zeta_{g,cur} = \frac{1}{|\mathbf{V_g}|^2}\left[-u_g v_g\left(\frac{\partial u_g}{\partial x} - \frac{\partial v_g}{\partial y}\right) + {u_g}^2\frac{\partial v_g}{\partial x} - {v_g}^2\frac{\partial u_g}{\partial y}\right], \tag{A3.1b}$$

where $\mathbf{V_g} = u_g\mathbf{i} + v_g\mathbf{j}$ is the geostrophic wind evaluated at 38°N.

A4. Wave activity flux by stationary Rossby wave

To visualize the propagation of Rossby wave, the phase-independent wave activity flux defined by Takayha and Nakamura (2001) is computed. Only the horizontal component is considered and formulated in the spherical coordinate as

$$\mathbf{WAF} = \frac{\hat{p}cos\phi}{2\sqrt{\bar{U}^2+\bar{V}^2}}\left[\frac{\bar{U}}{a^2cos^2\phi}\left\{\left(\frac{\partial\psi'_g}{\partial\lambda}\right)^2 - {\psi'}_g\frac{\partial^2\psi'_g}{\partial\lambda^2}\right\} + \frac{\bar{V}}{a^2cos\phi}\left\{\frac{\partial\psi'_g}{\partial\lambda}\frac{\partial\psi'_g}{\partial\phi} - {\psi'}_g\frac{\partial^2\psi'_g}{\partial\lambda\partial\phi}\right\}\right]\mathbf{i} +$$
$$\frac{\hat{p}cos\phi}{2\sqrt{\bar{U}^2+\bar{V}^2}}\left[\frac{\bar{U}}{a^2cos\phi}\left\{\frac{\partial\psi'_g}{\partial\lambda}\frac{\partial\psi'_g}{\partial\phi} - {\psi'}_g\frac{\partial^2\psi'_g}{\partial\lambda\partial\phi}\right\} + \frac{\bar{V}}{a^2}\left\{\left(\frac{\partial\psi'_g}{\partial\phi}\right)^2 - {\psi'}_g\frac{\partial^2\psi'_g}{\partial\phi^2}\right\}\right]\mathbf{j}, \tag{A4.1}$$

where $\hat{p} = \frac{p}{1000\ \mathrm{hPa}}$ is the nondimensional pressure factor; $\bar{U}$ and $\bar{V}$ are the background (time-independent) wind in the zonal and meridional direction, respectively, ϕ and λ are the latitude and longitude, respectively; $\psi'_g = \Phi'/f$ is the perturbation geostrophic streamfunction where Φ' and f are the perturbation geopotential and Coriolis parameter, respectively. The phase speed term [see Eq. (38) therein] is omitted on the assumption of *stationary* Rossby wave. It is conventional to use climatology as the background and anomaly as the perturbation. Figure A4.1 exemplifies **WAF** at three different levels in the two subperiods of 2020 when multiple HREs occurred (P1 and P2; see chapter 6 for details).

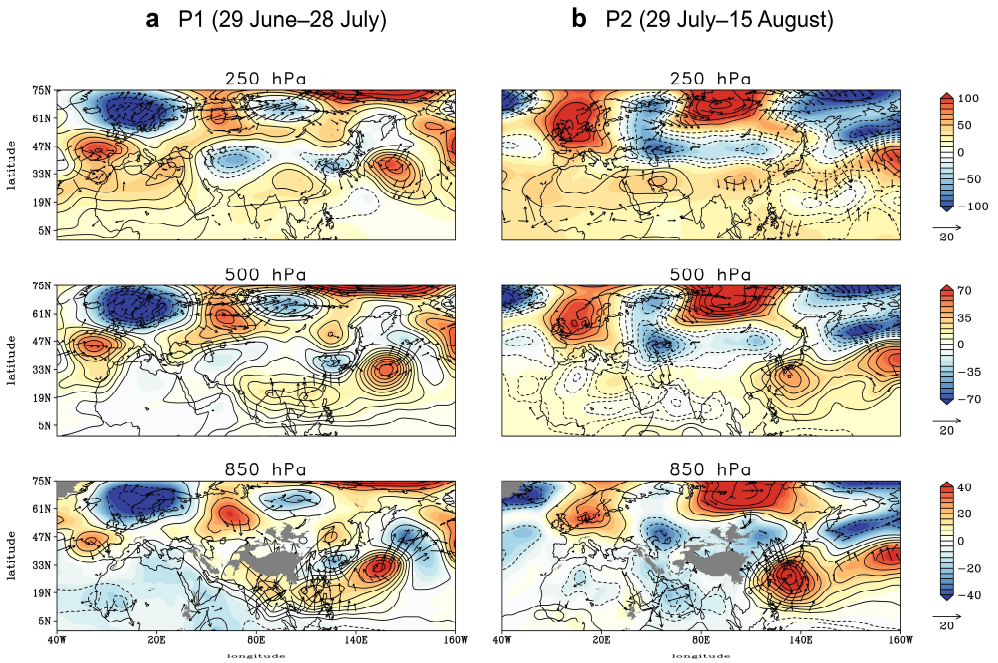

Figure A4.1. ψ anomaly (contours), GPH anomaly (shading) and **WAF** for stationary Rossby waves (vectors) at (top) 250 hPa, (middle) 500 hPa and (bottom) 850 hPa in **a** 29 June–28 July 2020 (P1) and **b** 29 July–15 August 2020 (P2). Contour intervals are 0.2×10^{-7}, 0.1×10^{-7} and 0.1×10^{-7} $m^2\ s^{-1}$ in the top, middle and bottom panels, respectively. For clarity, the vectors are shown only for values greater than 5 $m^2\ s^{-2}$ in magnitude. In the bottom panels, the topography higher than 1500 m is masked with gray shading.

Appendix B

B1. Q-vector-form QG omega equation

A key physical insight of the QG omega equation is that the *ageostrophic* vertical motion is required to keep the atmosphere *geostrophic* and *hydrostatic* (i.e., thermal wind balance) on the synoptic time scale by counteracting the balance-destroying geostrophic forcing. Although a generalized omega equation that considers the terms of higher-order Rossby number is available (Krishnamurti 1968; Pauley and Nieman 1992), the QG omega equation nicely explains the leading-order pattern of vertical motion associated with synoptic-scale circulation.

There are several alternative formulations of the QG omega equation [e.g., traditional formulation, Trenberth–Sutcliffe formulation, PV formulation and Q-vector formulation; see review by Davies (2015)]. In this dissertation, the Q-vector formulation is utilized owing to its usefulness in delineating the specific underlying dynamics behind vertical motion:

$$\left(\sigma_0\nabla^2 + f_0^2\frac{\partial^2}{\partial p^2}\right)\omega = -2\boldsymbol{\nabla}\cdot\mathbf{Q} + f_0\beta_0\frac{\partial v_g}{\partial p} - \frac{\kappa}{p}\nabla^2 J, \qquad \text{(B1.1)}$$

where $\nabla^2 = \frac{\partial^2}{\partial x^2} + \frac{\partial^2}{\partial y^2}$, $\boldsymbol{\nabla} = \frac{\partial}{\partial x}\mathbf{i} + \frac{\partial}{\partial y}\mathbf{j}$, and $\mathbf{i}$ and $\mathbf{j}$ are the unit vectors in the zonal and meridional directions, respectively. The three terms on the right-hand side are the dynamic, beta and diabatic forcings, respectively. The vertical motion by these all QG forcings is identical to the sum of vertical motion obtained with each QG forcing one by one because $\left(\sigma_0\nabla^2 + f_0^2\frac{\partial^2}{\partial p^2}\right)$ is the linear differential operator.

The static stability parameter $\sigma_0 = -\frac{1}{\rho_0}\frac{dln\theta_0}{dp}$ is computed using the area-averaged and event-averaged air density (ρ_0) and potential temperature (θ_0), which are functions of only pressure (p). The Coriolis parameter f_0 and its meridional gradient β_0 are evaluated at 38°N. The $\mathbf{Q}$ denotes the Q vector; v_g is the meridional geostrophic wind; κ is $\frac{R_d}{C_{pd}}$, where R_d and C_{pd} are the dry gas constant and the specific heat of dry air at constant pressure, respectively. The $J = C_{pd}\dot{T}_{Dia}$ is the diabatic heating rate per unit mass (unit: J s^{-1} kg^{-1}), where $\dot{T}_{Dia}$ is the diabatic

temperature tendency (unit: K s^{-1}). The $\dot{T}_{Dia}$ can be either directly retrieved from the ECMWF model (chapters 3 and 4) or indirectly estimated by computing the thermodynamic equation (chapter 5). The Q vector is expressed in the Cartesian coordinate as

$$\mathbf{Q} = Q_x\mathbf{i} + Q_y\mathbf{j},$$

$$Q_x = -\gamma\left(\frac{\partial \mathbf{V}_g}{\partial x}\cdot\boldsymbol{\nabla}\theta\right),\ Q_y = -\gamma\left(\frac{\partial \mathbf{V}_g}{\partial y}\cdot\boldsymbol{\nabla}\theta\right), \qquad \text{(B1.2)}$$

where the coefficient γ is $\frac{R_d}{p}\left(\frac{p}{p_s}\right)^{\kappa}$, and p_s =1000 hPa; $\mathbf{V}_g$ is the geostrophic wind vector calculated at 38°N; θ is the potential temperature. Before computing the dynamic and beta forcings, $\mathbf{V}_g$ and θ are smoothed at a T42 spectral resolution (~750-km resolution at 38°N) to remove mesoscale fluctuations violating the QG assumption. The $\dot{T}_{Dia}$ is also smoothed at a T128 spectral resolution (~246-km resolution at 38°N) before computing the diabatic forcing. Nevertheless, the essentially same inversion result is obtained when no smoothing is applied (figure not shown).

By virtue of the elliptic nature of Eq. (B1.1), the static stability parameter, σ_0, can influence the spatial spread of the inversed omega. Following the derivation of QG omega equation, σ_0 is set to be constant at each pressure level by compositing all HREs and taking the horizontal average over the inversion domain. Figure B1.1 shows the vertical profile of σ_0 for 318 non-TC HREs in chapter 3. The σ_0 is an order of 10^{-6} m^2 Pa^{-2} s^{-2} in the troposphere but rapidly increases in the stratosphere.

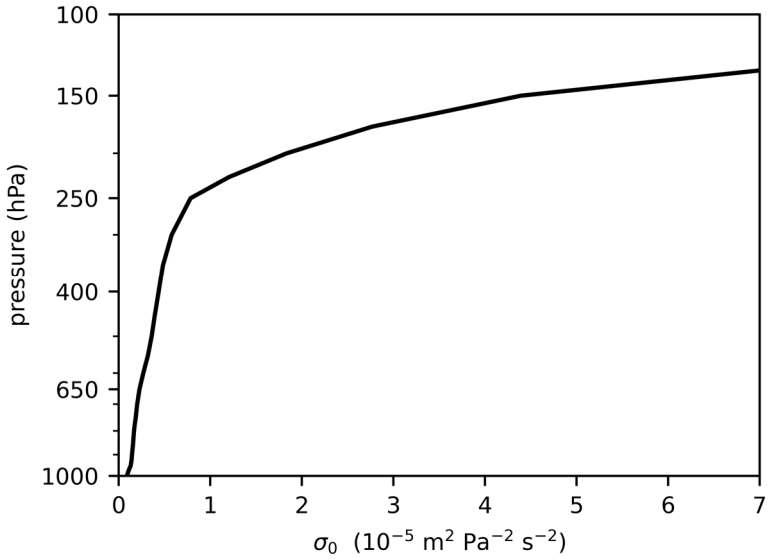

Figure B1.1. Vertical profile of σ_0 averaged for 318 non-TC HREs in chapter 3.

B2. Numerical details of the QG omega equation inversion

Since Eq. (B1.1) is the elliptic partial differential equation, it is numerically solvable if the coefficients of differential operators are positive (σ_0 and f_0^2 are always positive), and the boundary condition is properly given. The inversion begins with an introduction of a hyperbolic partial differential equation:

$$\frac{\partial \omega}{\partial t} = \left(\sigma_0 \nabla^2 + f_0^2 \frac{\partial^2}{\partial p^2}\right)\omega - \mu, \qquad \text{(B2.1)}$$

where μ is the QG forcings in Eq. (B1.1). With sufficient iterations, $\frac{\partial \omega}{\partial t}$ will approach 0, which assures that the solution of Eq. (B2.1) approaches the solution of Eq. (B1.1). There are several numerical schemes for iterative solving of Eq. (B2.1). In this dissertation, the successive overrelaxation (SOR) method is adopted as it allows us to obtain the converged solution with a few number of iterations. By applying the SOR method and the second-order finite difference to Eq. (B2.1), the numerically solved omega after the t-th iteration can be expressed as follows:

$$\omega_{i,j,k}^{t+1} = \omega_{i,j,k}^{t} + \tau\Delta t \left[\frac{\sigma_{0k}}{\Delta x^2}\left(\omega_{i+1,j,k}^{latest} - 2\omega_{i,j,k}^{latest} + \omega_{i-1,j,k}^{latest}\right) + \frac{\sigma_{0k}}{\Delta y^2}\left(\omega_{i,j+1,k}^{latest} - 2\omega_{i,j,k}^{latest} + \omega_{i,j-1,k}^{latest}\right) + \frac{f_0^2}{\Delta p^2}\left(\omega_{i,j,k+1}^{latest} - 2\omega_{i,j,k}^{latest} + \omega_{i,j,k-1}^{latest}\right) - \mu_{i,j,k}\right]. \qquad \text{(B2.2)}$$

The subscripts i, j and k denote the indices for longitude, latitude and pressure, respectively. The Δx, Δy (unit: m) and Δp (unit: Pa) are the grid intervals along the longitude, latitude and pressure, respectively.

The second term on the right-hand side of Eq. (B2.2) is the correction to a pre-defined solution with a weighing factor $\tau\Delta t$. The superscript "$latest$" is either t or $t+1$ depending on whether the given grid point has been updated already (the word "successive" refers to using the latest data to evaluate the correction). This depends on the order of loops for (i, j, k) and can be readily implemented in the algorithm by using an identical array for either $\omega_{i,j,k}^{t}$ or $\omega_{i,j,k}^{t+1}$[2]. The τ is a relaxation parameter ($\tau > 1$ for overrelaxation, $\tau < 1$ for underrelaxation). In this

[2]It may not work in parallel-computing architecture in which each grid point is updated independently.

dissertation, $\tau = 1.4$ is adopted. The Δt should be carefully determined depending on grid spacings. For numerical stability, the following inequality should be satisfied:

$$\frac{1}{\Delta t} \geq 2\left(\frac{\sigma_0}{\Delta x^2} + \frac{\sigma_0}{\Delta y^2} + \frac{f_0^2}{\Delta p^2}\right) \text{ where } \sigma_0, f_0^2 > 0. \quad \text{(B2.3)}$$

Here, Δt is set to be $\frac{1}{2}\left(\frac{\sigma_0}{\Delta x^2} + \frac{\sigma_0}{\Delta y^2} + \frac{f_0^2}{\Delta p^2}\right)^{-1}$. Note that Δt spatially varies unless Δx, Δy and Δp are all constant.

Equation (B2.2) is iterated at least 150 times for each event. To encompass the synoptic environment around the Korean Peninsula, the sufficiently wide horizontal domain is considered (110°–145°E & 28°–48°N in chapters 3 and 4, and 108°–152°E & 22°–50°N in chapter 5). However, the overall result is not much sensitive to the choice of the horizontal domain over which Eq. (B2.2) is solved (figure not shown). The vertical domain is set to 1000–100 hPa. Although this includes the lower stratosphere (see Fig. B1.1), it results in more accurate inversion results than those derived with only the tropospheric layer (figure not shown).

As boundary conditions, the homogeneous Dirichlet boundary condition $\omega = 0$ is applied in the lateral and vertical boundaries in chapters 3 and 4, which resembles the reanalyzed omega. However, in chapter 5, the vertical motion in the bottom level (1000 hPa) is non-zero. To consider the bottom boundary effect in QG omega budget, Eq. (B2.2) is additionally solved without any forcing (i.e., $\mu = 0$) but with the reanalyzed in the bottom boundary. The resulting vertical motion ω_{bf} can be linearly combined with other omega components ($\omega_{QG} = \omega_{Dyn} + \omega_{Beta} + \omega_{Dia} + \omega_{bf}$)[3].

[3]This is the typical procedure to obtain the general solution of the nonhomogeneous-form linear differential equation. Note that ω_{Dyn}, ω_{Beta} and ω_{Dia} correspond to particular solutions of Eq. B1.1 with $\omega = 0$ at all boundaries, while ω_{bf} corresponds to homogeneous solution of Eq. B1.1 with non-zero bottom boundary condition.

B3. Transverse and shearwise Q vectors

B3.1. Mathematical expression and key physical meanings

Because the Q-vector forcing is dry dynamic forcing, Eq. (B1.2) can be rewritten under the adiabatic and nondivergent condition as follows (Keyser et al. 1988, 1992; Bluestein 1993):

$$\mathbf{Q} = \gamma \frac{\mathrm{D_g}}{\mathrm{Dt}} \boldsymbol{\nabla}\theta \tag{B3.1}$$

where $\frac{\mathrm{D_g}}{\mathrm{Dt}} \equiv \frac{\partial}{\partial t} + \mathbf{V}_\mathrm{g} \cdot \boldsymbol{\nabla}$. By considering the orientation of $\mathbf{Q}$ with respect to $\boldsymbol{\nabla}\theta$, $\mathbf{Q}$ can be decomposed in a natural coordinate into the transverse ($Q_n\mathbf{n}$) and shearwise ($Q_s\mathbf{s}$) components:

$$Q_n\mathbf{n} = \left(\gamma \frac{\mathrm{D_g}}{\mathrm{Dt}} |\boldsymbol{\nabla}\theta|\right)\mathbf{n},\ Q_s\mathbf{s} = \left(\gamma \frac{\mathrm{D_g}}{\mathrm{Dt}} \boldsymbol{\nabla}\theta \cdot \mathbf{s}\right)\mathbf{s}. \tag{B3.2}$$

Here, $\mathbf{n} = \frac{\boldsymbol{\nabla}\theta}{|\boldsymbol{\nabla}\theta|}$ is the cross-isentropic unit vector pointing to the warm air, and $\mathbf{s} = \mathbf{k} \times \mathbf{n}$ is the along-isentropic unit vector with warm air to the right. The $Q_n\mathbf{n}$ and $Q_s\mathbf{s}$ are parallel and perpendicular, respectively, to $\boldsymbol{\nabla}\theta$. The $Q_n\mathbf{n}$ is generated when the geostrophic wind is confluent (or diffluent) toward the potential temperature gradient (Fig. 3.1a). As such, the $Q_n\mathbf{n}$ pointing to warm air is indicative of geostrophic frontogenesis. In contrast, $Q_s\mathbf{s}$ is generated when geostrophic wind rotates the isentropes (Figs. 3.1b,c). The $Q_s\mathbf{s}$ with warm air to the right is indicative of the cyclonic rotation of the isentropes. Figure B3.1 shows $Q_n\mathbf{n}$ and $Q_s\mathbf{s}$ overlaid with the potential temperature at 500 hPa for 318 non-TC HREs.

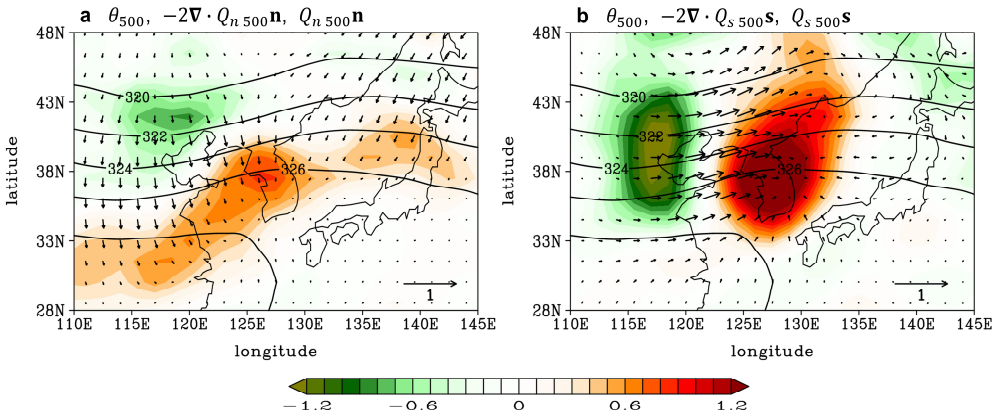

Figure B3.1. Composites of 318 non-TC HREs considered in chapter 3: **a** θ (K, contours), $Q_n\mathbf{n}$ (10^{-12} m^2 kg^{-1} s^{-1}, vectors) and $Q_n\mathbf{n}$ forcing (10^{-18} m kg^{-1} s^{-1}, shading) at 500 hPa in the mature stage of HREs (0 h). **b** As in **a** but for $Q_s\mathbf{s}$ and $Q_s\mathbf{s}$ forcing.

B3.2. Further physical meanings

The Q vector is the geostrophic version of the vector-generalized Petterssen's kinematic frontogenesis function (Keyser et al. 1998) expressed as

$$\mathbf{F} = \frac{\mathrm{D}}{\mathrm{Dt}}\boldsymbol{\nabla}\theta = F_n\mathbf{n} + F_s\mathbf{s}, \qquad \text{(B3.3a)}$$

$$F_n = -\frac{1}{2}|\boldsymbol{\nabla}\theta|(D - E\cos 2\beta),\ F_s = -\frac{1}{2}|\boldsymbol{\nabla}\theta|(\zeta - E\sin 2\beta). \qquad \text{(B3.3c,d)}$$

Here, $\frac{\mathrm{D}}{\mathrm{Dt}}$, D, E and β are identical to those in appendix A2, and ζ is the relative vorticity. By applying the QG approximation, the kinematic properties are replaced by their geostrophic counterparts, and $\frac{\mathrm{D}}{\mathrm{Dt}}$ is also replaced by $\frac{\mathrm{D_g}}{\mathrm{Dt}}$ so that Eq. (B3.3) becomes

$$\mathbf{Q} = \gamma\frac{\mathrm{D_g}}{\mathrm{Dt}}\boldsymbol{\nabla}\theta = Q_n\mathbf{n} + Q_s\mathbf{s}, \qquad \text{(B3.4a)}$$

$$\mathrm{Q}_n = \frac{\gamma}{2}|\boldsymbol{\nabla}\theta|E_g\cos 2\beta,\ \mathrm{Q}_s = \frac{\gamma}{2}|\boldsymbol{\nabla}\theta|\left(\zeta_g + E_g\sin 2\beta\right) \qquad \text{(B3.4c,d)}$$

with multiplication by γ (geostrophic wind is nondivergent in QG framework, i.e., $D_g = 0$). While the transverse Q vector is driven solely by the geostrophic deformation, the shearwise Q vector is induced by both the geostrophic relative vorticity and geostrophic deformation. Both Q-vector components are proportional

to the magnitude of the potential temperature gradient in the horizontal direction. Thus, Q vector magnitude is determined not only by the fluid kinematics but also by the local baroclinicity.

It is of note that Q_n is identical to the half of dry dynamic forcing in the Sawyer–Eliassen equation (Sawyer 1956; Eliassen 1962):

$$\left(\gamma\frac{\partial\theta}{\partial p}\right)\frac{\partial^2\varphi_M}{\partial y^2}+\left(-2f_0\frac{\partial M}{\partial p}\right)\frac{\partial^2\varphi_M}{\partial p\partial y}+\left(f_0\frac{\partial M}{\partial y}\right)\frac{\partial^2\varphi_M}{\partial p^2}=2Q_n+\frac{R_d}{pC_{pd}}\frac{\partial J}{\partial y}, \qquad \text{(B3.5)}$$

where φ_M is the two-dimensional streamfunction, and $M=u_g-f_0y$ is the absolute geostrophic momentum in the semigeostrophic system where y axis is set to be aligned with the cross-frontal direction (i.e., $\mathbf{n}$). By recalling Eq. (B3.4c), the transverse (i.e., cross-frontal or ageostrophic) secondary circulation is induced when the geostrophic wind has deformation along the baroclinic zone. For the Boussinesq expression of the Sawyer-Eliassen equation, see (9.15) in Holton (2004).

Meanwhile, the shearwise Q-vector forcing for vertical motion (i.e., $-2\boldsymbol{\nabla}\cdot Q_s\mathbf{s}$) can be alternatively expressed by using Eq. (B3.4d) after some vector manipulation and using the thermal wind balance (Martin 1999a):

$$-2\boldsymbol{\nabla}\cdot Q_s\mathbf{s}=f_0\frac{\partial\mathbf{v}_g}{\partial p}\cdot\boldsymbol{\nabla}\left(\zeta_g+E_g\sin2\beta\right). \qquad \text{(B3.6)}$$

Equation (B3.6) states that the shearwise Q-vector forcing is identical to the advection of the geostrophic vorticity and geostrophic deformation by thermal wind. According to Martin (1999b), it is generally well approximated to the advection of the geostrophic vorticity by thermal wind ($-2\boldsymbol{\nabla}\cdot Q_s\mathbf{s}\approx f_0\frac{\partial\mathbf{v}_g}{\partial p}\boldsymbol{\nabla}\cdot\zeta_g$) for the synoptic-scale vertical motion. Such approximation also holds for the composite of 318 non-TC HREs in chapter 3 (figure not shown). Note that $f_0\frac{\partial\mathbf{v}_g}{\partial p}\boldsymbol{\nabla}\cdot\zeta_g$ was previously discussed by Sutcliffe (1947) as a key factor for the development and propagation of midlatitude cyclones. It is also closely related to the forcing in the Trenberth (1978)'s approximated QG omega equation:

$$\left(\sigma_0\nabla^2+f_0^2\frac{\partial^2}{\partial p^2}\right)\omega\approx f_0\frac{\partial\mathbf{v}_g}{\partial p}\cdot\boldsymbol{\nabla}\left(2\zeta_g+f\right). \qquad \text{(B3.7)}$$

B3.3. Cartesian expression

By considering the geometric relation between isentropes and Q vectors, the zonal and meridional components of the transverse and shearwise Q vectors can be derived. First, let Q_x and Q_y be the sum of their transverse and shearwise components as

$$Q_x = Q_{n,x} + Q_{s,x}, \tag{B3.8a}$$

$$Q_y = Q_{n,y} + Q_{s,y} \tag{B3.8b}.$$

From the parallelism of $Q_n\mathbf{n}$ and the perpendicularity of $Q_s\mathbf{s}$ to $\nabla\theta$, the following relations hold:

$$Q_{n,x}\frac{\partial\theta}{\partial y} - Q_{n,y}\frac{\partial\theta}{\partial x} = 0, \tag{B3.8c}$$

$$Q_{s,x}\frac{\partial\theta}{\partial x} + Q_{s,y}\frac{\partial\theta}{\partial y} = 0. \tag{B3.8d}$$

Given that Q_x and Q_y are directly computed from Eq. (B1.2), $Q_{n,x}$, $Q_{n,y}$, $Q_{s,x}$ and $Q_{s,y}$ can be determined by solving Eqs. (B3.8a–d) as follows:

$$Q_{n,x} = \frac{1}{|\nabla\theta|^2}\left\{Q_x\left(\frac{\partial\theta}{\partial x}\right)^2 + Q_y\left(\frac{\partial\theta}{\partial x}\right)\left(\frac{\partial\theta}{\partial y}\right)\right\}, \tag{B3.9a}$$

$$Q_{n,y} = \frac{1}{|\nabla\theta|^2}\left\{Q_x\left(\frac{\partial\theta}{\partial x}\right)\left(\frac{\partial\theta}{\partial y}\right) + Q_y\left(\frac{\partial\theta}{\partial y}\right)^2\right\}, \tag{B3.9b}$$

$$Q_{s,x} = \frac{1}{|\nabla\theta|^2}\left\{-Q_y\left(\frac{\partial\theta}{\partial x}\right)\left(\frac{\partial\theta}{\partial y}\right) + Q_x\left(\frac{\partial\theta}{\partial y}\right)^2\right\}, \tag{B3.9c}$$

$$Q_{s,y} = \frac{1}{|\nabla\theta|^2}\left\{Q_y\left(\frac{\partial\theta}{\partial x}\right)^2 - Q_x\left(\frac{\partial\theta}{\partial x}\right)\left(\frac{\partial\theta}{\partial y}\right)\right\} \tag{B3.9d}$$

Note that the total Q vector and the sum of its two components are numerically identical to each other when the second-order centered difference is used. It should be also noted that Q-vector divergence in the natural coordinate is mathematically identical to that in the Cartesian coordinate since the divergence is a Galilean-invariant property.

Appendix C

C1. SOM algorithm

C1.1. Overview

The SOM algorithm is a type of artificial neural network that reduces high-dimensional data into a manageable low-dimensional (mostly, two-dimensional) array of nodes based on the Euclidean distance through iterative training (Kohonen 1998, 2013). It accommodates nonlinearities within the dataset with no forced orthogonality between clusters, which contrasts with principal component analysis and empirical orthogonal function (Reusch et al. 2005; Liu et al. 2006; Rousi et al. 2015). As based on unsupervised learning, the SOM does not require any prior knowledge of the expected results, allowing a more reliable and objective summary of the data. The most important feature of SOM distinct from other clustering algorithms (e.g., k-means cluster) is that it represents the continuum of data by placing similar nodes nearby. This "self-organizing" nature of SOM enables a more physical interpretation of the clustering result. As such, the SOM has been widely used in weather classification and climate research (Liu and Weisberg 2011; Sheridan and Lee 2011; Gibson et al. 2017).

C1.2. Topology and arrangement of nodes

Several parameters should be pre-specified in the SOM algorithm. Among others, the node arrangement is the most crucial one. The topology of nodes (i.e., map lattice) determines the connectivity of each node on the map. The node can be either rectangular or hexagonal (Fig. C1.1). Due to the self-organizing nature of SOM, the clustering result with rectangular nodes is different from that with hexagonal nodes although other parameters are the same. If one is interested in the visually illustrative summary of data, the hexagonal node is recommended. If the classification of data is of interest, however, the rectangular node is desirable owing to its less complexity.

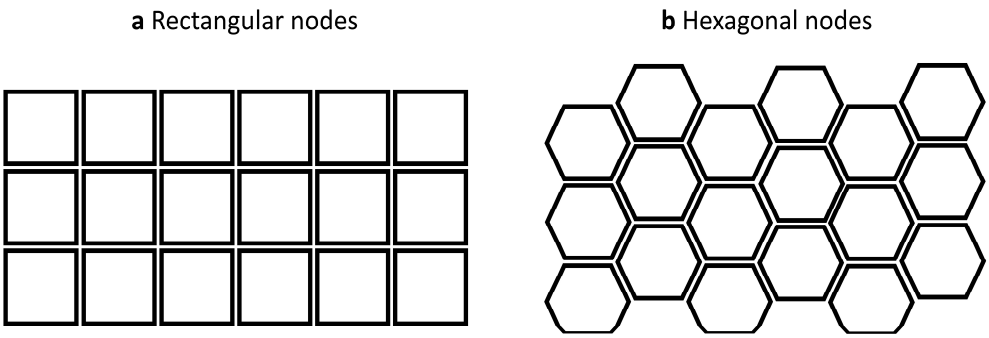

Figure C1.1. a Rectangular nodes and **b** hexagonal nodes in 3×6 array.

The shape of the map determines how nodes are organized on the map. There are several options including sheet, cylinder, and toroid maps (Fig. C1.2). In the sheet map, the number of neighborhoods at the edges of map is smaller than its maximum. This can be remedied by using the cylinder or toroid shape in which the nodes are cyclic in one or two dimensions., but those options result in a more complex clustering result. For simplicity, the sheet map with rectangular nodes is widely considered (also in this dissertation).

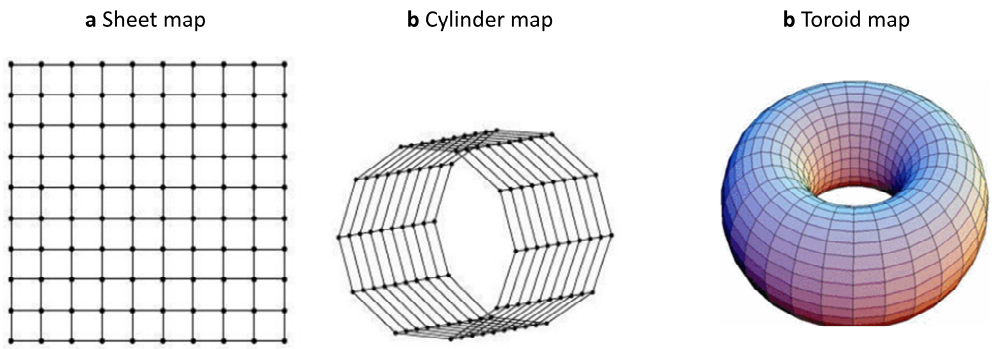

Figure C1.2. Examples of **a** sheep map, **b** cylinder map and **c** toroid map with rectangular nodes. **a** and **b** are taken from Wang et al. (2007). **c** is taken from Miljković (2017).

Perhaps, determining the number of nodes is most crucial in SOM clustering analysis. In general, applying excessive nodes causes fewer input data to be sorted into each node, leading to a loss of generality. In contrast, adopting too few nodes results in severe overfitting of the input data with less accuracy. To ascertain

the optimal node arrangement, statistical methods have been considered in climate sciences (e.g., Johnson 2013; Rousi et al. 2015; Liu et al. 2016). However, a trial-and-error approach after seeing the quality of the first-guess result has also been popularly adopted to obtain more interpretable and physically meaningful clustering result (e.g., Nigro and Cassano 2014; Ohba et al. 2015; Jung et al. 2019). In this dissertation, the optimal number of nodes is chosen based on multiple sensitivity tests with varying sizes of nodes (see sections 4.2.2 and 5.3.3).

C1.3. Iterative training procedure

The SOM performs a nonlinear iterative training to project each input data $\mathbf{X}_i$ onto the pre-defined array of M nodes. The i is an index of input data ($1 \leq i \leq N$ where N is the number of input data). Each node on the map also has its reference vector $\mathbf{W}_j$ with the same dimension as $\mathbf{X}_i$ where j is an index of node ($1 \leq j \leq M$). Before training, the reference vector is initialized randomly or linearly. In the random initialization, the reference vectors are initialized with random values within the input data. In the linear initialization, the reference vectors are initialized using the two leading eigenvectors obtained by applying principle component analysis to the input data. The latter is beneficial in terms of reproducibility and computational efficiency (it requires fewer iterations for a converged result).

The node whose reference vector is closest to a given input data is called the best matching unit (BMU) or winning node. The BMU of $\mathbf{X}_i$ is determined based on the Euclidian distance

$$\mathbf{W}_c = \mathbf{W}_j(t) \text{ for } \min\|\mathbf{X}_i - \mathbf{W}\|, \qquad \text{(C1.1)}$$

where c is an index of BMU, and t is the iteration step. During the training, the BMU and its neighboring nodes are updated so that the nodes are arranged in a topologically ordered way. There are two training methods: "sequential" and "batch". When the input data $\mathbf{X}_i$ is given, the sequential training updates the reference vector of node j as

$$\mathbf{W}_j(t+1) = \mathbf{W}_j(n) + \alpha(t)h_{cj}(t)\left[\mathbf{X}_i - \mathbf{W}_j(t)\right], \qquad \text{(C1.2)}$$

where $\alpha(t)$ is the learning rate monotonically decreasing with t, and $h_{cj}(t)$ denotes the neighborhood function defined for the BMU of $\mathbf{X}_i$ (i.e., $\mathbf{W}_c$) and the node j.

In contrast, batch training is expressed as

$$\mathbf{W}_j(t+1) = \frac{\sum_{i=1}^{N} h_{cj}(t)\mathbf{X}_i}{\sum_{i=1}^{N} h_{cj}(t)}. \quad \text{(C1.3)}$$

This is still an implicit expression since c depends on $\mathbf{X}_i$ and $\mathbf{W}_j(t)$ (Kohonen 2013). Instead, Eq. (C1.3) can be equivalently rewritten as

$$\mathbf{W}_j(t+1) = \frac{\sum_{k=1}^{M} n_k h_{kj}(t)\mathbf{P}_k}{\sum_{k=1}^{M} n_k h_{kj}(t)}, \quad \text{(C1.4)}$$

where $\mathbf{P}_k$ is the mean of n_k input data whose BMU is $\mathbf{W}_k$, and h_{kj} is the neighboring function defined for the nodes k and j. Unlike sequential training, the learning rate $\alpha(t)$ is no longer necessary. Besides, all input data are simultaneously used at each iteration step to update reference vectors. This allows batch training to obtain a converged result faster than sequential training.

The neighborhood function dictates the connectivity between neighboring nodes on the map (i.e., self-organized feature). There are several neighborhood functions (e.g., bubble, Gaussian, cut-Gaussian and Epanechnikov types). Among others, the Epanechnikov function least smooths the nodes, preserving their detailed structure (Liu et al. 2006). Between the nodes c and j on the map, the Epanechnikov-type neighborhood function is defined as:

$$h_{cj}(t) = \max\{0, 1 - [\sigma(t) - \|\mathbf{r}_i - \mathbf{r}_c\|]^2\}, \quad \text{(C1.5)}$$

where $\sigma(t)$ is the neighborhood radius either constant or decreasing with t, and $\mathbf{r}_i$ and $\mathbf{r}_c$ denote the location vectors of nodes i and j, respectively, on the map. Two training phases can be considered by setting $\sigma(t)$ [and learning rate $\alpha(t)$ for the sequential training] to be large in the rough-training phase and to be small in the fine-tuning phase.

Appendix D

D1. PV tendency equation

The PV tendency equation is formulated in the isobaric surface as:

$$\frac{\partial P}{\partial t} = -\mathbf{V}\cdot\nabla P - \omega\frac{\partial P}{\partial p} - g\left[(\zeta+f)\frac{\partial \dot{\theta}_{Dia}}{\partial p} + \frac{\partial \dot{\theta}_{Dia}}{\partial y}\frac{\partial u}{\partial p} - \frac{\partial \dot{\theta}_{Dia}}{\partial x}\frac{\partial v}{\partial p}\right], \qquad \text{(D1.1)}$$

where $P = -g(\zeta+f)\frac{\partial \theta}{\partial p} - g\left(\frac{\partial \theta}{\partial y}\frac{\partial u}{\partial p} - \frac{\partial \theta}{\partial x}\frac{\partial v}{\partial p}\right)$ is Ertel's PV (Ertel 1942) defined in the pressure coordinate. The P is directly retrieved from the reanalysis dataset; $\mathbf{V} = u\mathbf{i} + v\mathbf{j}$, $\nabla = \frac{\partial}{\partial x}\mathbf{i} + \frac{\partial}{\partial y}\mathbf{j}$, and $\mathbf{i}$ and $\mathbf{j}$ are the unit vectors in the zonal and meridional directions, respectively; ζ is the vertical component of relative vorticity; f is the planetary vorticity; g is the gravitational acceleration; $\dot{\theta}_{Dia} = \dot{T}_{Dia}(p_s/p)^{\kappa}$ is the diabatic tendency of potential temperature, where p_s and κ is 1000 hPa and R_d/C_{pd}, respectively; R_d and C_{pd} are the gas constant and the specific heat at constant pressure, respectively, of dry air. The other symbols follow the convention in meteorology.

Before computing each budget term, each variable in Eq. (D1.1) is smoothed at a T42 spectral resolution (~750-km resolution at 38°N) to remove the synoptically unimportant features. If the spatial smoothing is not applied, the small patches emerge in the composite PV budget fields emerge (figure not shown), but the overall results do not change. The first-order forward scheme and the second-order centered scheme are used in time and spatial differentiations, respectively.

REFERENCES

Agel, L., M. Barlow, F. Colby, H. Binder, J. L. Catto, A. Hoell, and J. Cohen, 2019: Dynamical analysis of extreme precipitation in the US northeast based on large-scale meteorological patterns. *Climate Dyn.*, **52**, 1739–1760, https://doi.org/10.1007/s00382-018-4223-2.

Araki, K., T. Kato, Y. Hirockawa, and W. Hashiko, 2021: Characteristics of atmospheric environments of quasi-stationary convective bands in Kyushu, Japan during the July 2020 heavy rainfall event. *SOLA*, **17**, 8–15, https://doi.org/10.2151/sola.2021-002.

Archambault, H. M., L. F. Bosart, D. Keyser, and J. M. Cordeira, 2013: A climatological analysis of the extratropical flow response to recurving western North Pacific tropical cyclones. *Mon. Wea. Rev.*, **141**, 2325–2346, https://doi.org/10.1175/MWR-D-12-00257.1.

——, D. Keyser, L. F. Bosart, C. A. Davis, and J. M. Cordeira, 2015: A composite perspective of the extratropical flow response to recurving western North Pacific tropical cyclones. *Mon. Wea. Rev.*, **143**, 1122–1141, https://doi.org/10.1175/MWR-D-14-00270.1.

Atallah, E. H., and L. F. Bosart, 2003: The extratropical transition and precipitation distribution of Hurricane Floyd (1999). *Mon. Wea. Rev.*, **131**, 1063–1081, https://doi.org/10.1175/1520-0493(2003)131<1063:TETAPD>2.0.CO;2.

——, and ——, and A. R. Aiyyer, 2007: Precipitation distribution associated with landfalling tropical cyclones over the eastern United States. *Mon. Wea. Rev.*, **135**, 2185–2206, https://doi.org/10.1175/MWR3382.1.

Baek, E.-H., J.-H. Kim, J.-S. Kug, and G.-H. Lim, 2015: Midtropospheric frontogenesis associated with antecedent indirect precipitation ahead of tropical cyclones over the Korean Peninsula. *Tellus*, **67A**, 27476, https://doi.org/10.3402/tellusa.v67.27476.

Bell, G. D., and D. Keyser, 1993: Shear and curvature vorticity and potential-vorticity interchanges: Interpretation and application to a cutoff cyclone event. *Mon. Wea. Rev.*, **121**, 76–102, https://doi.org/10.1175/1520-0493(1993)121<0076:SACVAP>2.0.CO;2.

Bluestein, H. B., 1993: *Synoptic–Dynamic Meteorology in Midlatitudes*. Vol. 2. Oxford University Press, 594 pp.

Bowley, K. A., J. R. Gyakum, and E. H. Atallah, 2019: A new perspective toward cataloging Northern Hemisphere Rossby wave breaking on the dynamical tropopause. *Mon. Wea. Rev.*, **147**, 409–431, https://doi.org/10.1175/MWR-D-18-0131.1.

Browning, K. A., 1990: Organization of clouds and precipitation in extratropical cyclones. *Extratropical Cyclones: The Erik Palmén Memorial Volume*, C. W. Newton and E. O. Holopainen, Eds., Amer. Meteor. Soc., 129–153.

Byun, K.-Y., and T.-Y. Lee, 2012: Remote effects of tropical cyclones on heavy rainfall over the Korean Peninsula—Statistical and composite analysis. *Tellus*, **64A**, 14983, https://doi.org/10.3402/tellusa.v64i0.14983.

Cha, D.-H., and Coauthors, 2016: Future changes in summer precipitation in regional climate simulations over the Korean Peninsula forced by multi-RCP scenarios of HadGEM2-AO. *Asia-Pac. J. Atmos. Sci.*, **52**, 139–149, https://doi.org/10.1007/s13143-016-0015-y.

Chen, T.-C., S.-Y. Wang, W.-R. Huang, and M.-C. Yen, 2004: Variation of the East Asian summer monsoon rainfall. *J. Climate*, **17**, 744–762, https://doi.org/10.1175/1520-0442(2004)017%3C0744:VOTEAS%3E2.0.CO;2.

Cho, H.-O., S.-W. Son, and D.-S. Park, 2018: Springtime extratropical cyclones in Northeast Asia and their impacts on long-term precipitation trends. *Int. J. Climatol.*, **38**, 4043–4050, https://doi.org/10.1002/joc.5543.

Cho, W., J. Park, J. Moon, D.-H. Cha, Y.-M. Moon, H.-S. Kim, K.-J. Noh, and S.-H. Park, 2022: Effects of topography and sea surface temperature anomalies on heavy rainfall induced by Typhoon Chaba in 2016. *Geosci. Lett.*, **9**, 1–18, https://doi.org/10.1186/s40562-022-00230-1.

Choi, S.-J., D.-H. Cha, and D.-K. Lee, 2008: Simulation of the 18-day summer heavy rainfall over East Asia using a regional climate model. *J. Geophys. Res. Atmos.*, **113**, D12101, https://doi.org/10.1029/2007JD009213.

Choi, Y., K.-S. Yun, K.-J. Ha, K.-Y. Kim, S.-J. Yoon, and J. C. L. Chan, 2013: Effects of asymmetric SST distribution on straight-moving Typhoon Ewiniar (2006) and recurving Typhoon (2003). *Mon. Wea. Rev.*, **141**, 3950–3967, https://doi.org/10.1175/MWR-D-12-00207.1.

Chowdary, J. S., K. Hu, G. Srinivas, Y. Kosaka, L. Wang, and K. K. Rao, 2019: The Eurasian jet streams as conduits for East Asian monsoon variability. *Curr. Climate Change Rep.*, **5**, 233–244, https://doi.org/10.1007/s40641-019-00134-x.

Davies, H. C., 2015: The quasigeostrophic omega equation: Reappraisal, refinements, and relevance. *Mon. Wea. Rev.*, **143**, 3–25, https://doi.org/10.1175/MWR-D-14-00098.1.

Dee, D. P., and Coauthors, 2011: The ERA-Interim reanalysis: Configuration and performance of the data assimilation system. *Quart. J. Roy. Meteor. Soc.*, **137**, 553–597, https://doi.org/10.1002/qj.828.

Ding, Q., and B. Wang, 2005: Circumglobal teleconnection in the Northern Hemisphere summer. *J. Climate*, **18**, 3483–3505, https://doi.org/10.1175/JCLI3473.1.

Doswell, C. A., III, H. E. Brooks, and R. A. Maddox, 1996: Flash flood forecasting: An ingredients-based methodology. *Wea. Forecasting*, **11**, 560–581, https://doi.org/10.1175/1520-0434(1996)011,0560:FFFAIB.2.0.CO;2.

Du, Y., S.-P. Xie, G. Huang, and K. M. Hu, 2009: Role of air–sea interaction in the long persistence of El Niño–induced north Indian Ocean warming. *J. Climate*, **22**, 2023–2038, https://doi.org/10.1175/2008JCLI2590.1.

Eliassen, A., 1962: On the vertical circulation in frontal zones. *Geofys. Publ.*, **24**, 147–160.

Ertel, H., 1942: Ein neuer hydrodynamischer Erhaltungssatz. *Naturwissenschaften*, **30**, 543–544, https://doi.org/10.1007/BF01475602.

Evans, C., and R. E. Hart, 2008: Analysis of the wind field evolution associated with the extratropical transition of Bonnie (1998). *Mon. Wea. Rev.*, **136**, 2047–2065, https://doi.org/10.1175/2007MWR2051.1.

——, and Coauthors, 2017: The extratropical transition of tropical cyclones. Part I: Cyclone evolution and direct impacts. *Mon. Wea. Rev.*, **145**, 4317–4344, https://doi.org/10.1175/MWR-D-17-0027.1.

Fink, A. H., S. Pohle, J. G. Pinto, and P. Knippertz, 2012: Diagnosing the influence of diabatic processes on the explosive deepening of extratropical cyclones. *Geophys. Res. Lett.*, **39**, L07803, https://doi.org/10.1029/2012GL051025.

Finocchio, P. M., and J. D. Doyle, 2019: How the speed and latitude of the jet stream affect the downstream response to recurving tropical cyclones. *Mon. Wea. Rev.*, **147**, 3261–3281, https://doi.org/10.1175/MWR-D-19-0049.1.

Galarneau, T. J., L. F. Bosart, and R. S. Schumacher, 2010: Predecessor rain events ahead of tropical cyclones. *Mon. Wea. Rev.*, **138**, 3272–3297, https://doi.org/10.1175/2010MWR3243.1.

Gill, A. E., 1980: Some simple solutions for heat-induced tropical circulation. *Quart. J. Roy. Meteor. Soc.*, **106**, 447–462, https://doi.org/10.1002/qj.49710644905.

Grams, C. M., and H. M. Archambault, 2016: The key role of diabatic outflow in amplifying the midlatitude flow: A representative case study of weather systems surrounding western North Pacific extratropical transition. *Mon. Wea. Rev.*, **144**, 3847–3869, https://doi.org/10.1175/MWR-D-15-0419.1.

——, S. C. Jones, C. A. Davis, P. A. Harr, and M. Weissmann, 2013a: The impact of Typhoon Jangmi (2008) on the mid-latitude flow. Part I: Upper-level ridgebuilding and modification of the jet. *Quart. J. Roy. Meteor. Soc.*, **139**, 2148–2164, https://doi.org/10.1002/qj.2091.

——, ——, and ——, 2013b: The impact of Typhoon Jangmi (2008) on the midlatitude flow. Part II: Downstream evolution. *Quart. J. Roy. Meteor. Soc.*, **139**, 2165–2180, https://doi.org/10.1002/qj.2119.

Gibson, P. B., S. E. Perkins-Kirkpatrick, P. Uotila, A. S. Pepler, and L. V. Alexander, 2017: On the use of self-organizing maps for studying climate extremes. *J. Geophys. Res. Atmos.*, **122**, 3891–3903, https://doi.org/10.1002/2016JD026256.

Guo, L., N. P. Klingaman, P. L. Vidale, A. G. Turner, M. Demory, and A. Cobb, 2017: Contribution of tropical cyclones to atmospheric moisture transport and rainfall over East Asia. *J. Climate*, **30**, 3853–3865, https://doi.org/10.1175/JCLI-D-16-0308.1.

Folland, C. K., J. Knight, H. W. Linderholm, D. Fereday, S. Ineson, and J. W. Hurrell, 2009: The summer North Atlantic Oscillation: Past, present, and future. *J. Climate*, **22**, 1082–1103, https://doi.org/10.1175/2008JCLI2459.1.

Hamada, A., and Y. N. Takayabu, 2018: Large-scale environmental conditions related to midsummer extreme rainfall events around Japan in the TRMM region. *J. Climate*, **31**, 6933–6945, https://doi.org/10.1175/JCLI-D-17-0632.1.

Harr, P. A., and J. M. Dea, 2009: Downstream development associated with the extratropical transition of tropical cyclones over the Western North Pacific. *Mon. Wea. Rev.*, **137**, 1295–1319, https://doi.org/10.1175/2008MWR2558.1.

——, and R. L. Elsberry, 2000: Extratropical transition of tropical cyclones over the western North Pacific. Part I: Evolution of structural characteristics during the transition process. *Mon. Wea. Rev.*, **128**, 2613–2633, https://doi.org/10.1175/1520-0493(2000)128,2613:ETOTCO.2.0.CO;2.

Hart, R. E., 2003: A cyclone phase space derived from thermal wind and thermal asymmetry. *Mon. Wea. Rev.*, **131**, 585–616, https://doi.org/10.1175/1520-0493(2003)131<0585:ACPSDF>2.0.CO;2.

——, J. L. Evans, and C. Evans, 2006: Synoptic composites of the extratropical transition life cycle of North Atlantic tropical cyclones: Factors determining posttransition evolution. *Mon. Wea. Rev.*, **134**, 553–578, https://doi.org/10.1175/MWR3082.1.

Hersbach, H., and Coauthors, 2020: The ERA5 global reanalysis. *Q. J. R. Meteorol. Soc.*, **146**, 999–2049. https://doi.org/10.1002/qj.3803.

Holton, J. R., 2004: *An Introduction to Dynamic Meteorology*. 4th ed. Academic Press, 535 pp.

Hong, S.-Y., 2004: Comparison of heavy rainfall mechanisms in Korea and the central US. *J. Meteor. Soc. Japan*, **82**, 1469–1479, https://doi.org/10.2151/jmsj.2004.1469.

——, and J.-W. Lee, 2009: Assessment of the WRF model in reproducing a flash-flood heavy rainfall event over Korea. *Atmos. Res.*, **93**, 818–831, https://doi.org/10.1016/j.atmosres.2009.03.015.

Hong, X., and R. Lu, 2016: The meridional displacement of the summer Asian jet, Silk Road pattern, and tropical SST anomalies. *J. Climate*, **29**, 3753–3766, https://doi.org/10.1175/JCLI-D-15-0541.1.

Horinouchi, T., 2014: Influence of upper tropospheric disturbances on the synoptic variability of precipitation and moisture transport over summertime East Asia and the northwestern Pacific. *J. Meteor. Soc. Japan*, **92**, 519–541, https://doi.org/10.2151/jmsj.2014-602.

——, and A. Hayashi, 2017: Meandering subtropical jet and precipitation over summertime East Asia and the northwestern Pacific. *J. Atmos. Sci.*, **74**, 1233–1247, https://doi.org/10.1175/JAS-D-16-0252.1.

——, Y. Kosaka, H. Nakamigawa, H. Nakamura, N. Fujikawa, and Y. N. Takayabu, 2021: Moisture supply, jet, and Silk-Road wave train associated with the prolonged heavy rainfall in Kyushu, Japan in early July 2020. *SOLA*, **17B**, 1–8, https://doi.org/10.2151/sola.2021-019.

Hoskins, B. J., and M. A. Pedder, 1980: The diagnosis of middle latitude synoptic development. *Quart. J. Roy. Meteor. Soc.*, **106**, 707–719, https://doi.org/10.1002/qj.49710645004.

——, I. Draghici, and H. C. Davies, 1978: A new look at the ω-equation. *Quart. J. Roy. Meteor. Soc.*, **104**, 31–38, https://doi.org/10.1002/qj.49710443903.

Imada, Y., H. Kawase, M. Watanabe, M. Arai, H. Shiogama, and I. Takayabu, 2020: Advanced risk-based event attribution for heavy regional rainfall events. *npj Climate Atmos. Sci.*, **3**, 37, https://doi.org/10.1038/s41612-020-00141-y.

Iwao, K., and M. Takahashi, 2008: A precipitation seesaw mode between northeast Asia and Siberia in summer caused by Rossby waves over the Eurasian continent. *J. Climate*, **21**, 2401–2419, https://doi.org/10.1175/2007JCLI1949.1.

Jeong, J.-H., D.-I. Lee, and C.-C. Wang, 2016: Impact of the cold pool on mesoscale convective system-produced extreme rainfall over southeastern South Korea: 7 July 2009. *Mon. Wea. Rev.*, **144**, 3985–4006, https://doi.org/10.1175/MWR-D-16-0131.1.

Jo, E., C. Park, S.-W. Son, J.-W. Roh, G.-W. Lee, and Y.-H. Lee, 2020: Classification of localized heavy rainfall events in South Korea. *Asia-Pac. J. Atmos. Sci.*, **56**,77–88, https://doi.org/10.1007/s13143-019-00128-7.

Johnson, N. C., 2013: How many ENSO flavors can we distinguish? *J. Climate*, **26**, 4816–4827, https://doi.org/10.1175/JCLI-D-12-00649.1.

Jung, I.-W., D.-H. Bae, and G. Kim, 2011: Recent trends of mean and extreme precipitation in Korea. *Int. J. Climatol.*, **31**, 359– 370, https://doi.org/10.1002/joc.2068

Jung, M.-I., S.-W. Son, H.-C. Kim, S.-W. Kim, and R. J. Park, 2019: Contrasting synoptic weather patterns between non-dust high particulate matter events and Asian dust events in Seoul, South Korea. *Atmos. Environ.*, **214**, 116864, https://doi.org/10.1016/j.atmosenv.2019.116864.

Kang, J. M., J. Lee, S.-W. Son, J. Kim, and D. Chen, 2020: The rapid intensification of East Asian cyclones around the Korean Peninsula and their surface impacts. *J. Geophys. Res. Atmos.*, **125**, e2019JD031632, https://doi.org/10.1029/2019JD031632.

Kang, Y., J.-H. Jeong, and D.-I. Lee, 2021: Influence of sea surface temperature on a mesoscale convective system producing extreme rainfall over the Yellow Sea. *Mon. Wea. Rev.*, **149**, 2613–2632, https://doi.org/10.1175/MWR-D-20-0335.1.

Kawasaki, K., Y. Tachibana, T. Nakamura, and K. Yamazaki, 2021: Role of the cold Okhotsk Sea on the climate of the North Pacific subtropical high and baiu precipitation. *J. Climate*, **34**, 495–507, https://doi.org/10.1175/JCLI-D-20-0432.1.

Keller, J. H., 2017: Amplification of the downstream wave train during extratropical transition: Sensitivity studies. *Mon. Wea. Rev.*, **145**, 1529–1548, https://doi.org/10.1175/MWR-D-16-0193.1.

——, and Coauthors, 2019: The extratropical transition of tropical cyclones. Part II: Interaction with the midlatitude flow, downstream impacts, and implications in predictability. *Mon. Wea. Rev.*, **147**, 1077–1106, https://doi.org/10.1175/MWR-D-17-0329.1.

Keyser, D., M. J. Reeder, and R. J. Reed, 1988: A generalization of Petterssen's frontogenesis function and its relation to the forcing of vertical motion. *Mon. Wea. Rev.*, **116**, 762–781, https://doi.org/10.1175/1520-0493(1988)116<0762:AGOPFF>2.0.CO;2.

——, B. D. Schmidt, and D. G. Duffy, 1992: Quasigeostrophic vertical motions diagnosed from along- and cross-isentrope components of the Q vector. *Mon. Wea. Rev.*, **120**, 731–741, https://doi.org/10.1175/1520-0493(1992)120<0731:QVMDFA>2.0.CO;2.

Kim, D., C.-H. Ho, D.-S. R. Park, and J. Kim, 2019: Influence of vertical wind shear on wind and rainfall areas of tropical cyclones making landfall over South

Korea. *PLoS ONE*, **14**, e0209885, https://doi.org/10.1371/journal.pone.0209885.

Kim, G., and Coauthors, 2018: Future changes in extreme precipitation indices over Korea. *Int. J. Climatol.*, **38**, e862–e874, https://doi.org/10.1002/joc.5414.

Kim, S., and J.-S. Kug, 2021: Delayed impact of Indian Ocean warming on the East Asian surface temperature variation in boreal summer. *J. Climate*, **34**, 3255–3270, https://doi.org/10.1175/JCLI-D-20-0691.1.

Kitabatake, N., 2011: Climatology of extratropical transition of tropical cyclones in the western North Pacific defined by using cyclone phase space. *J. Meteor. Soc. Japan*, **89**, 309 – 325, https://doi.org/10.2151/jmsj.2011-402.

Klein, P. M., P. A. Harr, and R. L. Elsberry, 2000: Extratropical transition of western North Pacific tropical cyclones: An overview and conceptual model of the transformation stage. *Wea. Forecasting*, **15**, 373–395, https://doi.org/10.1175/1520-0434(2000)015<0373:ETOWNP>2.0.CO;2.

Kobayashi, S., and Coauthors, 2015: The JRA-55 Reanalysis: General specifications and basic characteristics. *J. Meteor. Soc. Japan*, **93**, 5–48, https://doi.org/10.2151/jmsj.2015-001.

KMA, 2011: *Typhoon White Book (in Korean)*. Korea Meteorological Administration, 342 pp., http://www.kma.go.kr/download_01/typhoon/typwhitebook_2011.pdf.

——, 2021: Abnormal Climate Report 2020 (in Korean). KMA, 212 pp., http://www.climate.go.kr/home/bbs/view.php?code=93&bname=abnormal&vcode=6494.

Kodama, Y., 1992: Large-scale common features of subtropical precipitation zones (the Baiu frontal zone, the SPCZ, and the SACS) Part I: Characteristics of subtropical frontal zones. *J. Meteor. Soc. Japan*, **70**, 813–836, https://doi.org/10.2151/jmsj1965.70.4_813.

Kohonen, T., 1998: The self-organizing map. *Neurocomputing*, **21**, 1–6, https://doi.org/10.1016/S0925-2312(98)00030-7.

——, 2013: Essentials of the self-organizing map. *Neural Networks*, **37**, 52–65, https://doi.org/10.1016/j.neunet.2012.09.018.

Komaromi, W. A., and J. D. Doyle, 2018: On the dynamics of tropical cyclone and trough interactions. *J. Atmos. Sci.*, **75**, 2687–2709, https://doi.org/10.1175/JAS-D-17-0272.1.

Kosaka, Y., and H. Nakamura, 2006: Structure and dynamics of the summertime Pacific–Japan teleconnection pattern. *Quart. J. Roy. Meteor. Soc.*, **132**, 2009–2030, https://doi.org/10.1256/qj.05.204.

——, S.-P. Xie, and H. Nakamura, 2011: Dynamics of interannual variability in summer precipitation over East Asia. *J. Climate*, **24**, 5435–5453, https://doi.org/10.1175/2011JCLI4099.1.

Krishnamurti, T. N., 1968: A diagnostic balance model for studies of weather systems of low and high latitudes, Rossby number less than 1. *Mon. Wea. Rev.*, **96**, 197–207, https://doi.org/10.1175/1520-0493(1968)096<0197:ADBMFS>2.0.CO;2.

Kubota, H., Y. Kosaka, and S.-P. Xie, 2016: A 117-year long index of the Pacific–Japan pattern with application to interdecadal variability. *Int. J. Climatol.*, **36**, 1575–1589, https://doi.org/10.1002/joc.4441.

Kwon, Y., C. Park, S.-Y. Back, S.-W. Son, J. Kim, and E. J. Cha, 2022: Influence of atmospheric rivers on regional precipitation in South Korea (in Korean with English abstract). *Atmosphere*, **29**, 343–353, https://doi.org/10.14191/Atmos.2019.29.4.343.

Lee, D., S.-K. Min, I.-H. Park, J.-B. Ahn, D.-H. Cha, E.-C. Chang, and Y.-H. Byun, 2022: Enhanced role of convection in future hourly rainfall extremes over South Korea. *Geophys. Res. Lett.*, **49**, e2022GL099727. https://doi.org/10.1029/2022GL099727.

Lee, D.-K., H.-R. Kim, and S.-Y. Hong, 1998: Heavy rainfall over Korea during 1980-1990. *J. Korean Meteor. Soc.*, **1**, 32–50.

——, J.-G. Park, and J.-W. Kim, 2008a: Heavy rainfall events lasting 19 days from July 31 to August 17, 1998, over Korea. *J. Meteor. Soc. Japan*, **86**, 313–333, https://doi.org/10.2151/jmsj.86.313.

——, J.-C. Ha, and J. Kim, 2008b: Application of the Sawyer–Eliassen equation to the interpretation of the synoptic-scale dynamics of a heavy rainfall case over East Asia. Asia-Pac. *J. Atmos. Sci.*, **44**, 49–68.

——, and S.-J. Choi, 2010: Observation and numerical prediction of torrential rainfall over Korea caused by Typhoon Rusa (2002). *J. Geophys. Res. Atmos.*, **115**, D12105, https://doi.org/10.1029/2009JD012581.

Lee, J., S.-W. Son, H.-O. Cho, J. Kim, D.-H. Cha, J. R. Gyakum, and D. Chen, 2020: Extratropical cyclones over East Asia: Climatology, seasonal cycle, and long-term trend. *Climate Dyn.*, **54**, 1131–1144, https://doi.org/10.1007/s00382-019-05048-w.

Lee, J. Y., B. Wang, M. C. Wheeler, X. Fu, D. E. Waliser, and I.-S. Kang, 2013: Real-time multivariate indices for the boreal summer intraseasonal oscillation over the Asian summer monsoon region. *Climate Dyn.*, **40**, 493–509, https://doi.org/10.1007/s00382-012-1544-4.

——, and Coauthors, 2017: The long-term variability of Changma in the East Asian summer monsoon system: A review and revisit. *Asia-Pac. J. Atmos. Sci.*, **53**, 257–272, https://doi.org/10.1007/s13143-017-0032-5.

Lee, T.-Y., and Y.-H. Kim, 2007: Heavy precipitation systems over the Korean Peninsula and their classification. *Asia-Pac. J. Atmos. Sci.*, **11**, 367–396.

Li, J., and Coauthors, 2021: Effect of horizontal resolution on the simulation of tropical cyclones in the Chinese Academy of Sciences FGOALS-fs climate system model. *Geosci. Model Dev.*, **14**, 6113–6133, https://doi.org/10.5194/gmd-14-6113-2021.

Li, J., and C. Ruan, 2018: The North Atlantic–Eurasian teleconnection in summer and its effects on Eurasian climates. *Environ. Res. Lett.*, **13**, 024007, https://doi.org/10.1088/1748-9326/aa9d33.

Liebmann, B., and C. A. Smith, 1996: Description of a complete (interpolated) outgoing longwave radiation dataset. *Bull. Amer. Meteor. Soc.*, **77**, 1275–1277.

Liu, B., C. Zhu, J. Su, and S. Ma, 2019: Record-breaking northward shift of the western North Pacific subtropical high in July 2018. *J. Meteor. Soc. Japan*, **97**, 913–925, https://doi.org/10.2151/jmsj.2019-047.

——, Y. Yan, C. Zhu, S. Ma, and J. Li, 2020: Record-breaking Meiyu rainfall around Yangtze River in 2020 regulated by the subseasonal phase transition of North Atlantic Oscillation. *Geophys. Res. Lett.*, **47**, e2020GL090342, https://doi.org/10.1029/2020GL090342.

Liu, W., L. Wang, D. Chen, K. Tu, C. Ruan, and Z. Hu, 2016: Large-scale circulation classification and its links to observed precipitation in the eastern and central Tibetan Plateau. *Climate Dyn.*, **46**, 3481–3497, https://doi.org/10.1007/s00382-015-2782-z.

Liu, Y., and R. H. Weisberg, 2011: A review of self-organizing map applications in meteorology and oceanography. *Self-OrganizingMaps: Applications and Novel Algorithm Design*, J.I.Mwasiagi, Ed., InTech, 253–272.

——, ——, and C. N. K. Mooers, 2006: Performance evaluation of the self-organizing map for feature extraction. *J. Geophys. Res. Oceans*, **111**, C05018, https://doi.org/10.1029/2005JC003117.

Martin, J. E., 1999a: Quasigeostrophic forcing of ascent in the occluded sector of cyclones and the trowal airstream. *Mon. Wea. Rev.*, **127**, 70–88, https://doi.org/10.1175/1520-0493(1999)127,0070:QFOAIT.2.0.CO;2.

——, 1999b: The separate roles of geostrophic vorticity and deformation in the midlatitude occlusion process. *Mon. Wea. Rev.*, **127**, 2404–2418, https://doi.org/10.1175/1520-0493(1999)127,2404:TSROGV.2.0.CO;2.

——, 2014: Quasi-geostrophic diagnosis of the influence of vorticity advection on the development of upper level jet-front systems. *Quart. J. Roy. Meteor. Soc.*, **140**, 2658–2671, https://doi.org/10.1002/qj.2333.

Martius, O., C. Schwierz, and H. C. Davies, 2010: Tropopause-level waveguides. *J. Atmos. Sci.*, **67**, 866–879, https://doi.org/10.1175/2009JAS2995.1.

Matsumoto, S., K. Ninomiya, K., and S. Yoshizumi, 1971: Characteristics features of "Baiu" front associated with heavy rainfall. *J. Meteor. Soc. Japan*, **49**, 267–281, https://doi.org/10.2151/jmsj1965.49.4_267.

Miljković, D., 2017: Brief review of self-organizing maps. *40th International Convention on Information and Communication Technology, Electronics and Microelectronics (MIPRO)*, 1061–1066, https://doi.org/10.23919/MIPRO.2017.7973581.

Milrad, S. M., E. H. Atallah, and J. R. Gyakum, 2009: Dynamical and precipitation structures of poleward-moving tropical cyclones in eastern Canada, 1979–2005. *Mon. Wea. Rev.*, **137**, 836–851, https://doi.org/10.1175/2008MWR2578.1.

Moore, B. J., L. F. Bosart, D. Keyser, and M. L. Jurewicz, 2013: Synoptic-scale environments of predecessor rain events occurring east of the Rocky Mountains in association with Atlantic basin tropical cyclones. *Mon. Wea. Rev.*, **141**, 1022–1047, https://doi.org/10.1175/MWR-D-12-00178.1.

Nakamura, H., and T. Fukamachi, 2004: Evolution and dynamics of summertime blocking over the Far East and the associated surface Okhotsk high. *Quart. J. Roy. Meteor. Soc.*, **130**, 1213–1233, https://doi.org/10.1256/qj.03.101.

Nam, C. C., D.-S. R. Park, C.-H. Ho, and D. Chen, 2018: Dependency of tropical cyclone risk on track in South Korea. *Nat. Hazards Earth Syst. Sci.*, **18**, 3225–3234, https://doi.org/10.5194/nhess-18-3225-2018.

Nguyen-Le, D., T. J. Yamada, and D. Tran-Anh, 2017: Classification and forecast of heavy rainfall in northern Kyushu during Baiu season using weather pattern recognition. *Atmos. Sci. Lett.*, **18**, 324–329, https://doi.org/10.1002/asl.759.

Nie, J., and A. H. Sobel, 2016: Modeling the interaction between quasigeostrophic vertical motion and convection in a single column. *J. Atmos. Sci.*, **73**, 1101–1117, https://doi.org/10.1175/JAS-D-15-0205.1.

Nigro, M. A., and J. J. Cassano, 2014: Identification of surface wind patterns over the Ross Ice Shelf, Antarctica, using self-organizing map. *Mon. Wea. Rev.*, **142**, 2361–2378, https://doi.org/10.1175/MWR-D-13-00382.1.

Ninomiya, K., 1984: Characteristics of Baiu front as a predominant subtropical front in the summer Northern Hemisphere. *J. Meteor. Soc. Japan*, **62**, 880–894, https://doi.org/10.2151/jmsj1965.62.6_880.

——, and Y. Shibagaki, 2007: Multi-scale features of the Meiyu-Baiu front and associated precipitation systems. *J. Meteor. Soc. Japan*, **85B**, 103–122, https://doi.org/10.2151/jmsj.85B.103.

Nitta, T., 1987: Convective activities in the tropical western Pacific and their impact on the Northern Hemisphere summer circulation. *J. Meteor. Soc. Japan*, **65**, 373–390, https://doi.org/10.2151/jmsj1965.65.3_373.

Noh, E., J. Kim, S.-Y. Jun, D.-H. Cha, M.-S. Park, J.-H. Kim, and H.-G. Kim, 2021: The role of the Pacific–Japan pattern in extreme heatwaves over Korea and Japan. *Geophys. Res. Lett.*, **48**, e2021GL093990, https://doi.org/10.1029/2021GL093990.

Ohba, M., S. Kadokura, Y. Yoshida, D. Nohara, and Y. Toyoda, 2015: Anomalous weather patterns in relation to heavy precipitation events in Japan during the baiu season. *J. Hydrometeor.*, **16**, 688–701, https://doi.org/10.1175/JHM-D-14-0124.1.

Orsolini, Y. J., L. Zhang, D. H. W. Peters, K. Fraedrich, X. Zhu, A. Schneidereit, and B. van den Hurk, 2015: Extreme precipitation events over north China in August 2010 and their link to eastward-propagating wave-trains across Eurasia: Observations and monthly forecasting. *Quart. J. Roy. Meteor. Soc.*, **141**, 3097–3105, https://doi.org/10.1002/qj.2594.

Osborne, J. M., M. Collins, J. A. Screen, S. I. Thomson, and N. Dunstone, 2020: The North Atlantic as a driver of summer atmospheric circulation. *J. Climate*, **33**,7335–7351, https://doi.org/10.1175/JCLI-D-19-0423.1.

Park, C., S.-W. Son, and H. Kim, 2021a: Distinct features of atmospheric rivers in the early versus late East Asian summer monsoon and their impacts on monsoon rainfall. *J. Geophys. Res. Atmos.*, **126**, e2020JD033537, https://doi.org/10.1029/2020JD033537.

——, ——, J. Kim, E.-C. Chang, J.-H. Kim, E. Jo, D.-H. Cha, and S. Jeong, 2021b: Diverse synoptic weather patterns of warm-season heavy rainfall events in South Korea. *Mon. Wea. Rev.*, **149**, 3875–3893, https://doi.org/10.1175/MWR-D-20-0388.1.

——, ——, and J.-H. Kim, 2021c: Role of baroclinic trough in triggering vertical motion during summertime heavy rainfall events in Korea. *J. Atmos. Sci.,* **78**, 1687–1702, https://doi.org/10.1175/JAS-D-20-0216.1.

——, ——, and Coauthors, 2021d: Record-breaking summer rainfall in South Korea in 2020: Synoptic characteristics and the role of large-scale circulations. *Mon. Wea. Rev.*, **149**, 3085–3100, https://doi.org/10.1175/MWR-D-21-0051.1.

Park, H., B. R. Lintner, W. R. Boos, and K. Seo, 2015: The effect of midlatitude transient eddies on monsoonal southerlies over eastern China. *J. Climate*, **28**, 8450–8465, https://doi.org/10.1175/JCLI-D-15-0133.1.

Park, S. K., and E. Lee, 2007: Synoptic features of orographically enhanced heavy rainfall on the east coast of Korea associated with Typhoon Rusa (2002). *Geophys. Res. Lett.*, **34**, L02803, https://doi.org/10.1029/2006GL028592.

Pauley, P. M., and S. J. Nieman, 1992: A comparison of quasigeostrophic and nonquasigeostrophic vertical motions for a model-simulated rapidly intensifying marine extratropical cyclone. *Mon. Wea. Rev.*, **120**, https://doi.org/10.1175/1520-0493(1992)120<1108:ACOQAN>2.0.CO;2.

Petterssen, S., 1936: *Contribution to the Theory of Frontogenesis*. Vol. 11, Cammermeyer, 27 pp.

——, and S. J. Smebye, 1971: On the development of extratropical cyclones. *Quart. J. Roy. Meteor. Soc.*, **97**, 457–482, https://doi.org/10.1002/qj.4970974140.

Powell, M. D., 1982: The transition of the hurricane Frederic boundary-layer wind field from the open gulf of Mexico to landfall. *Mon. Wea. Rev.*, **110**, 1912–1932, https://doi.org/10.1175/1520-0493(1982)110<1912:TTOTHF>2.0.CO;2.

Quinting, J. F., and S. C. Jones, 2016: On the impact of tropical cyclones on Rossby wave packets: A climatological perspective. *Mon. Wea. Rev.*, **144**, 2021–2048, https://doi.org/10.1175/MWR-D-14-00298.1.

Ren, X., D. Yang, and X. Yang, 2015: Characteristics and mechanisms of the subseasonal eastward extension of the South Asian high. *J. Climate*, **28**, 6799–6822, https://doi.org/10.1175/JCLI-D-14-00682.1.

Reusch, D. B., R. B. Aley, and B. C. Hewitson, 2005: Relative performance of self-organizing maps and principal component analysis in pattern extraction from synthetic climatological data. *Polar Geogr.*, **29**, 188–212, https://doi.org/10.1080/789610199.

Riboldi, J., C. M. Grams, M. Riemer, and H. M. Archambault, 2019: A phase locking perspective on Rossby wave amplification and atmospheric blocking downstream of recurving western North Pacific tropical cyclones. *Mon. Wea. Rev.*, **147**, 567–589, https://doi.org/10.1175/MWR-D-18-0271.1.

Riemer, M., S. C. Jones, and C. A. Davis, 2008: The impact of extratropical transition on the downstream flow: An idealized modeling study with a straight jet. *Quart. J. Roy. Meteor. Soc.*, **134**, 69– 91, https://doi.org/10.1002/qj.189.

——, and ——, 2010: The downstream impact of tropical cyclones on a developing baroclinic wave in idealized scenarios of extratropical transition. *Quart. J. Roy. Meteor. Soc.*, **136**, 617–637, https://doi.org/10.1002/qj.605.

——, and ——, 2014: Interaction of a tropical cyclone with a high-amplitude, midlatitude wave pattern: Waviness analysis, trough deformation and track bifurcation. *Quart. J. Roy. Meteor. Soc.*, **140**, 1362–1376, https://doi.org/10.1002/qj.2221.

Rousi, E., C. Anagnostopoulou, K. Tolika, and P. Maheras, 2015: Representing teleconnection patterns over Europe: A comparison of SOM and PCA methods. *Atmos. Res.*, **152**, 123–137, https://doi.org/10.1016/j.atmosres.2013.11.010.

Ritchie, E. A., and R. L. Elsberry, 2003: Simulations of the extratropical transition of tropical cyclones: Contributions by the midlatitude upper-level trough to reintensification. *Mon. Wea. Rev.*, **131**, 2112–2128, https://doi.org/10.1175/1520-0493(2003)131<2112:SOTETO>2.0.CO;2.

——, and ——, 2007: Simulations of the extratropical transition of tropical cyclones: Phasing between the upper-level trough and tropical cyclone. *Mon. Wea. Rev.*, **135**, 862–876, https://doi.org/10.1175/MWR3303.1.

Sawyer, J. S., 1956: The vertical circulation at meteorological fronts and its relation to frontogenesis. *Proc. Roy. Soc. London*, **234A**, 346–362, https://doi.org/10.1098/rspa.1956.0039.

Schumacher, R. S., and R. H. Johnson, 2008: Mesoscale processes contributing to extreme rainfall in a midlatitude warm-season flash flood. *Mon. Wea. Rev.*, **136**, 3964–3986, https://doi.org/10.1175/2008MWR2471.1.

Seo, K.-H., J.-H. Son, and J.-Y. Lee, 2011: A new look at Changma (in Korean with English abstract). *Atmosphere*, **21**, 109–121, https://doi.org/10.14191/Atmos.2011.21.1.109.

——, ——, S.-E. Lee, T. Tomita, and H.-S. Park, 2012: Mechanisms of an extraordinary East Asian summer monsoon event in July 2011. *Geophys. Res. Lett.*, **39**, L05704, https://doi.org/10.1029/2011GL050378.

——, ——, J.-Y. Lee, and H.-S. Park, 2015: Northern East Asian monsoon precipitation revealed by airmass variability and its prediction. *J. Climate*, **28**, 6221–6233, https://doi.org/10.1175/JCLI-D-14-00526.1.

Sheridan, S. C., and C. C. Lee, 2011: The self-organizing map in synoptic climatological research. *Prog. Phys. Geogr.*, **35**, 109– 119, https://doi.org/10.1177/0309133310397582.

Shin, C.-S., and T.-Y. Lee, 2005: Development mechanisms for the heavy rainfalls of 6–7 August 2002 over the middle of the Korean Peninsula. *J. Meteor. Soc. Japan*, **83**, 683–709, https://doi.org/10.2151/jmsj.83.683.

Shin, U., and T.-Y. Lee, 2015: Origin, evolution and structure of meso-α-scale lows associated with cloud clusters and heavy rainfall over the Korean peninsula.

Asia-Pac. J. Atmos. Sci., **51**, 259–274, https://doi.org/10.1007/s13143-015-0076-3.

——, ——, and S.-H. Park, 2019: Environment and processes for heavy rainfall in the early morning over the Korean Peninsula during episodes of cloud clusters associated with mesoscale troughs. *J. Meteor. Soc. Japan*, **97**, 633–655, https://doi.org/10.2151/jmsj.2019-036.

Sohn, B. J., G.-H. Ryu, H.-J. Song, and M.-L. Oh, 2013: Characteristic features of warm-type rain producing heavy rainfall over the Korean Peninsula inferred from TRMM measurements. *Mon. Wea. Rev.*, **141**, 3873–3888, https://doi.org/10.1175/MWR-D-13-00075.1.

Song, H.-J., and B.-J. Sohn, 2015: Two heavy rainfall types over the Korean Peninsula in the humid East Asian summer environment: A satellite observation study. *Mon. Wea. Rev.*, **143**, 363–382, https://doi.org/10.1175/MWR-D-14-00184.1.

Stuecker, M. F., A. Timmermann, F.-F. Jin, S. McGregor, and H.-L. Ren, 2013: A combination mode of the annual cycle and the El Niño/Southern Oscillation. *Nat. Geosci.*, **6**, 540–544, https://doi.org/10.1038/ngeo1826.

——, F.-F. Jin, A. Timmermann, and S. McGregor, 2015: Combination mode dynamics of the anomalous Northwest Pacific anticyclone. *J. Climate*, **28**, 1093–1111, https://doi.org/10.1175/JCLI-D-14-00225.1.

Sutcliffe, R. C., 1947: A contribution to the problem of development. *Quart. J. Roy. Meteor. Soc.*, **73**, 370–383, https://doi.org/10.1002/qj.49707331710.

Sun, J., and T.-Y. Lee, 2002: A numerical study of an intense quasi-stationary convection band over the Korean Peninsula. *J. Meteor. Soc. Japan*, **80**, 1221–1245, https://doi.org/10.2151/jmsj.80.1221.

Takaya, K., and H. Nakamura, 2001: A formulation of a phase-independent wave-activity flux for stationary and migratory quasigeostrophic eddies on a zonally varying basic flow. *J. Atmos. Sci.*, **58**, 608–627, https://doi.org/10.1175/1520-0469(2001)058,0608:AFOAPI.2.0.CO;2.

Takaya, Y., I. Ishikawa, C. Kobayashi, H. Endo, and T. Ose, 2020: Enhanced meiyu–baiu rainfall in early summer 2020: Aftermath of the 2019 super IOD event. *Geophys. Res. Lett.*, **47**, e2020GL090671, https://doi.org/10.1029/2020GL090671.

Tomita, T., T. Yamaura, and T. Hashimoto, 2011: Interannual variability of the Baiu season near Japan evaluated from the equivalent potential temperature. *J. Meteor. Soc. Japan*, **89**, 517–537, https://doi.org/10.2151/jmsj.2011-507.

Torn, R. D., and G. J. Hakim, 2015: Comparison of wave packets associated with extratropical transition and winter cyclones. *Mon. Wea. Rev.*, **143**, 1782–1803, https://doi.org/10.1175/MWR-D-14-00006.1.

Trenberth, K. E., 1978: Interpretation of the diagnostic quasi-geostrophic omega equation. *Mon. Wea. Rev.*, **106**, 131–137, https://doi.org/10.1175/1520-0493(1978)106<0131:OTIOTD>2.0.CO;2.

Tziperman, E., M. A. Cane, S. E. Zebiak, Y. Xue, and B. Blumenthal, 1998: Locking of El Niño's peak time to the end of the calendar year in the delayed oscillator picture of ENSO. *J. Climate*, **11**, 2191–2199, https://doi.org/10.1175/1520-0442(1998)011,2191:LOENOS.2.0.CO;2.

Uccellini, L. W., and D. R. Johnson, 1979: The coupling of upper and lower tropospheric jet streaks and implications for the development of severe convective storms. *Mon. Wea. Rev.,* **107**, 682–703, https://doi.org/10.1175/1520-0493(1979)107,0682:TCOUAL.2.0.CO;2.

Wang, B., and LinHo, 2002: Rainy season of the Asian–Pacific summer monsoon. *J. Climate*, **15**, 386–398, https://doi.org/10.1175/1520-0442(2002)015,0386:RSOTAP.2.0.CO;2.

Wang, L., E. Ambikairajah, and E. H.C. Choi, 2007: Multi-layer Kohonen self-organizing feature map for Language identification. *Proc. Interspeech 2007*, 174–177, doi:10.21437/Interspeech.2007-73.

Wirth, V., M. Riemer, E. K. M. Chang, and O. Martius, 2018: Rossby wave packets on the midlatitude waveguide—A review. *Mon. Wea. Rev.*, **146**, 1965–2001, https://doi.org/10.1175/MWR-D-16-0483.1.

Wu, Z., B. Wang, J. Li, and F.-F. Jin, 2009: An empirical seasonal prediction model of the East Asian summer monsoon using ENSO and NAO. *J. Geophys. Res. Atmos.*, **114**, D18120, https://doi.org/10.1029/2009JD011733.

Xie, S.-P., H. Annamalai, F. A. Schott, and J. P. McCreary, 2002: Structure and mechanisms of South Indian Ocean climate variability. *J. Climate*, **15**, 864–878, https://doi.org/10.1175/1520-0442(2002)015,0864:SAMOSI.2.0.CO;2.

——, K. Hu, J. Hafner, H. Tokinaga, Y. Du, G. Huang, and T. Sampe, 2009: Indian Ocean capacitor effect on Indo-western Pacific climate during the summer following El Niño. *J. Climate*, **22**, 730–747, https://doi.org/10.1175/2008JCLI2544.1.

——, Y. Kosaka, Y. Du, K. Hu, J. S. Chowdary, and G. Huang, 2016: Indo-western Pacific Ocean capacitor and coherent climate anomalies in post-ENSO summer: A review. *Adv. Atmos. Sci.*, **33**, 411–432, https://doi.org/10.1007/s00376-015-5192-6.

Xu, P., L. Wang, and W. Chen, 2019: The British–Baikal Corridor: A teleconnection pattern along the summertime polar front jet over Eurasia. *J. Climate*, **32**, 877–896, https://doi.org/10.1175/JCLI-D-18-0343.1.

Yamaura, T., and T. Tomita, 2011: Spatiotemporal differences in the interannual variability of Baiu frontal activity in June. *Int. J. Climatol.*, **31**, 57–71, https://doi.org/10.1002/joc.2058.

Yin, J. H., and D. S. Battisti, 2004: Why do baroclinic waves tilts poleward with height? *J. Atmos. Sci.*, **61**, 1454–1460, https://doi.org/10.1175/1520-0469(2004)061,1454:WDBWTP.2.0.CO;2.

Yokoyama, C., Y. N. Takayabu, and T. Horinouchi, 2017: Precipitation characteristics over East Asia in early summer: Effects of the subtropical jet and lower tropospheric convective instability. *J.Climate*, **30**, 8127–8147, https://doi.org/10.1175/JCLI-D-16-0724.1.

——, H. Tsuji, and Y. N. Takayabu, 2020: The effects of an upper-tropospheric trough on the heavy rainfall event in July 2018 over Japan. *J. Meteor. Soc. Japan*, **98**, 235–255, https://doi.org/10.2151/jmsj.2020-013.

Yuan, Z. P., X. Y. Zhuge, and Y. Wang, 2020: The forced secondary circulation of the Mei-yu front. *Adv. Atmos. Sci.*, **37**, 766–780, https://doi.org/10.1007/s00376-020-9177-8.

Zhang, W., Z. Huang, F. Jiang, M. F. Stuecker, G. Chen, and F.-F. Jin, 2021: Exceptionally persistent Madden-Julian Oscillation activity contributes to the extreme 2020 East Asian summer monsoon rainfall. *J. Geophys. Res. Atmos.*, **48**, e2020GL091588, https://doi.org/10.1029/2020GL091588.

Zhao, Y., and Coauthors, 2019: The large-scale circulation patterns responsible for extreme precipitation over the North China plain in midsummer. *J. Geophys. Res. Atmos.*, **124**, 12794–12809, https://doi.org/10.1029/2019JD030583.

——, C. Park, and S.-W. Son, 2023: Importance of diabatic heating for the eastward-moving heavy rainfall events along the Yangtze River, China. *J. Atmos. Sci.*, **80**, 151–165, https://doi.org/10.1175/JAS-D-21-0321.1.

Zhou, Z.-Q., S.-P. Xie, and R. Zhang, 2021: Historic Yangtze flooding of 2020 tied to extreme Indian Ocean conditions. *Proc. Natl. Acad. Sci. USA*, **118**, e2022255118, https://doi.org/10.1073/pnas.2022255118.

국문초록

여름철 집중호우는 해마다 발생하는 가장 빈번한 자연재해이나 그간의 국내 연구들은 주로 사례 연구나 정성정 분석에 집중되어 있어 관련 메커니즘에 대한 완전한 이해는 담보되지 않은 상태이다. 본 논문에서는 최근 40 년 동안 발생한 모든 여름철 집중호우 사례들을 활용하여 집중호우의 종관기상학적 특성을 정성적, 정량적으로 상세분석하였다. 기상청 호우주의보 기준인 12 시간 누적강수량 110 mm 로 정의된 집중호우 사례들을 태풍에 의해 발생한 사례(TC-HREs; 전체의 약 18.9%)와 태풍과 직접적으로 연관되지 않은 사례(HREs; 전체이 약 81.1%)로 구분하고, 합성장 및 통계적 분석을 통해 각각의 기후학적 특성을 먼저 도출하였다. 이를 기반으로 HREs 와 TC-HREs 의 종관 및 역학적 특징을 아래와 같이 더욱 상세화하였다.

HREs 의 경우, 집중호우 발생 전부터 상층 요란이 유의미하게 풍상측에 나타났으며 이는 시간에 따라 조직화된 상층골로 발달하는 것으로 확인되었다. 준지균 오메가 방정식의 수치적 해를 통해 집중호우의 발달기에는 역학적 강제력과 비단열적 강제력이 상승운동에 비슷한 정도의 역할을 하지만 집중호우 최성기가 되면 연직운동은 비단열 강제력에 지배되는 것으로 나타났다. 이는 집중호우가 역학적 강제력에 의해 촉발되고 이어 역학적-비단열적 되먹임 통해 빠르게 발달함을 암시한다. Q 벡터의 자연좌표계에서의 물리적 분해를 통해 역학적 강제력은 특히 하층 저기압과 경압불안정을 통해 발달하는 상층 골에 의해 지배되는 것으로 확인되었는데, 이는 선행연구에서 강조되어온 상층제트 입구에서 발생하는 이차순환의 역할이 다소 과장되었음을 의미한다.

집중호우 연직운동의 준지균적 진단은 대부분의 사례에 적용될 수 있으나, 집중호우는 조직화된 저기압의 위치/유무, 북태평양 고기압의 위치/강도 등의 차이 등에 따라 다양한 지상 일기 패턴하에서 발생할 수 있다. 이러한 집중호우의 다양성은 인공신경망 알고리즘을 이용한 군집분석을 통해 발견되었는데, 각 군집들은 저마다 다른 일기 패턴의 발달양상을 보여주며 주요

발생시기 및 발생지역 또한 뚜렷한 차이를 보이는 것으로 나타났다. 따라서 지상 일기 패턴 기반 집중호우 유형 분류는 여름철 집중호우의 종합적인 이해 뿐만 아니라 예보에 있서도 도움이 될 것으로 기대된다.

TC-HREs 에 관한 기존의 연구들은 주로 태풍 자체의 특성이나 지형 등과 같은 국지적인 요소들에 집중해왔으나, 태풍에 의한 집중호우는 중위도 조건에 의해서도 매우 민감하게 반응하는 것으로 확인되었다. 중위도 순환이 경압적으로 불안정한 조건에 놓여있는 경우, 태풍이 유도한 상층 발산류가 음의 잠재와도 이류를 일으켜 중위도 대류권계면의 파동활동이 두드러지고(예: 상층 기압골의 정체 및 상층 기압능, 제트의 강화), 북상하는 태풍의 온대저기압화 또한 빠르게 이루어진다. 이는 태풍과 중위도 순환 사이에 강한 상호작용이 이루어지기 때문인데, 이는 태풍 전면의 넓은 지역에 강한 준지균 상승운동을 유발하고 그 결과 태풍이 한반도에 미처 상륙하기 전부터 집중호우가 발생할 위험을 초래한다. 반면, 중위도 경압 조건이 약한 경우 이러한 태풍-중위도 순환 상호작용이 거의 나타나지 않으며 태풍 또한 중위도로 진입 후 빠르게 약화되는 특성을 보인다. 집중호우와 연관된 연직운동은 주로 태풍의 잔여 비단열적 대류에 지배되는 양상을 보이며 그 결과 태풍이 한반도에 상륙하거나 가까이 접근했을 때 비로소 집중호우가 발생한다.

마지막으로, 이례적으로 많은 호우 피해가 발생한 2020 년 여름에 대한 사례분석을 수행하였다. 특히, 집중호우의 양상이 7 월 말 갑자기 바뀐 것에 주목하였는데, 6 월 29 일부터 7 월 27 일까지의 기간(P1) 동안 집중호우는 온대저기압의 통과에 의해 발생한 반면, 7 월 28 일부터 8 월 15 일까지의 기간(P2) 동안 집중호우는 정체한 몬순강우대 상의 중규모 불안정에 의해 발생하였다. 이러한 종관적 특성의 급변을 이해하기 위해 대규모 순환을 분석한 결과, P1 에는 북태평양 고기압이 서쪽으로 강하게 확장했으나 남중국해 대류 약화에 따른 파동 반응에 의해 북상하지 못한 채 남쪽에 머물렀고 그 결과 한반도로 온대저기압이 통과하기 좋은 조건이 만들어진 것으로 나타났다. 반면, P2 에는 다시 대류가 강화되어 북태평양 고기압의 가장자리의 강한 기압경도가 한반도 위에 놓이게 되어 몬순 정체전선이 발달하기 좋은 환경이 형성된 것으로

확인되었다. 특히 P1 시기의 남중국해 대류활동은 인도-북태평양에서 이루어진 대규모 대기-해양 상호작용과 연관되어 있었으며, 북대서양 여름 진동 또한 7 월 말 갑작스런 위상 변화를 통해 P1 과 P2 의 동아시아 몬순 순환에 서로 다른 영향을 준 것으로 판단된다. 2020 년 사례는 향후 집중호우 연구에서 중규모-종관규모-대규모 순환을 아우르는 다중규모 분석이 필요함을 시사한다.